Tumour Specific Targeted *In Vitro* Theranostics Application of Fabricated Nanostructures in a Multi-drug Resistant Ovarian Carcinoma Cell Line

A thesis submitted in fulfilment of the requirements for the award of Philosophiae Doctor (Biotechnology) in the Department of Biotechnology, Faculty of Natural Sciences, University of the Western Cape

CJF Taute

Supervisor: Dr M. Meyer
Co-supervisor: Dr. A. Madiehe

January 2013

ABSTRACT

Ovarian cancer is called the "Silent Killer" as it is often diagnosed in advanced stages of the disease or misdiagnosed which ends with a poor prognostic outcome for the patient. A high rate of disease relapse, a high incidence-to-mortality ratio as well as acquired multidrug resistance makes it necessary to find alternative diagnostic- and therapeutic tools for ovarian cancer. Nanotechnology describes molecular devices with at least one dimension in the sub-1μm scale and has been suggested as a possible solution for overcoming challenges in cancer multidrug resistance as well as early diagnosis of the disease. One-pot synthesized gold nanoparticles were used to demonstrate *in vitro* drug delivery of doxorubicin in a manner which overcame the cytoprotective mechanisms of a multidrug resistant ovarian carcinoma cell line (A2780cis) by inducing apoptosis mediated by caspase-3 within 3h of treatment. The gold nanoparticles were further functionalized with nitrilotriacetic acid and displayed specific interaction with a 6xHis-tagged cancer targeting peptide, chlorotoxin. Proprietary indium based quantum dots were functionalized with the same surface chemistry used for gold nanoparticles and bioconjugated with chlorotoxin. Wide field fluorescence studies showed the peptide-quantum dot construct specifically targeted enhanced green fluorescent tagged matrix metalloproteinase-2 transfected A2780cis cells in a specific manner. The cytoprotective multidrug resistant mechanisms of the ovarian carcinoma was overcome successfully with a single dose of doxorubicin loaded gold nanoparticles and tumour specific targeting was demonstrated using quantum dots with a similar surface chemistry used for the gold nanoparticles.

Chapter 1 is a literature overview of ovarian cancer with regards to statistics, therapeutic strategies, metastasis and mechanisms of acquired drug resistance. A cancer specific protease enzyme associated with metastasis, matrix metalloprotease-2 (MMP-2), and the highly specific interaction with a small venom peptide, chlorotoxin, was discussed with focus on cancer diagnostics as well as therapeutic targeting. The topic of nanotechnology was also discussed with a more topical review of gold nanoparticles and quantum dots. Applications of nanotechnology as proposed anti-cancer theranostic tools were also highlighted.

Chapter 2 describes the materials and methods used for this study.

Chapter 3 focused on the cloning, bacterial expression as well as the purification of the small venom peptide, chlorotoxin (CTX). A truncated C-terminal enhanced green fluorescent protein (EGFP) tagged MMP2 vector was transfected into A2780 cells for stable expression of the tMMP2-EGFP product. Quantum dot functionalized CTX demonstrated specific co-localization with tMMP2-EGFP during wide field fluorescence microscopy studies. The CTX interaction with recombinant MMP2 was investigated by enzyme kinetics which suggested an uncompetitive inhibition mechanism. Both experiments confirmed the interaction between CTX and MMP2, where the interaction was questioned in a recent publication.

Chapter 4 described the synthesis, functionalization and physicochemical characterization of ligands as well as nanoparticles utilized in this study. The gold nanoparticles were evaluated for colloidal stability in solution, with and without doxorubicin covalently loaded bound to the nanoparticle surface. The drug loading capacity of the gold nanoparticles were evaluated. Techniques used in this chapter included UV-Vis spectroscopy, high resolution transmission electron microscopy, energy-dispersive X-ray dispersive spectroscopy and fluorescence emission spectroscopy.

Chapter 5 focused on the *in vitro* drug delivery of gold nanoparticles surface functionalized with doxorubicin. A possible mechanism for the induced cell death was investigated and proposed to be caspase-3 mediated in response to oxidative stress within 3h of treatment. The sub-cellular localization of the gold nanoparticles was investigated by transmission electron microscopy and demonstrated peri-nuclear as well as cytoplasmic loci. Techniques used in this chapter included immunoblotting, luminescence- and colorimetric detection assays.

Chapter 6 is the overall discussion of the research conducted, followed by a conclusion and suggested future work.

Keywords: ovarian cancer, matrix metalloproteinase-2, multidrug resistance, gold nanoparticles, quantum dots, doxorubicin, synthesis, polyethyleneimine

DECLARATION

I declare that *"Tumour Specific Targeted in Vitro Theranostics Application of Fabricated Nanostructures in a Multi-drug Resistant Ovarian Carcinoma Cell Line" i*s my own work that has not been submitted for any degree or examination in any other university, and that all the sources I have used or quoted have been indicated or acknowledged by complete references.

C.J.F. Taute   January 2013

Signed: _____

ACKNOWLEDGEMENTS

ABBREVIATIONS

μL	Microlitre
μM	Micromolar
ABC	ATP-binding cassette
Amp	Ampicillin
APMA	p-Aminophenylmercuric acetate
APS	Ammonium persulphate
ARE	Antioxidant response element
ATR	Attenuated total reflectance
AuNP	Gold nanoparticle
BCA	Bichinconinic acid
BiPS	(2R)-[(4-Biphenylylsulfonyl)amino]-N-hydroxy-3-phenyl-propionamide
BME	β-mercaptoethanol
bp	Base pairs
BRCA	Breast cancer gene
BSA	Bovine serum albumin
C-terminal	Carboxyl terminus
CA-125	Cancer antigen 125
CAT scan	Computerized axial tomography scan
CD27	TNF superfamily member
cDNA	Complementary DNA
Cisplatin	Cis-diammineplatinum-(II) chloride

CPR1	Copper transporter protein-1
CTAB	Cetyltrimethyl ammonium bromide
CTX	Chlorotoxin
Da	Dalton
DAPI	4',6-diamidino-2-phenylindole
dH_2O	Deionised water
DMSO	Dimethyl sulfoxide
DNA	Deoxyribonucleic acid
DOX	Doxorubicin
DTT	Dithiothreitol
ECM	Extracellular matrix
EDC	1-Ethyl-3-(3-dimethylaminopropyl) carbodiimide
EDTA	Ethylene diamine tetra acetic acid
EDX (EDAX/EDS)	Energy-dispersive X-ray spectroscopy
EGFP	Enhanced green fluorescent protein
EOC	Epithelial ovarian cancer
EPR	Enhanced perfusion and retention
ESI	Electron spray ionization
FBS	Foetal bovine serum
FDA	Food and drug administration
FITC	Fluoroisothiocyanite
FPW	Full-peak width
FRET	Fluorescence resonance energy transfer

g.mol^{-1}	Gram per mole
GFP	Green fluorescent protein
GLOBOCAN	Global cancer statistics
GSH	Glutathione, reduced
GSSG	Glutathione, oxidised
GST	Glutathione S-transferase
HEPES	N-(2-Hydroxyethyl)-piperazine-N'-ethanesulfonic acid
HIV	Human immunodeficiency virus
HPLC	High pressure liquid chromatography
HPW	Half-peak width
HRP	Horseradish peroxidase
HR-TEM	High resolution TEM
HSP60	Heatshock protein 60
IC$_{50}$	50% Inhibitory concentration
IPTG	Isopropyl-β-D-thiogalactoside
kDa	Kilo Dalton
Keap1	Kelch-like ECH-associated protein
LB	Luria Bertani
LD$_{50}$	50% Lethal dosage
MDR	Multidrug resistance
MES	2-(*N*-morpholino) ethanesulfonic acid
mL	Millilitre
MLH1	MutL homologue-1

mM	Millimolar
MMP2	Matrix metalloproteinase-2
MMR	Mismatch repair
MNP	Magnetic nanoparticle
MOPS	3-(N-Morpholino)-propanesulfonic acid
mRNA	Messenger ribonucleic acid
MRI	Magnetic resonance imaging
MRP1	Multidrug resistance- associated protein-1
MT1-MMP	Membrane type I matrix metalloproteinase
MS	Mass spectrometry
MTT	(3-(4,5-Dimethylthiazol-2-yl)-2,5-diphenyl-tetrazolium bromide
MWCO	Molecular weight cut-off
N-terminal	Amino terminus
NER	Nucleotide excision repair
NGF	Nerve growth factor
nm	Nanometre
nM	Nanomolar
NMR	Nuclear magnetic resonance
NRF2	Nuclear factor-erythroid2-related factor 2
NTA	Nitrilotriacetic acid
OCT	Organic cation transporter
PAGE	Polyacrylamide gel electrophoresis
PBS	Phosphate buffered saline

PCR	Polymerase chain reaction
PET	Positron emission topography
PMA	12-O-tetradecanoylphorbol-13-acetate
ppm	Parts per million
PS	Penicillin-streptomycin
PSA	Prostate specific antigen
PEG	Polyethylene glycol
PEI	Polyethyleneimine
PEI-SH	Polyethyleneimine, thiolated
pI	Isoelectric point
PVDF	Polyvinyldifluoride
PVP	Polyvinyl-(pyrrolidone)
QD	Quantum dot
QD_{625}	Quantum dot, peak emission 625nm
qRT-PCR	Quantitative realtime PCR
RGD	Arginine-glycine-aspartic acid
RNA	Ribonucleic acid
SDS	Sodium dodecyl sulphate
SERS	Surface enhanced Raman spectroscopy
siRNA	Small interference RNA
SPR	Surface plasmon resonance
TBS	Tris buffered saline
TEM	Transmission electron microscopy

TEMED	*N,N,N',N'*-tetramethylethylenediamine
Tfb	Transformation buffer
TIMP	Tissue inhibitor of MMP2
tMMP2-EGFP	Truncated MMP2 tagged EGFP
TNF	Tumour necrosis factor
Tris	2-amino-2-hydroxymethylpropane-1,3-diol
TYM	Tryptone-yeast-maltose
WHO	World Health Organization
WST-1	(2-[4-iodophenyl]-3-[4-nitrophenyl]-5-[2,4-disulfophenyl]-2H-tetrazolium
UV-Vis	Ultraviolet-visible

UNIVERSITY *of the*
WESTERN CAPE

TABLE OF CONTENTS

Chapter 3: The Interaction between Chlorotoxin and Matrix Metallproteinase-2 – Tumour Specific Targeting   **91**

LIST OF FIGURES

LIST OF TABLES

List of Schemes

Chapter 1: Literature   Review

1.1   Introduction

1.1.1 Cancer: Overview of the Collective Noun

Cancer, as a disease, is a collective noun for a group of related diseases where normal cellular proliferation and division becomes abnormal. Altered molecular events prevent the cell from responding to inhibitory signals during the cell cycle checkpoints [1, 2]. Cellular immortalization takes place with loss of original cellular function and the cell will continue to proliferate, divide and confer the same ability to daughter cells which developed further abnormalities, resulting in tumour formation or tumourigenesis [1, 2]. If a tumour is not invasive to other tissues it is a benign tumour. If a tumour is invasive to nearby tissues or organs, the tumour is classified as malignant. Tumourigenesis should not be confused with carcinogenesis, in which the origin of a tumour can be traced directly to a relationship with a specific carcinogen [2]. Cancer has no specific identified individual cause where prevention is unlikely, but it has been suggested that altering lifestyle can act as a preventative measure [3-5]. Genetic inheritance can predispose an individual to developing certain types of cancer. Should a proto-oncogene or tumour suppressor gene be affected by a mutation, the risk of cancer can increase [1, 3-5]. The following non-inherited factors have been found to also play a role in tumour initiation:

(i)   Lifestyle factors − viral sexually transmitted disease, diet, alcohol consumption and smoking tobacco products [2, 4, 5];

(ii)   Gender − hormone specific cancers, e.g. testosterone or oestrogen dependant cancers and [1, 2];

(iii)   Environmental factors − biological toxins, chemical carcinogens or ultraviolet irradiation [2, 4, 5].

The traditional theory of somatic mutation being the only origin of cancer has fallen out of favour, as genetic events alone cannot explain the inherent complexity of cancer as shown by the genetic diversity of cells within the same tumour [1, 2, 6]. This paradigm shift is slowly replacing traditional views of cancer molecular biology.

1.1.2 The Statistics of Cancer

Global cancer statistics (GLOBOCAN) aim to consolidate data generated in different countries as well as the World Health Organization (WHO) to represent a uniform dataset. By time of going to press, the most recent worldwide consolidated published and peer reviewed cancer data set was for 2008. In 2008 12.7 million new cases of cancer were diagnosed globally and 7.6 million deaths were attributed to cancer in that same year, with 70% of these deaths in middle- to low income countries [7]. An estimated cancer related death toll of 13.1 million is being expected in 2030 according to the WHO [8]. The three cancers with the highest incidence of mortality for all ethnic groups and genders in 2008, expressed as percentage of total cancer deaths, were lung (18%); stomach (9.6%) and liver cancer (9.1%) [7, 8]. Breast cancer had the highest incidence of mortality in developing countries (Africa, Asia and South America) [7, 8]. Global incidence of cancer diagnosis as a collective disease for 2008 can be seen in Figure 1.1. North America, Western Europe and South-Central Asia had the highest diagnosis rates. Southern Africa and Middle Africa had comparative low incidences of cancer when compared to the developed countries.

Estimated Number of New Cancer Cases by World Area, 2008*

Worldwide*
12,667,500

1 Eastern Africa (221,100)
2 Middle Africa (66,900)
3 Northern Africa (164,400)
4 Southern Africa (79,200)
5 Western Africa (184,100)
6 Caribbean (79,300)
7 Central America (176,600)
8 South America (650,100)
9 Northern America (1,603,900)
10 Eastern Asia (3,720,700)
11 South-Eastern Asia (725,600)
12 South-Central Asia (1,423,100)
13 Western Asia (223,300)
14 Central and Eastern Europe (985,200)
15 Northern Europe (480,200)
16 Southern Europe (713,900)
17 Western Europe (1,034,300)
18 Australia/New Zealand (127,000)
19 Melanesia (7,000)
20 Micronesia (700)
21 Polynesia (1,100)

*Region estimates do not sum to the worldwide estimate due to calculation method.
Source: GLOBOCAN 2008.

Figure 1.1: Incidence of new cases of cancer worldwide in 2008 (Global Cancer Facts and Figures, 2nd Ed).

1.2 Ovarian Cancer: A Model for Therapeutics Development and Multi-drug Resistance Studies

1.2.1 A Statistical Perspective on Ovarian Cancer

At the end of 2011, ovarian cancer was the 8th most common diagnosed cancer in women (±250 000) in the North America with ±140 000 deaths reported, and ±24 000 new cases each year since 2008 [7, 8]. Also in 2011, it was the 5th most common diagnosed cancer in women in Europe with ±41 500 deaths reported in 2008 [7, 8].

Ovarian cancer presents with a high cancer dormancy rate post-treatment and presents with disease relapse within 15 months of initial diagnosis [9-12]. The North American 5 year survival rate of 30-45% for ovarian cancer is comparatively a low survival rate compared to the 5 year survival rate for breast cancer which is 89%, which is attributed to ovarian cancer being detected only in advanced stages [7, 9-12]. Survival rates for ovarian cancer may be higher in cases where diagnosis occurs in the early stages of the cancer [10-12]. In examination of Figure 1.4, it becomes clear that the mortality-to-diagnosis rate (per 100 000 population) of ovarian cancer is higher than the same ratio for breast cancer in North America, with women from Caucasian and African decent being most effected. Ovarian cancer has been identified by the WHO as the "Silent Killer".

Reliable statistical data of ovarian cancers relevant to the diverse multicultural South African population was not available. The statistical information was either outdated or non-informative. North America is a multi-cultural society and an argument can be made for data extrapolation to South Africa. If the socio-economic environment, traditional cultural beliefs as well as accessibility to proficient medical care are taken into consideration it begs to raise the question how many cases of ovarian cancer remains misdiagnosed or not diagnosed at all. Further, affordable medical care in the case of a cancer diagnosis is not available to the majority of South Africans. In the next sections, aspects of ovarian cancer will be discussed.
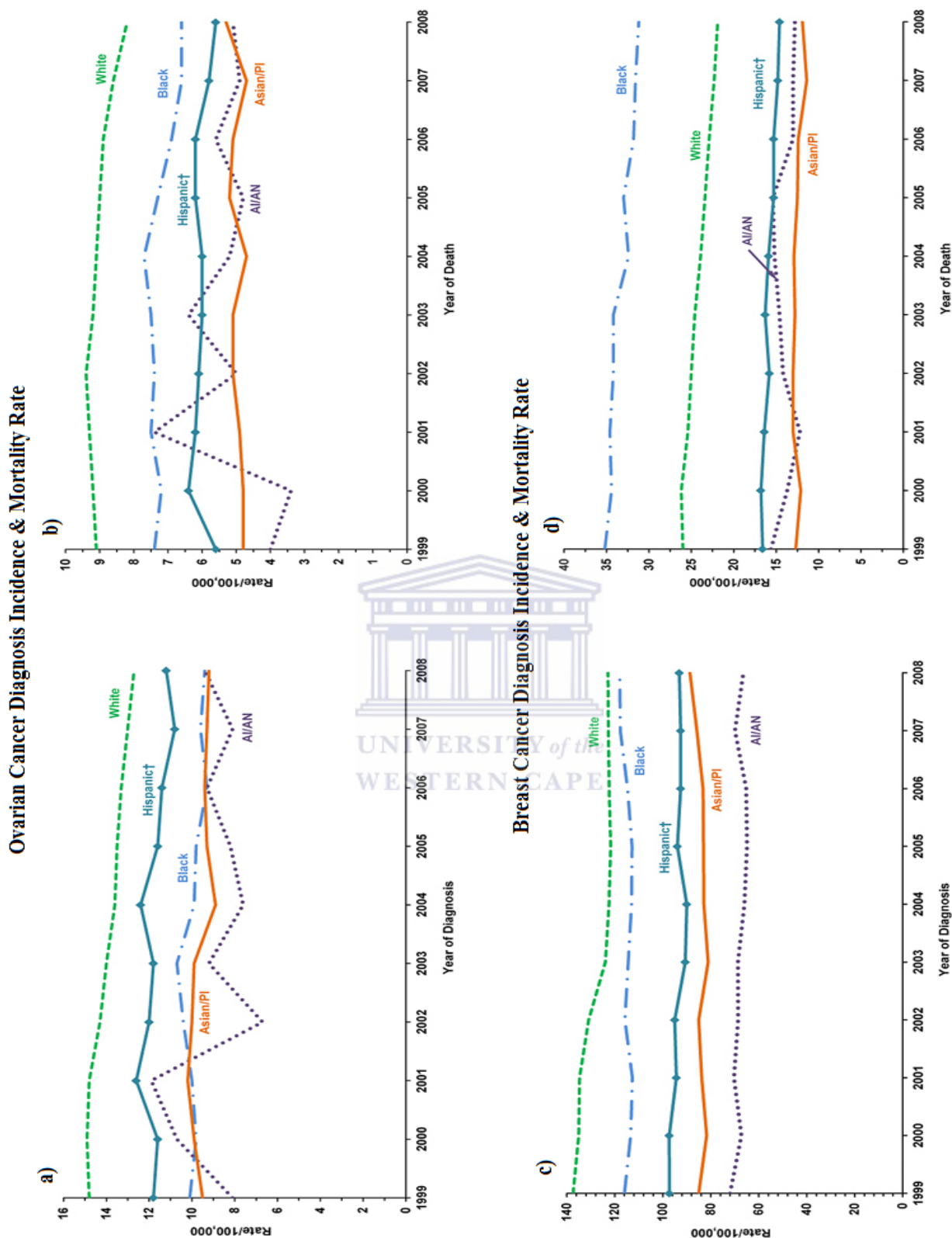
Figure 1.2: Comparative ovarian cancer and breast cancer diagnosis incidence and mortality rates for different ethnicities in North America. The diagnosis rate (per 100 000 population) for breast cancer (c) is higher than for ovarian cancer (a). When a comparison is drawn between the two cancers regarding mortality rates (per 100 000 population) in b) and d) it becomes clear that ovarian cancer has a higher mortality to diagnosis ratio than breast cancer, even across different ethnicities. (White – Caucasians; Black – African Americans; AI/AN – American Indian and Alaskan Native and Asian/PI – Asian and Pacific Islander). Figure obtained and modified from the North American Centre for Disease Control [9].

1.2.2 The Ovaries and Ovarian Cancer: Epidemiology and Pathology

Two ovaries (Figure 1.3) form part of the female reproductive system and are responsible for female sex hormone production, ovum production and regulation of the menstrual cycle. Ovary based hormone production will decrease with an increase in age until cessation of the menstrual cycle takes place. Ovum formation and release involves the formation of cysts on either ovary where physical rupture of the cysts releases the ovum into the fallopian tubes and the ruptures heal [10]. When cysts are present post-menstruation, have abnormal size or texture, or found in post-menopausal women a high risk for developing ovarian cancer is probable [10-14]. Further risks factors that may indicate an increased risk are: human papilloma virus (HPV) infections [10, 11], endometriosis [10, 11, 13], being overweight or above average height [10, 11], early-onset menstruation [10, 11, 13], late-onset menopause [10, 13], advanced age [10, 13] and smoking tobacco [10].
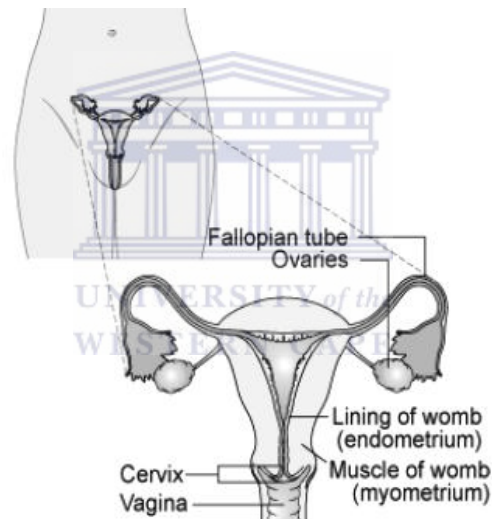
Figure 1.3: The female pelvic reproductive anatomy depicting the location of the ovaries (Image adapted from http://cancerhelp.cancerresearchuk.org).

In 1971, Fathalla and co-workers [15] hypothesized that accumulated repeated ovulation during a lifetime increased the risk for developing ovarian cancer. Selective apoptosis combined with cellular/DNA repair can increase the risk of developing chance mutations in the localized genome. This can be exacerbated by hormonal therapy, hyper ovulation and even diurnal disturbances. This hypothesis gained some evidence with observations by Fathalla *et al*, where hens developed peritoneal cancers under various hormonal treatments [15]. A familial history of ovarian cancer or breast cancer in two or more relatives indicates an increased risk of developing ovarian cancer [10-12, 16]. Mutations in the oncogenes

BRCA1 or BRCA2 are prognostic for a 23-54% increased chance of developing ovarian cancer [10-12, 14, 16].

Tumours can develop on the surface (epithelial cells) of the ovaries or the inside of the ovaries (germ cells and stromal cells). One or both ovaries can be affected. There are two main classifications of ovarian cancer, namely ovarian cancer of epithelial origin that makes up 90% of cases and the other 10% of ovarian cancer cases include germ cell cancer and sarcomas [10-12]. Only 5% of epithelial cancers are attributed to inheritance of a penetrative allele [10, 16]. Epithelial ovarian cancers (EOC) are further classified into serous; mucinous; endometrioid; clear cell; undifferentiated and unclassifiable cancers [10-12]. Epidemiological data suggests that the overwhelming majority of EOCs are serous in nature and defy the multistep model of tumourigenesis and are all treated as the same disease [10-12]. For the purposes of this review, the same assumption will be made regarding EOC.

Early stage symptoms of EOC are vague and ambiguous. The ovaries are located in the abdomen and as such any associated pain or discomfort can be mistaken for a benign condition, e.g.: pain in the lower abdomen, lower back pain and feeling bloated. Late stage symptoms are equally non-specific where abdominal pains, nausea, lower back pain, bloating, urinary tract symptoms, constipation, painful sexual intercourse, irregular periods and post-menopausal vaginal bleeding is predominant [10-14]. Cancer antigen 125 (CA-125), a surface glycosylated-protein, can be used as a disease biomarker, but unfortunately elevated serum levels of CA-125 do not always present in all cases of ovarian cancer with epidemiological data suggesting that detection is only significant in very late disease stages (III and IV) [10-12, 17]. CA-125 serum levels are more pronounced in late stages of the disease or for disease relapse, even if it was not present during initial diagnosis [10, 17]. Some findings demonstrated that CA-125 can present up to 9 months before macroscopic evidence of relapse is detectable [10, 17]. Other karyotyping techniques are less specific than CA-125 [10, 17]. Computerized Axial Tomography (CAT) scan [10, 14], ultrasound [10], x-ray imaging [10,] and explorative surgery (laparotomy) [10, 11, 18, 19] are the most reliable diagnostics tools for late stage detection but are still prone to a very high rate of misdiagnosis. All these techniques rely on how well a clinician can interpret the data. The same techniques are employed in determining the success of treatment and the rate of relapse, in which case the disease has become incurable [10-12, 17, 18]. Successful diagnosis

typically detects 70% of women in stage III or IV which leaves a poor prognosis for the patient [9-14, 18].

Ambiguous symptoms, ineffective screening technologies, invasive medical examinations, a high rate of misdiagnosis and a high incidence of disease relapse all accumulate into a poor prognosis for the patient. It becomes clear why ovarian cancer has such a comparative high mortality rate and a poor survival rate. In the next paragraph focus will be given to the current treatment strategies for EOC.

1.2.3 Current Treatment Strategies for Epithelial Ovarian Cancer (EOC)

Several factors play a crucial role when a clinician determines treatment strategies for ovarian cancer. Surgery is utilized for tumour debulking and complemented post-surgery with chemotherapy [18]. This is not always successful and neo-adjuvant strategies (chemotherapy pre-surgery) facilitate tumour shrinkage for ease of surgical excision [19]. Treatment should aim to improve the quality of life, delay the onset of symptoms related to disease progression and improve the survival rate of patients [10, 17-19]. Treatment strategies depend on:

(i) Tumour size [10, 18, 19]: The grade and stage of the tumour is under consideration. Early stage tumours can be treated without surgery if adequate chemotherapy strategies available. A tumour 5 cm in diameter is considered advanced. A malignant (invasive) tumour will typically be surgically excised.

(ii) Tumour position [10, 18, 19]: Metastasis, vascularity and accessibility of the tumour to excision will be evaluated. If the tumour is surgically inaccessible or excessive bleeding will follow as a result, chemotherapy and radiotherapy are the only options.

(iii) The physical condition of the patient [10, 18, 19]: The clinician will evaluate the patient's chance of surviving the surgery as well as recuperation ability. If the tumour is too far advanced, the clinician will only provide pain management measures.

It is feasible that the physician would also consider the mental and emotional condition of the patient as well as the wishes of the patient. It remains the prerogative of the patient to refuse treatment. The treatment options with regards to surgery and selected chemotherapies will be discussed in the following paragraphs.

1.2.3.1 Surgery

The physician will recommend that both ovaries and the uterus be removed (hysterectomy) unless childbirth is desired. Both ovaries will be removed, even if only one presents with a tumour growth, in a procedure termed a bilateral oophorectomy [18, 19]. Hormone replacement therapy will be recommended by most clinicians, post-chemotherapy [10, 18-20]. Excision of the tumour mass can lead to spontaneous metastasis which necessitates follow-up treatments with chemotherapeutics [10, 18-20]. Various internet-based ovarian cancer support groups suggest psychological counselling in the case of surgery. The hysterectomy and oophorectomy procedures are traumatic events which can exert a severe emotional and psychological stress on an individual.

1.2.3.2 Chemotherapy: Traditional Clinical Compounds

Chemotherapy is the utilization of small molecule-compounds that are administered orally, topically, intravenously or intra-peritoneal for the treatment of cancerous tissue [10, 20, 21]. Cancerous as well as non-cancerous cells are affected equally and even with tumour-specific targeting healthy tissue can still be affected presenting with side-effect symptoms such as nausea; vomiting; hair and nail loss; weight loss; cardiac complications; renal failure; hepatic failure and a compromised immune system [10, 20, 21]. Selected classes of anti-cancer compounds as applicable to this project will be briefly discussed in the following paragraphs.

1.2.3.2.1 Platinum-(IV) Compounds

Platinum-(IV) complexes have been used in combination therapy with alkylating agents as primary treatment for ovarian cancer and other epithelial cancers since the mid 1980's [20, 21]. Administration is intravenous or intra-peritoneal with systemic circulation time and half-life times being formulation specific [10, 20, 21]. These compounds all show poor aqueous solubility, poor cellular uptake which is also associated with neurotoxicity and nephrotoxicity [10, 22-24]. Modern analogues of these compounds show improvement of the aqueous solubility, lipophilic character and incorporate targeted delivery of these compounds to cancerous tissue [22, 24, 25].

Platinum-(IV) is reduced to platinum-(II) in the cellular milieu, activating the anti-cancer activity. The cis-position (Figure 1.4) of the chlorine atoms (electron withdrawing atoms) and primary amine molecules (electron donating molecules) facilitate the bio-reduction. Cell

ular uptake of compounds with a lipophilic character is optimal where there are sufficient electron donating groups for bio-reduction, such as primary amines (NH_2) and their derivatives [22].
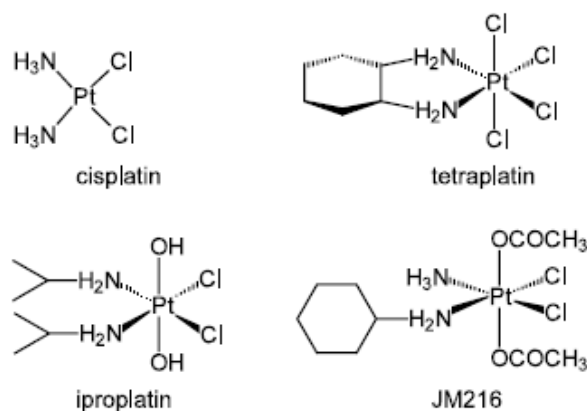
Figure 1.4: Examples of platinum-(IV) compounds used as chemotherapy agents. A motif shared by all molecules are the chlorine atoms (Cl) and primary amine molecules (NH_2) being in cis-positions. Figure is taken from [22].

Platinum-(II) forms cross-strand adducts with DNA, specifically on the adenine and guanine residues. This effectively destabilizes the double helix structure and acts as a steric hindrance to DNA-associated proteins [10, 22, 24]. Sulfhydryl (-SH) containing biomolecules have a high reactivity towards platinum-(II) and will form a covalent bond, nullifying the anti-cancer activity of the platinum-(II) compound [22, 24, 25]. EOC readily acquire drug resistance to treatment with platinum compounds, in some instances developing cross resistance [10, 18-21, 24, 25] and will be discussed in Section 2.4.

1.2.3.2.2 Anthracycline Anticancer Antibiotics: Adriamycin (Doxorubicin, DOX)

Doxorubicin (Adriamycin, 14-OH Daunomycin, DOX) is a potent anticancer antibiotic from the anthracycline class of molecules (Figure 1.5), produced by the fungus *Streptomyces peucius* [26]. DOX is used in the treatment of a variety of cancers: epithelial, endothelial and leukaemia [10, 26]. Mono- and combination therapy of DOX have been utilized for ovarian cancers since 1995 and was found to cause a lowered rate of disease relapse [10, 20-22, 26]. Currently all approved DOX formulations approved by the North American Food and Drug Administration (FDA) are under patent by Pfizer. Tissue distribution of the active metabolite indicates 50% bio-availability with systemic spread to all major organs and tissues with inactive doxorubicin excreted in the biliary system [26].

1 R= OCH₃, R'=H   Daunorubicin (Daunomycin)
2 R= OCH₃, R'=OH   Doxorubicin (Adriamycin)
3 R=OH,   R'=H   Carminomycin (Carubicin)
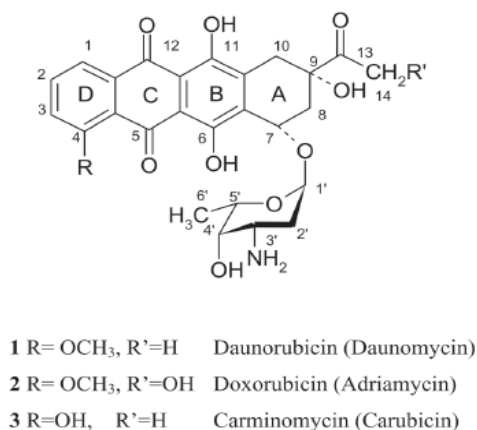
Figure 1.5: The structure of anthracycline anti-tumour antibiotics. Each analogue has a similar mechanism of anticancer activity, with carminomycin having the lowest systemic toxicity (A – cyclo-hexane ring; B – hydroquinone ring; C – semiquinone ring; D – phenyl ring). Figure is taken from [27].

There are two routes of administration according to the Pfizer CCO formulatory for physicians [26]:

(i)   Intravenous as a bolus, at a dosage between 10 mg/m² to 75 mg/m² and a half-life of 20 - 48 hours. The treatment frequency is dependent on the patients' physical condition, but not more than once a week as a recovery period is required.

(ii)   Intravesicle by bladder instillation, 50-100 mL, at a dosage of 50-80 mg/m² with subsequent bladder voiding after two hours. Frequency of administration is dependent on similar criteria as in (i).

Suggested mechanisms for DOX anti-cancer activity based on *in vitro* and *in vivo* models are: (1) DNA-intercalation (guanine and cytosine residues) and induction of single and double strand breaks [27, 30, 31]; (2) hydrogen-peroxide (H_2O_2) and / or superoxide ($O_2^{\cdot-}$) induced generation of oxygen- and nitrate free radicals [27, 28, 29]; (3) oxidative stress induced DNA mutagenesis [28, 30, 31]; (4) loss of mitochondria inner membrane potential [28, 30] and (5) inhibition of topoisomerase II [27, 31]. Patients have presented with side-effects related to cardiotoxicity, nephrotoxicity and hepatotoxicity as well as contact necrosis at site of administration [26]. Various *in vitro* and *in vivo* studies suggested that co-administration with reduced glutathione (GSH) [32], propionyl-L-carnitine [33] and L-carnitine [34] prevented cardiotoxicity and nephrotoxicity. *In vitro* genetics studies found that overexpression of peptides from the metallothionein family negates overall DOX associated toxicity [35]. Cross-reactivity with a host of other medications, food related compounds and bio-molecules have been extensively reported [34]. Ovarian epithelial cancers develop acquired drug resistance to DOX treatment [10, 21, 31] and will be discussed in section 2.4. Doxil®

(Caelyx) is a pharmaceutical grade nanoparticle based liposomal formulation with a decreased systemic toxicity and enhanced anti-cancer efficacy which has replaced traditional DOX therapy for ovarian- and other cancers [10, 11, 21, 36, 37].

1.2.3.3 Alternative Chemotherapeutics Treatment Strategies

No single treatment or specific combinations of treatments are equally effective in cancer therapy and as such adaptive strategies should be adopted for successful cancer therapeutics. There are many classes of chemotherapy agents available to physicians to treat ovarian cancers. They are typically used in combination therapy based on the required pharmacology effect required by physicians. A few will be briefly mentioned:

(i)   Taxanes (e.g. Paclitaxel/Taxol): Alkylating reagents that target microtubules and polarizes tubulin, interfering with mitosis [10, 11, 38, 39].

(ii)   Anti-angeogenics (e.g. Avastatin): Compounds that prevent or inhibit the formation of new tumour vasculature. Subsequently this induces tumour hypoxia and nutrient starvation [10, 20, 21, 39].

(iii)   Anti-oestrogenics (e.g. Tamoxifen): This class of compounds bind to oestrogen receptors and prevent hormone dependent signalling. Growth and survival signals are thus inhibited [13, 20, 21, 23, 39].

1.2.4 Mechanism of Disease Progression: Metastasis and Acquired Multidrug Resistance of Epithelial Ovarian Cancer

1.2.4.1 Metastasis of Epithelial Ovarian Cancer (EOC)

The multi-step hypothesis of tumourigenesis doesn't fully explain the disease development and progression of ovarian cancer. Evidence points to a cancerous stem cell as the origin of the disease [1, 6, 40, 41, 43, 44]. Support for this theory is strengthened by the various histologically distinct subtypes of EOC (see section 2.2) as well as the pattern of disease progression to metastases having no set course as opposed to other types of non-ovarian cancers. This suggests a distinct early cellular differentiation event in tumour development [40-42, 44].

Metastasis (Figure 1.6A) describes the spread of a single tumour cell from the site of origin to a secondary adjacent locus in the body. Current understanding of metastasis is based on studies done in murine models with subsequent *ex vivo* immuno-histological examination of the tissues [40, 42-44]. In humans only the final stage of metastasis is observed, where the

degree of metastasis is directly associated with prognosis and survival [40-44]. Disease progression is divided into four stages according to the Federation Internationale de Ginecologie et d'Obstetrique (FIGO, http://www.figo.org):

(i)   Stage I – The cancerous tissue is confined to one or both ovaries and is treatable with chemotherapy.

(ii)   Stage II – The tumour has grown in size and proceeded to invade nearby tissues in the peritoneal cavity. Combination therapy is recommended.

(iii) Stage III – The grade of the tumour has become aggressive with metastasis to the majority of the abdominal cavity and the lymphatic system. Combination therapy is recommended but prognostic outcome is poor with potential disease relapse.

(iv)   Stage IV – The final stage. Secondary tumour formation is found at distant organs not associated with the peritoneum.

Feki *et al* demonstrated in a murine model the aggressive metastasis of ovarian cancer into the peritoneal cavity via the lymphatic system by using a lentiviral-green fluorescent protein (GFP) reporter construct with *ex vivo* analysis of fluorescence tissue distribution [45]. Based on murine models, metastasis occurs in three main stages (Figure 1.6, A and B) where the tumour cell has to (1) invade the vascular system, (2) survive extracellular pro-apoptotic signals and evade the immune system and (3) colonize a new secondary site by tissue invasion [45, 46]. The first and last steps of metastasis are dependent on the metastatic potential or invasiveness of tumour cells. Metastatic potential is determined by suppressors or inducers in signalling pathways, where the cumulative effect will determine how invasive a tumour will be [40, 43, 44]. Various suppressors have been identified e.g.: cadherin on the cell membrane, members of the Rho-family of proteins in the cytoskeleton or caspase-8 in the mitochondria [40, 43, 44, 47]. Altered gene expression patterns, epigenetic gene modifications as well as chance mutations have been implicated in the metastatic potential of ovarian tumours, being demonstrated in both *in vitro* and *in vivo* studies [40, 44, 45, 47]. Induction of metastasis in EOC is associated with extensive extracellular matrix (ECM) remodelling, where matrix metalloproteinase-2 (MMP2) was identified as being a crucial protease with a prognostic link to disease progression, increased tissue invasion and metastasis [47, 48]. MMP2 will be discussed more in-depth in 1.3.
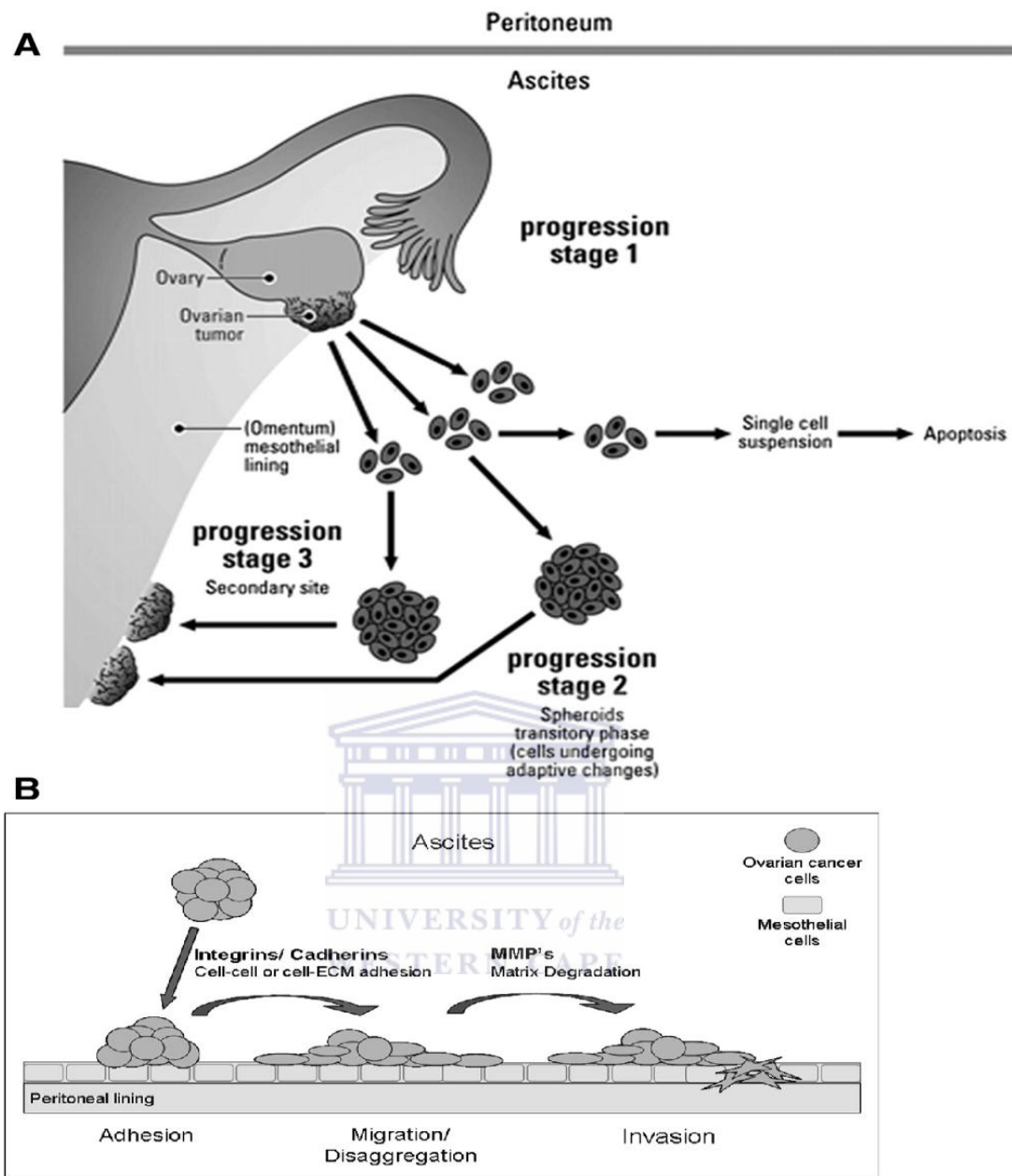
Figure 1.6: Metastasis of EOC from the primary tumour to a new site. New paradigms suggest that tumour spheroids have a higher success rate of metastasis than single suspension cells (A). Spheroids will disassociate and spread along the mesothelial surface, eventually leading to tissue invasion and formation of a secondary tumour (B). Figure is taken and adapted from [46].

The second step of metastasis requires the tumour cell to evade the immune system (macrophages and natural killer cells) successfully by suppression of gene expression for antigens or death-ligand receptors [46, 49]. Figure 1.6A gives a graphical representation of the traditional view on metastasis and the new hypothesis of tumour spheroid migration. During detachment and migration, single cells in suspension are vulnerable to the immune system as well as chemotherapy. A spheroid structure provides the cancer cells protection in multilayer cocoon. This increases the survival rate of the cancer cells during progression of

metastasis significantly. The chance that cells at the core of the spheroid survive to invade new sites is enhanced. Multiple cells which express tissue invasion proteins have a higher success rate of establishing a secondary tumour. This is proposed to be a potential explanation for the aggressive and invasive nature of EOC [45]. A 2009 review by Shield and colleagues provided significant evidence to suggest that in the case of ovarian carcinomas, the tumour cells metastasize in a spheroid [46]. In 2003, Zhang *et al* applied immune-histological techniques to examine tumour tissue isolated from cancer patients and came to the conclusion that tumour spheroids had a lower intra-tumour T-cell content than the rest of the cancerous tissue [48]. The outer layer of cells in the spheroid will be exposed to the immune system of chemotherapeutics. Based on the reported literature, it is feasible that the outer layer of tumour cells act as a protective layer for cells within the spheroid, effectively enhancing the survival and metastasis of the tumour.

Acquired multidrug resistance as a tumour survival mechanism will be the focus of the next few paragraphs.

1.2.4.2 Acquired Multidrug Resistance (MDR) in Epithelial Ovarian Cancer (EOC)

Tumour acquired multidrug resistance is considered to be multifactorial in origin and associated with primary tumours with possible causes being (1) increased resistance to DNA damage [50-53], (2) increased DNA repair mechanisms [50-53], (3) direct inactivation of cytotoxic compounds [52, 53], (4) decreased cellular accumulation of cytotoxic compounds [50, 52, 53], (5) sequestration of cytotoxic compounds in intracellular vesicles [50, 52] and (6) avoidance of pro-apoptotic signals [50-53]. This will be discussed with the focus on platinum based compounds and doxorubicin. The main focuses of these studies are all based on *in vitro* models. The full complement of acquired multidrug resistance mechanisms mentioned above has been identified in EOC.

1.2.4.2.1 DNA Repair Mechanisms and Gene Mutations

MutL homologue-1 (MLH1) is a mismatch repair (MMR) protein and has been found to be epigenetic silenced in various *in vitro* EOC models of acquired drug resistance [54, 55]. A reduced ability to repair DNA strand breaks at 3' loci induces microsatellite instability and has been shown to increase drug resistance [54, 55] as well as impairment of apoptosis induction [54-56]. In contrast, in a 2006 study no correlation was found between inactivated

MLH1 and increased drug resistance. This study made use of quantitative real-time polymerase chain reaction (qRT-PCR) experiments on tissue obtained from 75 ovarian cancer patients on cisplatin treatment [56]. DNA alkylation and strand breaks are proposed mechanisms for platinum-compounds and doxorubicin (see 1.2.3). The overexpression of pro-apoptotic and inhibition of anti-apoptotic proteins failed to induce apoptosis in drug resistant MLH1 deficient A2780 cells [54, 55, 63]. Increased nucleotide excision repair (NER) has been shown to be the predominant DNA repair mechanism in drug resistant cancers and with NER inhibition the cells displayed increased sensitivity to cisplatin [55, 57].

Mutations in essential and diverse cellular homeostasis genes and their protein products have also been linked to acquired multi drug resistance. Genes which have been found mutated in acquired MDR in EOC reported in the literature include DNA-topoisomerase II [51], Bcl-2 protein family [58, 59] and caspases [60]. The regulators of caspase gene expression have been reported to inhibit apoptosis in cancer as well as lead to acquired multidrug resistance [61, 62]. In the case of acquired drug resistance for alkylating chemotherapeutics it was found that the levels of pro- and anti-apoptotic proteins did not play a role in the tumour cell survival [63], suggesting a re-evaluation of current dogmas. Mutations in the tumour suppressor *p53* have been directly linked to multidrug resistance in EOC [64, 65]. In a 2001 publication Reles *et al* identified through genetic studies that 110 of 178 (62%) EOC patients had several mutations in the exons as well as introns for *p53* [65].

1.2.4.2.2 The Glutathione Pathway and Antioxidant Response to Cytotoxicity of Anti-cancer Compounds

Glutathione (GSH) is the main cellular antioxidant defence molecule. It has a thiol (-SH) moiety with a strong nucleophilic character. Aqueous solubility is conferred by the carboxylic acid (-COOH) and primary amine (-NH$_2$) groups. Glutathione pathways can be seen in Figure 1.7, where consumption and synthesis is depicted. Xenobiotic compounds, hydrophobic molecules and cytotoxic compounds can be glutathiolated [66]. This can be by direct nucleophilic substitution of the thiol moiety on reactive electrophilic centres or by enzymatic bioconjugation catalysed by glutathione-S-transferase (GST) [66]. The glutathiolated compounds will undergo exocytosis from the cell, either by passive means or facilitated in an ATP-dependent process by drug efflux pumps (Figure 1.8). Feedback inhibition determines glutathione metabolism and regulates the tempo of *de novo* synthesis, salvage and bio-conjugation (Figure 1.7). The role of glutathione synthesis and glutathione-S-

transferase activity was implicated in the early 1990's in the development of acquired drug resistance in ovarian cancers [67, 68]. The glutathione pathway plays a role in a larger antioxidant defence pathway which includes cytochrome p450, phase II detoxification enzymes, membrane transport proteins and cytoskeleton associated proteins.

The whole antioxidant defence pathway is regulated by a transcription factor nuclear factor-erythroid 2-related factor 2 (NRF2) [69, 70]. A study done in 2005 by Cho and colleagues on a murine model identified 446 genes directly associated with the transcription factor NRF2 [69]. The antioxidant response element (ARE) is a DNA sequence on the promotor region of cyto-protective genes to which NRF2 will bind in response to oxidative stress. NRF2 was assumed to be induced by a chemo-preventative pathway. The assumption regarding NRF2 has been called into question recently. In an invited review Lau *et al* proposed very strong evidence that indicates NRF2 may promote cancer disease progression, especially in response to chemotherapeutic compounds [71, 72]. This was supportive evidence for a 2009 publication where Hayes *et al* found that somatic mutations in *nrf2* as well as its inhibitor gene, *keap1*, may predispose an adaptive response to chemotherapy in the form of acquired drug resistance [70].

Evidence emerged for acquired doxorubicin resistance in ovarian carcinomas in 2009 when Shim *et al* demonstrated involvement of the NRF2 pathway. Increased antioxidant capacity paired with increased drug efflux was identified in the A2780 cell when it became drug resistant to doxorubicin. When NRF2 was knocked down using siRNA, the cells were sensitive to doxorubicin treatment again [72]. Nrf-2 regulates glutathione biosynthesis and glutathione redox-cycling independently [73], where up-regulation of both pathways is associated with increased- and acquired multidrug resistance [51, 66-68]. The result is a very active antioxidant defence mechanism which has an adaptive response to oxidative stress.

The glutathione pathways are well characterized and form an essential part of any oxidative stress study. This makes the glutathione pathways an essential tool to investigate drug resistance as well as antioxidant capacity of cells. Glutathione is one of the many biomolecules which is involved in drug efflux (Figure 1.8), which will be the focus of the following section.
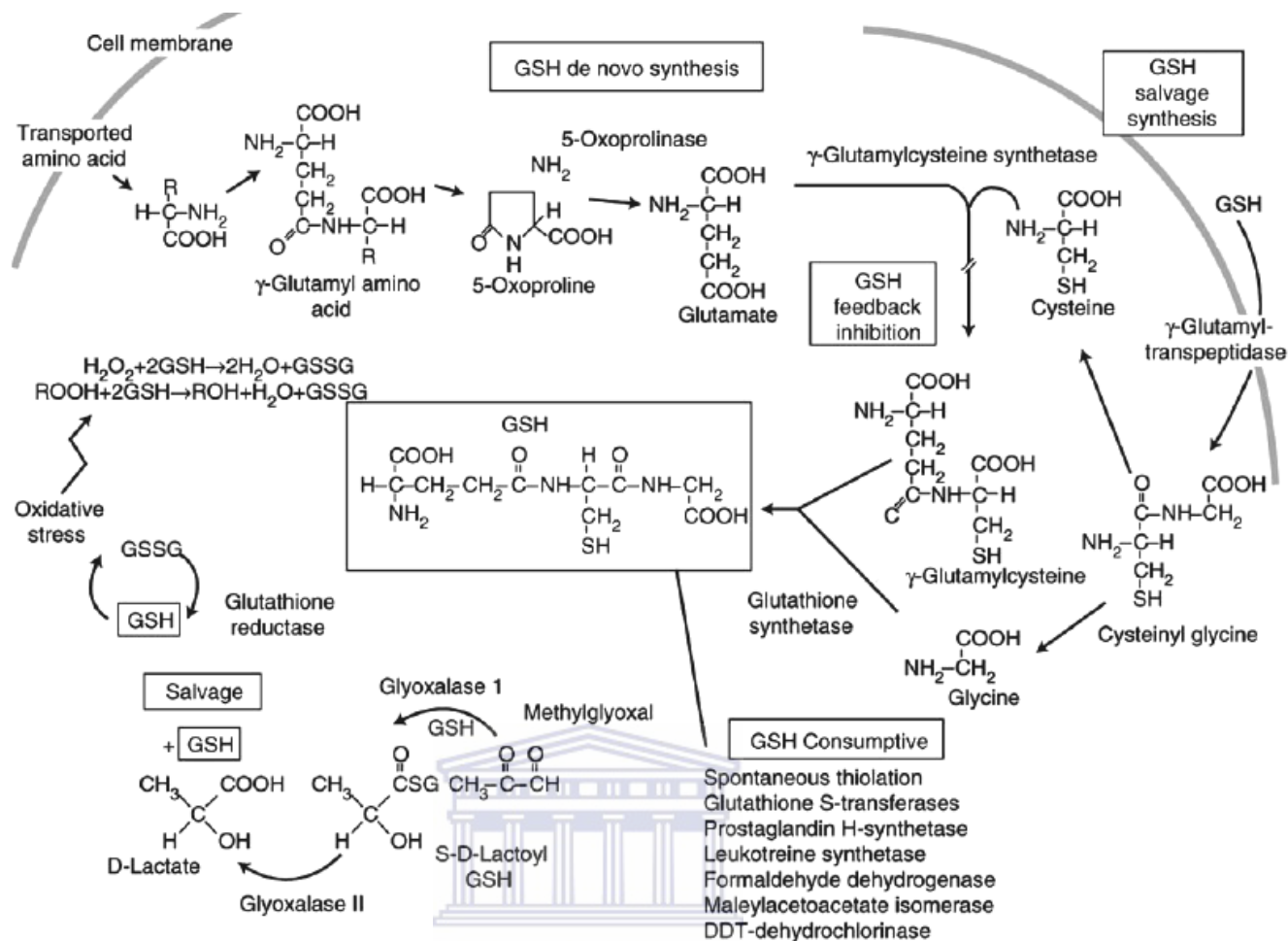
Figure 1.7: Glutathione metabolism and its role in the antioxidant defence of the cell (GSH – Reduced glutathione; GSSG – Oxidised glutathione). Figure is taken and adapted from [66].

1.2.4.2.3 Internalization, Transport and Efflux of Chemotherapeutic Compounds

Efficacy of treatment with anticancer compounds requires adequate intracellular drug accumulation. Cellular membrane bound influx proteins such as copper transporter protein-1 (CPR1) [74, 77] and the family of organic cation transporters (OCTs) [75, 77] were shown to facilitate cisplatin influx in the A2780 ovarian carcinoma cell line. With acquired drug resistance, these transporters will be internalized or inhibited at a translational level, effectively preventing cisplatin cellular internalization and accumulation [74-77]. Vacuole-like structures (Figure 1.8) and other vesicles are used to sequester cytotoxic compounds and exocytose their contents, in an ATP-dependent manner, from the cell [75, 77]. The ATP-binding cassette (ABC) transport protein family are ATP-dependent trans-membrane proteins which have been shown to decrease cellular drug accumulation for various anti-cancer

compounds [76, 77]. All members of this family can be induced by NRF2 in a tissue specific manner [69].

Sensitivity to liposomal doxorubicin treatment was enhanced in an *in vitro* A2780 cell line by using antisense oligonucleotides targeted to MRP1-mRNA and Bcl-2-mRNA. Western blotting and fluorescence microscopy confirmed decreased protein expression, enhanced cellular doxorubicin accumulation and apoptosis induction [78]. Annexin A3 was identified as a new biomarker for multidrug resistant ovarian cancer when Yan and colleagues found elevated mRNA and protein in various models: *in vitro, in vivo* murine and in cancer patient tissue samples [79]. Decreased cellular accumulation of cisplatin was associated with increased expression of Annexin A3, suggesting a drug efflux role for this protein. It was reported to be present in the urine of prostate cancer patients, but no study has yet investigated if similar findings have been found for ovarian cancer.
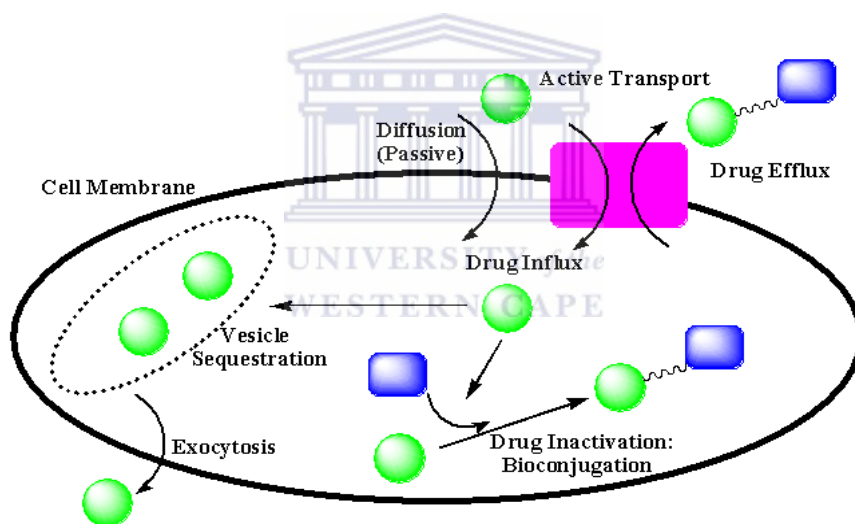
Figure 1.8: A simplified schematic representation of the fate of chemotherapeutic compounds in a MDR cancer cell. A drug (green sphere) internalize passively by diffusion, endocytosis or active transport. In multidrug resistant cancer cells the drug will be either sequestered in vesicles to be shielded away from the cytoplasm or the drug will be inactivated. The inactivation will be either enzymatic or by bioconjugation (blue rectangle). Exocytosis or active transport will be the mechanisms by which the drug will be transported out of the system.

Ovarian cancers adapt with consecutive treatments to obtain acquired multidrug resistance. This is true especially for disease relapse, such as with EOC. Mortality is directly correlated to acquired multidrug resistance and late stage initial disease diagnosis. Socio-economic factors are implicated to play a significant role in timely cancer diagnosis. If the disease cannot be diagnosed in an early stage, improvement of treatment strategies should be an alternate focus area.

1.3 The Role of Matrix Metalloproteinase-2 (MMP2) in Epithelial Ovarian Cancer

1.3.1 Matrix metalloproteinase-2: Nomenclature, Structure and Function

Matrix metalloproteinase-2 (Gelatinase A / Collagenase IV, EC 3.4.24.24) is a soluble 72kDa enzyme which is part of a family of zinc-dependent proteases [80, 81, 86]. This endopeptidase is secreted as an inactive pro-enzyme (zymogen, Figure 1.9) in mesenchymal and epithelial cells during tissue development and extracellular matrix remodelling [80, 81]. MMP2 recognises the following amino acid motif: Pro-Gln-Gly-/-Ile-Ala-Gly-Gln [81,82]. Cleavage takes place between the glycine (Gly) and isoleucine (Ile) residues in the above mentioned motif. Substrates which have been identified for MMP2 include collagen type IV [80-82, 92], collagen type V [82, 83, 92], gelatin [80-83, 92], fibronectin [82, 83, 92] and elastin [82, 83, 92]. Collagen type IV forms part of the basement membrane of the extracellular matrix (Figure 1.8). Serum- and tissue MMP2 activity appears to be directly correlated to a poor prognosis for cancer patients [47, 48, 84, 86] and MMP2 has been identified as a key role-player in extracellular matrix remodelling [80, 81, 83, 92], cell detachment from the primary tumour [84, 86, 92], angiogenesis [83, 84, 86, 92], tissue invasion [83, 84, 86, 92] and avoidance of apoptosis [84, 92]. Solid tumours of epithelial origin are particularly associated with MMP2 dependent disease progression [84, 86, 92]. A range of solid and metastatic tumours in which MMP2 mRNA and MMP2 protein were reported can be seen in Table 1. Cardiovascular disease [96, 97] and HIV-associated neuroencephalopathy [98, 99] have shown to have a direct correlation between MMP2 activity and a poor prognostic outcome as well.
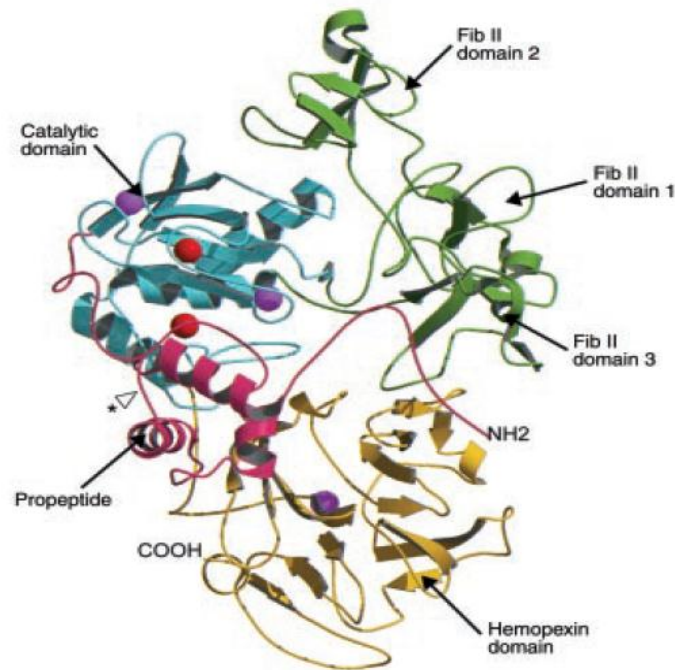
Figure 1.9: The structure of pro-MMP2. The catalytic domain (magenta) has two zinc cations (red) and two calcium cations (purple) bound. The C-terminal hemopexin domain (yellow) has one calcium cation (purple) bound and is exposed to the cytoplasm when the protein is in a transmembrane position. Figure is taken from [80].

Table 1.1: Matrix metalloproteinase-2 expression in solid- and metastatic tumours

Cancer Type	Tissue Type	mRNA	Protein	Reference
Ovarian	Human Biopsy; *in vitro*	↑	↑	[85, 86]
Melanomas	*In vitro; in vivo*	↑	↑	[87, 88]
Brain	Human Biopsy; *in vitro*	↑	↑	[88, 90, 95]
Breast	Human Biopsy; *in vitro*	↑	↑	[86, 90, 91, 95]
Cervix	Human Biopsy; *in vitro*	↑	↑	[86, 90]
Prostate	Human Biopsy; *in vitro*	↑	↑	[86, 90, 92, 95]
Renal And Bladder	Human Biopsy; *in vitro*	↑	↑	[86]
Lung	Human Biopsy; *in vitro*	↑	↑	[86, 95]
Head And Neck	Human Biopsy; *in vitro*	↑	↑	[86, 90]
Gastrointestinal	Human Biopsy; *in vitro*	↑	↑	[86, 93, 94, 95]
Testes	*In vitro*	↑	-	[90]
Bone	*In vitro*	↑	-	[90, 95]
Eye	*In vitro*	↑	-	[90]
Thyroid	*In vitro*	↑	-	[95]
Leukemia	*In vitro*	↑	-	[95]

*↑ **indicates an increase in the respective intracellular level**

During protease activation (Figure 1.10) the signalling peptide and pro-domain will be cleaved, yielding a mature protease of ~62kDa [85, 93]. It has been shown that autolytic cleaved variants of MMP2 (68kDa [99], 58kDa [90, 93], 54kDa [90], 50kDa [99] and 44kDa [99]) still retain catalytic activity. Three fibronectin domains are embedded in the catalytic domain which allow for substrate binding [80]. In the pro-enzyme the cysteine residues are bound covalently to the Zn^{2+}-binding sites to prevent autocatalytic activation [80, 82]. A C-terminal hemopexin-like domain contains a Ca^{2+}-binding site and is linked to the catalytic domain by a hinge region [80, 82]. The hemopexin domain structure is speculated to determine the substrate specificity and is cytoplasmic orientated in the event that MMP2 is in a transmembrane position [80]. MMP2 activity is optimal at physiological pH to mildly basic conditions at $37\,^{\circ}C$ [82, 98].
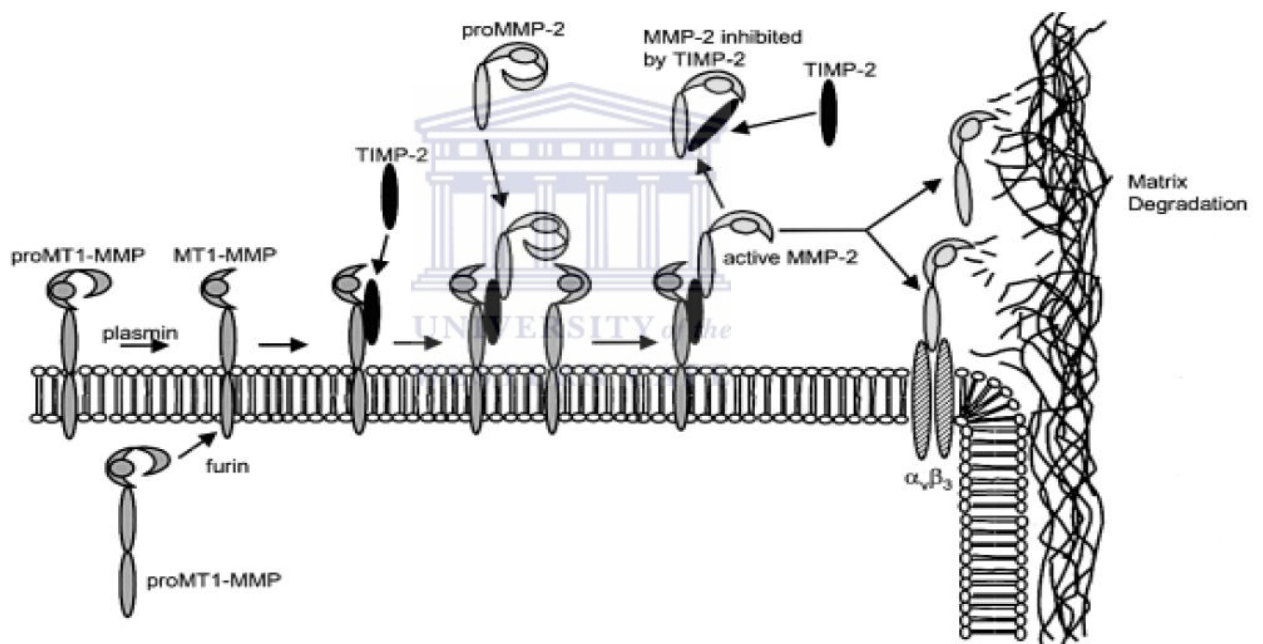
Figure 1.10: The activation of pro-MMP2 by MT1-MMP on the cell plasma membrane. Active MMP2 will degrade collagen and gelatin in the extracellular matrix. Figure is taken from [86].

There is discrepancy as to where pro-MMP2 is sequestered within the cell, as it can be activated by various cytosolic proteases [86, 100]. MMP2 has been implicated in PARP-cleavage during apoptosis which implies nuclear translocation and catalytic activation [97].The natural inhibitor of MMP2 is tissue inhibitor of MMP2 (TIMP-2) which binds to the protease in the hemopexin domain [80, 82, 101]. The pro-enzyme and mature enzyme can also be found as part of a trans-membrane protein complex with TIMP-2 and membrane type 1 matrix metalloproteinase (MT1-MMP) in close proximity to the integrin $\alpha_V\beta_3$ (Figure 1.10) [85-87, 102-104].The trans-membrane complex bound pro-enzyme will stay inactive in a

stoichiometric ratio of 1:1 with TIMP-2 [86, 101]. Overexpression of pro-MMP2 or decreased expression of TIMP-2 will facilitate MMP2 catalytic activation by MT1-MMP [102-104]. Mature MMP2 can be secreted into the extracellular matrix or be internalized into the intracellular environment [86, 102-104]. Proteolytic activity of MMP2 is delicately regulated on transcriptional- and post-translational level. Phosphorylation has been identified to play regulatory roles in zymogen transcription and translational activation [105] where ERK1/2 and p38-MAPK have also been implicated [106]. Increased superoxide dismutase transcription and translation increased MMP2 mRNA levels [107]. Non-enzymatic activation of MMP2 can be induced by organomercurial compounds [80] and sulfhydryl (SH) containing molecules [80].

The substrate specificity of MMP2 has allowed for the development of colorimetric- [81] and fluorometric [82] peptide-based probes as well as various inhibitors [108, 109], which has been utilized in *in vitro*-based diagnostics as well as *in vivo* tumour imaging. These probes all employ variations on the fluorescence resonance energy transfer (FRET) technique. MMP2 synthetic inhibitors showed promise *in vitro* but were less effective for *in vivo* models and clinical trials and were less effective in cases where the disease was in advanced stages [108-110]. Similarly antibody-based therapeutic targeting was promising by using anti-MMP2 drug delivery systems but has yielded disappointing results *in vivo* [109, 110]. In the above mentioned studies the respective authors did not venture to provide reasons for the disappointing results. Radio-labelled inhibitor peptides have gained some success in MMP2 imaging with techniques such as positron emission tomography (PET) and magnetic resonance imaging (MRI) in cancer patients [108, 109]. Confirmation of MMP2 activity in tissues and biopsy samples still has to be routinely done with laborious zymography techniques [110-112]. Currently the use of MMP2 specific ligands and inhibitors are being utilized to target nanoparticle liposomal formulations to cancer cells [113, 114].

1.3.2 The Role of MMP2 in Epithelial Ovarian Cancer

Davidson *et al* utilized *in situ* colorimetric RNA hybridization techniques on tissue biopsy samples from ovarian cancer patients in various disease stages to determine mRNA expression patterns of MMP2, MT1-MMP, TIMP2 and MMP9 [115]. The data suggested a poor prognosis in direct correlation to high MMP2 mRNA expression levels. This relationship was even more evident for cases of late stage disease or disease relapse. Davidson *et al* reported similar results were observed for corresponding protein levels but

results were not published. In a 2009 *in vitro* study on ovarian carcinoma cells, Roomi and co-workers found that phorbol myristate acetate (PMA) induced MMP2 protein activation [90]. Preferential expression of active MMP2 was observed for ovarian carcinoma cells and not MMP9. The converse was true for some cervical cell lines. A 2006 study by Shen *et al* found that PMA and lipopolysaccharide induction of MMP2 in glioma cells was inhibited by dietary flavonoid compounds [116]. Although this study was not done on ovarian cancer cells it is feasible that a similar effect could be expected for dietary flavonoids which may indicate potential therapeutic applications. These results appear to add merit to the theory of metastasis-to-evade-apoptosis and as such, MMP2 could be an early stage indicator of development of acquired multidrug resistance. This idea receives additional support if it is considered that superoxide dismutase is regulated by NRF2. A recent study on the role of NRF2 in epithelial ovarian cancer found a strong link between acquired drug resistance and mutations in the inhibitor of NRF2, Keap1 [117]. A diagnostic test which predicts the development of acquired multidrug resistance can give clinicians a foot in the door. Preventative measures can be taken to alter the combinatorial treatment strategy before full blown drug resistance sets in.
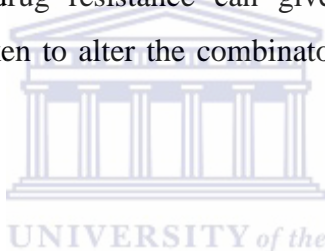
1.4 Chlorotoxin: A Matrix Metalloproteinase-2 Targeting Venom Peptide from the Deathstalker Scorpion

1.4.1 Origins and Biochemistry

Chlorotoxin (CTX) is a 4.3kDa, 36 amino acid residue peptide that was first isolated from the venom of the "Deathstalker" scorpion (*Leiurus quinquestriatus*) by Debin *et* al in 1991 [118]. There are 8 cysteine residues which contribute to 4 disulphide bridge formations in this small peptide [119, 120] and can be seen in Figure 1.11. The cysteine residues are thought to play a role in stabilizing the structure of the peptide [121]. This peptide is a potent invertebrate neurotoxin and has been shown to bind to chlorine channels [118]. Deshane *et al* were the first to find that CTX inhibits glioma progression, metastasis and angiogenesis [122]. Deshane and colleagues filed for and obtained a patent on the CTX-MMP2 interaction as treatment for glioma in 2003. In mammals histological [122, 123] as well as *in vivo* studies [123] implicated CTX as having a high affinity to the majority of glioma subtypes where this association was directly associated with MMP2 activity in these tumours. Zymography studies determined that the IC_{50} value of CTX for inhibition with MMP2 was 100nM [119]. The exact nature of the interaction between CTX and MMP2 has not yet been fully described

in the literature. CTX itself will enter the cell through a chlathrin mediated endocytotic pathway in the absence of membrane bound proteins to interact with [124]. No systemic toxicity towards vertebrates and no cytotoxic effects to mammalian cells have been reported [122, 123]. The typical RGD-motif is not present in the sequence of CTX as for other cancer targeting peptides, but the 3 lysine residues have been shown to play a direct role in CTX affinity for glioma cells [125]. With alteration of the lysines (K) to alanines (A), a decreased affinity to target glioma was observed in murine magnetic resonance imaging (MRI) studies. This study did not investigate the direct CTX-MMP2 mechanistic interactions.

CTX is commercially available from various distributors. It can also be obtained by direct purification from the venom gland of the scorpion or it can be produced by using molecular biology methods. The strategy most researchers employ is to introduce an affinity tag onto the peptide for ease of purification [126]. Undirected chemical conjugation techniques, e.g.: carbodiimide chemistry [127], are typically utilized to attach CTX to various types of molecules.

1.4.2 Current Research and Therapeutic Strategies Exploiting the CTX-MMP2 Interaction

The therapeutic and diagnostic applications of CTX have been explored by various cancer researchers. Veiseh *et al* developed a Cy5.5-CTX tumour contrast dye which can fluorescently label the tumour and facilitate surgeons to image cancer cells in a realtime bi-photonic imaging system during surgery [128]. Conjugation of dyes or other molecules to CTX has not been reported to affect the affinity of CTX for glioma cells. It is to be expected that this holds true for other solid tumours as well. Mamelak and colleagues developed an iodine-131 labelled synthetic version of CTX, TM601, as an intravenous glioma treatment in 2006 for Phase-I clinical trials [129]. The cross application to other tumours was investigated by Lyons *et al*, with his research group confirming that normal non-cancerous tissues showed no traces of TM-601 [130]. A group under the leadership of Douglas Jacoby found that TM-601 has potent anti-angiogenic, anti-metastasis and growth inhibitory effects on various types of cancers [131]. As of 2010, TM-601 was in phase II clinical trials. TM-601 is retained up to 8 days at the tumour site and excreted in the urine, with significant tumour shrinkage taking place in the said duration of treatment [131]. Recently, in 2010, the CTX-MMP2 interaction was called into question by a study done on TM601 which identified Annexin A2 as the

molecular target [132]. The authors however did not indicate if this altered molecular target may be an effect of the modification of the peptide. Also, the authors did not include contrasting experimental data with MMP2 included in the study. The question arises whether there is a conserved sequence homology between MMP2 and Annexin A2.

CTX itself has been identified as a viable targeting vector for various nanoparticle based strategies in the past decade. Magnetic nanoparticles have been functionalized with CTX to act either as diagnostic agents, multimodal imaging-drug delivery agents or gene delivery agents [133, 134, 136]. Fluorescent nanoparticle-CTX conjugations have also been employed effectively in *in vitro* and *in vivo* fluorescent imaging applications [126, 137].

The application of CTX as a diagnostic tool [136, 137] or an anticancer targeting moiety becomes more apparent if one considers the expression of MMP2 in cancer cells (1.3, Table 1.1). The range of cancers that can be investigated makes this peptide a very important investigative tool. Further application goes above and beyond cancer treatment. Any disease where MMP2 levels are elevated (e.g. cardiovascular disease or HIV) can be targeted in a CTX based strategy to achieve either a diagnosis or to facilitate therapy. The diagnostics as well as therapeutic potential of CTX becomes more evident if the ability of said peptide to cross the blood-brain-barrier is considered. There may be an application for CTX in neurodegenerative diseases such as Alzheimer's, Parkinson's and Huntington's disease. In all these diseases some variant of tissue remodelling and breakdown occur.

1.5 Current Therapeutic and Diagnostic (Theranostic) Applications of gold nanoparticles (AuNPs) and semiconductor nanocrystals quantum dots (QDs)

A trend in peer reviewed literature as well as international conferences seems to indicate that AuNPs are losing favour as drug delivery vehicles with soft nanoparticles, such as liposomes and polymer nanoparticles, are seen to be more suited for diagnostics. AuNPs and other metallic based nanoparticles were still favoured for diagnostic as well as biosensor applications. The Gordon's Conference Noble Metal Nanoparticles 2012 as well as the Elsevier-Oxford Journals Colloids and Nanomedicine 2012 conference confirmed this shift in nanoparticle applications. In the next few paragraphs some applications of nanoparticles, in

particular gold nanoparticles and fluorescent quantum dots, will be highlighted. Terminologies as well as applicable in-depth aspects of nanoparticles will be discussed in section 1.6.

Frank Caruso's research group demonstrated at the Colloids and Nanomedicine conference the use of capsosomes [138]. A capsosomes is a "Russian doll" liposomal or polymer nanoparticle in which each liposomal layer can be systematically stripped away to release a chemotherapeutic or chromophore payload. Each liposomal layer can be engineered to have a pH or protease dependent release. In such a way a multimodal theranostic nanoparticle is created. Molly Steven's group demonstrated an *in situ* gold nanoparticle based diagnostic for prostate specific antigen (PSA) [139] at the Gordon's Research Conference Noble Metal Nanoparticles 2012. Glucose oxidase (Gox) is covalently immobilized on the AuNP surface, where the AuNP-Gox nanoconstructs are suspended in an aqueous hydrogen peroxide (H_2O_2) solution with a predetermined concentration of silver nitrate ($AgNO_3$). In the presence of glucose, silver nanoparticles will be synthesized in the reducing environment facilitated by the enzymatic action of glucose oxidase and its cofactor H_2O_2. The UV-Vis spectra as well as surface plasmon band of the newly formed silver nanoparticles will be proportionate to the amount of analyte present.
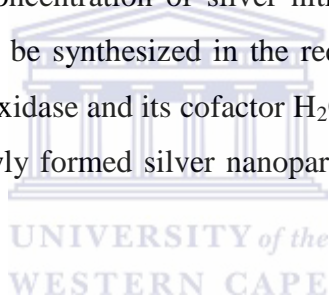
Gold nanoparticles (AuNPs) have been used as drug delivery vehicles *in vitro* and *in vivo* (Table 1.2). The chemotherapeutic compounds are immobilized on the AuNP surface and as such will be exposed to the surrounding environment which can have unwanted side reactions. These concerns will be highlighted and discussed in Sections 1.6 and 1.7. The utilization of metallic nanoparticles as drug delivery systems is still a novel tool which is being developed as most studies are *in vitro* based as seen in Table 1.2. The surface plasmon resonance (SPR) of AuNPs makes them ideal for colorimetric based diagnostics [140-142]. Antibody functionalized AuNPs have been successfully applied as high contrast stains for immunohistology darkfield microscopy [141]. Further, the physicochemical character of AuNPs make them ideal candidates for *in vivo* imaging techniques such as X-ray imaging [140, 141, 145] and surface enhanced Raman spectroscopy (SERS) [140-144]. In such a manner the AuNPs can act as multimodal drug delivery vehicles as well as high contrast imaging reagents, creating theranostic nanoparticles. Unfortunately the equipment needed for the above mentioned *in vivo* imaging techniques are expensive and using animal models for

research requires ethics approval, which discourages some researchers from developing the field.

Table 1.2: Gold nanoparticles in nanomedicine: Drug delivery, imaging, diagnostics and multipurpose applications

Compound	Model	Imaging / Diagnostic	Other Applications	Reference
Doxorubicin	*In vitro*	Fluorescence	Drug delivery	[146], [147]
Bombesin	*In vitro; in vivo*	-	Drug delivery	[148]
Pthalocyanines	*In vivo*	-	Drug delivery, Photothermal therapy	[149]
5-Fluorouracil	*In vitro*	-	UV-drug release	[150]
Paclitaxel	*In situ*	-	Drug delivery	[151]
Collagen-Cy5.5	*In vitro; in vivo*	FRET	MMP2 Activity	[152]
Cisplatin	*In situ*	-	Drug delivery	[153]
Oxaliplatin	*In vitro*	-	Drug delivery	[154]
Modified platinum(IV) drugs	*In vitro*	Fluorescence	Drug delivery	[155]
Coumarin	*In vitro*	Fluorescence	Drug delivery	[156]
Alexa647	*In vivo, ex vivo*	Fluorescence, SERS	Drug delivery	[157]
Heparin	*In vivo*	-	Drug delivery	[158]
DNA	*In vitro*	-	Gene delivery	[159]
DNA	*In vitro*	Fluorescence	Gene therapy	[160]

The intrinsic toxicity of quantum dots (QDs) (Section 1.6.3) restricts the *in vivo* applications but they still remain as very useful as sensitive fluorescence diagnostics tools [161-163]. QDs have been labelled with antibodies [162, 163, 164, 174], peptides [162, 163] and oligonucleotides [162, 163]. The most common applications for QDs are for immuno-staining techniques such as Western blotting [164], ELISA [162] and immuno-histology [162, 164, 165]. QDs have also been successfully utilized in multiplexed multi-chromatic flow cytometry experiments [166], cellular tracking [173, 180] as well as for single molecule

imaging *in vitro* [167, 174]. *In vivo* murine studies have also shown that QDs gave a very high signal-to-noise ratio over tissue auto-fluorescence, even at a similar wavelength where tissue auto-fluorescence occurs [162, 165, 168-170]. A new generation of near-infra red non-toxic QDs are showing great potential in deep tissue diagnostics due to light penetration depth [170-172] as well as avoiding tissue auto-fluorescence completely by exploiting the near-infrared optical window for *in vivo* imaging [170, 174].

The currently approved FDA (2012) nanoparticle formulations can be seen in Table 1.3. A specific colloidal gold device has been approved for use as an *in vitro* assay. The only FDA accepted gold nanoparticle formulation is targeted towards solid tumours by exploiting an interaction with tumour necrosis factor (TNF) and is currently in Phase-II clinical trials [174]. This is a PEGylated TNF passivated 27nm diameter gold nanoparticle which exploits the leaky tumour vasculature (passive targeting) to induce cell death in tumour masses and was reported to have an 85% response rate in cancer patients. This is a proprietary commercial preparation with the trade name Aurimune™ (CYT-6091). The manufacturer, Cytimmune Sciences Inc., aims to use this AuNP formulation to treat solid tumours such as ovarian-, breast- and pancreatic cancer. Multimodal theranostic nanoparticles which are currently under investigation by the FDA can be seen in Table 1.4. Currently there is no gold nanoparticle based therapeutic or diagnostic formulation under investigation. A gold nanoshell (Auroshell™) nanoparticle is currently being investigated for the use of near infrared laser technology to selectively destroy cancer cells [175]. The gold shell encapsulates a silica core. Nanospectra Biosciences developed this nanoparticle system to exploit the leaky vasculature of tumours and as such utilizes a passive targeting system.

It is clear from Table 1.4 that the FDA currently accepts QDs for *in vitro* use only which limits the QDs to be used as high contrast fluorescence imaging reagents for molecular biology- and histology techniques. However, with advances in QD synthesis techniques acceptable levels of *in vivo* QD toxicity may be attained. The toxicity of QDs begs to raise the question "Why would the toxicity of nanoparticles matter if the application is for cancer treatment or cancer diagnostics?". At the risk of controversy, if a toxic nanoparticle can be specifically targeted towards a cancer cell it may negate the need for chemotherapeutics which are known to induce systemic toxicity.

Table 1.3: Actively targeted nanoparticle therapeutic and diagnostic devices currently being investigated by the FDA (2012), taken from [176]

Confirmed and likely nanomedicine applications and products identified that utilize active targeting

Application(s)/Product(s)	Company	Status	Condition	Nanocomponent	Targeting Mechanism
Ontak [45,46]	Seragen, Inc.	Approved (1999)	T-Cell Lymphoma	Protein NP	IL-2 Protein
MBP-Y003, MBP-Y004, MBP-Y005 [47]	Mebiopharm Co., Ltd	Preclinical	Lymphoma	Liposome	Transferrin
MBP-426 [47–49]	Mebiopharm Co., Ltd	Phase I/II	Solid Tumors	Liposome	Transferrin
CALAA-01 [19,50]	Calando Pharmaceuticals	Phase I	Solid Tumors	NP	Transferrin
SGT-53 [19,51]	SynerGene Therapeutics, Inc.	Phase I	Solid Tumors	Liposome	Transferrin
MCC-465 [48,52]	Mitsubishi Tanabe Pharma Corp	Phase I	Stomach Cancer	Liposome	GAH Antibody
Actinium-225-HuM195 [53]	National Cancer Institute	Phase I	Leukemia	NP	HuM195 Antibody
AS15 [54]	GlaxoSmithKline Biologicals	Phase I/II	Metastatic Breast Cancer	Liposome	dHER2 Antibody
PK2 [48,55]	Pharmacia & Upjohn Inc.	Phase I	Liver Cancer	Polymeric NP	Galactose
Rexin-G, Reximmune-C [56,57]	Epeius Biotechnologies	Phase I/II	Solid Tumors	NP	von Willebrand factor (Collagen-Binding)
Aurimune (CYT-6091) [19,58] Auritol (CYT-21001) [59]	CytImmune Sciences, Inc.	Phase II Preclinical	Solid Tumors	Colloid Gold	TNF-α
SapC-DOPS [60,61]	Bexion Pharmaceuticals, Inc.	Preclinical	Solid Tumors	Liposome	Saposin C
Targeted Emulsions [62,63]	Kereos, Inc.	Preclinical	*In Vivo* Imaging	Emulsion	"Ligands"
Opaxio [42,64]	Cell Therapeutics, Inc.	Phase III	Solid Tumors	Polymeric NP	Enzyme-Activated
ThermoDox [43]	Celsion Corporation	Phase II/III	Solid Tumors	Liposome	Thermosensitive
DM-CHOC-PEN [44,65]	DEKK-TEC, Inc.	Phase I	Brain Neoplasms	Emulsion	PenetrateBlood-Brain-Barrier

Table 1.4: Actively targeted multimodal nanoparticle therapeutic and diagnostic devices currently being investigated by the FDA (2012), taken from [176]

Confirmed and likely nanomedicine products that exhibit active behavior, beyond active targeting, identified

Use	Application(s)/Product(s)	Company	Status	Nanocomponent	Active Mechanism
Solid Tumor Hyperthermia	NanoTherm [77]	MagForce Nanotechnologies AG	Approved	Iron Oxide NPs	AC Magnetic Heating
	Targeted Nano-Therapeutics [105]	Aspen Medisys, LLC. (Formerly Triton BioSystems, Inc.)	Pre-Clinical	Iron Oxide NPs	AC Magnetic Heating
	AuroShell [83]	Nanospectra Biosciences	Phase I	Gold Nanoshell	IR Laser Heating
Solid Tumor Treatment	NanoXray [77]	Nanobiotix	Phase I	Proprietary NP	X-Ray-Induced Electron Emission
In Vivo Imaging	Feridex IV, GastromarkCombidex (Ferumoxtran-10) [79,106]	Advanced Magnetics	Approved (1996)Phase III	Iron Oxide NPs	Enhanced MRI Contrast
	Endorem, Lumirem, Sinerem [79,106]	Guebert	Approved / Investigational	Iron Oxide NPs	Enhanced MRI Contrast
	FeraSpin [107]	Miltenyi Biotec	Research Use Only	Iron Oxide NPs	Enhanced MRI Contrast
	Clariscan [79]	Nycomed	Phase III	Iron Oxide NPs	Enhanced MRI Contrast
	Resovist [79,106] Supravist [80]	Schering	Approved (2001)Phase III	Iron Oxide NPs	Enhanced MRI Contrast
In Vitro Imaging	Qdot Nanocrystals [108]	Invitrogen Corporation	Research Use Only	Quantum Dot	Fluorescent Emission
	Nanodots [109]	Nanoco Group PLC	Research Use Only	Quantum Dot	Fluorescent Emission
	TriLite™ Nanocrystals [110]	Crystalplex Corporation	Research Use Only	Quantum Dot	Fluorescent Emission
	eFluor Nanocrystals [111]	eBiosciences	Research Use Only	Quantum Dot	Fluorescent Emission
	NanoHC [112]	DiagNano	Investigational (Research Only)	Quantum Dot	Fluorescent Emission
In Vitro Cell Separation	CellSearch® EpithelialCell Kit [99]	Veridex, LLC (Johnson & Johnson)	Approved (2004)	Iron Oxide NPs	Magnetic Separation
	NanoDX [113]	T2 Biosystems	Research Use Only	Iron Oxide NPs	Magnetic Separation

Currently, liposomes and magnetic nanoparticles are favoured for drug delivery and multimodal applications (Table 1.4). Liposomes can be engineered to have biodegradable components [25, 176, 177] and iron based magnetic nanoparticles will be oxidised in the biological milieu and incorporated in metabolism [176, 178]. The use of liposomes and magnetic nanoparticles has had the most success up to date to create a multimodal nanoparticle system which can act simultaneously as a diagnostic as well as a therapeutic platform. The FDA is investigating targeted single- and multimodal nanoparticle formulations (Table 1.4) which are in various phases of human clinical trials.

In the next section some background information will be given on nanotechnology with the focus on gold nanoparticles and quantum dots. This will include synthesis and some unique physicochemical phenomena of these nanoparticles as well as some considerations that need to be taken into account for applications in biological systems.

1.6 Nanotechnology: A Brief Review

Cancer therapeutics and diagnostics have developed into a very complex multidisciplinary field of research. Nanotechnology is a rapidly expanding multidisciplinary field that has emerged as an important contributor to theranostics of cancer. Theranostics describes the multimodal applications of nanoparticles as therapeutic (thera-) and diagnostic (-nostic) agents. The terminology "theranostics" has been introduced recently at international conferences and publications [179-182]. Due to the complex nature and numerous permutations of the various nanotechnology sub-disciplines which has developed, a basic and then applied discussion of nanoparticles applicable to this project will follow.

1.6.1 Overview: Big Implications of a Small Science

Nanotechnology describes the study of devices and materials where at least one of the dimensions is on the "nano" (10^{-9} meter) scale [178, 183, 186, 187]. If Figure 1.11 is examined it becomes clear that nanotechnology deals with devices so small they are magnitudes smaller than cells and in the same size category as biomolecules. These devices can be created by a bottom-up or top-down approach [184, 186, 187]. The former is based on synthesis from the atomic scale to the required size, and the latter is based on using existing templates with nano-dimensions, such as membranes or thin-films, to create nanostructures. The nanoparticles can be varied in size, shape and elemental composition [184, 186, 187].

The physicochemical properties of nanoparticles vary considerably when compared to the elemental atomic and the elemental bulk scale [178, 186, 187], e.g. gold nanoparticles have a red hue in solution where atomic and bulk gold will have a yellow colour [185, 187]. Further, the physicochemical properties of nanoparticles are size-dependent, called the quantum confinement effect [184, 186, 187]. The increased surface area-to-volume ratio creates a highly reactive surface with unique chemistry or optical phenomena [184, 187]. This can be exploited for catalysis [187], disease therapeutics [184-187] and in medical diagnostics [185-187].
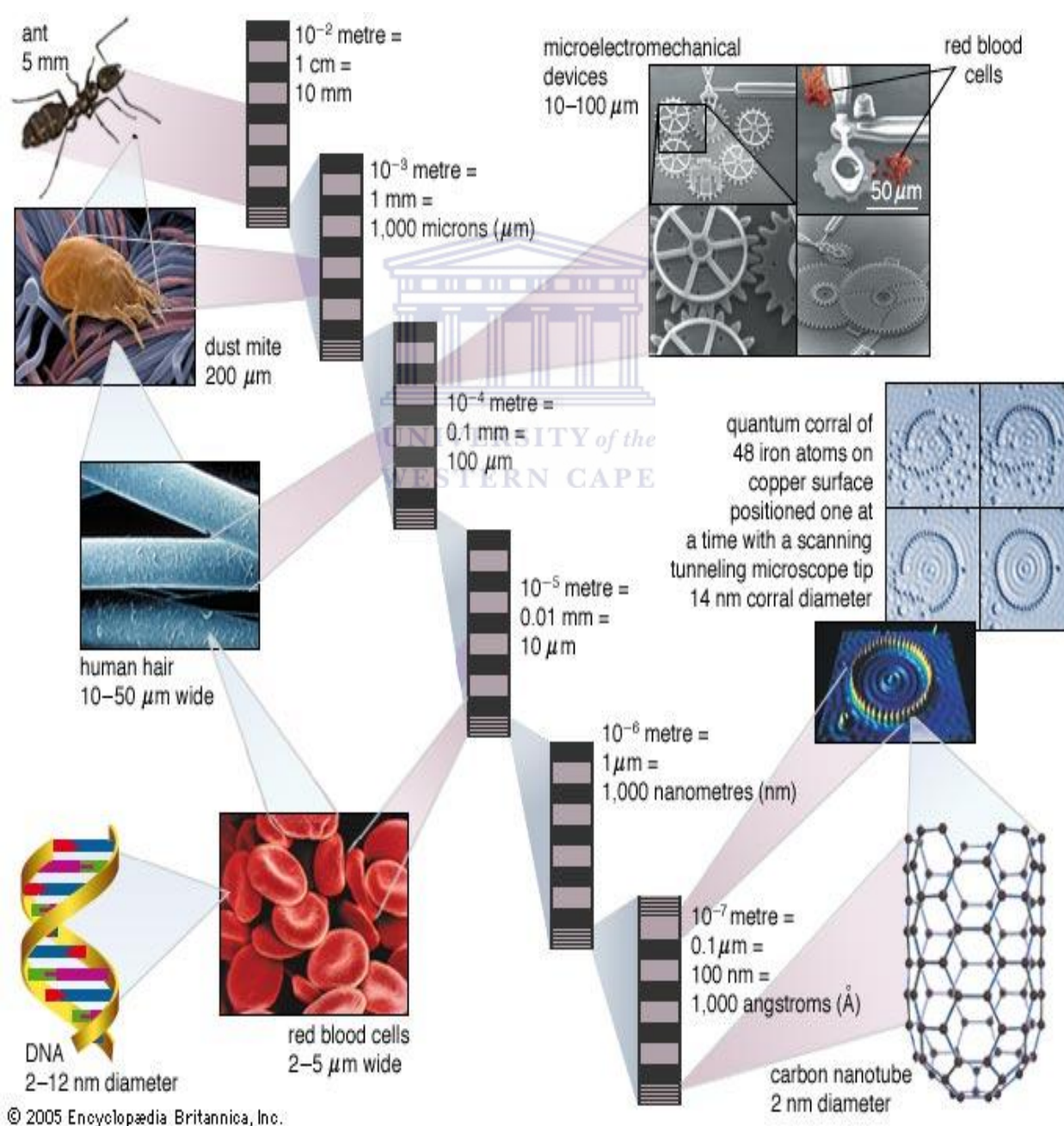
Figure 1.11: A comparative size scale putting nanoparticles in perspective to known structures and biological molecules. (Encyclopedia Britannica, 2005)

There are currently many permutations on nanoparticle classifications. For ease of explanation, 3 groupings will be made:

(i)   Hard nanoparticles:

Metallic nanoparticles have at least one metallic element in their composition and include noble metal-, magnetic- and semiconductor fluorescent nanoparticles. Typical applications include but are not limited to: (bio-) chemical sensors [186-188, 190], medical optical diagnostics [186, 187, 189, 190], drug delivery vehicles [186, 187, 189, 190] and magnetic contrast reagents [186, 187, 191]. The noble metal nanoparticles (Pd, Pt, Au, Au) are expensive to produce and other than for gold these noble metal nanoparticles have been reported to pose potential health [192, 193]- and environmental risks [163, 193]. The toxicity of selected types of nanoparticles will be discussed in Section 1.6.4.

(ii)   Soft nanoparticles:

Polymers, dendrimers, carbon nanotubes, micelles and liposomes are the main types of nanoparticles in this category [179, 186, 194]. They mainly consist of synthetic organic molecules which are to a certain extent bio-degradable. Applications of these nanoparticles include water/air differentially permeable purification membranes [195] and drug-encapsulation vehicles [186, 194]. An example of a bio-degradable liposomal therapeutic formulation is Doxil® (Section 1.2.3.2).

(iii)   Ultrafine particles:

These are nanoparticles that are mostly the by-products of combustive processes in industry [193, 196], fossil fuel combustion engines [193, 196], asbestos [193], biomass burning [196] and even tobacco smoking [196]. The composition of these nanoparticles is a complex mixture of organic compounds and metal impurities, displaying a wide range of physical morphologies and sizes [193, 196-198]. These nanoparticles are inhaled, ingested or absorbed on a daily basis [198]. Ultrafine nanoparticles pose personal health well as environmental risks and have been linked to increased incidence of pulmonary diseases [193, 196, 198] as well as variety of cancers [193, 198].

In the next few paragraphs attention will be given to gold nanoparticles and fluorescent semi-conductor quantum dots.

1.6.2 Gold Nanoparticles (AuNPs)

Gold nanoparticles (AuNPs) or gold colloids have been around long before Turkevich rediscovered the synthetic route in 1951 [190]. The use of colloidal gold dates back to 2500BC in ancient Egypt and China where it was used in health elixirs, paint for urns and dyes for clothes [141, 185]. Medieval Christians used gold nanoparticles to give the red tint to stained glass windows in their cathedrals and churches [141, 185].

1.6.2.1 Synthesis and Functionalization

In the Turkevich method an aqueous gold salt (Au^{3+}) solution is brought to near boiling point and a citric acid solution is added [141, 199, 200, 202]. The solution colour will change within a few minutes from yellow, to black and then finally a shade of red [141, 199, 200, 202]. Mechanistic studies determined this colour shift corresponds to the various steps of nanoparticle formation. Addition of the reducing agent leads to nucleation seeding [141, 200, 203], nanoparticle growth and maturation (Ostwaldt ripening [141, 200, 203]) to the desired AuNP size [141, 200, 201, 203]. This mechanism is represented in Figure 1.12.
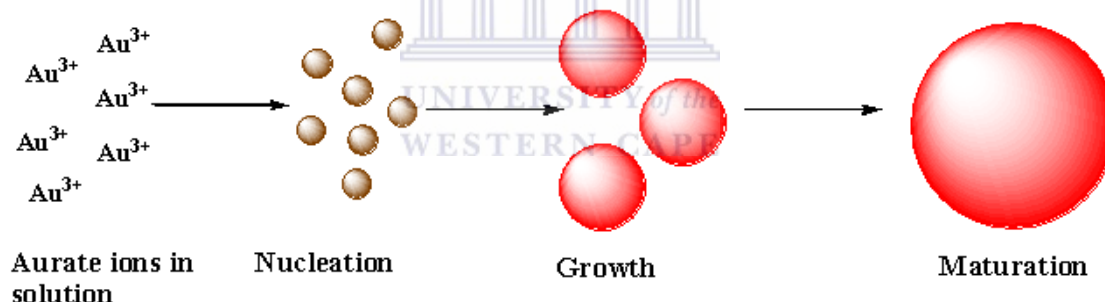
Figure 1.12: The stepwise synthesis of AuNPs. After addition of the reducing agent nucleation of gold clusters will occur where the solution will go from yellow to brown or black. A red colour indicates nanoparticle growth is occurring with maturation leaving AuNPs of the desired size.

The nanoparticles would aggregate if the surfaces weren't shielded from direct collision interactions with one another [140, 141, 190, 202]. The citrate is electrostatically adsorbed onto the AuNP surface [199, 202]. Citrate has a dual role in this synthesis technique by acting as an inducer/controller to growth (reducing agent) [202] as well as surface protectant (capping agent) [141, 187, 202]. Frens later expanded this synthesis to the Frens-Turkevich (seed-mediated synthesis) method. Pre-synthesized AuNPs are added to additional gold salt to the solution and the Turkevich method is applied [204]. Larger and more size monodisperse AuNPs with increased colloidal stability are produced in this way [185, 204]. The ratio of citrate to gold in solution is the determining factor for the final size distribution of the nanoparticles in solution for the Turkevich [199] as well as the Frens-Turkevich

methods [204]. Colloidal stable spherical gold nanoparticles of 5-40nm in diameter (ø) can be prepared this way. Ascorbic acid [205, 206], cetyltrimethyl ammonium bromide (CTAB) [141, 205-207], and polyvinyl-(pyrrolidone) (PVP) [141, 207] in combination with citrate can be utilized in permutations of the Turkevich- and Frens-Turkevich methods to synthesize AuNPs of different shapes and sizes.

Ligand exchange (Figure 1.13) is the process used to prepare AuNPs prepared by the Turkevich method for biological applications [141, 185, 190]. This can be done in a binary or in an analogue solvent system [141, 185, 189, 208, 209]. The solvent system is dependent on the desired solubility of the final AuNP surface functionalization where the solubility of the AuNPs will be dictated by the solubility of the molecule (ligand) found on the AuNP surface. A hydrophobic molecule will confer organic solvent solubility and a hydrophilic molecule will confer aqueous solubility. A molecule that has a higher affinity for the AuNP surface would displace the citrate [141, 194, 208, 209]. Depending on the functional group it can be a chelation (-COOH) [141, 184, 194], a covalent bond (-SH, -NH$_2$) [141, 184, 194, 209] or an electrostatic interaction with an electron rich molecule like a phenyl compound [209, 210]. The most stable capping ligands are those with a thiol (-SH) moiety [141, 185, 187, 189, 209]. Addition of a chaotropic salt will enhance the bond between the AuNP surface and the new ligand but this is not essential for successful ligand exchange [189, 194, 209]. Biomolecules can be proteins [141, 186, 189, 194, 209], peptides [141, 186, 189, 194, 209], oligonucleotides (DNA and RNA) [141, 186, 189, 194, 209, 210], carbohydrates [189, 194, 209] and polymers [189, 194, 209]. This can be a laborious and time consuming process as each biomolecule will require the ligand exchange reaction conditions to be refined. In the case of siRNA or novel proteins/peptides, this can be an expensive experiment. Additional modification of the AuNP surface can be done using self-assembly techniques, such as layer-by-layer hydrophobic- [209, 210] or electrostatic interactions [209, 210], as well as bioconjugation techniques [194, 210].
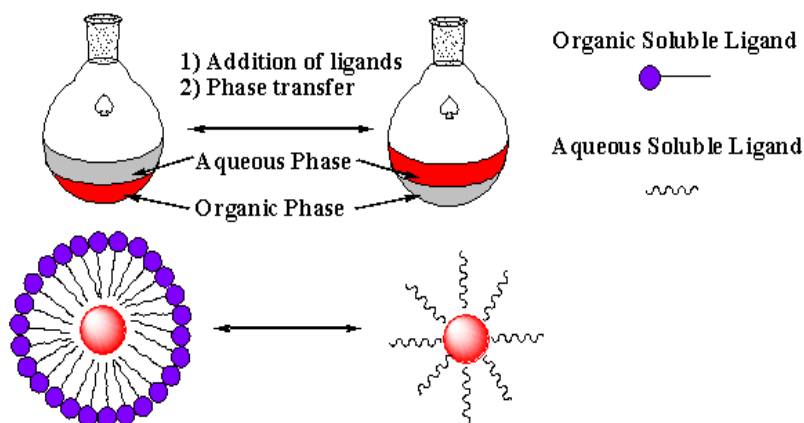
Figure 1.13: Schematic representation of ligand exchange or place exchange. In this example a biphasic system is used for illustration of how the solubility chemistry can change using this reversible method. The AuNPs will be in the phase containing the ligand which has a higher affinity for the AuNP surface. The biphasic system can readily be adapted to an aqueous system, the principle remains the same: molecules that preferentially bind to the AuNP surface will confer corresponding solubility to the AuNPs.

The Brust-Schiffren method introduced a facile one-pot method for the production of thioalkane capped AuNPs in a binary solvent system [141, 212]. The gold salt is dissolved in the aqueous layer and the thioalkane capping agent(s) in a toluene solution. It is possible to use more than one capping ligand. Sodium borohydride (NaBH$_4$), the reducing agent, is added to the rapidly stirring solution. Spherical thioalkane capped nanoparticles with good monodispersity are produced, ranging from 6nm $\leq \varnothing \leq$ 10nm [212]. Brust *et al* further speculated that the thiolate ligand will contribute to size- and shape control of the AuNPs under different experimental conditions [212]. The mechanism of nanoparticle formation is the same as for the Turkevich method with the exception that the gold salt (Au^{3+}) will complex with the thioalkane ligand beforehand to make an Au^1-thioalkane precursor which may facilitate the formation of a more narrow size dispersion of nanoparticles due to slower nanoparticle growth [212, 213]. In a permutation of this one-pot synthesis Brinas *et al* demonstrated the stepwise reduction of the aurate salt by glutathione and how the final shape of the AuNP was dependent on the size of the thioalkane-Au(I) precursor polymer size [213]. The thioalkane will reduce Au^{3+} to Au^{+1}, reducing the chemical reactivity of the gold cations slightly and that the pH of the reaction solution influenced the size of the AuNPs [213]. Mayes *et al* reported that the AuNP size can be manipulated by altering the ratio of thiol to aurate salt where a large thiol:aurate ratio will favour smaller AuNPs and a small thiol:aurate ratio will favour larger AuNPs [214]. Mayes *et al* also demonstrated in this same study that variation in the temperature influenced the size and shape of the AuNPs [214].

There are many more synthetic routes to produce gold nanoparticles of various shapes (triangles, cubes, rods, etc.) and sizes (2nm $\leq \varnothing \leq$ 100nm) and functionalities [141, 187, 204-214]. The desired characteristics of the AuNPs would be dependent on the downstream applications.

1.6.2.2 Physicochemical Properties

The surface reactivity of AuNPs differs distinctly from the atomic or bulk scale [186, 187]. Bulk gold is chemically inert and does not oxidize. The *d* and *f* orbitals of the gold atoms on the surface of the nanoparticle (Au^0) overlap [141, 187, 190] and the absorption of electromagnetic radiation can be monitored at 450nm where the electromagnetic radiation absorption facilitates electron transitions between the *d* and *f* orbitals [141, 187, 190]. These are high energy orbitals with the electrons delocalizing across the increased surface area and creates an electron density cloud or electron conduction band over the whole AuNP surface [141, 187, 216]. The observed red colour of AuNPs in solution are size, shape and size-distribution dependent [141, 187, 190, 216]. The visible part of the electromagnetic spectrum (photons), have wave properties as well as particle properties. If radiation from the visible range of the electromagnetic spectrum (Figure 1.14) floods across the surface of the AuNPs it will excite and polarize the delocalized electrons creating an electron cloud which will absorb wavelengths of the light of the same frequency. The wavelength(s) that are not absorbed are transmitted through the solution being dictated by the size of the AuNP [141, 187, 190, 215]. The absorbed radiation will result in the electrons oscillating continuously across the AuNP surface (Figure 1.15). This oscillating of the electrons at the same frequency as the incident electromagnetic radiation is called surface plasmon resonance (SPR) [140, 141, 187, 190].

SPR associated with spherical AuNPs is the result of short wavelength light (green, yellow and blue) being absorbed and red light being transmitted [140, 187, 190]. The electromagnetic radiation doesn't reach the AuNP surface due to the density of the electron cloud and as such the yellow colour of bulk gold will not be reflected [140, 187, 190]. Light scattering will still be observed [187, 190].
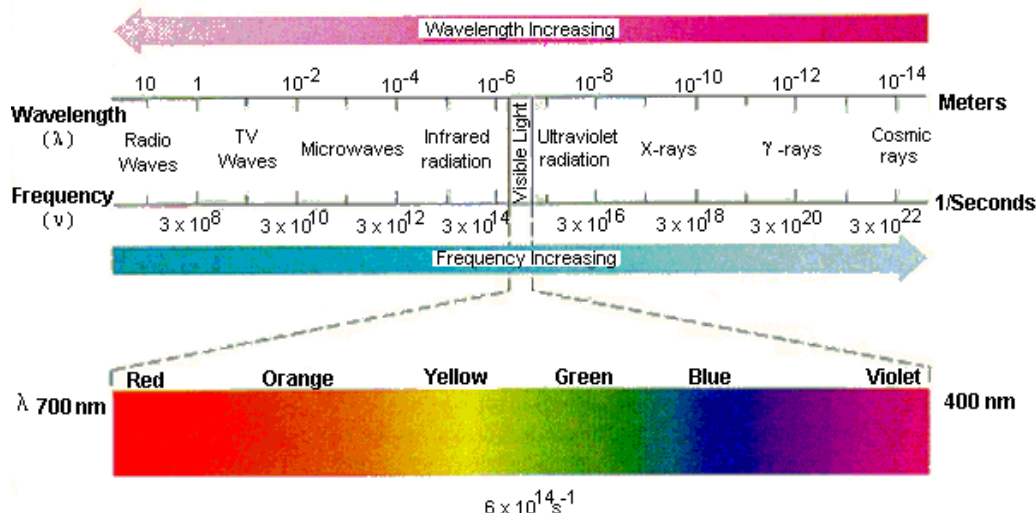
Figure 1.14: The electromagnetic spectrum. Visible light ranges from 400nm to 700nm. The absorption and transmittance is determined by size and shape of the nanoparticle (Image obtained from http://chemed.chem.purdue.edu/genchem/topicreview/bp/ch6/atom_emr.html).
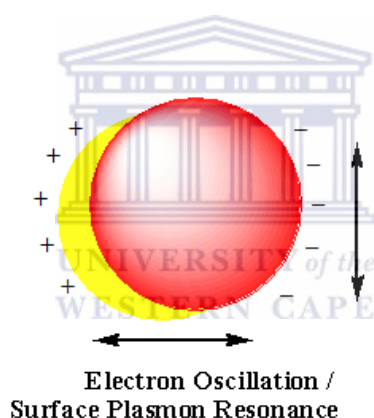
Figure 1.15: A graphical representation of the surface plasmon resonance effect. Electrons will flood or oscillate across the AuNP surface in response to an incident light wave passing close to the surface. This causes a resultant redshift in the electromagnetic spectrum from yellow to red.

Larger AuNPs will have an increased surface area for the plasmons to oscillate across than for smaller AuNPs, the former displaying rosé red colour and the latter a red-purple colour [140, 141, 187, 217]. The amount of light that is absorbed by the SPR-effect is described by the molar extinction coefficient (ε; 10^6 Mol^{-1}.L.cm^{-1} < ε < 10^{12} Mol^{-1}.L.cm^{-1}) [141, 187, 190]. The molar extinction coefficient is directly proportional to gold nanoparticle size and as such would be dependent on the mean diameter of all the AuNPs in solution [140, 141, 190]. Turkevich obtained UV-Vis spectra of the citrate capped AuNPs and discovered that the nanoparticles in solution obeyed the Beer-Lambert law [140, 141, 199]. The optical density of the AuNP solution is directly proportional to the concentration as well as the average size dispersion of the nanoparticles (Figure 1.16). There is however a bathochromic shift where

the linearity of this relationship does not hold true for nanoparticles 15nm < ⌀ < 25nm [140, 141, 217]. To mathematically compensate for this phenomenon Haiss *et al* determined that the ratio of the optical density at the plasmon peak (λ_{SPR}) to the optical density at 450nm (λ_{450}) is directly proportional to the AuNP diameter [218]. Haiss *et al* however only evaluated this mathematical compensation for AuNPs produced by the Turkevich and Frens-Turkevich method with citrate as capping agent [218]. This mathematical compensation provides a more accurate estimation of the extinction coefficient, translating into a more accurate determination of the AuNP concentration.

The SPR band peak is the value where the optical density of the solution is at its maximum, corresponding to the size and shape of the AuNP [140, 153, 187, 190, 199]. This can be seen in Figure 1.16 where the maximum peak absorption shifts according to the size of the AuNPs. Molecules which are electron rich (e.g. biomolecules and polymers) will have a more pronounced effect on the surface properties of AuNPs than citrate and alter the SPR band [140, 187, 215]. In such a manner the SPR effect can be exploited for molecule-molecule interaction studies on the AuNP surface. Surface functionalization during ligand exchange affects the SPR and as such a blueshift or a redshift of a few nanometres in the electromagnetic spectrum can be observed with UV-Vis spectroscopy. This change in the SPR band is attributed to the change in the energy levels of the electron conduction band which occur on the AuNP surface [140, 141, 187, 216]. Other factors that can affect the SPR band are temperature [140, 210, 215, 219], pH [140, 210], ionic strength [140, 210] and the type of solvent (dielectric constant) [140, 210, 215, 216].
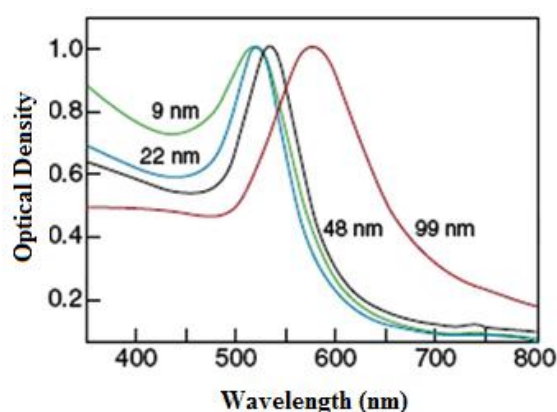
Figure 1.16: The UV-Vis spectra of spherical AuNPs. The spectrum is dependent on the average size distribution of the nanoparticles in the sample. The image was obtained and adapted from http://www.grin.com/en/doc/247330/surface-engineering-of-gold-nanoparticles-and-their-applications.

1.6.3 Quantum Dots (QDs)

These fluorescent semi-conductor nano-crystals have acquired popularity in biomedical research in the past few years due to the applications in (bio-)chemical sensors [172, 220, 221], *in vitro* diagnostics [172, 222, 223] and potential *in vivo* diagnostic applications [224-226]. These spherical nanoparticles typically have diameters which range between 4nm and 25nm [170].

1.6.3.1 Synthesis and Functionalization

The synthesis of QDs is a fairly complex and intricate process being conducted at high temperatures in organic solutions under inert atmospheres [172, 174, 227, 228]. Initially an organometallic precursor is injected into a hot organic solution where the temperature will be incrementally increased to induce crystal growth of the metallic component [170, 227, 228]. Accurate temperature control is crucial for uniform crystal growth [172, 227, 228]. This is termed core-formation (Figure 1.17) with typical elements being cadmium (Cd) [163, 170, 227, 228], selenium (Se) [163, 170, 227, 228], tellurium (Te) [163, 170, 229], indium (In) [163, 170], arsenic (As) [163, 170] and gallium (Ga) [163, 170, 227]. Other elements can be used for core formation where the limiting factor determined by similarity in crystal lattice structure [171, 227, 228]. To prevent auto-oxidation the core is capped with a shell (shell-formation) [170, 227, 228]. This typically is a combination of zinc (Zn) [170, 227, 228] and sulphur (S) [170, 228] or selenium (Se) [170, 227]. The crystal structure of the shell element components should be complementary to each other as well as the core elements [171, 227, 228]. A typical core-shell QD can be seen in Figure 1.17. QDs display quantum containment effects regarding surface reactivity and physico-chemical properties [162, 170]. Nanoparticle surface passivation is done with a capping ligand, such as tri-n-octyl phosphine oxide (TOPO) [174, 227-229], which is usually incorporated into the reaction mixture from the start of synthesis [171, 174, 227-229]. Various research groups have reported the synthesis of noble metal (gold) fluorescent quantum dots [230, 231].
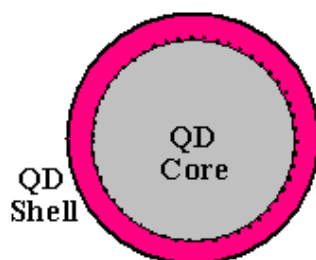
Figure 1.17: The structure of spherical semiconductor nanocrystals QDs. The core and shell both consist of semiconductor elements. The restriction on elements that can be used is cubic crystal lattice compatibility.

Ligand exchange [162, 170, 210, 233] is once again the preferred method of facilitating bio-functionalization of the QDs and would be a biphasic place exchange reaction, similar as for AuNPs (Figure 1.13, 1.6.2.1). Ligands which have a thiol moiety show a high affinity for the cadmium (Cd) in the core and the zinc (Zn) in the shell of the QD [171, 174, 230, 233]. One-pot synthesis of water-soluble ligand passivated QDs without shells have been reported [170, 228].

1.6.3.2   Physicochemical Properties

The cubic crystal lattice compatibility of the different substituents in the QD core and shell contributes to the unique optical properties resulting from the quantum confinement effects for these colloids [170, 171, 174, 227-229, 234, 235]. The Bohr radius can be defined for three variables for the electron (a_e), electron hole (a_h) and the exciton (a_{exc}) [234, 235]. When a nanoparticle has a radius (a) smaller than the Bohr radius the quantum confinement associated phenomena will be observed [234, 235]. The bandgap energy is defined as the minimum energy necessary to excite an electron from a relaxed state to a higher energy level [170, 234, 235]. The relaxation of the electron to the ground state will release energy in the form of fluorescence. Each individual semiconductor or semiconductor alloys will have unique bandgap energy [170, 234, 235]. In layman's terms, the emission wavelength of QDs is dependent on the diameter of the sphere, with small diameters displaying blue emission and larger diameters displaying increasing redshift emission (Figure 1.18b).

Fluorescence excitation can be achieved with any wavelength of light with a shorter wavelength than the emission wavelength providing the excitation energy exceeds the bandgap energy [170, 174, 234-236] and this can be seen in Figure 1.18a where the excitation and emission spectra of different QDs are displayed. In a mixed QD sample, simultaneous fluorescence emission can be achieved by using a single light source [234-237]. Compared to organic fluorophores, QDs have a high resistance to photobleaching [227-229, 234-237] with highly symmetrical emission spectra [227-229, 234-237] presenting relative narrow half-peak width (HPW) and full peak-width (FPW) emission profiles (Figure 1.18a). For large QDs the HPW and FPW broaden significantly, especially for the case of QDs that emit in the near-infrared part of the electromagnetic spectrum (Figure1.18a) [227-229, 236, 237]. QDs have a fluorescence intensity that is 1000 – 10 000 fold higher than most typical organic fluorophores [170, 174, 234-237].
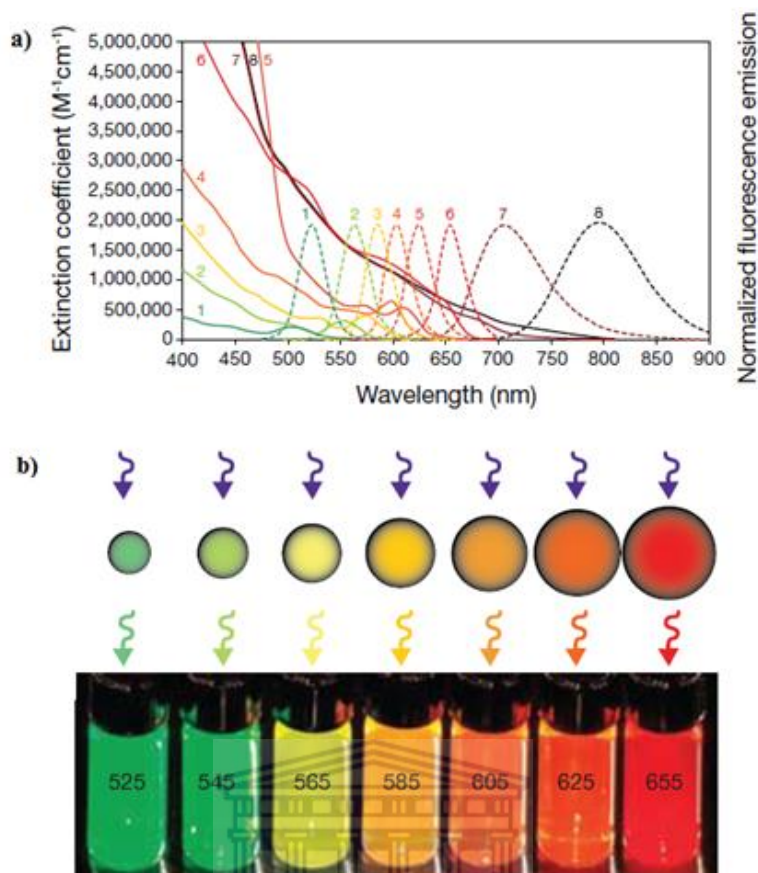
Figure 1.18: The quantum confined effect optical properties of QDs. Symmetrical emission spectra with excitation by any wavelength of light below the emission maximum can be seen in a). The fluorescence emission profile can be fine-tuned based on the QD size as seen in b). Image was taken and adapted from Invitrogen Qdot® Nanocrystal catalogue (http://www.invitrogen.com).

1.6.4 Current Challenges in Nanoparticle Based Therapeutic Strategies

For any therapeutic drug to be cleared for clinical trials and ultimately FDA approval, it needs to adhere to stringent conditions [36, 186, 238]. A few points will be raised which should be taken into consideration and are proving to be quite challenging. This is even more so in the case of nanoparticles, as the inherent toxicity (1.6.5) of these emerging medical devices still needs to be sufficiently studied.

1.6.4.1 Administration Route

Oral administration involves the acidity of the stomach and various digestive enzymes. Also, the formulation has to undergo first pass metabolism before systemic spread. Intravenous administration delivers formulations directly into systemic circulation, bypassing first pass metabolism [186, 198, 238]. This however can cause site-injection accumulation of the formulation resulting in sub-effective dosages reaching the site of action and even an immune response paired with inflammation [36, 198, 238]. Topical application would require

sufficient diffusion through the skin, but once again site specific irritation can occur and contact necrosis has been reported [239].

1.6.4.2 Tumour Specific Targeting

The aim of any anticancer treatment is to only affect the cancerous tissue and not healthy tissue. Due to the complexity of cancer there exists no universal cancer targeting system. Folate receptor targeting is a viable route as most cancer cells will up-regulate this receptor for the increased metabolism in the cells and a nanoparticle-folic acid conjugate will then preferentially accumulate in these cells [160, 186, 238, 240]. Similarly ferritin assisted targeting have been employed [160, 241, 250]. Healthy non-cancerous cells also express folate- and ferritin receptors as these form part of normal cellular metabolism. Thiamine [186] and transferrin [241] assisted targeting to cancer cells has also been reported. More attention has been given to peptide and antibody assisted tumour targeting. Novel cancer targeting peptides are identified either by phage-display techniques [241-243] or synthetically produced by combinatorial chemistry methods [244-247]. The peptides have good specificity and usually have the RGD (arginine-glycine-aspartic acid)-motif [186, 248] but can be difficult to produce and purify, whether by recombinant or protein chemistry methods. Antibodies (monoclonal) display a high specificity [186, 238, 249] but are costly to produce or purchase commercially. General drawbacks for peptides as well as antibodies are that they are not produced in a human host and as such evoke an immune response with subsequent sequestration in the lymphatic system decreasing the efficacy for drug delivery [238, 240]

Tumour specific targeting received a fair amount of criticism at the Gordon's Noble Metal Nanoparticle Research Conference 2012. The majority of researchers where in favour of passive tumour targeting claiming antibodies as well as other targeting molecules do not enhance the ability of drug loaded nanoparticles to localize and internalize to tumours. This is in direct contrast with the current paradigm in the literature.

1.6.4.3 Avoidance of the Immune System and Prevention of Biomolecule Interaction

The immune system will sequester any foreign body in the lymphatic system leading to the excretion of the foreign body. A potential solution for this problem is to humanize [251] peptides, proteins and antibodies to be used for therapeutics, however this is expensive. Another complication is non-specific interaction with serum proteins and biomolecules such

as albumin [160, 185, 186, 238, 240]. Polyethylene glycol (PEG) conjugate-versions of the drug or nanoparticles improve circulation half-life [151, 153, 156, 160, 186], minimizes non-specific interactions with biomolecules [142, 151, 153, 156, 160, 186] as well as assists in avoidance of the immune system [151, 153, 156, 160, 186]. Polyethylene glycol is FDA approved [185, 186]. The majority of liposomal anticancer formulations utilize polyethylene glycol incorporation in their structure [113, 114, 169, 186, 238].

1.6.4.4 Tumour Penetration, Cellular Penetration and Overcoming Multidrug Resistance

The enhanced perfusion and retention effect (EPR) is a controversial topic currently in nanomedicine. The EPR describes the potential of a therapeutic formulation to penetrate the tumour epicentre and destroy the tumour radially outward from the epicentre [160, 182, 185, 186, 238, 240]. The tumour penetrating potential of the therapeutic formulation is dependent on the circulation half-life, the interstitial radial outward tumour pressure, the size of the formulation as well as the extent of the leaky tumour vasculature [160, 182, 185, 186, 238, 240]. At two recent conferences, Gordon Research Noble Metal Nanoparticles 2012 and Elsevier Colloids and Nanomedicine 2012, various speakers contended EPR. The consensus was that to effectively treat cancer, systematic radial inward decrease in tumour size has to take place with consecutive treatments. This is the converse to the traditional view on EPR.

Tumour cell membrane physiology differs from non-tumour cells due to increased expression of specific proteins and other bio-molecules on the surface. Annexin A2 is an example of a protein that confers a more negative charge to the cancer cell membrane and has been identified as a prognostic marker in ovarian carcinomas [132, 252, 253]. The proton sponge effect can be exploited if the nanoparticle has a cationic detergent surface coating which can facilitate internalization into the cell [160, 254, 255]. The cationic nature is due to a primary amine (-:NH_2) or secondary amine (-:NH-) the lone pair electrons on the nitrogen will act as proton acceptors during endosome sequestration. The endosomes will attempt to maintain pH homeostasis through osmosis [160, 241, 254, 255]. Adequate cationic character will cause osmotic rupture of the endosomes and release the contents into the cytoplasm.

1.6.5 Nanotoxicology: The Need to Investigate the Uncertainty

The unique physicochemical properties of nanoparticles raises the question of how safe are these materials [186, 192, 193, 198, 238-240]. Carbon is the atom of life being biologically inert and carbon nanotubes have been utilized in *in vitro* therapeutics [256, 257]. The assumption was made that carbon nanotubes would be equally biologically inert. Typical biochemical based toxicity assays showed favourable cell viability and mechanistic studies indicated no oxidative stress [198, 256]. High resolution microscopy studies told another story: the carbon nanotubes have sharp edges which pierced the cell membranes, similar to a needle piercing a balloon, causing lesions which can lead to mesothelioma [193, 198]. The stiff structures of the carbon nanotubes are also associated with chronic inflammation [193, 198, 256, 257]. The nanotube surface was not as chemically inert and displayed direct chemical interaction with the substituents of the biochemical assays [192. 238], inducing DNA strand breaks [192], inducing platelet aggregation [36] as well as generating reactive oxygen species [193, 198, 239]. A controversial question arises regarding carbon nanotubes as drug delivery vehicles [258]: How sure are the authors that the *in vivo* results for overcoming multidrug resistance is not an artefact?

Magnetic nanoparticles (MNPs) are currently one of the most acceptable nanoparticles, next to liposomes, for being chosen for FDA clinical trials as multimodal drug delivery vehicles and imaging agents (section 1.5, Table 1.3 and Table 1.4). MNPs consist mainly of ferric (Fe^{2+}) or ferrous (Fe^{3+}) ions, where the iron will eventually be biodegraded by oxidation and will either be absorbed and used for cellular processes or excreted [238]. The *in* vivo stability and safety of iron magnetic nanoparticles was brought into question when it was reported that biological oxidation induced nanoparticle aggregation, even with biomolecule surface coatings [192, 238]. In a recommended review by McNeil *et al* in 2009 it was reported that iron containing nanoparticles showed significant differences in tumour uptake as well as biological clearance dependent on tumour- and organism types [238]. Pisanic and co-workers reported in 2007 that iron nanoparticles induced dose-dependent disturbances in the PC12 rat neural cell line: cytoskeletal disruptions; decreased intracellular contact and unresponsive to stimuli by nerve growth factor (NGF) [259]. It is not known how MNPs would affect individuals that have genetic defects in iron metabolism or even severe liver and kidney damage. Cobalt (Co) doped magnetic nanoparticles showed significant toxicity *in vitro* [192, 198] and outcompeted magnesium (Mg) for DNA binding [192]. It is possible that doping

magnetic nanoparticles with other heavy metals such as nickel (Ni) and manganese (Mn) should show similar toxic effects *in vitro* and *in vivo*.

Various studies claim that citrate capped AuNPs are biologically inert [140, 141, 185, 192, 194]. If biologically inert means "to have no interactions with biological molecules", one would dispute these findings. A more accurate definition would be "have no cytotoxic effects under specific conditions". Aqueous ligand exchange (1.6.2.1) specifically exchanges citrate on the AuNP surface with biomolecules. In the cell there are many molecules in the biological milieu that have carboxylic acids (-COOH), primary amines (-NH$_2$), thiols (-SH) and electron rich phenolic compounds. This also holds true for whole blood and serum proteins [36, 260]. Citrate capped AuNPs have also been reported to induce oxidative stress and interact with DNA repair genes such as *BRCA1* [261]. Essential transcription factors with cysteine residues can also potentially react with AuNPs and have been reported for activator protein (AP)-1 [192]. AuNPs may interact with and deplete intracellular glutathione (GSH) and have been demonstrated *in situ* by Su Deep *et al* [262]. Gao and co-workers demonstrated *in vitro* GSH depletion, 48h after treatment with AuNPs, which subsequently leads to increased intracellular H$_2$O$_2$ production and cell death [263]. The chemical reactivity and spectroscopic properties of AuNPs have led to speculation that biochemical assays were prone to interference from AuNPs. The propidium iodide absorbs to the surface of the AuNP and the fluorescence of the dye is quenched which leads to altered results when determining cellular necrosis [238]. Similar concerns have been raised for the 3-(4,5-Dimethylthiazol-2-yl)-2,5-diphenyltetrazolium bromide, a tetrazolium (MTT) assay where there is significant spectral overlap for the tetrazolium dye and AuNPs [264, 265]. MTT can also be absorbed onto the AuNP surface [264, 265]. Bio-impedance *in vitro* assays have been suggested as a solution to determining cellular responses to AuNPs [266]. The consensus in peer reviewed literature is that the cellular distribution of AuNPs is directly related to the size and shape although endocytosis appears to be the main internalization method reported [185, 267, 268]. Small AuNPs are localized in peri-nuclear or intra-nuclear regions [267, 268]. Larger AuNPs are found in the cytoplasm or plasma membrane bound [267, 268]. The cellular distribution is further also dependent on the surface functionality of the AuNPs [267-269, 271, 272] as well as the cell type [269-271]. Cationic functionalities appear to be more readily sequestered in endosomes than anionic functionalities [271-275]. An anionic nanoparticle will be repulsed from the membrane and may have decreased cellular internalization. This may be the reason why anionic nanoparticles display a lesser degree of toxicity than their cationic counterparts.

It has been reported that cationic nanoparticles are intrinsically toxic [271-275]. Whole animal imaging studies elucidated organ specific distribution of AuNPs [269, 273, 274]. Citrate capped AuNPs would be sequestered in the lymphatic system, liver or kidneys [269, 273] but larger AuNPs may be found in the lungs as well [269, 273]. AuNPs will be gradually degraded in the biological milieu [275] and diameters smaller than 5nm are readily excreted through the kidneys [275].

The elements which make up the core of the QDs are toxic and induce severe oxidative stress [161-163, 170, 275, 276]. Oxidation of the QDs in the biological environment releases the toxic elements from the nanocrytal structure [161-163, 170, 276]. Non-genomic [162, 170, 269, 276], genomic [162, 170, 269, 276] as well as epigenetic [162, 269, 276] changes *in vitro* have also been reported with the use of QDs and as such live cell imaging using QDs proves to be a challenge since toxicity from the QD may affect the cellular event being studied [162, 276]. It has been reported that if the capping ligand on the QD surface is sufficiently dense it can prevent or decrease the leakage of the QD-core elements to the biological environment [170, 275, 276]. It is speculated that polymers, dendrimers as well as liposomal ligands are the best suited for *in vivo* QD applications as these ligands resist biological oxidation and desorption from the QDs surface more readily than smaller ligands [168-170, 223, 276, 277]. *In vivo* models have shown that untargeted QDs will eventually be sequestered in the lymphatic system, the kidneys, liver as well as bone marrow for up to 4 months after administration [277, 278]. Renal- and hepatic failure can be induced by micromolar quantities of cadmium [161, 269, 275, 276]. In all these QD toxicity reports the consensus is that toxicity is time- and dose-dependent.

It is clear that the toxicity of various nanoparticles is called into question. This is especially important for nanoparticles which have traditionally been seen as "bio-inert" where the chemical- as well as mechanical stress mechanisms still have to be fully elucidated. Care should be taken when considering which biochemical toxicity assays to use for nanoparticle types. Biochemical- and microscopy toxicity assays can experience (bio-)chemical-, fluorescence quenching- or fluorescence superposition interference which is dependent on the size, shape or composition of the nanoparticle.

1.7 Problem Statement and Objectives

1.7.1 Problem statement

Early as well as accurate diagnosis of ovarian cancer is a challenge where diagnosis occurs when the disease is an advanced stage with a poor prognosis for the patient (Sections 1.2.1 and 1.2.2). Ambiguity of the symptoms as well as the lack of specific molecular biomarkers exacerbates the difficulty of a correct and early diagnosis (Section 1.2.2). Successful diagnosis and treatment still requires the patient to have regular invasive examinations to monitor the potential disease relapse (Section 1.2.2). Ovarian cancer has a higher mortality-to-incidence ratio than breast cancer or any other gynaecological cancer (Section 1.2.1). Surgery is typically used to reduce overall tumour mass, but may cause metastasis of the cancer, with chemotherapy as follow-up treatment (Section 1.2.3). Successive chemotherapy administration is required, over a time frame of weeks or months, for ovarian cancers which leads acquired multidrug resistance. In cases of disease relapse, epithelial ovarian cancer will be non-responsive to chemotherapy and incurable (Sections 1.2.2 and 1.2.3). The adverse side-effects of chemotherapy include physical- as well as psychological symptoms (Sections 1.2.2 and 1.2.3). From a personal perspective and experience, some individuals would rather suffer the effects of the disease than suffer the effects of treatment. In a South African context, where the majority of the population lives in rural areas without adequate health care or access to a physician, ovarian cancer proves even more challenging. If the specific diagnosis cannot be improved, attempts should be made to improve the treatment of the disease.

MMP2 has been identified as a non-specific prognostic marker for solid- and metastatic tumours, where the levels of MMP2 are directly correlated to how aggressive and advanced the tumour is (Table 1.1, Section 1.3.1). CTX is a small venom peptide which has been identified to specifically bind to MMP2 in glioma cells and has been shown to bind to MMP2 in other cancers as well (Sections 1.4.1 and 1.4.2). Various diagnostic- and therapeutic strategies have utilized the CTX-MMP2 interaction with success (Section 1.4.2). The interaction of CTX-MMP2 can thus be utilized to develop a targeted nanoparticle drug delivery vehicle and has been shown to be feasible (Section 1.4.2). Delivery of a therapeutic payload still has cellular internalization, intracellular accumulation and intracellular retention to contend with. Multidrug resistance involves the ability of a cancer cell to inactivate, export or evade a chemotherapeutic treatment.

The cellular internalization and intracellular localization of gold nanoparticles (AuNPs) is dependent on nanoparticle size as well as surface functionalization. Cationic nanoparticles proved to be superior for internalization but also proved to be more toxic to the cell (Section 1.6.5). Small AuNPs would in theory deliver a chemotherapeutic payload to peri-nuclear regions and larger AuNPs would deliver a chemotherapeutic payload to the cytoplasm and plasma membrane (Section 1.6.5). However, endosome sequestration and cellular efflux is the typical fate of AuNPs (Section 1.6.5). *In vitro* imaging of AuNPs can be done with techniques such as dark field microscopy [178] and SERS- and X-ray imaging for *in vivo* (Section 1.5). A successful drug delivery vehicle will need to overcome cellular drug efflux, display increased intracellular accumulation as well as deliver the chemotherapeutic payload to the site of action. A chemotherapeutic drug like doxorubicin (DOX) has multiple sites of action within the cell, with the nucleus, mitochondria and cytoplasm being the most prominent targets (1.2.3.2.2). Monodisperse AuNPs have been used to deliver DOX and other chemotherapeutics to cancer cells *in vitro* and *in vivo* with varying degrees of success (Table 1.2, 1.5).

Shuming Nie and co-workers described an approach where quantum dots (QDs) were functionalized with hyper branched polyethyleneimine (PEI) and were successfully used as gene delivery vectors, showing an increased transfection efficiency of the genetic payload which was attributed to the increased cellular retention [226, 255, 279]. This event was monitored with fluorescence based techniques such as fluorescence microscopy as well as flow cytometry. The success of these studies mentioned above was attributed to the exploitation of the enhanced perfusion and retention (EPR) effect as well as endosomal escape due to the proton sponge effect [226, 255, 279]. A similar use of PEI on silica nanoparticles to transfect cells *in vitro* for effective siRNA delivery has been reported [280]. In a similar manner, gold nanoparticles were functionalized with PEI and acted as siRNA delivery agents but have not yet been reported as drug delivery vectors. PEI has been shown to be biodegradable in co-block polymer formulations which included polyethylene glycol (PEG) and is a superior transfection reagent [280-283].

Utilizing PEI as a surface functionalization for size polydisperse AuNPs has the potential as a drug delivery vehicle which can deliver its therapeutic payload (DOX) to multiple sites in the cell with enhanced drug accumulation and retention. Further modification of the surface of the PEI-functionalized AuNPs (AuNP-PEI) with PEG can enhance the cellular retention of

the formulation. Increased cellular retention of nanoparticles will enable not only enhanced drug delivery within the cell, but also enable more specific and sensitive diagnostics. In such a manner a multimodal theranostic AuNP can be developed.

1.7.2 Aims and Objectives

The primary aim of this study is to synthesize and functionalize a multimodal theranostic gold nanoparticle for the *in vitro* drug delivery to a multidrug resistant ovarian carcinoma cell line in an attempt to overcome the cellular drug resistance and induce significant programmed cell death.

The primary objectives of the study are the following:

- Synthesize, bio-functionalize and physicochemically characterize gold nanoparticles;
- Evaluate the biomolecular interactions of the gold nanoparticles
- Refine the surface chemistry and colloidal stability of the gold nanoparticles to act as drug delivery vehicles for doxorubicin
- Evaluate if the doxorubicin functionalized gold nanoparticles could overcome multidrug resistance in a multidrug resistant ovarian carcinoma cell line (A2780cis)
- Suggest a mechanism for cell death induced by the doxorubicin functionalized gold nanoparticles

The secondary aims of this study are to evaluate if the above mentioned drug delivery platform can be transferred to fluorescent nanoparticles (quantum dots) to evaluate *in vitro* tumour-specific targeting by exploiting the matrix metalloproteinase-2 interaction with the venom peptide chlorotoxin.

The secondary objectives of the study are:

- Generate a stable transfected A2780cis cell line which expresses enhanced green fluorescent (EGFP) tagged full length pro-MMP2
- Clone, produce and purify a recombinant variant of chlorotoxin with a 6xHis-tag
- Biofunctionalize nitrilotriacetic acid (NTA) functionalized gold nanoparticles and quantum dots with CTX
- Investigate the *in vitro* co-localization of chlorotoxin and matrix metalloproteinase-2 with the use of wide field fluorescence microscopy

Chapter 2: Materials and Methods

2.1 Materials and Stock Solutions

2.1.1 Materials and Suppliers

1-Ethyl-3-(3-dimethylaminopropyl) carbodiimide hydrochloride, (EDC.HCl)	Sigma
12-*O*-tetradecanoylphorbol-13-acetate, (PMA)	Sigma
12-well Flat bottom clear plates	Greiner
2000 MWCO concentrator tubes, 15mL	Millipore
2-(*N*-morpholino) ethanesulfonic acid, (MES)	Sigma
(2R)-[(4-Biphenylylsulfonyl)amino]-N-hydroxy-3-phenyl-propionamide, (BiPS)	Merck
24-well Flat bottom clear plates	Greiner
3-(N-Morpholino)-propanesulfonic acid, (MOPS)	Sigma
40% 37.5:1 acrylamide:bisacrylamide	Promega
5,5'-Dithiobis(-2-nitrobenzoic acid), (DTNB)	Sigma
6x Green DNA loading buffer	Fermentas
6-well Flat bottom clear plates	Greiner
96-well Flat bottom (F) clear microplates	Greiner
96-well Round bottom (U) black microplates	Merck
10 000 MWCO concentrator tubes, 50mL	Millipore
β-actin mouse anti-human monoclonal antibody, HRP conjugated	Santa Cruz
β-mercaptoethanol	Sigma
γ-thiobutyrolactone	Sigma

Acetone	Merck
Acetonitrile	Sigma
Agarose	Promega
Ammonium persulphate	Merck
Ampicillin	Roche
ApoPercentage™ Assay Kit	Biocolor
Aurotetrachloro trihydrate ($HAuCl_4.3H_2O$)	Sigma / Merck
BamHI FastDigest® restriction enzyme	Fermentas
BCA Protein quantification kit	Pierce
BcglII FastDigest® restriction enzyme	Fermentas
Boric acid (Ortho boric acid)	Merck
Bovine serum albumin, (BSA)	Roche
Bromoacetic acid, ($BrCH_2COOH$)	Sigma
Bugbuster™ GST Bind Purification Kit	Novagen
Calcium chloride, ($CaCl_2$)	Merck
CD27L, mouse anti-human monoclonal antibody, FITC conjugated	Santa Cruz
FluoroShield® with DAPI	Sigma
Chloramphenicol	Sigma
Chloroform-D1, ($CDCl_3$)	Sigma
Chloroform	Merck
Cis-diammineplatinum-(II) chloride (cisplatin)	Sigma
Coomassie Brilliant Blue R-250	Sigma
Coverslips, 22 x 22 mm	Lasec

Cysteine hydrochloride	Sigma
Cytobuster™ Protein Extraction Reagent	Novagen
Dansyl chloride	Sigma
Di-deuterium oxide (D_2O, 99.5%)	Sigma
Di-sodium hydrogen phosphate	Merck
Doxorubicin (Adriamycin)	Wuhan-Sunrise Tech. Dev. Ltd.
DreamTaq® Green PCR master mix	Fermentas
Ethanol	Merck
Ethylene diamine tetra acetic acid, (EDTA)	Merck
FastDigest® x10 restriction digest green buffer	Fermentas
G418 hydrochloride	Sigma
G418 Solution	Roche
GelRed™	Biotium
Glacial acetic acid	Merck
Glutathione, reduced (GSH)	Sigma
Glutaraldehyde solution	Sigma
Glycerol	Merck
Glycine hydrochloride	Merck
Goat anti-mouse polyclonal antibody, HRP conjugated	Santa Cruz
GSH/GSSG-Glo™ Assay	Promega
HiFi™ Hotstart Taq master mix	Kapa Biosystems
Holey carbon film, 400 mesh Cu (50)	Agar Scientific
Hydrochloric acid	Merck

HSP60 mouse anti-human monoclonal antibody	Santa Cruz
Immersion oil, mineral	Zeiss
Iodine (I_2 crystals)	Merck
Isopropanol	Merck
Isopropyl-β-D-thiogalactopyranoside, (IPTG)	Roche
Kanamycin mono-phosphate	Roche
Lipopolysaccharide	Sigma
Magnesium chloride, ($MgCl_2$)	Merck
Metafectene®Pro	Biontex
Methanol	Merck
Microscope slides	Lasec
MLH1 mouse anti-human monoclonal antibody	Santa Cruz
MMP2 goat anti-human polyclonal antibody	Pierce
MMP Chromogenic substrate, thiopeptolide	Enzo Life Science
N^6-Cbz-L-Lysine	Sigma
N-(2-Hydroxyethyl)-piperazine-N'-ethanesulfonic acid, (HEPES)	Sigma
N-hydroxysulfosuccinimidyl ester, (Sulfo-NHS)	Sigma
N, N, N', N'-Tetra methylethylene-diamine, (TEMED)	Sigma
Nickel sulphate, ($NiSO_4$)	Sigma
Ninhydrin	Merck
Nutrient agar	Merck
O'GeneRuler™ DNA 100bp ladder	Fermentas
p-Aminophenylmercuric acetate, (APMA)	Sigma

p-Anisaldehyde	Sigma
PageRuler™ unstained protein ladder	Pierce
Palladium/Carbon (5% Pd/C)	Sigma
Parafilm	Lasec
Paraformaldehyde	Sigma
Polyethyleneimine 2kDa (PEI)	Sigma
Potassium acetate (CH$_3$COOK)	Merck
Potassium chloride (KCl)	Merck
Potassium di-hydrogen phosphate	Merck
Procaspase-3 mouse anti-human monoclonal antibody	Santa Cruz
Pro-Matrix metalloproteinase-2, recombinant	Merck
QIAquick® Gel Extraction Kit	Qiagen
RPMI-1640 with 1mM glutamine	Lonza
SalI FastDigest® restriction enzyme	Fermentas
SM-PEG$_6$ bifunctional crosslinker, 100mg	Pierce
Sodium borohydride, (NaBH$_4$)	Sigma / Merck
Sodium chloride, (NaCl)	Merck
Sodium dodecyl sulphate, (SDS)	Sigma
Sodium hydroxide (NaOH)	Merck
SuperSignal® West Pico chemiluminescent kit	Pierce
T4 ligase	Fermentas
TLC plates, silica gel on aluminium, F254	Merck

Tetrabutyl-ammonium hydroxide	Sigma
Tetrahydrofuran, (THF)	Sigma
Trifluoroacetic acid	Sigma
Tris-[hydroxymethyl]-aminomethane	Merck
Trisodium citrate	Merck
Triton X-100	Fluka
Tryptone	Merck
Tween-20	Fluka
Wizard® SV DNA preparation kit	Promega
WST-1 Cell viability / Cytotoxicity Reagent	Roche
Yeast extract	Merck
XhoI FastDigest® restriction enzyme	Fermentas

2.1.2 Stock Solutions and Buffers

3C Protease buffer: 50mM Tris, pH 8.0, 200mM NaCl, 20mM β-mercaptoethanol in dH$_2$O.

4% Paraformaldehyde solution: 4% paraformaldehyde was dissolved in dH$_2$O at 60°C in a fume hood and the pH was adjusted to pH 8. The solution was kept at 4°C. Do not autoclave.

4X SDS gel sample buffer: 8% SDS, 0.25M Tris pH 6.8, 30% glycerol, 2 mg/mL bromophenol blue and 20% β-mercaptoethanol in dH$_2$O. This buffer was stored in in 2mL portions at -20°C.

10X PBS (1L): 80g NaCl, 2g KCl, 14.4g Na$_2$HPO$_4$ and 2.4g KH$_2$PO$_4$ dissolved in dH$_2$O. The pH was adjusted to pH 7.4 and autoclaved. The stock solution was stored at room temperature and diluted 10-fold as needed.

10X TBE: 0.9M Tris (pH 8.3), 0.89M boric acid and 25mM EDTA dissolved in dH_2O. The solution pH was adjusted to pH 8.3 with NaOH and then autoclaved. The stock solution was stored at room temperature and diluted ten-fold when needed.

10X SDS: 10% SDS in in dH_2O. The stock solution was stored at room temperature.

10X SDS electrophoresis buffer: 50mM Tris, 0.2% SDS and 500mM glycine, pH 8.3.

Ampicillin: A 200mg/mL solution was made in dH_2O, filter-sterilised and stored at -20 °C.

APMA Buffer (MMP2 Activation Reagent): 1mM p-Aminophenylmercuric acetate (APMA) and 80mM NaOH in 1mL dH_2O. This solution as kept at -20°C.

Aurotetrachloro trihydrate solution, methanolic: 50mM aurotetrachloro trihydrate was made in 10mL methanol, 0.2μm filter purified, wrapped in aluminium foil and stored at room temperature.

BiPS Solution: 1mg/mL (2R)-[(4-Biphenylylsulfonyl)amino]-N-hydroxy-3-phenyl-propion-amide (BiPS) was dissolved in MMP2 assay buffer and the solution was stored at -20°C.

Coomassie gel staining solution: 40% EtOH, 10% acetic acid and 0.1% Coomassie Brilliant Blue R-250 in dH_2O. The solution was kept at room temperature.

Coomassie destaining solution: 40% EtOH and 10% acetic acid in dH_2O. The solution was kept at room temperature.

Ellman's Reagent: 2mM DTNB, 50mM Sodium acetate in dH_2O and kept at 4°C. Do not autoclave.

G418 (Gentamycin): A 50mg/mL stock solution was prepared in dH_2O and stored at -20°C.

HEPES buffer: 20mM N-(2-Hydroxyethyl)-piperazine-N'-ethanesulfonic acid in dH_2O. The pH was adjusted to pH 8 and stored at room temperature.

IPTG: A 1.0M stock solution was prepared in dH_2O, filter-sterilised and stored at -20 °C.

Kanamycin: A 50mg/mL stock solution was prepared in dH$_2$O and stored at -20 $^\circ$C.

Luria broth (LB): 1% Tryptone, 0.5% yeast extract and 0.5% NaCl in dH$_2$O. The solution was autoclaved and kept at room temperature.

MES Buffer: 20mM 2-(*N*-morpholino) ethanesulfonic acid (MES) in dH$_2$O and adjusted to pH 6. Do not autoclave.

MMP2 Assay Buffer: 50mM Tris, 200mM NaCl, 4mM CaCl$_2$, 0.007% ZnCl$_2$ and 0.2% NaN$_3$ in dH$_2$O with pH adjusted to pH 7.5. The solution was kept at 4°C.

Nickel Binding Buffer: 50mM NaH$_2$PO$_4$, 500mM NaCl, 10mM imidazole, 0.1% Triton X-100 and 10% glycerol in dH$_2$O. The solution pH was adjusted to pH 8 and stored at room temperature.

Ninhydrin solution: 1.5g Ninhydrin and 3mL glacial acetic acid in 300mL n-BuOH. The solution was stored at room temperature. Do not autoclave.

p-Anisaldehyde solution: 3.5mL p-Anisaldehyde, 15mL glacial acetic acid and 50mL H$_2$SO$_{4(C)}$ in 350mL ice cold EtOH. The solution was stored at 0°C. Do not autoclave.

Permeation buffer: 0.2% Triton-X100 dissolved in PBS (pH 7.4) and kept at 4°C until needed. Do not autoclave.

Transfer buffer 1 (Tbf1): 30mM potassium acetate, 50mM MnCl$_2$, 0.1M KCl, 10mM CaCl$_2$ and 15% glycerol (v/v) in dH$_2$O. Do not autoclave.

Transfer buffer 2 (Tbf2): 9mM MOPS, 50mM CaCl$_2$, 10mM KCl and 15% glycerol (v/v) in dH$_2$O. Do not autoclave.

Transfer buffer, immunoblotting: 25mM Tris base, 0.2M glycine and 20% methanol (v/v) in dH$_2$O. Do not autoclave.

Tris-buffered saline with Tween-20 (TBS-T20): 17.6g NaCl, 0.4g KCl, 6g Tris and 500μL Tween-20 per 1L dH$_2$O. The solution pH was adjusted to pH 7 and kept at 4°C until needed. Do not autoclave.

TYM broth: 20% Tryptone, 0.5% yeast extract, 0.1M NaCl, 0.2% glucose and 10mM MgCl$_2$ in dH$_2$O. Autoclave and store at room temperature.

2.2   Chemistry and Nanotechnology Methods

2.2.1 Characterization Techniques and Assays

2.2.1.1   Ellman's Assay for Reduced Thiols

The reaction mixture for Ellman's assay was set up as follows: 840μL ddH$_2$O, 100μL 1M Tris (pH 8), 50μL DTNB and 10μL of the sample [284]. A standard series was prepared with cysteine hydrochloride of reduced glutathione (GSH), ranging from 0.001mM to 100mM. The reaction mixture was vortexed for 30sec then left to incubate at room temperature for 30-60min. The formation of a yellow colour indicated a positive for reduced thiol content and 200μL of the reaction mixture was transferred to a 96-well flat bottom microplate (Greiner) with the optical density determined at 412nm (OD$_{412}$) on a Omega® POLARStar (BMG Labtech) multimodal plate reader. Data capture was done with Omega™ Reader Control software package and data analysis was done with Microsoft® Excel™ 2010. The concentration of the unknown thiol, in molar (M), can be determined using the Beer-Lambert law ($\varepsilon_{DTNB} = 13\ 600M^{-1}cm^{-1}$) [285].

2.2.1.2   Nuclear Magnetic Resonance (NMR) Spectroscopy

1-D proton (^{1}H) nuclear resonance spectroscopy characterization was done at the Central Analytical Facility (CAF) at Stellenbosch University (Stellenbosch, Western Cape, South Africa). The experiments were conducted on a 600MHz Varian Inova Spectrometer (Varian Inc.). The samples were dissolved in 750μL deuterium oxide (D$_2$O) or 750μL deuterated chloroform (CDCl$_3$) in 5mm NMR tubes. Data deconvolution was done with SpinWorks© V3.1.8.1.

2.2.1.3   Attenuated Total Reflectance (ATR) Infrared Spectroscopy

ATR infrared spectroscopy experiments were carried out with a Nexus (Thermo Scientific) spectrometer with a Smart Golden Gate Accessory (Thermo Scientific) equipped with a zinc

selenide (ZnSe) lens. Solid- and liquid state samples were readily analysed by deposition on the optic sample window. Data acquisition was done with Omnic® for a spectral range of 600-4000cm^{-1} with 32 scans read per sample and automated refractive index correction for the ZnSe crystal (refractive index = 2.1). Background acquisition was done for 32 scans with background gain 8, set for automated compensation for ambient atmospheric CO_2 and H_2O content. Data analysis was done with Essential FTIR® V3.00.00.19.

2.2.1.4 High Resolution Transmission Electron Microscopy (HR-TEM) and Qualitative Energy Dispersive X-ray Spectroscopy (EDX)

a) Sample Preparation

A sterile dust free surface was prepared and a holey carbon film (400 mesh Cu) was placed with the reflective side facing upward. The nanoparticle samples were suspended in dH$_2$O at 5mg/mL and 3 drops were dropped onto the holey copper film with a stub-nosed Pasteur pipette. The sample prepared copper grids were allowed to dry at room temperature before being placed in a sample cartridge. The cartridge was dried *in vacuo* for at least 24h before analysis.

b) High Resolution Transmission Electron Microscopy (HR-TEM) and Qualitative Energy Dispersive X-Ray Spectroscopy (EDX)

Sample analysis was conducted by Dr S. Botha with a Tecnai F20 high resolution Field Emission Transimission Electron Microscope (TEM) equipped with modules for EDS, STEM (Scanning TEM), EELS (Electron Energy Loss Spectroscopy) and a HAADF (High Angle Angular Dark Field) detector. The obtained micrographs were analysed with ImageJ V1.46r.

2.2.1.5 Quantitative Energy Dispersive X-Ray Spectroscopy (EDX)

Synthesized gold nanoparticles were lyophilized and 30-50mg of the appropriate sample was transferred to a 15mL polypropylene tube and sealed with parafilm. The samples were sent for quantitative EDX analysis by Dr J.D. Painter at the Department of Engineering and Applied Materials Science, Cranfield University, Cranfield, Bedfordshire, United Kingdom.

2.2.1.6 Ultra Violet-Visible (UV-Vis) Spectroscopy, UV-Vis Spectrometry and Luminescence

UV-Vis spectroscopy and luminescence assays were conducted on an Omega® POLARStar (BMG Labtech, Offenburg) multimodal plate reader. The plate reader has an absorbance

spectrometer, preselected fluorescence excitation/emission filter wheels and luminescence modules. Data acquisition can be done for endpoint- as well as kinetic analysis for all above mentioned spectral functions and was done with the Omega® Reader Control software package with acquired data exported in Microsoft® Excel™ 2010 format. Acquisition parameters which were typically used are given below.

(a) UV-Vis spectroscopy and UV-Vis Spectrometry

An absorbance spectrometer with a xenon flash-lamp was used for spectral- and absorbance acquisition. Spectral acquisition was in the range 220-850nm with a resolution of 1nm. Absorbance data acquisition was done with up to 8 different specified discrete wavelengths simultaneously, dependent on the assay requirements. Both data acquisition modes utilized 200 scans per well with the THERMOStar™ incubator pre-set at 25°C and 6-well to 96-well clear microplates were read with the bottom optic. Assay specifics will be discussed in the appropriate sections.

(b)   Luminescence

The luminescence module was installed as required and the THERMOStar™ incubator pre-set at the required assay temperature. The fluorescence emission filter wheels were set to "lens" and the integration time was set at 0.5sec per well with data normalized to 0.1sec. Luminescent samples were prepared in 96-well U-bottom black plates (Merck) and read with the top optic.

2.2.1.7   Fluorescence Emission Spectroscopy

Fluorescent quantum dots samples were prepared in the appropriate buffer solutions at equal concentrations and 400µL was transferred to precision cell Quarzglas SUPRASIL® cuvettes (Hellma Analytics, Mullheim, Germany). Fluorescence emission spectra were obtained using a Nanolog^{TM} 3-22-TRIAX (Horiba, USA) fitted with double grating excitation and emission monochromators (slit width of 5nm) for a spectral range of 400-800nm.

.

2.2.1.8   High Pressure Liquid Chromatography Electron Spray Ionization Mass Spectrometry (HPLC-ESI-MS)

The protocol was utilized for accurate mass determination of small molecules by Dr T. Kudanga (Biocatalysis and Technical Biology, Cape Peninsula University of Technology, Cape Town, South Africa). LC-MS was performed on an Ultimate 3000 Dionex HPLC

system (Dionex Softron, Germering, Germany) equipped with a binary solvent manager and autosampler and coupled to a Brucker ESI Q-TOF mass spectrometer (Bruker Daltonik GmbH, Germany). The products were separated by reversed phase chromatography, on a Waters Sunfire C18-column (5µm; 4.6×150mm; Dublin Ireland). Methanol, water and trifluoroacetic acid (30:70:0.1 v/v/v) was used as solvent with isocratic elution for 20min at a flow rate of 1mL.min^{-1} with an oven temperature of 30°C. MS spectra were acquired in positive mode using the full scan and auto MS/MS (collision energy 25eV) scan modes with dual spray for reference mass solution. Electrospray voltage was set to -4500V. Dry gas flow was set to 9L.min^{-1} with a temperature of 300°C and nebulizer gas pressure was set to 35psi.

2.2.1.9   Agarose Gel Electrophoresis of Gold Nanoparticles

Gold nanoparticles were resolved by agarose gel electrophoresis on 0.25-0.5% gels and electrophoresed in 1x TBE buffer. The loading sample was prepared by mixing gold nanoparticles with 30% glycerol in a ratio of 1:1 and loaded into the wells at a volume of 15-20µL. The samples were electrophoresed at 40V for 30-45min. Agarose gels were visualized and photographed with the UVP BioSpectrum® Imaging System.

2.2.2 Synthesis of Ligands to be used in Gold Nanoparticle Functionalization

Glassware and magnetic stirrer bars were stripped with 5M NaOH, rinsed with ultrapure water (18.2MΩ), treated with high purity acetone (Merck) and over dried at 90°C. Solvents and chemicals of highest purity were used in the synthesis. Reactions were monitored with thin layer chromatography on silica coated aluminium foil plates (Merck). The TLC analysis was done by using functional group specific staining solutions (p-anisaldehyde and ninhydrin), ultraviolet (254nm) staining and iodine staining. Inert reaction atmospheres were not used.

2.2.2.1   Synthesis of 6-*N*-2-(*N*-bis(carboxymethyl))-hexanoic acid (NH₂-NTA)

This synthesis is adapted from the literature [286]. Bromoacetic acid (30.2mM) was dissolved in 15mL of ice cold 1.5N NaOH aqueous solution and kept at 0°C while stirring. N^{ε}-Z-L-lysine (0.5eq) was dissolved in 25mL ice cold 1.5M NaOH solution and added drop wise to the bromoacetic acid solution. The solution was heated to 50°C with stirring for 2h and left to cool to ambient room temperature string overnight. To this stirring solution 45mL of 1M HCl was added drop wise with the immediate formation of a white precipitate (N^{ε}-Z-NTA). The

reaction was allowed to go to completion for 2h (monitored by TLC) and the precipitate was washed with ultrapure water (18.2MΩ) three times on a Buchner funnel. The precipitate was dissolved 50mL methanol:H_2O (20:1) with the addition of a spatula tip of 5% Pd/C under stirring at room temperature and atmospheric pressure. The hydrogenation reaction reached completion within 5 days, monitored with TLC. The catalyst was filtered off with a Buchner funnel and the solvent was then removed *in vacuo*. The white-yellow precipitate was dissolved in 200mL ethanol:dH_2O (97.5:2.5) and left to crystallize at 0°C for 2-4 days. The crystals were washed with ethanol (Merck), oven dried and analysed by proton NMR spectroscopy (Section 2.2.1.2).

2.2.2.2 Synthesis of 6-*N*-Thiobutyro-2-(*N*-bis(carboxymethyl))-hexanoic acid (SH-NTA)

The 6-*N*-2-(*N*-bis(carboxymethyl))-hexanoic acid (NH$_2$-NTA) crystals (Section 2.2.2.1) were dissolved in 50mL 20mM MES buffer (pH 6) at room temperature with rapid stirring. Thiobutyrolactone (5eq) was added to the stirring solution and allowed to reach completion within 16h, confirmed by TLC. The whole reaction solution was freeze-dried (Section 2.3.4) and the lyophilized powder was resuspended in 200mL ethanol:dH_2O (97.5:2.5) and left to crystallize at 0°C for 2-4 days. The crystals were washed with ethanol (Merck), oven dried and analysed by proton NMR spectroscopy (Section 2.2.1.2).

2.2.2.3 Synthesis of thiolated Hyperbranched High Molecular Weight Polyethyleneimine (SH-PEI)

Hyperbranched polyethyleneimine (~15.4kDa, PEI) was dissolved in 50mL 20mM MES buffer (pH 6) at room temperature with rapid stirring. Thiobutyrolactone (1.1eq) was added to the stirring solution and reached completion after 24h, monitored with TLC. The whole reaction solution was freeze-dried (Section 2.3.4) and suspended in 5mL ultrapure water (18.2MΩ). The 5mL solution was dialyzed with a 3500 MWCO dialysis cartridge (Pierce Biotechnology) against ultrapure water (18.2MΩ) for 2 days with the addition of fresh buffer twice daily. The contents of the dialysis cartridge were transferred to a 50mL polypropylene tube. The product was confirmed to be thiolated and quantified with Ellman's assay (Section 2.2.1.1).

2.2.3 One-pot Synthesis and Bio-functionalization of Gold Nanoparticles (AuNPs)

2.2.3.1 Synthesis

Glassware and magnetic stirrer bars were stripped with 5M NaOH, rinsed with ultrapure water (18.2MΩ), treated with high purity acetone (Merck) and over dried at 90°C. Solvents of highest purity were used in the synthesis. The one-pot synthesis is adapted from Zheng *at al* [287]. 600μL of a methanolic aurotetrachloro trihydrate solution was dissolved in 55mL methanol:acetic acid (0.73:0.27) stirring at room temperature. The desired surface ligand was prepared in ultrapure water (18.2MΩ) and added all at once at a predetermined ratio to aurate ions in solution, Ligand:Au^{3+}, ranging from 0.25:1 → 1:1. The solution was left to stir for 5-20min and aqueous sodium borohydride ($NaBH_4$) was added drop wise at a predetermined ratio to aurate ions in solution, $NaBH_4$:Au^{3+}, ranging from 0.25:1 → 1.1. The reaction solution turned brown, black then a hue of red. The reaction was monitored, by taking 500μL aliquots at 30min intervals, using UV-Vis spectroscopy (Section 2.2.1.6) for the formation of gold nanoparticles (AuNPs). The reaction was complete after 5h when no further change was observed for the UV-Vis spectra. The one-pot functionalized AuNPs were sedimented by centrifugation at 8000g for 45min in a Beckman Coulter centrifuge (SX4750A swing rotor). The AuNP sediment was resuspended and washed 5 times with 10mL PBS (pH 7.4) by centrifugation at 8000g for 45min in a Beckman Coulter centrifuge (SX4750A swing rotor). The AuNPs were transferred to a 10 000MWCO dialysis cartridge (Pierce Biotechnology) and dialysed against PBS (pH 7.4) for 2 days with fresh buffer added twice daily. The AuNPs were freeze-dried (Section 2.3.4) and the lyophilized powder was kept at room temperature in the dark. The lyophilized AuNP powder was grey to black in colour and was readily resuspended in ultrapure water (18.2MΩ) at 5mg/mL-100mg/mL without loss in optical density for up to 1 year after synthesis.

2.2.3.2 Evaluation of Gold Nanoparticle (AuNP) Aqueous Stability

The lyophilized AuNPs (2.2.4.1) were suspended in ultrapure water (18.2MΩ) at 5mg/mL-50mg/mL. The AuNP samples were adjusted to an optical density (OD) ~1.6 and 25μL was transferred to a 96-well flat bottom clear microplate (Greiner). The appropriate buffer was pipetted to the corresponding wells to a final volume of 200μL with the AuNPs final OD ~0.2. The UV-Vis spectrum of each well was determined (Section 2.2.1.6a) and monitored at different time intervals for the following parameters: ionic strength, pH and biomolecule interactions. Citrate (pH 5 and pH 6) was used from 0.001M to 1M; sodium chloride (NaCl) was used from 0.001M to 1M and β-mercaptoethanol was used from 0.25mM to 25mM.

Biomolecule interactions were done with bovine serum albumin (BSA), at a final concentration of 1mg/mL, as well as tissue culture media, with and without foetal bovine serum supplemented.

2.2.3.3 Bioconjugation to Functionalize Gold Nanoparticle Surfaces
2.2.3.3.1 Differential Functionalization of the Gold Nanoparticle Surface with Commercial Crosslinker SM-PEG$_6$

Quantitative EDX analysis (Section 2.2.1.5) was used to determine the nitrogen content of the lyophilized AuNP samples. The assumption was made that nitrogen contributing to the elemental composition of the AuNP samples were from the surface ligand. PBS does not contain nitrogen and atmospheric nitrogen was discounted as the EDX analysis was conducted *in vacuo*. The estimated amount of primary- (149mol), secondary- (90mol) and tertiary amines (120mol) cumulatively delivers 359mol nitrogen for 1mol PEI-SH on the surface of the AuNPs. As an example, if EDX indicated an average nitrogen content of 10% for 5mg/mL AuNPs, this would mean: $\frac{149\text{mol primary amines}}{359\text{mol total amines}}$ x 10% x 5mg/mL = 0.21mg/mL primary amines (-NH$_2$) for 5mg/mL AuNPs. The SM-PEG$_6$ bifunctional crosslinker (Pierce Biotechnology) utilizes carbodiimide and maleimide bioconjugation chemistry to crosslink primary amines (NH$_2$) and thiols (SH) [288]. The SM-PEG$_6$ was attached to the primary amines of PEI-SH on the AuNP surface in the following manner: 10% (0.02mg/mL primary amines), 20% (0.04mg/mL primary amines) and 30% (0.06mg/mL primary amines) SM-PEG$_6$ to total primary amines.

The crosslinking reaction times were conducted for the maximum time recommended by the manufacturer. The AuNPs (5mg/mL) was dissolved in 20mL 20mM HEPES buffer (pH 8) stirring at room temperature. SM-PEG$_6$ (1.1eq) was added to the calculated amount of primary amines and the reaction was left to proceed for 40-60min. A 500μL aliquot was taken for UV-Vis spectroscopy analysis of the surface plasmon band (λ_{SPR}). Equimolar amounts of SH-NTA (Section 2.2.2.2) to SM-PEG$_6$ were added to the solution and the reaction was left to proceed for 60-80min. A 500μL aliquot was taken for UV-Vis spectroscopy analysis of the surface plasmon band (λ_{SPR}). The surface modified AuNPs were sedimented and washed three times with 10mL PBS (pH 7.4) by centrifugation at 8000g for 45min in a Beckman Coulter centrifuge (SX4750A swing rotor). Colloidal stability of the surface modified AuNPs was determined as in Section 2.2.3.2.

2.2.3.3.2 Glutaraldehyde Mediated Amine-to-Amine Crosslinking of Doxorubicin to the Gold Nanoparticle (AuNP) Surface

The glutaraldehyde crosslinking of primary amines is from known drug loading [289] and protein crosslinking protocols [290]. Surface modified AuNPs (2.2.4.3.1) were suspended at 5mg/mL in a rapidly stirring 50mL 20mM HEPES (pH 8) which contained 45mg doxorubicin (0.9mg/mL). The reaction vessel was protected from direct ambient light by aluminium foil and the mixture was stirred for 15-20min. A freshly prepared 2.5% glutaraldehyde solution (20mM HEPES, pH 8) was added to the stirring solution in four equal 250μL portions over 10min. The solution colour slowly changed from bright clear red to a turbid orange colour. The reaction was quenched with 500μL 1M Tris (pH 8). The doxorubicin loaded AuNPs were sedimented and washed (5x) with PBS (pH 7.4) by centrifugation at 8000g for 10min in a Beckman Coulter centrifuge (SX4750A swing rotor) precooled to 4°C. The doxorubicin loaded AuNPs were freeze-dried and kept protected from light at -20°C.

2.2.3.3.3 Quantification of the Doxorubicin on the Surface of Gold Nanoparticles

(a) Acid hydrolysis drug release

Acid hydrolysis of doxorubicin release is typically done with 1M HCl [291] but was adapted to a lower concentration to determine if doxorubicin was gradually released from the AuNP surface. The amine-sugar which is attached by an ether linkage to the anthracine-like structure of doxorubicin (Figure 1.5, Section 1.2.3.2.2) is labile in acidic environments and will facilitate doxorubicin release without the need for a pH-sensitive linker. The doxorubicin loaded AuNPs (100pM) were suspended in dH_2O at and aliquotted into different 1.5mL Eppendorf tubes containing 750μL 0.1N HCl. The contents of the tubes were mixed by gentle inversion and left to incubate at room temperature for different time intervals to determine acid hydrolysis facilitated drug release of doxorubicin from the AuNP surface. At the appropriate time interval the AuNPs were sedimented by centrifugation at 16 000g in an Eppendorf 5415D bench top centrifuge (Rotor: F45-24-11). The doxorubicin containing supernatant was snap frozen in liquid nitrogen and stored at -20°C.

(b) High pressure liquid chromatography (HPLC) quantification

High pressure liquid chromatography was performed on an Ultimate 3000 Dionex HPLC system (Dionex Softron, Germering, Germany) equipped with a binary solvent manager, an autosampler and a coupled photodiode array. The acid hydrolyzed supernatants (Section

2.2.3.3.3a) were separated by reversed phase chromatography on a Hypersil Gold C18-column (5μm; 4.6×250mm; Thermo). The mobile phase was a mixture of methanol, acetonitrile, water and trifluoroacetic acid (25:15:60:0.1 v/v/v) with isocratic elution for 20min at a flow rate of $0.8mL.min^{-1}$ and an oven temperature of 40°C. UV detection of doxorubicin was done at 272nm and confirmed with corresponding UV-Vis spectra which showed doxorubicin absorbance maxima at 495nm. Quantification of doxorubicin was done with a doxorubicin standard series ranging from 0.001μg/mL to 1μg/mL.

2.2.4 Ligand Exchange and Bio-functionalization of Indium Phosphide Quantum Dots

Surface changes on the quantum dot surface were monitored with fluorescence spectrometry (Section 2.2.1.7).

2.2.4.1   Ligand Exchange of Indium Phosphide Quantum Dots

The following protocol is an adaptive amalgation of various protocols [223, 292-294]. A methanolic solution of 1μM palmitic acid passivated indium phosphide quantum dots with a maximum emission wavelength at 625nm (QD_{625}) were obtained from Mr Paul Mushonga [388] (Chemistry Department, University of the Western Cape, Cape Town, South Africa). The QD_{625} was sedimented and washed three times with 1mL methanol by centrifugation at 16 000g in an Eppendorf 5415D bench top centrifuge (Rotor: F45-24-11) and suspended in 500μL chloroform in a 1.5mL Eppendorf tube. In a separate Eppendorf tube a 500μL aqueous solution containing 1mM thiolated polyethyleneimine (PEI-SH, Section 2.2.2.3) and 1mM tetrabutyl-ammonium hydroxide (Sigma) was incubated at room temperature for 30min. The contents of the tubes were mixed together and vortexed for 2-4h at room temperature. Ligand exchange was completed when the red QD_{625} exchanged from the chloroform layer to the aqueous layer. The water soluble PEI-SH functionalized QD_{625} was sedimented by centrifugation at 16 000g in an Eppendorf 5415D bench top centrifuge (Rotor: F45-24-11) and suspended in 500μL ultrapure water (18.2MΩ). Fluorescence spectroscopy indicated no fluorescence signal was left in the organic layer and it was assumed that all QD_{625} were successfully ligand exchanged with PEI-SH into the aqueous layer. The PEI-SH functionalized quantum dots were kept at 4°C until needed.

2.2.4.2   Bio-functionalization of Indium Phosphide Quantum Dots

(a) Differential Functionalization of the Quantum Dot Surface with Commercial Crosslinker SM-PEG$_6$

The assumption was made that the quantum dots were of the same size range as the gold nanoparticles used in this study. A further assumption was made that the amount of the PEI-SH on the surface of QD$_{625}$ would have the same packing density as on the surface of AuNP. The quantum dots (Section 2.2.4.1) were lyophilized (Section 2.4.3) then resuspended in dH2O at 5mg/mL with the appropriate amount of SM-PEG$_6$ (10%, 20% and 30%) and SH-NTA added. The reaction conditions and purification were as described in Section 2.2.3.3.1.

(b) Carbodiimide Crosslinking of Chlorotoxin to the Quantum Dot Surface

The modified quantum dots (Section 2.2.4.2a) were suspended in 20mL HEPES buffer (20mM, pH 8) stirring at room temperature and recombinant chlorotoxin (Section 2.3.3) was added at a final concentration of 1μg/mL. The reaction mixture was left to stir for 5-10min and 1.5 equivalents of freshly prepared 1-Ethyl-3-(3-dimethylaminopropyl) carbodiimide HCl (EDC) was added and the reaction was left to proceed for 40-60min. The peptide functionalized quantum dots were sedimented and washed three times with 10mL PBS by centrifugation at 6000g for 10min in a Beckman Coulter centrifuge (SX4750A swing rotor) precooled to 4°C and suspended in ultrapure water (18.2MΩ) to a final concentration of 10nM. The peptide functionalized quantum dots were protected from light kept at 4°C.

2.3 Molecular Biology Techniques

2.3.1 Bacterial Cell Culture

2.3.1.1   Bacterial Strains

Escherichia coli **strain DH$_{5α}$:**

F⁻ Φ80*lac*ZΔM15 Δ(*lac*ZYA-*arg*F) U169 *rec*A1 *end*A1 *hsd*R17 (rK–, mK+) *pho*A *sup*E44 λ⁻ *thi*$^{-1}$ *gyr*A96 *rel*A1. This strain was used to produce plasmid DNA.

Escherichia coli **strain ArcticExpress™ (DE3):**

B F⁻ *ompT hsdS*(rB⁻ mB⁻) *dcm*$^+$ Tet^r *gal* λ(DE3) *end*A Hte [*cpn10 cpn60* Gent^r]. This strain was used to produce recombinant peptides.

2.3.1.2 Antibiotic Selection

Transformed *E. coli* containing ampicillin or kanamycin (G418) resistant plasmids were plated on nutrient agar with the appropriate concentration of antibiotics. Ampicillin was used at 200µg/mL and kanamycin (G418) was used at 35µg/mL. Antibiotic specific selection was maintained for bacterial growth in liquid culture by inclusion of the appropriate antibiotic at similar concentration as was used for nutrient agar growth.

2.3.1.3 Preparation of Competent Bacterial Strains for Transformation

Nutrient agar plates with were used to streak a desired bacterial strain onto with incubation overnight at 37°C. A single colony was picked and inoculated into 20mL TYM broth. The liquid culture was put on a shaker (200rpm) at 37°C and monitored until the optical density (OD$_{550}$) was ~0.2. This liquid culture was then transferred to 100mL TYM broth and grown at 37°C until OD$_{550}$ reached 0.2. To this culture 400mL fresh TYM broth was added and grown until OD$_{550}$ was between 0.4-0.6. The cells were rapidly cooled on ice water by swirling and then transferred to 250mL centrifuge tubes. The cells were pelleted by centrifugation at 6000g for 10min in a Beckman Coulter centrifuge (SX4750A swing rotor) precooled to 4°C. The cell pellet was resuspended in ice cold 250mL Tfb1 and left to equilibrate for 30min. The cells were then pelleted by centrifugation. The cell pellet was resuspended in 30mL Tfb2. The cells were snap frozen in 300µL portions with liquid nitrogen and stored at -80°C.

2.3.1.4 Bacterial Transformations

Competent cells (Section 2.3.1.3) were thawed on ice for 30min. A 100µL of the competent cells were transferred to two autoclaved Eppendorf tubes and kept on ice. A negative control was setup by adding 1µL water to the competent cells and treating the control identical as the plasmid DNA experiment. Plasmid DNA, 1µL of 100-300ng DNA, was added and gently mixed by inversion of the tube and incubated on ice for 30min. ells were then heat shocked at 37°C for 5min and cooled on ice for 5min with immediate addition of 500µL pre-warmed LB without antibiotics. The mixture was incubated at 37°C for 1h. The cells (50µL) were then plated with glass beads onto nutrient agar plates containing the appropriate antibiotic(s) and grown overnight at 37°C.

2.3.2 Acquisition, Preparation and Manipulation of DNA

2.3.2.1 Acquisition of Template DNA

A synthetic variant of chlorotoxin gene was designed based on the published amino acid sequence [118] and commercially synthesized by GenScript (GenScript Inc., New Jersey, USA) to be subcloned into a pGEX-6P-2 expression construct. The construct obtained was named pGEX-6P-2-CTX. A pGEM-T-Easy cDNA clone of MMP2 was prepared from MCF-7 breast cancer cells by Miss C Dodgen (Biotechnology Department, University of the Western Cape, Bellville, Cape Town, South Africa). The sequence was confirmed to be a perfect match for wild type MMP2 and was named pGEM-T-MMP2.

2.3.2.2 Isolation of plasmid DNA

A single colony of transformed (2.3.1.4) *E. coli* was picked at random from an overnight nutrient agar plate and inoculated into 10mL LB containing the appropriate antibiotic(s). The inoculated culture was incubated at 37°C with shaking for 16h. The cells were harvested by centrifugation at 6000g for 10min in a Beckman Coulter centrifuge (SX4750A swing rotor). The plasmid DNA was isolated with the Promega Wizard® SV plasmid isolation kit. The protocol was completed according to the manufacturer's instructions.

2.3.2.3 PCR Amplification of Gene Fragments

PCR reactions were done at a final volume of 25μL. The amount of template DNA used was concentration dependent. The composition typical for a PCR reaction can be seen in Table 2.1.

Table 2.1: PCR reaction composition

	Volume (μL)	Final [ ]
HiFi hotstart Taq Mastermix (x2)	12.5	x1
Forward primer (10μM stock)	1.0	0.4μM
Reverse primer (10μM stock)	1.0	0.4μM
Template DNA	1.0 – 2.0	1-5ng/μL
ddH$_2$O	8.5 – 9.5	-
Total	**25.0**	-

Oligonucleotide melting temperatures (T_m) was provided by the supplier (IDT Technologies) and was confirmed by using an online tool OligoCalc (www.basic.northwestern.edu/biotools
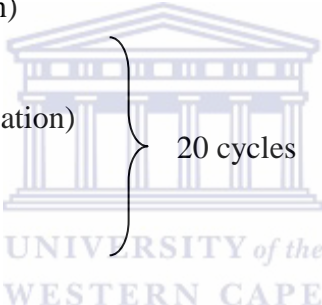
[/oligocalc.html).](/oligocalc.html) Thermal cycling conditions used for the different templates are given in (a) and (b), respectively. PCR products were analysed by electrophoresis on 1% agarose gels with 1x TBE as electrophoresis buffer.

(a)   Thermal cycling conditions for amplification of pGEX-6P-2-CTX

94°C for 2min (Initial denaturation)

94°C for 1min (Denaturation)

98°C for 20sec (Hotstart Taq activation)

60°C for 15sec (Annealing)   25 cycles

72°C for 30sec min (Extension)

72°C for 5 min (Final extension)

(b)   Thermal cycling conditions for amplification of pGEM-T-MMP2

94°C for 2min (Initial denaturation)

94°C for 1min (Denaturation)

98°C for 20sec (Hotstart Taq activation)

65°C for 45sec (Annealing)   20 cycles

72°C for 30sec min (Extension)

72°C for 5 min (Final extension)

2.3.2.4 Gel Extraction and Purification of PCR Products and DNA

DNA bands of the desired size were excised from the agarose gel under brief UV-assisted visualization and purified with the QIAquick® gel extraction kit (Qiagen). The protocol was completed according to the manufacturer's recommendations. The purified amplicons were used immediately or stored at 4°C until needed. Plasmid DNA was purified in a similar manner.

2.3.2.5 Restriction Enzyme Digestion of PCR Products and Plasmids

Restriction enzymes were used and inactivated as recommended by the manufacturer (Fermentas). Typically, restriction enzyme digestion reaction final volume was 50μL where the reaction constituents were as follows: 5μL FastDigest® 10x green buffer; 4-6μL for the appropriate combination of FastDigest® double digestion restriction enzymes; 2-10μL DNA with the remainder of the volume made up with nuclease free water. The reaction mixtures were mixed by gentle pipetting or inversion and incubated at 37°C for 90min. The restriction

enzymes were inactivated by the addition of 1μL 0.2M EDTA (pH 8) or by heating the reaction mixture at 80°C for 5min, dependent on the manufacturer's recommendations. The reaction mixtures were resolved on an agarose gel and purified with QIAquick® gel extraction kit (Qiagen) as per manufacturer's recommendations.

PCR amplicons (Sections 2.3.2.3a and 2.3.2.3b) were purified as described in Section 2.3.2.4 and were double digested with *BamHI* and *XhoI*. Plasmid DNA (pGEX-6P-2) obtained as described in 2.3.2.2 was also double digested with *BamHI* and *XhoI*. This enabled insertion of the PCR amplicon sequence in the correct 5' to 3' orientation in the multiple cloning site (MCS) of the pGEX-6P-2 plasmid. The restriction enzymes left the pGEX-6P-2 with non-complementary ends which prevented self-ligation. The pGEX-6P-2 vector enabled the recombinant fusion of an N-terminal glutathione-S-transferase (GST) which allows for specific fusion protein purification downstream.
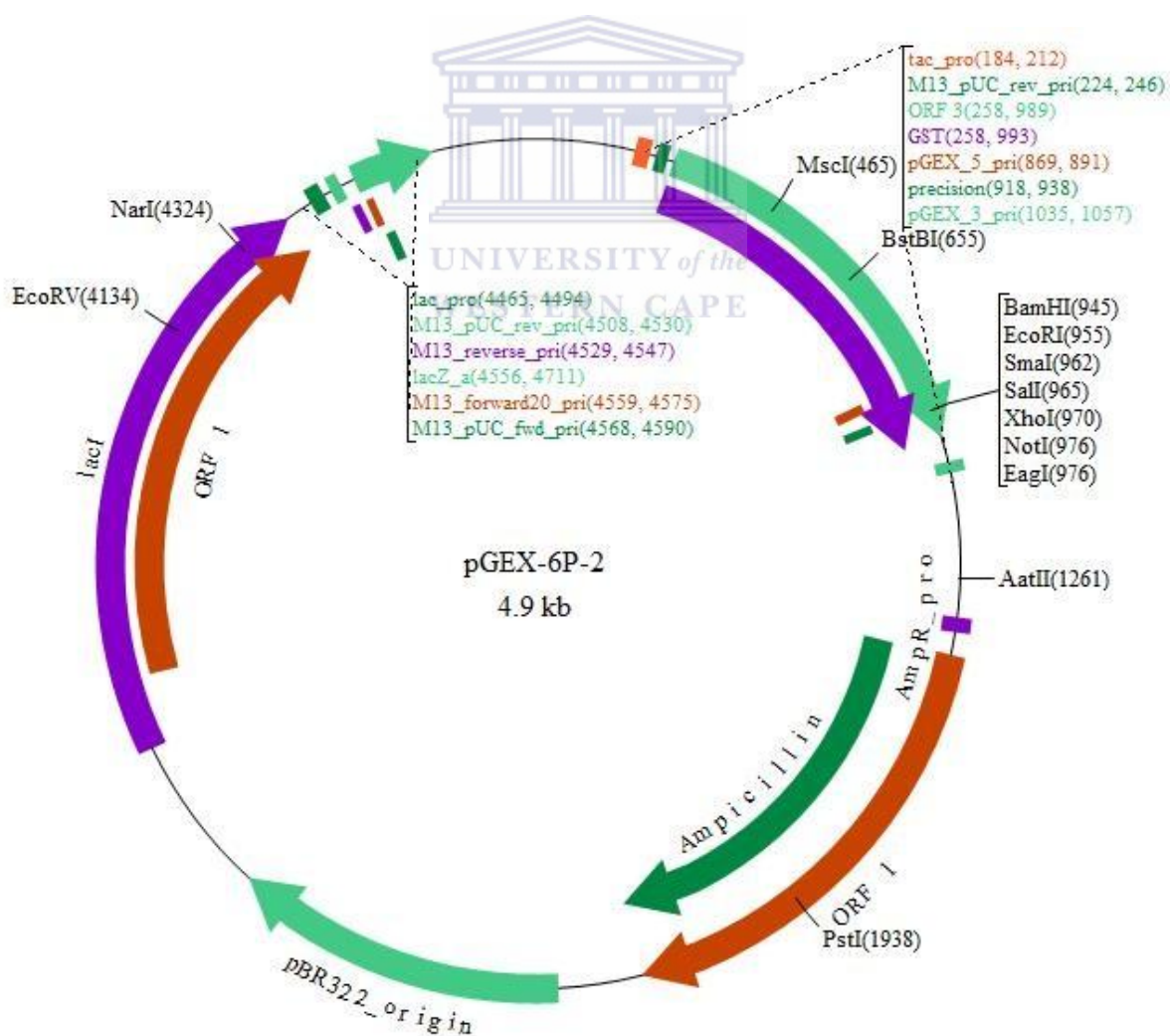
Figure 2.1: Circular vector map of pGEX-6P-2

The pEGFP-N3 plasmid was double digested with *SalI* and *BglII*, isoschizomers for *BamHI* and *XhoI*, respectively. The restriction enzymes left the pEGFP-N3 construct with non-complementary ends, preventing self-ligation. This enabled the insertion of PCR amplicons (Sections 2.3.2.3a and 2.3.2.3b), digested with *BamHI* (5') and *XhoI* (3'), in the correct 5' to 3' orientation. Ligation into this vector would destroy the respective restriction sites, making it impossible to release the inserted DNA sequence. The pEGFP-N3 vector enabled the fusion of enhanced green fluorescent protein (EGFP) to the C-terminal of recombinant proteins.
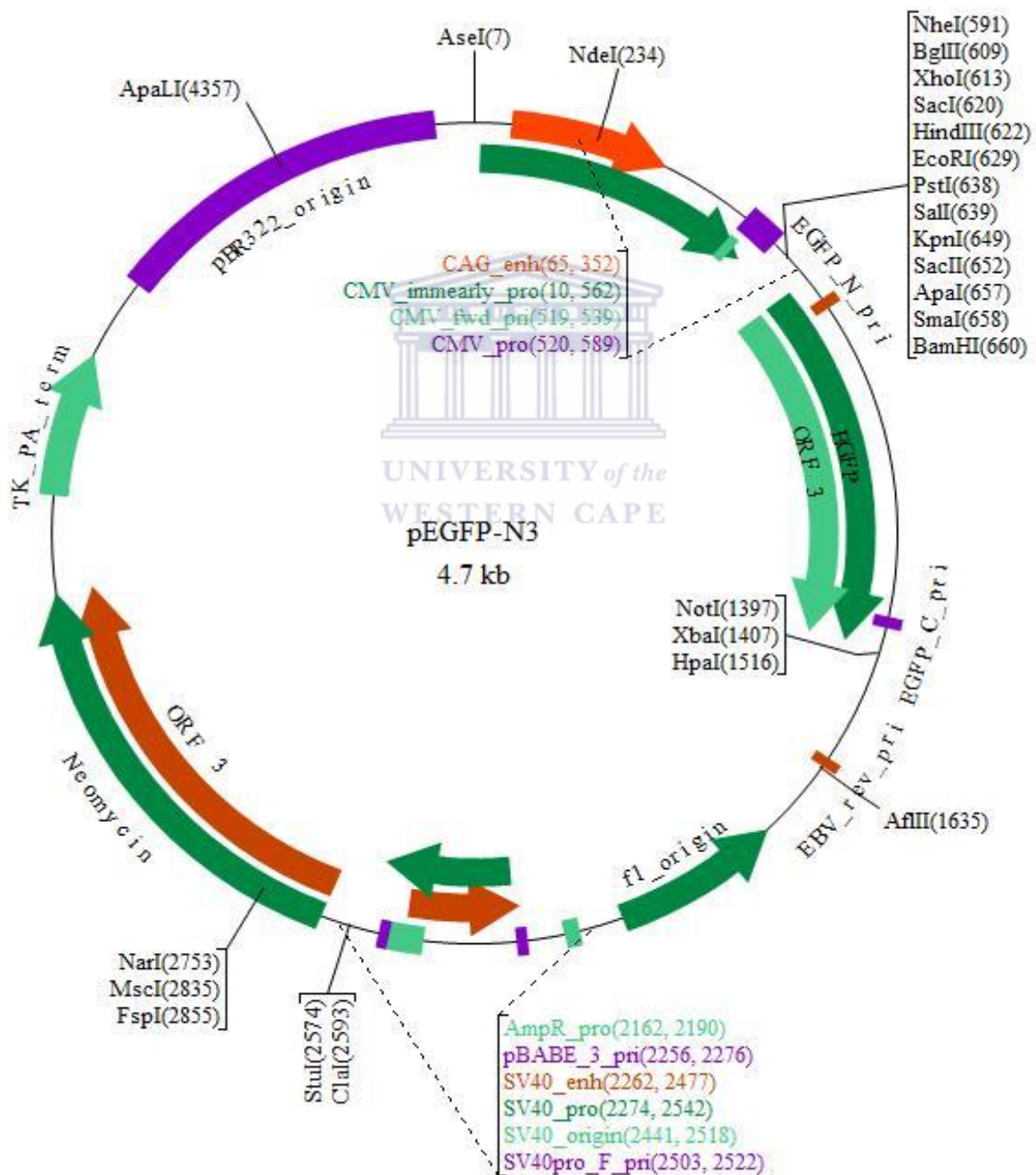
Figure 2.2: Circular vector map of pEGFP-N3

2.3.2.6 Ligation of DNA

PCR amplicons and plasmid DNA, prepared as in Sections 2.3.2.4 and 2.3.2.5, was used in ligation reactions. Typically, the ratio of PCR amplicon insert DNA to plasmid DNA was calculated at a ratio of 3:1 to 6:1 depending on the amount of DNA. The following equation was used for the above mentioned calculation:

$$\left(\frac{\text{(amount of plasmid DNA in ng).(size of insert in kb)}}{\text{(size of plasmid in kb)}} \right) . \text{(ratio of insert to plasmid)}$$

A typical ligation reaction can be seen in Table 2.2. The ligation was left to proceed at 4°C for 16h and then used to transform competent *E. coli* (Section 2.3.1.4).

Table 2.2: The composition for a typical ligation reaction

	Volume (µL)	Final [ ] (ng/µL)
*PCR Amplicon	12-24	24-72
*Plasmid	2-6	4-12
T4 ligase	2	-
ddH$_2$O	24-8	-
Total	40	

*Purified and restriction enzyme digested

2.3.2.7 Colony PCR to Screen for Positive Bacterial Transformants

Transformed *E. coli* (Section 2.3.1.4) was plated onto nutrient agar and left to grown overnight at 37°C. Colonies were picked at random with a sterile pipette tip and gently mixed into the appropriate PCR tube containing the PCR reaction mixture by pipetting the mix ten times. The composition for a typical colony PCR reaction can be seen in Table 2.3. Gene specific primers were used. Thermal cycling conditions used for colony PCR were:

94°C for 2min (Initial denaturation)
94°C for 1min (Denaturation)
T$_m$-5°C for 1min (Annealing)   30 cycles
72°C for 45sec (Extension)
72°C for 5 min (Final extension)

Table 2.3: colony PCR reaction composition

	Volume (µL)	Final [ ]
DreamTaq Mastermix (x2)	12.5	x1
Forward primer (10µM stock)	1.0	0.4µM
Reverse primer (10µM stock)	1.0	0.4µM
ddH$_2$O	10.5	-
Total	**25.0**	-

PCR products were analysed by electrophoresis on 1% agarose gels with 1x TBE as electrophoresis buffer.

2.3.2.8 Agarose Gel Electrophoresis of DNA

DNA was resolved by agarose gel electrophoresis on 1% gels with GelRed (20µL per 100mL agarose) and electrophoresed in 1x TBE buffer. The loading sample was prepared by mixing sample DNA with commercial loading buffer (Fermentas) in a ratio of 5:1 and loaded into the wells at a volume of 5-10µL. A DNA molecular marker, O'GeneRuler™ DNA 100bp ladder (Fermentas) was utilized to estimate DNA fragment sizes and was loaded at a volume of 2.5µL. The samples were electrophoresed at 100V for 45-60min. Agarose gels were visualized and photographed with the UVP BioSpectrum® Imaging System.

2.3.2.9 Quantification of DNA

DNA content of samples were analysed using the Nanodrop-1000 spectrophotometer. The sample pedestal was wiped clean and the spectrophotometer was blanked with 1µL ddH$_2$O. The appropriate sample was loaded onto the sample pedestal at 1µL. This was repeated three times and the average value was the estimated DNA content in ng/µL.

2.3.2.10 Sequence Analysis of Clones

The desired clones identified by colony PCR (Section 2.3.2.7) were streaked onto nutrient agar plates and left to grow overnight at 37°C. The plates were sealed with parafilm and sent for sequencing at Inqaba Biotechnologies. The sequencing was done for all clones with the following:

(i) Plasmid specific primers in both directions (5' → ,3' ←)

(ii) Gene specific primers flanking the restriction enzyme sites of sequence insertion (5' → ,3' ←)

(iii)   Internal sequence primers, reading the gene sequence from the centre of the gene towards the ends (3' ←, 5' →)

Sequencing data obtained was analysed with various programs. FinchTV© (V1.4.0) was used to determine sequence chromatogram quality. BioEdit© Sequence Alignment editor was used to do multiple sequence alignments as well as generate a consensus sequence. The BLAST® (GenBank) algorithm was used to align the consensus sequence with the wild type oligonucleotide sequences.

2.3.3 Recombinant Protein Production, Extraction and Purification

2.3.3.1   Protein Expression

Expression construct (pGEX-6P-2) transformed ArcticExpress™ E. coli were gown overnight at 37°C on nutrient agar plates with the appropriate antibiotics. Single colonies were picked and used to inoculate 100mL LB agar containing the appropriate antibiotics and grown overnight at 37°C on a rotary shaker (200rpm). Fresh 900mL LB with appropriate antibiotics was inoculated with the 100mL overnight culture and grown at 37°C on a rotary shaker until an optical density (OD) of 0.8 was reached. The incubation temperature was decreased to 10°C and Isopropyl-b-D-thiogalactopyranoside (IPTG) was added to the liquid culture to a final concentration of 2mM to induce protein production. The culture was left to grow for 48h at 10°C and the cells were harvested. The cell suspension was transferred to 250mL centrifuge tubes and centrifuged at 6000g for 10min in a Beckman Coulter centrifuge (SX4750A swing rotor) precooled to 4°C. The cell pellets were stored at -20°C.

2.3.3.2   Protein Extraction

Cell pellets were thawed on ice and resuspended in BugBuster™ (Bugbuster™ GST Bind Purification Kit, Novagen) bacterial cell lysis reagent, 5mL BugBuster™ per 1g wet cell paste, by pipette mixing the cell paste with the lysis reagent. Benzoase™ Nuclease (Bugbuster™ GST Bind Purification Kit, Novagen) was added to the cell suspension, 1μL Benzoase™ Nuclease per 1mL BugBuster™, and thoroughly mixed by pipetting. The cell suspension mixture was incubated at 37°C for 30min. The lysates were cleared from cellular debris by centrifugation at 10 000g for 10min in a Beckman Coulter centrifuge (SX4750A swing rotor) precooled to 4°C. The lysates was kept at -20°C until needed.

2.3.3.3 Recombinant Protein Purification

The chromatography columns, glutathione agarose as well as buffers used in this section are all components of the Bugbuster™ GST Bind Purification Kit (Novagen) unless mentioned otherwise.

(a) Column Preparation

A glutathione agarose chromatography column was packed under gravity flow according to the manufacturer's recommendations. The column was equilibrated with 30 column volumes of 1x GST Bind/Wash buffer prepared from 10x GST Bind/Wash buffer. This column was used for the purification of GST tagged fusion proteins.

(b) Purification of Crude Cell Lysate

The cell lysate prepared as described in Sections 2.3.3.2 was loaded onto the column prepared in Section 2.3.3.3a and collected for reloading onto the column. This was repeated twice and the flow through was collected. The column was washed with 40 column volumes of 1x GST Bind/Wash buffer and then eluted with 15 volumes 1x GST Elute buffer. The column was washed with 40 column volumes of 5M NaCl and stored in 20% ethanol (aq) for future use. The flow through-, wash- and elute fractions were resolved on a 16% SDS-PAGE gel with 1x SDS electrophoresis buffer.

(c) Cleavage of Recombinant Proteins

The GST fusion proteins were cleaved by recombinant 3C Protease™ which was obtained from Mr F. Hassem. The elute fractions (Section 2.3.3.3b) were pooled then suspended in an equal volume of 3C Protease buffer with the addition of 10U 3C Protease per mg total GST fusion protein in a 50mL polypropylene tube and left at 4°C with gentle agitation overnight.

(d) Buffer Exchange, Fractionation and Concentrating of Protein Samples

The protein mixture obtained in Section 2.3.3.3c was concentrated and buffer exchanged using a 2000 MWCO concentrator tube (Millipore) into 1x PBS (pH 7.4) by centrifugation at 6000g for in a Beckman Coulter centrifuge (SX4750A swing rotor) precooled to 4°C. The 3C Protease™ (46kDa) and GST (26kDa) was fractionated from the recombinant peptide (< 10 000kDa) with a 10 000 MWCO concentrator tubes (Millipore) by centrifugation as above and 1x PBS (pH 7.4) as the buffer. The fractionated samples were individually concentrated with 2000 MWCO concentrator tubes. The samples were kept at -20°C until needed.

(e)   Determination of Protein Concentration

Protein samples were quantified with the BCA assay kit (Pierce) in Greiner 96-well microplates. A bovine serum albumin (BSA) standard series was used with a concentration range from 0.02-2.0mg/mL. The assay was conducted as recommended by the manufacturer's recommendations and the optical density was read at 562nm on a BMG Labtech Omega® POLARStar multimodal plate reader. Data acquisition was done with Omega® Control software and analysis was done with Microsoft® Excel™ 2010.

2.3.3.4   SDS-PAGE Analysis of Recombinant Proteins

Samples were prepared for polyacrylamide gel electrophoresis by mixing the 20-100μL of the appropriate sample with 4x SDS gel sample buffer in a ratio of 1:2. The samples were vortexed for 30sec then heated at 95°C for 5min and centrifuged at 16 000g for 5min in Eppendorf 5415D bench top centrifuge (Rotor: F45-24-11). The samples were kept on ice until loaded onto the SDS-PAGE gels. 14-16% SDS-PAGE gels were prepared from an established lab protocol and the typical composition of the preparation mixtures can be seen in Table 2.4.

The separating gel was poured between glass plates to a final volume of 4mL and covered with isopropanol until the gel had solidified. The isopropanol was decanted and the stacking gel mixture was poured on top of the solidified separating gel and the well combs were inserted. Samples were loaded at equal concentrations (determined in Section 2.3.3.3e) up to a final volume of 20μL a well. The sample loaded SDS-PAGE gels were electrophoresed in 1x SDS electrophoresis buffer at 120-140V for 70-90min. Gels were incubated post-electrophoresis in Coomassie gel staining solution overnight with gently agitation. Destaining solution was used to remove excess Coomassie gel stain from the gel. Destained SDS-PAGE gels were photographed using the UVP BioSpectrum® Imaging System (Cambridge).

Table 2.4: Composition of 14-16% SDS-PAGE gels

	Stacking gel (8%)	Separating gel (14-16%)
	Volumes (mL)	Volumes (mL)
dH$_2$O	1.449	1.895 – 1.645
40% acrylamide:bis-acrylamide	0.375	1.750 – 2.000
Tris (0.5M, pH 6.8)	0.625	0
Tris (1.5M, pH 8.8)	0	1.250
10% Ammonium persulphate	0.025	0.050
10% SDS	0.025	0.050
TEMED	0.001	0.005
Total	2.500	5.000

2.3.3.5 Recombinant Peptide Sequence Analysis

The recombinant proteins were resolved on a 16% SDS-PAGE gel (2.3.3.4) and gel slices containing the appropriate band were excised. Protein sequence analysis was done at the Mass Spectrometry Unit (Proteomics Laboratory, Central Analytical Facility (CAF)) at Tygerberg Campus Stellenbosch University (Stellenbosch, Cape Town, South Africa). The gel slices were trypsin digested in-gel and then analysed liquid chromatography mass spectrometry. The protocols were supplied by the analyst, Dr S. Smit.

(a)   In-gel trypsin digestion

All gel pieces were cut into smaller cubes and washed twice with water followed by 50% (v/v) acetonitrile for 10min. The acetonitrile was replaced with 50mM ammonium bicarbonate and incubated for 10min, and repeated two more times. All the gel pieces were then incubated in 100% acetonitrile until they turned white, after which the gel pieces were dried *in vacuo*. Proteins were reduced with 10mM DTT for 1h at 57°C. This was followed by brief washing steps of ammonium bicarbonate followed by 50% acetonitrile before proteins were alkylated with 55mM iodoacetamide for 1h in the dark. Following alkylation the gel pieces were washed with ammonium bicarbonate for 10 min followed by 50% acetonitrile for 20 min, before being dried *in vacuo.* The gel pieces were digested with 20μL of a 10ng/μL trypsin solution at 37⁰C overnight. The resulting peptides were extracted twice with 70% acetonitrile in 0.1% formic acid for 30min, and then dried and stored at -20⁰C. Dried peptides were dissolved in 5% acetonitrile in 0.1% formic acid and 10μL injections were made for nano-LC chromatography.

(b)   Liquid Chromatography Mass Spectrometry (LC-MS)

All experiments were performed on a Thermo Scientific EASY-nLC II connected to a LTQ Orbitrap Velos mass spectrometer (Thermo Scientific, Bremen, Germany) equipped with a nano-electron spray source. For liquid chromatography, separation was performed on an EASY-Column (2cm, ID 100μm, 5μm, C18) pre-column followed by an EASY-column (10cm, ID 75μm, 3μm, C18) column with a flow rate of 300nL/min. The gradient used was from 5-40 % B in 20 min, 40-80% B in 5 min and kept at 80% B for 10 min. Solvent A was 100% water in 0.1 % formic acid, and solvent B was 100 % acetonitrile in 0.1% formic acid.

The mass spectrometer was operated in data-dependent mode to automatically switch between Orbitrap-MS and LTQ-MS/MS acquisition. Data were acquired using the Xcaliber software package. The precursor ion scan MS spectra (*m/z* 400–2000) were acquired in the Orbitrap with resolution R = 60000 with the number of accumulated ions being 1 x 106. The 20 most intense ions were isolated and fragmented in linear ion trap (number of accumulated ions $1.5x10^4$) using collision induced dissociation. The lock mass option (polydimethylcyclosiloxane; *m/z* 445.120025) enabled accurate mass measurement in both the MS and MS/MS modes. In data-dependent LC-MS/MS experiments, dynamic exclusion was used with 60 s exclusion duration. Mass spectrometry conditions were 1.5 kV, capillary temperature of 200 °C, with no sheath and auxiliary gas flow. The ion selection threshold was 500 counts for MS/MS and an activation Q-value of 0.25 and activation time of 10ms were also applied for MS/MS.

(c)   Data Analysis

Thermo Proteome Discoverer 1.3 (Thermo Scientific, Bremen, Germany) were used to identify proteins via automated database searching (Mascot, Matrix Science, London, UK) of all tandem mass spectra against the sequence provided by you. Carbamidomethyl cysteine was set as fixed modification, and oxidized methionine, N-acetylation and deamidation (NQ) was used as variable modifications. The precursor mass tolerance was set to 10 ppm, and fragment mass tolerance set to 0.8Da. Two missed tryptic cleavages were allowed. Proteins were considered positively identified when they were identified with at least 2 tryptic peptides per proteins, a Mascot or Sequest score of more that $p < 0.05$ as determined by Proteome Discoverer 1.3. Percolator was also used for validation of search results. In Percolator a decoy database was searched with a FDR (strict) of 0.02 and FDR (relaxed) of 0.05 with validation based on the q-value.

2.3.3.6 UV-Vis Spectroscopy Surface Plasmon Resonance Interactions of Affinity Tagged Recombinant Proteins with Nitrilotriacetic acid Functionalized Gold Nanoparticles

Nitrilotriacetic acid (NTA) functionalized gold nanoparticles (AuNP-NTA) was diluted to and optical density ~0.4 and transferred in 100µL aliquots to the wells of a 96-well clear flat bottom microplate (Greiner). A 1mM nickel sulphate ($NiSO_4$) solution was made in nickel binding buffer and used for titrating Ni^{2+} into the appropriate wells, at a final concentration of 0-500µM Ni^{2+} for a final volume of 200µL per well. The plate was carefully agitated to mix the constituents and incubated at room temperature for 10-15min followed by UV-Vis spectroscopy (Section 2.2.1.6a) to monitor the change in the surface plasmon resonance band (λ_{SPR}) with increased Ni^{2+} addition. An optimized nickel concentration of nickel ions was used for titrating proteins, with and without a recombinant 6xHis tag, at a concentration range of 0.1-50µg/mL. The plate was gently agitated and incubated at room temperature for 40-60min followed by UV-Vis spectroscopy (Section 2.2.1.6a) to monitor the change in the surface plasmon resonance band (λ_{SPR}). The acquired data was analysed with Microsoft® Excel™ 2010.

2.3.4 Lyophilization

Samples were snap-frozen in liquid nitrogen or gradually frozen at -20°C then lyophilized overnight on a Virtis Sentry (Virtis Company Inc.) freeze-drier. All lyophilized samples were kept at -20°C.

2.4 Mammalian Cell Culture

2.4.1 Cell Line and Tissue Culture Media

A2780cis ovarian carcinoma cells were used in this project. The cells were purchased from the European Collection of Cell Cultures (ECACC) through Sigma and received at passage 4 (p4). This is an adherent monolayer epithelial cell line cultured in RPMI1640 (with 1mM glutamine, Lonza) was supplemented with 10% foetal bovine serum (FBS, Gibco) and 10x penicillin-streptomycin (PS, Gibco). Working solutions of 10x PS and 2x trypsin (Gibco) was prepared in sterile phosphate buffered saline (PBS pH 7.0, Gibco). All other reagents used for tissue culture was prepared in sterile PBS. All media and reagents were allowed to equilibrate to 37°C before being used.

2.4.2 Propagation of Cell Lines

Cells were grown in the appropriate complete media (PS and FBS supplemented) in a 37°C incubator with 5% CO_2 atmosphere until the desired confluency was reached. Cells were gently rinsed with sterile PBS then trypsinized with 2x trypsin for 5min at 37°C. Trypsin was inactivated by the addition of 2 volumes of appropriate complete media. Cells were pelleted by centrifugation at 2000g with a Sorval TC (Du Pont) bench top centrifuge. The cells were resuspended in 5mL fresh appropriate complete media and cell density was determined with the Countess Automated Cell Counter (Life Technologies) as recommended by the manufacturer's instructions. The cell density for different culture vessels can be seen in Table 2.5. Seeding density of cells was done at 10%, 20% and 50% of the maximum seeding density for the appropriate culture vessel.

Table 2.5: Seeding densities for cell culture vessels (Data obtained from ATCC)

Type of Culture Vessel	Surface Area (mm^2)	Cell Density			
		Confluency	10% Confluency	20% Confluency	50% Confluency
6-well	962	1.2×10^6	0.12×10^6	0.24×10^6	0.6×10^6
12-well	401	0.4×10^6	0.04×10^6	0.08×10^6	0.2×10^6
24-well	200	0.2×10^6	0.02×10^6	0.04×10^6	0.1×10^6
96-well	63	0.06×10^6	0.006×10^6	0.012×10^6	0.03×10^6
T25	2500	2.8×10^6	0.28×10^6	0.56×10^6	1.4×10^6
T75	7500	8.4×10^6	0.84×10^6	1.68×10^6	4.2×10^6

2.4.3 Reversion of Cell Line from Drug Resistant to Drug Responsive

2.4.3.1 Differential Exposure of Cells to Cisplatin

A solution of 400μM cisplatin (Sigma) was prepared in sterile PBS. Dimethyl sulfoxide (DMSO) was not used to prepare cisplatin as it has been reported that adduct formation occurs between the former and latter compounds, which alters the pharmacologic activity of cisplatin [295]. Culture media was prepared by the addition of cisplatin to complete media to a final concentration of 2μM. Culture media with an equal volume of sterile PBS corresponding to the amount of used for cisplatin addition was prepared. A2780cis cells were seeded at p4 in T25 flasks as described in Section 2.4.2 and divided in two groups. The first group was cultured in 2μM cisplatin supplemented complete media and the second group was

cultured in complete media containing vehicle (PBS) only. The cells were propagated (Section 2.4.2) until p10.

2.4.3.2 Protein Extraction and Immunodetection of Biomarkers

Cells were grown until ~80% confluency for each passage (Section 2.4.3.1). The cells were rinsed with sterile PBS followed by covering the adherent cells in 500μL Cytobuster™ Protein Extraction Reagent (Novagen) with careful agitation at room temperature for 5min. A cell scraper (Greiner) was used to pool cell debris which was transferred to a 1.5mL Eppendorf tube. The lysate was separated from the cell debris by centrifugation at 16 000g for 5min in an Eppendorf 5415D bench top centrifuge (Rotor: F45-24-11). The protein content was quantified as described in Section 2.3.3.3e and proteins were resolved on a 14% SDS-PAGE gel (Section 2.3.3.4).

Proteins were transferred to PVDF membranes using immunoblotting transfer buffer with a BioRAD® Electro blotter at 110V for 90min on ice. Following the transfer, the membranes were blocked with 3% BSA in TBS-T20 for 2h. The membranes were washed three times with 5mL TBS-T20 for 5min followed by incubation with the appropriate primary antibodies (Table 2.6), diluted in 3% BSA in TBS-T20, overnight at 4°C. The membranes were washed three times with 5mL TBS-T20 for 5min and incubated with the appropriate secondary antibody (Table 2.6), diluted in 3% BSA in TBS-T20, for 1h at room temperature. A final wash step wash step was done as described above followed by immunodetection with SuperSignal®West Pico chemiluminescent substrate solution (Pierce). The chemiluminescent signal was detected and captured with the UVP BioSpectrum® Imaging System (Cambridge). Densiometric analysis was done with ImageJ V1.46r.

Table 2.6: Antibodies and Dilutions used for Immunodetection

	Primary Antibody		Secondary Antibody (HRP conjugated)	
Biomarker	Origin	Dilution	Origin	Dilution
MLH1	Mouse anti-human, monoclonal	1:500	Goat anti-mouse, polyclonal	1:5000
HSP60	Mouse anti-human, monoclonal	1:500	Goat anti-mouse, polyclonal	1:5000
β-actin	Mouse antihuman, monoclonal (HRP conjugated)	1:500	-	-

2.4.3.3 Flow Cytometry for the Detection of Biomarkers

Cells were grown to ~80% confluency (Section 2.4.3.1) and treated with trypsin for 5min at 37°C. The cells were pelleted at 2000g with a Sorval TC (Du Pont) bench top centrifuge and resuspended in 5mL complete media. The cell density was determined (Section 2.4.2) and the cell suspension was divided into two 2.5mL aliquots in flow cytometer sample tubes. A fluoroisothiocyanite (FITC) conjugated CD27L monoclonal antibody (Santa Crux Biotechnology) was added to one sample tube at 1μg per 1×10^6 cells, as per manufacturer's recommendations. The other tube served as a negative control. The samples were mixed by gentle inversion of the sample tubes and left to incubate in the dark for 30min at 37°C. The cell suspension was analysed utilizing the green channel fluorescence channel and front scatter with subsequent data capture on a BD Biosciences FACScan® flow cytometer.

2.4.4 Transfection of A2780 Cell Line with pEGFP-N3-MMP2

Cells were allowed to reach ~80% confluency in a T25 flask, trypsinized (Section2.4.2) then grown to 50-60% confluency (Table 2.5, Section 2.4.2) into 6-well clear plates (Greiner) and left to adhere overnight in a 37°C incubator with a 5% CO_2 atmosphere. Transfections were done with Metafectene®Pro (Biontex) as per manufacturer's recommendations. Two solutions were prepared, solution A and solution B. Solution A contained 1-2μg plasmid DNA in serum free media made to a final volume of 50μL. A control was setup with sterile PBS instead of plasmid DNA as described above. Solution B contained 2-8μL Metafectene®Pro in serum free media to a final volume of 50μL. Solution A was mixed with solution B and left to incubate at room temperature for 20-30min to allow the DNA to complex with the transfection reagent. The cells were washed twice with sterile PBS and 1mL fresh serum free media was added to each well. The mixed solution (A+B) was added drop wise to the plate with constant gentle agitation and thereafter incubated at 37°C with 5% CO_2 atmosphere for 3h. The plate was removed from the incubator and 1mL complete media was added to each well and the cells were further incubated for 48h at 37°C with 5% CO_2. Selection of transfected cells was initiated by preparing appropriate complete media that contained 100-800μg/mL G418 antibiotic. The old media was removed from the cells and freshly prepared 2mL complete media with the appropriate concentration of G418 was added to each well. Antibiotic selection was done for 8-12 days after which selection was stopped and the cells were then grown in complete media without antibiotic. The cells were allowed to reach 80-90% confluency before being propagated.

2.4.5 *In vitro* Assessment of Gold Nanoparticle Toxicity

2.4.5.1   WST-1 Cytotoxicity Assay

Cells were allowed to reach ~80% confluency in a T25 flask, trypsinized (Section 2.4.2) and seeded into 96-well clear microplates (Greiner) at ~70-80% confluency (Table 2.5, Section 2.4.2) per well and left to adhere overnight in a 37°C incubator with 5% CO_2 atmosphere. The spent media was removed and 100μL fresh complete tissue media was added per well. The different gold nanoparticle preparations were added at a concentration range of 32-1000pM (0.013 ≤ optical density (OD) ≤ 0.4) in sterile PBS to a final total volume of 200μL per well. The untreated control was PBS only. The microplate was gently agitated to ensure mixing of the well contents and incubated for 24h at 37°C in a 5% CO_2 atmosphere. After 24h the media in the wells was gently removed and the cells were gently washed twice with sterile PBS. Fresh complete media was added to each well to a final volume of 100μL and 10μL WST-1 reagent (Roche) was added per well, as per manufacturer's recommendations, and the plate was gently agitated and incubated at 37°C for 30-240min to allow for colour development. The optical density was read at 450nm (OD_{450}) with a reference wavelength at 620nm using the Omega® POLARStar multimodal plate reader (Section 2.2.1.6a). Acquired data was background as well as reference wavelength corrected. Data analysis was done with Microsoft® Excel™ 2010.
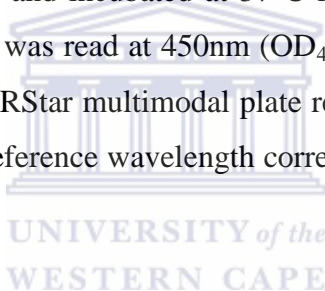
2.4.5.2   ApoPercentage™ Assay

The ApoPercentage™ assay was adapted to accommodate shorter assay duration as it was found that the result did not differ. Cells were allowed to reach ~80% confluency in a T25 flask, trypsinized (Section 2.4.2) and propagated into 24-well clear microplates (Greiner) at 70-80% confluency (Table 2.5, Section 2.4.2) per well and left to adhere overnight in a 37°C incubator with 5% CO_2 atmosphere. The spent media was removed and 300μL complete media was added per well. The different gold nanoparticle preparations were added at LD_{50} values (Sections 2.4.5.1, 5.2.2.2 and 5.2.3.2) in sterile PBS to a final total volume of 600μL per well. The untreated control was PBS only. After 24h the media in the wells was gently removed and the cells were gently washed twice with 600μL sterile PBS. Fresh complete media was added to each well to a final volume of 570μL and 30μL (5% v/v) ApoPercentage™ (Biocolor) dye was added to each well and the plate was incubated at 37°C for 30min as per manufacturer's recommendations. The cells were washed twice with 600μL sterile PBS to remove unbound dye with a final volume of 300μL PBS per well. Micrographs were obtained with a Leica EC3 Firecam (Leica Microsystems) camera attached to a Nikon

(TMS) inverted light microscope. After micrographs were obtained, the PBS was removed and 300μL Dye Release Agent was added to each well and the plate was incubated at 37°C with gentle agitation for 10min. The optical density was read at 550nm (OD_{550}) on the Omega® POLARStar multimodal plate reader (2.2.1.6a). Acquired data was analysed with Microsoft® Excel™ 2010.

2.4.5.3 Immunodetection of Procaspase-3

The dose-response as well as time-dose response was determined for procaspase-3. Cells were grown until ~80% confluency in T25 (Table 2.5, Section 2.4.2) flasks for each treatment. The spent media was decanted and 2.5mL fresh complete media was added. Gold nanoparticles were added at the LD_{50} values (Sections 2.4.5.1, 5.2.2.2 and 5.2.3.2) suspended in sterile PBS to a total final volume of 5mL and incubated at 37°C with 5% CO_2 atmosphere for 24h. The spent media was kept for the respective flasks. The cells were subsequently washed twice with 2mL sterile PBS where the PBS was added to the corresponding flask's spent media. The spent media-PBS mixture was centrifuged at 2000g for 5min and the supernatant was decanted. The cell pellets were resuspended in 500μL Cytobuster™ Protein Extraction Reagent (Novagen) and added to the corresponding T25 flasks. The flasks were incubated at room temperature for 5min with gentle agitation. A cell scraper (Greiner) was used to pool cell debris which was transferred to a 1.5mL Eppendorf tube. The lysate was separated from the cell debris by centrifugation at 16 000g for 5min in an Eppendorf 5415D bench top centrifuge (Rotor: F45-24-11). The protein content was quantified as described in Section 2.3.3.3e and proteins were resolved on a 14% SDS-PAGE gel (Section 2.3.3.4). Immunodetection of procaspase-3 (Santa Cruz) was done as described in Section 2.4.3.2.

2.4.5.4 GSH/GSSG-Glo™ (Promega) Total Glutathione Assay

Cells were allowed to reach ~80% confluency in a T25 flask, trypsinized (Section 2.4.2) and seeded into 96-well black microplates (Merck) at ~70-80% confluency (Table 2.5, Section 2.4.2) per well and left to adhere overnight in a 37°C incubator with a 5% CO_2 atmosphere. The spent media was removed and 100μL fresh complete tissue media was added per well. The different gold nanoparticle preparations were added at LD_{50} values (Section 2.4.5.1, 5.2.2.2 and 5.2.3.2) in sterile PBS to a final total volume of 200μL per well. The untreated control was PBS only. The microplate was gently agitated to ensure mixing of the well contents and incubated for 24h at 37°C in 5% CO_2 atmosphere. The assay kit was used as per manufacturer's recommendations to determine reduced glutathione (GSH) as well as oxidised

glutathione (GSSG). The luminescence signal which is generated is based on the well-known luciferrin-luciferase bioluminescence reaction. Addition of the kit reagents was followed by 15-20min incubation of the microplate at 37°C and the luminescence signal was quantified with the Omega® POLARStar multimodal plate reader (Section 2.2.1.6b). Acquired data was analysed with Microsoft® Excel™ 2010.

2.4.5.5 Transmission Electron Microscopy

Cells were grown to ~80% confluency in T25 (Table 2.5, Section 2.4.2) flasks for each treatment. The cells were washed twice with 2mL sterile PBS and fresh 2.5mL complete media was added to the flasks. The gold nanoparticles were added at the LD_{50} values (Sections 2.4.5.1, 5.2.2.2 and 5.2.3.2) suspended in sterile PBS to a total final volume of 5mL and incubated at 37°C with a 5% CO_2 atmosphere for 24h. The spent media was kept for the respective flasks. The cells were subsequently washed twice with 2mL sterile PBS where the PBS was added to the corresponding flask's spent media. The spent media-PBS mixture was centrifuged at 2000g for 5min and the supernatant was decanted with the pellet resuspended in 1mL 4% paraformaldehyde. The adherent cells in the flasks were covered with 3mL 4% paraformaldehyde solution and the resuspended pellet was added with the combined mixture incubated at 4°C for 15min. The cells were gently dislodged with a cell scraper (Greiner) then transferred to a 15mL polypropylene tube with a wide tip pipette and centrifuged at 2000g for 5min. The supernatant was discarded and the cell pellet was gently covered in 2.5% glutaraldehyde solution. The cell pellet was submitted to the NHLS Cytology Electron Microscopy Unit (Tygerberg Hospital, Cape Town, South Africa) with transmission electron microscopy done by Mrs N. Muller.

2.5 Protein-Protein Interactions: Matrix Metalloproteinase-2 (MMP2) and Recombinant Chlorotoxin (CTX)

2.5.1 Enzyme Kinetic Analysis

2.5.1.1 Acquisition of Chromogenic Peptide, Competitive Inhibitor of MMP2, Recombinant Full Length pro-MMP2 and MMP2 Activation by APMA

The chromogenic peptide [81] was purchased from Enzo Life Sciences and was received as a lyophilized powder which was made up to 5mg/mL in MMP2 assay buffer. The competitive inhibitor of MMP2, BiPS, and recombinant pro-matrix metalloproteinase-2 was purchased

from Merck. Pro-MMP2 activation to mature MMP-2 was done by incubating 1mM APMA buffer with 1μg/mL pro-MMP2 in 1mL MMP2 assay buffer for 2-4h at 37°C. The mature MMP2 was purified with 10 000 MWCO concentrator tubes (Eppendorf) by centrifugation at 16 000g for 10min in an Eppendorf 5415D bench top centrifuge (Rotor: F45-24-11) and resuspended in MMP2 assay buffer. The APMA activation of pro-MMP2 yields 70% active MMP2 [81-82].

2.5.1.2 Spectrophotometric Enzyme Kinetics Analysis

The MMP2 enzymatic activity was determined, with and without inhibitors present, to determine if the reported inhibition by chlorotoxin (CTX) was in the catalytic site of the protease enzyme. Typically MMP2 would be incubated with the chromogenic peptide and inhibitor, if applicable, in a 1mL cuvette for a predetermined amount of time. MMP2 cleavage of the chromogenic peptide releases a free reduced thiol group, after which the sample would be heat inactivated and fractionated followed by Ellman's (Section 2.2.1.1) assay for reduced thiol content in each fraction [81-82]. Here an adapted one-step assay is described to determine realtime MMP2 activity directly coupled to an increase in optical density at 412nm (OD_{412}) in a high-throughput 96-well plate format. The typical assay mixture can be seen in Table 2.7. Each chromogenic peptide concentration (Table 2.7), with or without inhibitor present, will generate a Michaelis-Menton graph.

Table 2.7: The typical composition of the MMP2 enzyme kinetic assay

	Volume (μL)	Final [ ]
Activated MMP2	10	40ng/mL
Ellman's reagent (DTNB)	4	1mM
Chromogenic peptide	6.25	0.225mM / 0.45mM / 0.9mM
Inhibitor*	0 - 70	-
MMP2 assay buffer	229.75 – 159.75	-
Total	**250**	

*The inhibitor volumes were concentration dependent, where BiPS (commercial competitive inhibitor) was used at 17nM (reported IC_{50} [296]) and 34nM and recombinant produced chlorotoxin (CTX) was used at 100nM (reported IC_{50}m [119]) and 200nM.**

The slope ($m = \frac{\Delta y}{\Delta x}$) of the linear region of the graph will be used to determine the initial velocity (V_o) of the enzyme for that specific concentration of chromogenic substrate. The unit of time (sec, min, h) is dependent on enzyme activity as well as the affinity of the enzyme for the substrate. The reciprocal of the obtained velocity will be plotted on the Y-axis with the

corresponding reciprocal of the chromogenic peptide concentration plotted on the X-axis of a Lineweaver-Burke graph. The intercept of the graph with the X-axis will correspond to $-{}^1/_{Km}$ where K_m is an indication of the substrate binding the enzyme has for the substrate. The intercept of the graph with the Y-axis will correspond to ${}^1/_{Vmax}$ where V_{max} is the maximum velocity of the enzyme for the substrate. Both K_m and V_{max} for a particular enzyme are dependent on the substrate, presence of inhibitors as well as the assay conditions. Differences in K_m and V_{max} describe the type of interaction an enzyme has with a substrate in the presence of an inhibitor. The assay was conducted on the Omega® POLARStar (BMG Labtech) multimodal plate reader using the discrete wavelength 412nm. The Omega® control software was set to absorbance for plate kinetics with 200 scans per well and a kinetic interval length of 2.5min for a total assay duration of 5h. Data analysis was done with Microsoft® Excel™ 2010.

2.5.2 Wide Field Fluorescence Microscopy Investigation of Protein-Protein Co-localization

2.5.2.1 Propagation of pEGFP-N3-MMP2 Transfected Cells on Coverslips

Transfected A2780 cells (Section 2.4.3) were allowed to reach ~80% confluency in a T25 flask, trypsinized (Section 2.4.2) and propagated at 30-40% confluency (Table 2.5, Section 2.4.2) into 6-well clear plates (Greiner) on top of an autoclaved coverslip (6mm X 6mm, Lasec) in each well. The cells were left to adhere overnight in a 37°C incubator with 5% CO_2 atmosphere. The spent media was pipetted off and 2mL fresh media was added per well. The cells were allowed to reach 50-60% confluency for further experiments.

2.5.2.2 Treatment of Cells with Inducers of MMP2

The subcellular localization of enhanced green fluorescent protein (EGFP) tagged MMP2 was investigated with different inducers of MMP2. The inducers were prepared in the appropriate complete media for each of the following compounds: 100ng/mL lipopolysaccharide (LPS), 100ng/mL phorbol-12-myristate-13-acetate (PMA) and 2μM cisplatin. Cells grown on coverslips (Section 2.5.2.1) were moved to a fresh 6-well plate and washed twice with 1mL sterile PBS followed by the addition of 2mL complete media containing the appropriate inducer and incubated for 24h at 37°C with a 5% CO_2 atmosphere.

2.5.2.3 Bioconjugation of Dansyl chloride / Rhodamine B to anti-MMP2

Dansyl chloride (Sigma) was dissolved in tetrahydrofuran at 1mg/mL in an aqueous solution containing 0.02mg/mL anti-MMP2 (Pierce) and incubated at 37°C for 40-60min with gentle agitation. The dansylated anti-MMP2 was washed and purified with 10 000 MWCO concentrator tube (Millipore) by centrifugation at 6000g in a Beckman Coulter centrifuge (SX4750A swing rotor) precooled to 4°C. The dansylated anti-MMP2 was kept at 4°C.

Rhodamine B (Sigma) was dissolved in dH$_2$O (18.2MΩ) at 1mg/mL together with 0.02mg/mL anti-MMP2 (Pierce) and 2mg/mL EDC. The mixture was mixed by inversion and left to incubate at 37°C for 40-60min. The Rhodamine B-anti-MMP2 was washed and purified by centrifugation and stored, as described in the previous paragraph.

2.5.2.4 Staining of Cells with Chlorotoxin Conjugated Quantum Dots and Fluorescent Labelled anti-MMP2

Cells grown on coverslips, prepared as described in Section 2.5.2.1, were moved to a fresh 6-well plate and washed twice with 1mL sterile PBS followed by addition of 1mL 4% paraformaldehyde per well. The cells were incubated at 4°C for 15-20min with gentle agitation and subsequently washed twice with 1mL sterile PBS followed by addition of 1mL permeation buffer per well and incubated at room temperature for 20-30min. The quantum dots (10-500pM) and fluorescent labelled antibody (1:500-1:2000) was prepared at the appropriate concentration, in TBS-T20 containing 3% bovine serum albumin (BSA). The permeations buffer was removed from the wells and the cells were washed twice with 1mL sterile PBS. The appropriate fluorescent stain was added per well followed with incubation protected from light at room temperature for 2-3h or overnight at 4°C. The cells were washed gently twice with 1mL sterile PBS.

2.5.2.5 Wide Field Fluorescence Microscopy

Cells propagated on coverslips, prepared as described in Sections 2.5.2.2 or 2.5.2.4, were washed twice with 1mL sterile PBS and carefully dried to remove excess moisture. Microscopy slides (Lasec) was cleaned with 80% ethanol and dried followed by the application of 25μL FluoroShield® (Sigma) in the centre of the microscope slide. The coverslip was carefully placed face down over the solution and left to dry protected from light for 2-3h at 4°C. The wide field fluorescence microscopy analysis was done at the Fluorescence Microscopy Unit of the Central Analytical Facility (CAF) at the University of

Stellenbosch (Stellenbosch, Cape Town, South Africa) with assistance from Mrs L. Engelbrecht. The microscope system used was the Olympus Cell^R system (Olympus Biosystems, GmbH) equipped with a Olympus IX81 inverted fluorescent microscope; F-view-II cooled CCD camera (Soft Imaging systems) and a Xenon-Arc burner (Olympus Biosystems, GmbH) as light source. The excitation filters used was 360 nm (for blue staining), 492 nm (for green staining) and 572 nm (for red staining) with emission collected with a UBG triple-band pass emission filter cube (Chroma). Image acquisition was done with Cell^R® Imaging software which was set for automated background removal pre- and post-image acquisition. Image analysis was done with ImageJ V1.46r.

2.6   Statistical Analysis

Statistical analysis was done with Microsoft® Excel™ 2010 utilizing the StatistiXL® (2009) and Excel™ 2010 Data Analysis Tools plugins. The student's two-tailed T-test as well as single factor ANOVA was used, depending on the type of statistical variance in data, and was explicitly indicated where applied.
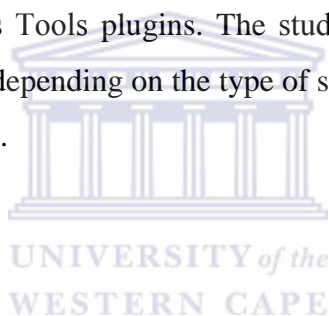
UNIVERSITY *of the*

WESTERN CAPE

Chapter 3: The Interaction between Chlorotoxin and Matrix Metallproteinase-2 – Tumour Specific Targeting

3.1 The Cloning, Expression and Purification of Chlorotoxin (CTX)

3.1.1 Introduction

Chlorotoxin (CTX) can be commercially purchased or be produced through recombinant molecular biology techniques. Recombinant production of CTX enabled the modification of the 36 amino acid residue peptide to suit different experimental requirements. A C-terminal hexa-histadine (6xHis) tag with a proline (pro, P) residue inserted between the tag and the peptide, which confers directionality of attachment to the peptide. The pro-6xHis tag enables the use of nickel affinity chromatography. In the following few paragraphs the cloning, expression and purification of CTX will be shown. CTX will be used to probe the interaction between itself and matrix metalloproteinase-2 (MMP2) in Sections 3.2 and 3.3.

3.1.2 Cloning of Chlorotoxin

A synthetic variant of chlorotoxin gene was designed based on the published amino acid sequence [118] and commercially synthesized by GenScript (GenScript Inc., New Jersey, USA) to be subcloned into a pGEX-6P-2 expression construct. The vector diagram of pGEX-6P-2 can be seen in Figure 2.1 (Section 2.3.2.5). The construct was named pGEX-6P-2-CTX and served as a PCR template (Section 3.1.2.1) as well as to produce a protein control, which had no 6xHis-tag, for nitrilotriacetic acid (NTA) functionalized gold nanoparticles (Section 3.1.4).

3.1.2.1 Primer Design and PCR Amplification

Primers (Table 3.1) were designed to amplify the full length synthetic sequence of CTX which included a hexa-histadine (6xHis) tag. Two sets of primers were designed and can be seen in Table 3.1. The first primer set included a C-terminal hexa-histadine (6xHis) tag sequence on the reverse primer (CTX-S1-R) flanked by an XhoI restriction recognition site. The second primer set also included a C-terminal 6xHis tag sequence on the reverse primer with a proline (pro, P) residue between the peptide and the tag (CTX-S2-R). Both primer sets used the same forward primer. The restriction enzyme sites, start codons, stop codons as well as tag sequences are indicated in Table 3.1.

Table 3.1: Primer sets used for Chlorotoxin PCR amplification

CTX-S₁F (5')	5'-GTTTGGATCCATGTGCATGCCG-3'
CTX-S₁R (3')	5'-GTAACTCGAGCTATTA*ATGATGATGATGATGATG*ACGACACAGGCACTGCGG-3'
CTX-S₂F (5')	5'-GTTTGGATCCATGTGCATGCCG-3'
CTX-S₂R (3')	5'-GTAACTCGAGCTATTA*ATGGTGATGGTGATGGTGTGG*ACGACACAGGCACTGCGG-3'

Restriction enzyme sites are underlined. The start codon is in green and the stop codon in red. The C-terminal 6xHis-tag and C-terminal Proline-6xHis tag is underlined and in italics. S$_i$ denotes primer set number (i = 1,2) with F – forward primer and R – reverse primer. The *BamHI* (GGATCC)- and *XhoI* (CTCTGAG) restriction enzyme sites are underlined.

3.1.2.2 PCR Amplification of Chlorotoxin

PCR amplification (Section 2.3.2.3a) yielded PCR products for both primer sets (Table 3.1). The expected size for *CTX-S₁* is 138bp and the expected size for *CTX-S₂* is 141bp. Both PCR products (Figure 3.1) appeared in a region on the gel between 100bp and 200bp relative to the DNA marker. The agarose gel electrophoresis was conducted as described in Section 2.3.2.8.
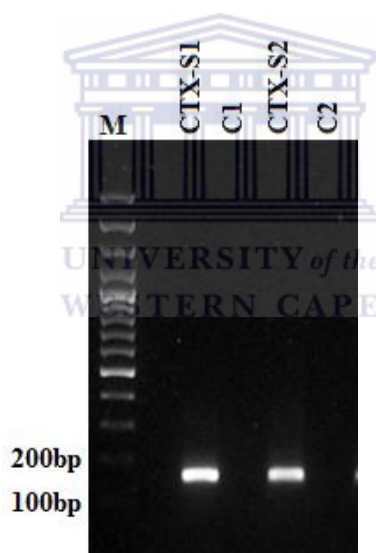
Figure 3.1: The PCR products for Amplification of synthetic Chlorotoxin (CTX). *CTX-S1* – Amplicon for primer set 1; *CTX-S2* – Amplicon primer for primer set 2; M is molecular marker; C1 and C2 are negative controls. The marker used is Fermentas O'Generuler 100bp Ladder. GelRed was used to stain DNA on a 1% agarose gel.

DNA was isolated from excised agarose gel slices which contained the PCR products (Section 2.3.2.4). The purified DNA was double digested with Fermentas FastDigest restriction enzymes *BamHI* (5') and *XhoI* (3') as described in Section 2.3.2.5. An empty pGEX-6P-2 vector was similarly double digested (Section 2.3.2.5) with *BamHI* (5') and *XhoI* (3'). The digested DNA was ligated (Section 2.3.2.6) into the corresponding restriction sites of pGEX-6P-2. In such a manner glutathione-S-transferase (GST) will be fused to the N-terminal of CTX, where the expected protein product would also include a C-terminal Pro-6xHis-tag. The

plasmid construct generated from the amplicon for primer set *CTX-S1* was named pGEX-6P-2-CTX-S1 and the corresponding plasmid construct for the amplicon *CTX-S2* was named pGEX-6P-2-CTX-S2. Colony PCR (Section 2.3.2.7) with gene specific primers was used to screen $DH_{5\alpha}$ (Section 2.3.1.1) transformants (Section 2.3.1.4) for the presence of the CTX gene (Figure 3.2). Nine bacterial colonies were randomly chosen per construct. The construct pGEX-6P-2-CTX-S1 was positive for CTX DNA in all 9 colonies (lanes 1-9, Figure 3.2) with the PCR product between 100bp and 200bp. Strong positive colonies as well as weak positive colonies were observed for the construct pGEX-6P-2-CTX-S2 (lanes 10-18, Figure 3.2). Non-specific bands (lanes 10-14 and lanes 17-18, Figure 3.2) were observed (< 100bp) which may be primer dimers or amplification products of a non-specific DNA sequence. All positive clones were sent for sequencing and will be discussed in Section 3.1.2.3.
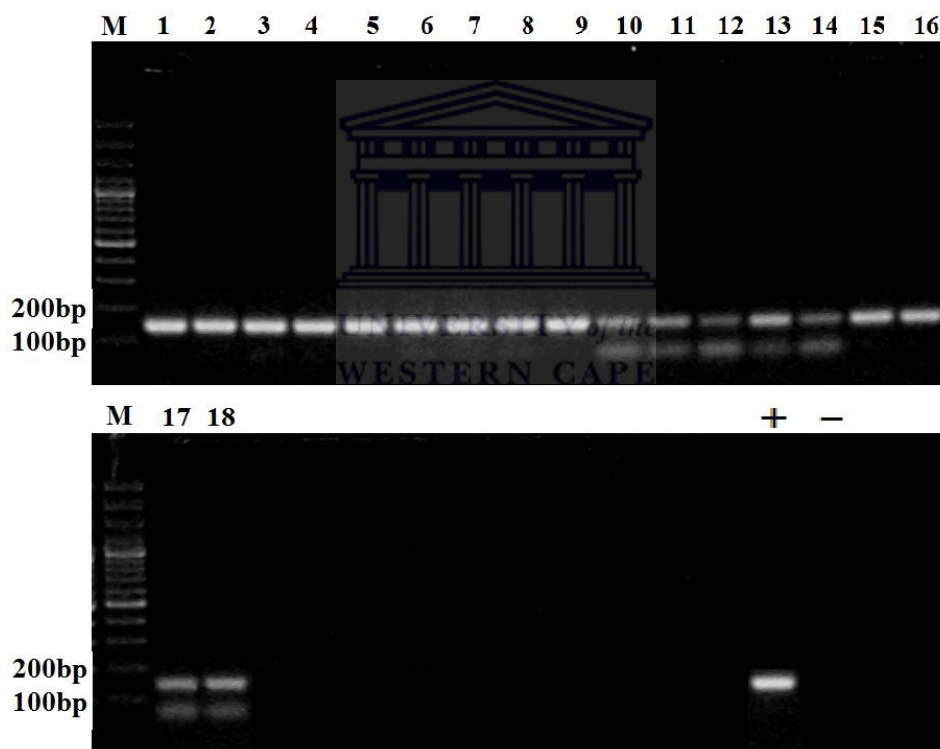
Figure 3.2: The colony PCR of pGEX-6P-2-CTX-S1 (Lanes 1-9) and pGEX-6P-2-CTX-S2 (Lanes 10-18). The positive control (+) was chlorotoxin template DNA and negative control (-) was H₂O. The marker used is Fermentas O'Generuler 100bp Ladder. GelRed was used to stain DNA resolved on a 1% agarose gel.

3.1.2.3 DNA Sequence Analysis of Putative Positive Clones for Chlorotoxin (CTX)

The sequence alignment of pGEX-6P-2-CTX-S1 and pGEX-6P-2-CTX-S2 relative to the synthetic designed CTX sequence (Section 3.1.2.1) can be seen in Table 3.2. All clones sent for sequencing (Section 2.3.2.10) for pGEX-6P-2-CTX-S1 and pGEX-6P-2-CTX-S2 yielded

identical results, respectively. A representative clone for each above mentioned construct was chosen at random. The 6xHis tags included on the C-terminal with primer design (Section 3.1.2.1) were present. The sequence for CTX-S1 included an additional start codon (ATG) and lacked the double stop codon which was incorporated in the primer design and this was observed for all clones sequenced. This was most probably due to a PCR experimental error. Restriction enzyme recognition sites (Table 3.2, italics and underlined) and tags (Table 3.2, underlined) correspond to the primers designed (Table 3.2). Both stop codons (red) were present for pGEX-6P-2-CTX-S2.

Table 3.2: Sequence alignment of pGEX-6P-2-CTX-S1 and pGEX-6P-2-CTX-S2

```
             -8          1                                                51
CTX                      ATGTGCATGCCGTGTTTTACCACGGATCATCAGATGGCGCGTAAATGCGAT
                         ||||||||||||||||||||||||||||||||||||||||||||||||||
CTX-S1        GGATCCATGATGTGCATGCCGTGTTTTACCACGGATCATCAGATGGCGCGTAAATGCGAT
                          |||||||||||||||||||||||||||||||||||||||||||||||||
CTX-S2          GGATCCATGTGCATGCCGTGTTTTACCACGGATCATCAGATGGCGCGTAAATGCGAT


             52                                                       108
CTX           GATTGCTGTGGCGGTAAAGGCCGCGGTAAATGTTATGGCCCGCAGTGCCTGTGTCGT
              |||||||||||||||||||||||||||||||||||||||||||||||||||||||||
CTX-S1        GATTGCTGTGGCGGTAAAGGCCGCGGTAAATGTTATGGCCCGCAGTGCCTGTGTCGTCAT
              ||||||||||||||||||||||||||||||||||||||||||||||||||||||||||
CTX-S2        GATTGCTGTGGCGGTAAAGGCCGCGGTAAATGTTATGGCCCGCAGTGCCTGTGTCGTCCA



CTX

CTX-S1        CATCATCATCATCATTAGCTCGAG

CTX-S2        CCACACCATCACCATCACCATTAATAGCTCGAG
```

*Restriction enzyme sites indicated by italics and underlining. Tags are indicated by underlining. Stop codons are in red. Start codons are in green. The synthetic construct used as an alignment reference is denoted CTX. The sequences obtained for the pGEX-6P-2 expression vectors are *CTX-S1* (primer set 1, Table 3.1) and *CTX-S2* (primer set 2, Table 3.1) respectively.

3.1.3 Recombinant Expression of Chlorotoxin

3.1.3.1 Protein Expression and Purification

The fusion proteins produced from the expression vectors (Section 3.1.2) were named GST-CTX-S1 and GST-CTX-S2 for pGEX-6P-2-CTX-S1 and pGEX-6P-2-CTX-S2, respectively. The protein production conditions were optimized (Section 2.3.3.1) with the ArcticExpress™ (DE3) *E.coli* strain (Section 2.3.1.1). The expected fusion protein molecular weight is the combined weight of GST (26kDa) and CTX (4.3kDa), namely 30.3kDa. All bacterial lysates

were obtained prepared as described in Section 2.3.3.2. The isopropyl-β-D-thiogalactopyranoside (IPTG) protein expression screens for 10mL cultures can be seen in Figure 3.3. The soluble fractions of the bacterial lysates were resolved on a 16% SDS-PAGE gel (Section 2.3.3.4). A protein band between 26kDa and 30kDa showed an increase in relative intensity corresponding to increasing amounts of IPTG (red block, Figure 3.3). The intensity of the protein bands for the IPTG treated cultures (0.25-2mM, red block, Figure 3.3) was observably different than the protein band for the uninduced culture (0mM, red block, Figure 3.3). Low molecular weight bands were observed in all lanes which may be indicative of autocleavage of CTX (4.3kDa) but was considered to be unlikely as no free GST (26kDa) was observed.
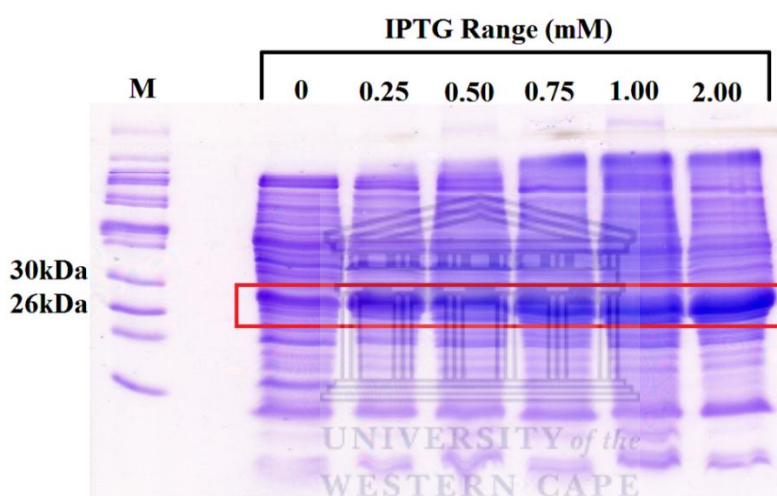
Figure 3.3: IPTG expression screen for bacterial lysates containing GST-CTX-S2. Lysates were resolved on a 16% SDS-PAGE gel with Thermo PageRuler Unstained Protein Ladder as a molecular marker. The gel was stained with Coomassie Brilliant Blue.

The bacterial lysates for 500mL cultures for GST-CTX-S1 (Figure 3.4a) and GST-CTX-S2 (Figure 3.4b) were resolved on 16% SDS-PAGE gels after GST purification (Section 2.3.3.3a-b). GST-CTX-S2 was more readily purified than GST-CTX-S1 under similar purification conditions. A prominent protein band (between 26kDa and 30kDa) was observed in the flow through (F)-, the first wash (W1)-, and eluted (E1-3) fractions. The above mentioned protein band corresponded to the protein band (between 26kDa and 30kDa) observed for the IPTG induction screens (Figure 3.2). The elute fractions indicate intact fusion protein. The eluted fractions (E1-3) were pooled for each fusion protein, respectively.
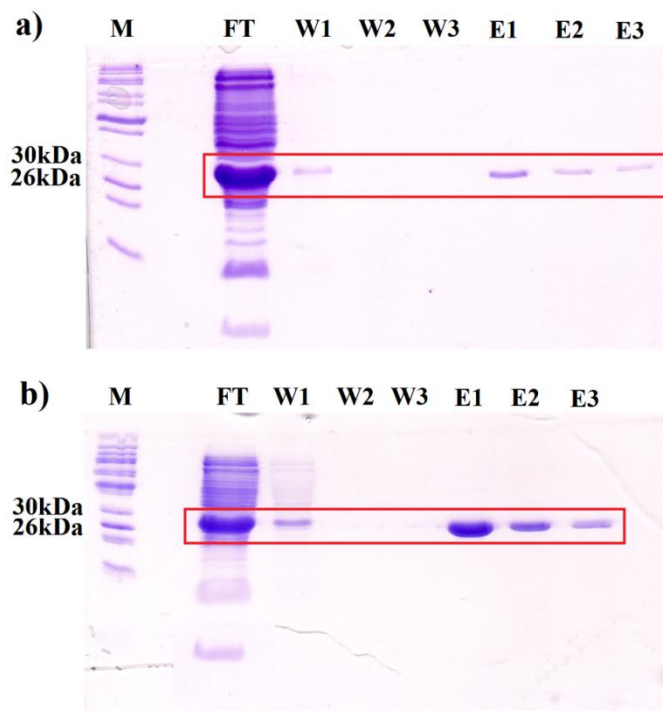
Figure 3.4: Purification of the GST-fusion proteins GST-CTX-S1 (a) and GST-CTX-S2 (b). M – Protein marker (Thermo PageRuler Unstained Protein Ladder); F – Flow through fraction; W1-3 – Wash step fractions; E1-3 – Eluted fractions. The protein fractions were resolved on a 16% SDS-PAGE gel with Thermo PageRuler Unstained Protein Ladder as a molecular marker. The gel was stained with Coomassie Brilliant Blue.

The pooled GST-fusion protein eluted fractions were treated with 3C-Protease™ (Section 2.3.3.3c) to release the peptide from the GST-fusion protein and resolved on a 16% SDS-PAGE gel. As an example, the cleavage of CTX-S2 from GST-CTX-S2 can be seen in Figure 3.5. The prominent band (~26kDa, Lane 1 and 2, Figure 3.5) displayed a decrease in product size as compared to the intact fusion protein observed in Figure 3.4 (E1-3). A green circle (Figure 3.4) indicates 3C-Protease™ (~46kDa). No other protein bands were observed in lane 1 (Figure 3.5). The sample was concentrated 10-fold (Section 2.3.3.3d) to observe a diffuse band (red circle, lane 2) which was less than 10kDa. This low molecular weight diffuse protein band was expected to be CTX-S2. The sample was then fractionated to separate the high- and low molecular weight constituents (Section 2.3.3.3d), where both high- and low molecular weight fractions were desalted by buffer exchange (Section 2.3.3.3d) into PBS (pH 7.2), concentrated (Section 2.3.3.3d) and lyophilized (Section 2.3.4). The low molecular weight protein band (red circle, Figure 3.5) was excised and sent for mass spectrometry amino acid sequence confirmation (Section 3.1.3.2). CTX-S1 was purified in a similar manner.
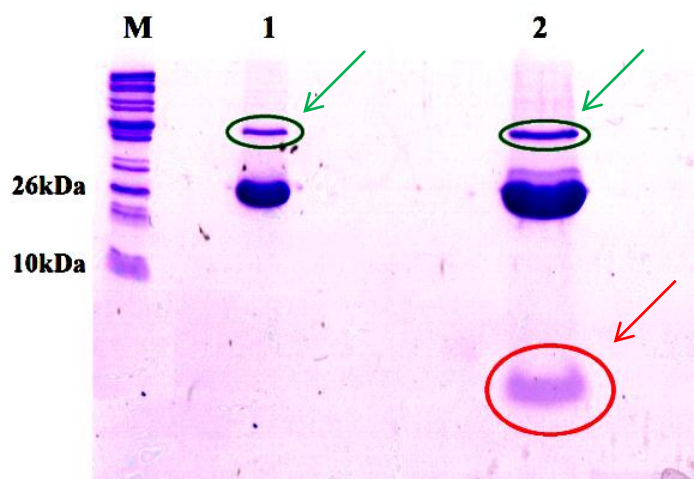
Figure 3.5: Cleavage of CTX-S2 from GST-CTX-S2. No CTX-S2 was observed for the protein fraction in lane 1. An x10 concentrate of the sample is in lane 2 where a low molecular weight protein band is observed (Green – 3C-Protease™; Glutathione-S-transferase (26kDa); Red - Low molecular weight diffuse band). The protein fractions were resolved on a 16% SDS-PAGE gel with Thermo PageRuler Unstained Protein Ladder (M). The gel was stained with Coomassie Brilliant Blue.

The lyophilized low molecular weight fractions obtained from the cleavage of GST-CTX-S1 and GST-CTX-S2 as well as the fusion proteins themselves were analysed for protein content using the BCA protein assay (Section 2.3.3.3e). The values obtained are given in Table 3.3. The BCA assay confirmed the presence of protein in the low molecular weight lyophilized samples.

Table 3.3: Protein concentrations obtained for the desalted and purified proteins fractions.

Fractions Analysed	Concentration (mg/mL)
GST-CTX-S1	0.612 ± 0.013
CTX-S1 (Cleaved from GST-CTX-S1)	0.085 ± 0.004
GST-CTX-S2	1.936 ± 0.056
CTX-S2 (Cleaved from GST-CTX-S2)	0.127 ± 0.011

*All experiments were done in triplicate. GST-CTX-S1 – GST fusion construct for recombinant CTX-S1; GST-CTX-S2 – GST fusion construct for recombinant CTX-S2; CTX-S1 – Recombinant CTX peptide from primer set 1 (Table 3.1); CTX-S2 – Recombinant CTX peptide from primer set 2.

3.1.3.2 Mass Spectrometry Characterization

To confirm the identity of the low molecular weight diffuse protein band (red circle, lane 2, Figure 3.5) a gel slice was excised and sent for liquid chromatography (LC) tandem mass

spectrometry (MSMS) analysis at the Central Analytical Facility (CAF) at Stellenbosch University, Tygerberg Campus (2.3.3.5).

The produced recombinant peptide (CTX-S2) was compared to the published amino acid sequence of the wild type (WT) chlorotoxin (CTX) [118, 122]. Comparative amino acid sequence analysis indicated three differences between the recombinant peptide and the wild type CTX. The N-terminal of the recombinant peptide had two additional amino acid residues: glycine (G) and serine (S) (green underlined, Table 3.4). These abovementioned residues were identified as remnants from the fusion construct cleavage site. The glycine (G) and arginine (R) residues, positions 24 and 25 (CTX-S2, red underlined italics, Table 3.4), was not detected by LC-MSMS analysis and as such their presence in CTX-S2 was not confirmed. The pro-6xHis tag (blue underlined italics, Table 3.4) was also not detected with LC-MSMS analysis. It is unknown why these 9 residues where not detected. The core sequence of CTX-S2 showed 34 of 36 WT amino acid residues present in the correct sequence. The predicted isoelectric point (pI 8.13, Table 3.4) of CTX-S2 indicates this is a cationic peptide. No LC-MSMS data was generated for CTX-S1 and it was decided to not continue with this variant of the peptide.

Table 3.4: A comparative of the amino acid sequence between the wild type (WT) CTX sequence and recombinant (CTX-S2) amino acid residue sequence of CTX

	Molecular Weight (kDa)	pI	Amino Acid Residue Sequence (N' → C')
WT [118, 122]	4.0	8.5	M C M P C F T T D H Q M A R K C D D C C G G K G R G K C Y G P Q C L C R
CTX-S2	4.1	8.13	*GS* M C M P C F T T D H Q M A R K C D D C C G G K *GR* G K C Y G P Q C L C R *P H H H H H H*

*Additional residues are depicted in green and underlined. Residues which were not detected in the core sequence of CTX-S2 are in red italics and underlined. The recombinant insert affinity tag of CTX-S2 is in navy italics and underlined. Additional and undetected residues were not taken into account for molecular weight prediction.

An alternative method was considered to confirm the presence of the Pro-6xHis tag on the recombinant peptide, based on surface plasmon resonance (Section 3.1.4).

3.1.4 Gold Nanoparticle Assisted Surface Plasmon Resonance Investigation for the Presence of the Affinity tag in Recombinant Chlorotoxin (CTX-S2)

The Pro-6xHis tag was not detected with LC-MSMS analysis of recombinant produced CTX-S2 (Section 3.1.3). The presence of the abovementioned affinity tag was investigated by utilizing the surface plasmon resonance (SPR) on the surface of noble metal nanoparticles (Section 1.6.2.2). The change in the SPR of nitrilotriacetic acid (NTA) functionalized gold nanoparticles (AuNP-NTA) was utilized to confirm the presence of a 6xHis-tag in the fusion protein (GST-CTX-S2) as well as the cleaved peptide (CTX-S2). The AuNP-NTA synthesis and characterization is described in detail in Sections 4.3.4 and 4.4.2. The AuNP surface was designed to be functionalized with polyethyleneimine (PEI) to confer a cationic surface charge. Further covalent surface modification was done to have 30% PEG_6-NTA functionalization. Optimization of the AuNP-NTA SPR interactions was done by nickel (Ni^{2+}) titrations and protein titrations as described in Section 2.3.3.6. The nickel activated AuNP-NTA was used for UV- Vis spectroscopy SPR based protein interactions. The expression construct pGEX-6P-2-CTX (Section 3.1.2) was used to express GST-CTX fusion protein, which did not have a 6xHis tag, with the same conditions described in Section 3.1.3.1. The samples used for AuNP-NTA interaction assays were GST-CTX (no affinity tag), GST-CTX-S2 (pro-6xHis-tag) and the latter's cleaved variant CTX-S2 (pro-6xHis-tag).

The SPR band (λ_{SPR}) showed a redshift from 525nm (red, Figure 3.6) to 530nm (green, Figure 3.6) upon interaction with Ni^{2+} with a minor decrease in optical density. Addition of GST-CTX to a final concentration of 20μg/mL caused a loss of the characteristic AuNP UV-Vis spectra with a blueshift in the λ_{SPR} to 525nm, compared to control (green, Figure 3.6), as well as a pronounced increase in the optical density (light blue, Figure 3.6). The loss of UV-Vis spectra is indicative of non-specific protein interactions on the AuNP surface as demonstrated for bovine serum albumin (Section CHECK) and may also indicate nanoparticle aggregation. The {AuNP-NTA + Ni} interaction for GST-CTX-S2 and CTX-S2 showed an increase in optical density, a redshift from 530nm (green, Figure 3.6) to 555nm (purple and black, Figure 3.6) and a conserved AuNP UV-Vis spectra. The AuNP-NTA interaction with GST-CTX-S2 and CTX-S2 indicates directionality coordinated attachment of the peptide to the AuNP-NTA surface.
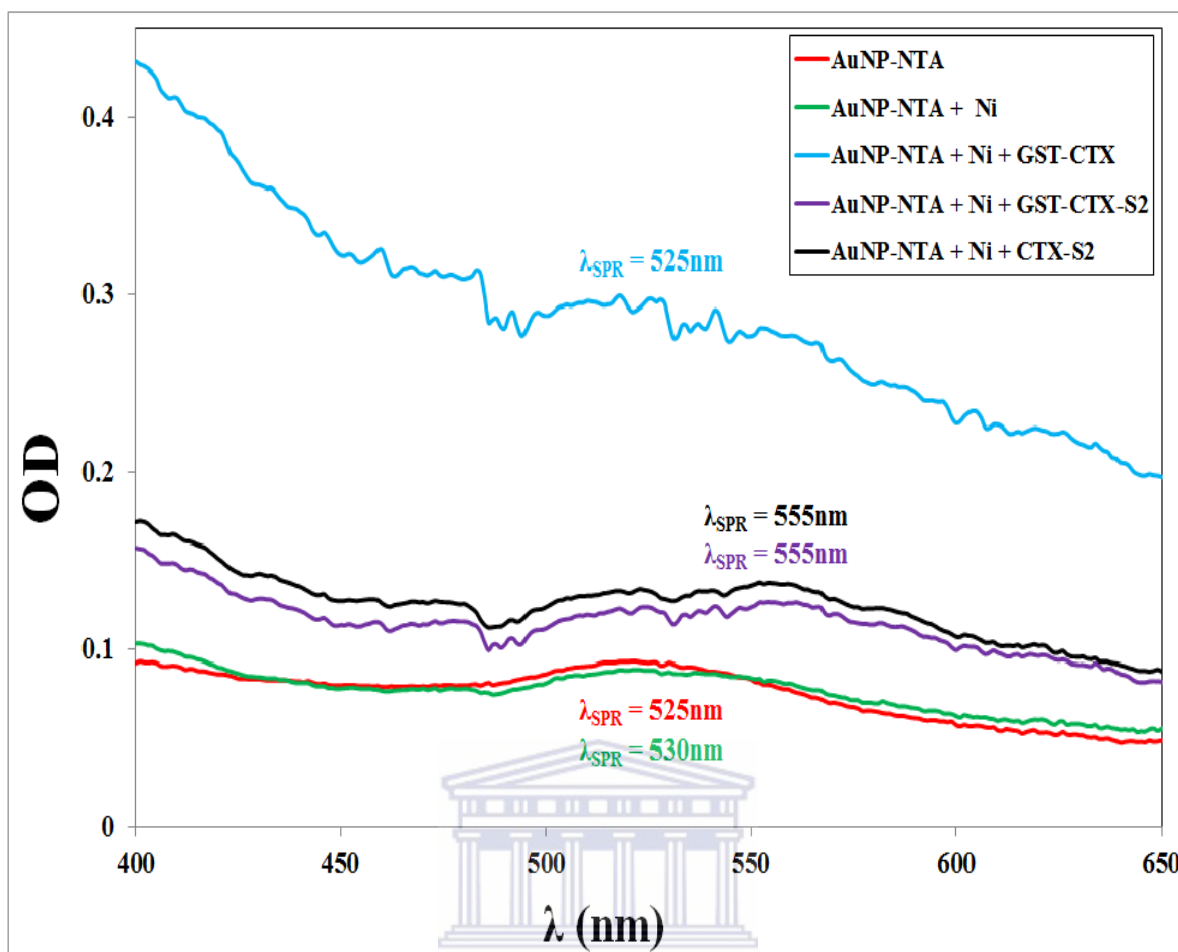
Figure 3.6: UV-Vis spectroscopy SPR investigation of changes on the AuNP-NTA surface. OD – Optical density; AuNP-NTA – NTA functionalized gold nanoparticles; Ni - 250μM nickel sulphate; GST-CTX (20μg/mL) – Fusion protein without recombinant pro-6xHis affinity tag; GST-CTX-S2 (20μg/mL) – recombinant fusion protein with affinity tag; CTX-S2 (20μg/mL) – recombinant peptide with affinity tag; λ_{SPR} – wavelength of surface plasmon resonance band. The results are representative of technical triplicates repeated on two different days.

3.1.5 Discussion

Research focused on the cloning and recombinant protein production of CTX is limited. This is most probably due to a US patent (held by Sontheimer and Deshane) on the wild type CTX gene as well as the difficulties associated with small peptide purification.

The DNA sequence for pGEX-6P-2-CTX-S2 showed no mutations and contained all the recombinant inserted elements. The amino acid sequence however did indicate that two specific internal residues were absent: G (glycine, position 24, G24) and R (arginine, position 25, R25). It is unclear if this is an experimental, instrumental or analysis error. However, in a site directed mutagenesis study conducted by Akcan *et al* in 2011 it was found that affinity of CTX was unaffected when lysine residues at position 15 and 23 were altered [125]. This

suggests that the basic nature of the peptide (pI 8.13) may not be a contributing factor to the cancer specific targeting activity observed in the literature. It is unclear what the effect of the absence of Glycine24 and Lysine25 were.

DNA sequencing results indicated that the PCR cloning of the CTX gene into the pGEX-6P-2 vector was successful and that the C-terminal 6xHis tags were incorporated into pGEX-6P-2-CTX-S1 (6xHis) and pGEX-6P-2-CTX-S2 (Pro-6xHis). Various *E.coli* strains were used to investigate optimal soluble protein yield and the ArcticExpress™ strain was chosen. Yu *et al* produced recombinant CTX utilizing the pGEX-6P-1 plasmid and a Rosetta BL21 *E.coli* strain with protein harvesting 4h post IPTG induction [126]. This study was unable to produce CTX with the same expression conditions using the pGEX-6P-2 construct. This particular strain contains additional protein folding chaperones which are cold induced. The ArcticExpress™ strain exploits colder temperatures where cold induced chaperones assist in protein folding. Another benefit is that the colder temperatures minimalize protein sequestration in inclusion bodies [297]. These factors all increase maximal soluble protein yield for perceived toxic proteins such as CTX. However, visualization of small peptides such as CTX on a SDS-PAGE gel presented a new challenge. The intact fusion proteins (GST-CTX-S1 and GST-CTX-S2) were readily resolved on a SDS-PAGE gel. Cleavage of the fusion proteins released the recombinant peptides (CTX-S1 and CTX-S2) which were observed after concentrating the sample 10-fold as a diffuse low molecular weight protein band. Three different approaches were used after sample fractionation and buffer exchange. A sample preparation was done for the corresponding diffuse protein band and was analysed by BCA protein assay, mass spectrometry as well as AuNP-NTA SPR assays. The BCA assay confirmed the presence of protein in the low molecular weight fraction.

Mass spectrometry analysis on the excised diffuse band (>10kDa, Figure 3.4) confirmed the presence of CTX. Also, 34 of the 36 wild type amino acid residues were present. The absence of glycine (G) and arginine (R) residues as well as the pro-6xHis tag cannot be explained by peer reviewed literature. The DNA sequencing confirms the presence of the codons for these residues. As such, the residues may have been cleaved and removed during sample preparation or that the ionization conditions used for the MALDI-QTOF MS was not optimal for CTX-S2 analysis. Sample preparation involved trypsin digestion. Trypsin has specificity for cleaving on the C-terminal of arginine (R) and lysine (K) residues [298]. As such, non-specific cleavage was not expected. The absence of the glycine (G) and arginine (R) residues

can also not be explained in a similar manner. Nucleotide sequencing (Section 3.1.2.3, Table 3.2) however indicates all residues, the Pro-6xHis tag as well as the glycine (G) and arginine (R), should be present. Software bias settings could have further contributed to the residues not being identified correctly.

The presence of the pro-6xHis tag was not confirmed by protein sequencing. A method for probing the presence of the affinity tag was developed and was based on the surface plasmon resonance (SPR) on the surface on gold nanoparticles. Gold nanoparticles were functionalized with NTA (AuNP-NTA). AuNPs (Section 1.6.2.2) have SPR that can be utilized to investigate interactions on the nanoparticle surface and is a well-known phenomenon [140]. The flood of electrons across the nanoparticle surface will give a specific surface plasmon maxima wavelength (λ_{SPR}). Interactions of molecules with the gold nanoparticle surface will affect the pathway of the electrons resulting in a change in λ_{SPR} which can be observed. This assay is based on the same technology utilized in surface plasmon resonance (SPR) equipment such as the BiaCore systems [299-301]. Targets are immobilized on gold coated sample plates and a SPR signal is generated when a ligand binds to the target. This can be used to investigate the interaction of AuNPs with proteins or peptides [139-142]. The use of AuNPs gives an additional benefit as the nanoparticles will aggregate or flocculate if there is a non-specific adsorption onto the surface. In a non-specific interaction large proteins can act as "glue" which will make the nanoparticles stick to each other in a similar manner as when a strong counter-ion is present [302] or when complementary DNA strands interact [211]. The interaction between NTA and a 6xHis tag is activated with nickel ions (Ni^{2+}) and has been demonstrated to be a highly specific interaction with x6His-tagged proteins during affinity chromatography [303-305]. NTA was synthesized (Sections 2.2.2.1-2.2.2.3) and immobilized on the surface of one-pot synthesized AuNP-PEI (Section 4.4.2). The NTA was covalently attached to the AuNP-PEI surface by using a bifunctional polyethylene glycol cross linker (SM-PEG$_6$) which covered 30% of the primary amines of the PEI on the AuNP-PEI surface (Section 2.2.3.3.1). This constructed AuNP was named AuNP-NTA (Section 4.4.2). The high molecular weight PEI on the AuNP surface confers a cationic character to the nanoparticles and will repel cationic molecules based on charge repulsion. The SM-PEG$_6$ reduces non-specific biomolecule interactions to a certain extent as shown with bovine serum albumin (BSA) in Section 4.4.2. Anionic molecules will however have an electrostatic attraction to the AuNP surface as demonstrated and discussed in Chapter 4 with citrate ions (Section 4.3.3.4). Negatively charged proteins, such as GST (pI

6.64) [306], bind non-specifically in an electrostatic manner to the PEI on the AuNP-NTA surface if no affinity tag is present on the protein. If an affinity tag is present, the GST will be directed away from the AuNP-NTA surface. The GST is on the N-terminus of the CTX and the affinity tag is on the C-terminus. GST-CTX was a negative protein control (no 6xHis-tag) and showed a loss of the characteristic UV-Vis spectra indicating non-specific protein interaction on the surface. This loss of spectra indicates that the anionic GST is interacting with the AuNP-NTA surface and inducing aggregation. CTX is a cationic peptide (pI 8.13, Table 3.4) repulsed by the cationic PEI on the AuNP-NTA surface, where interaction of CTX-S2 is dependent on the 6xHis-tag for directionality of attachment. GST-CTX-S2 and CTX-S2 showed a perceptible increase in the optical density with a redshift for λ_{SPR}, 520nm to 555nm, with typical AuNP-NTA UV-Vis spectra preserved which suggests an affinity tag is present and that there is a directional attachment of CTX-S2. Also, for GST-CTX-S2 this implies that the GST is directed radially away from the AuNP-NTA surface. It can be argued that the redshift is due to particle-to-particle interaction, but this is unlikely as only one affinity tag is present per peptide or fusion protein. The intact spectra as well as λ_{SPR} (Figure 3.6) for the interactions of AuNP-NTA with GST-CTX-S2 and CTX-S2 suggested directional attachment of the recombinant peptides on the nanoparticle surface. The AuNP-NTA UV-Vis SPR interaction assay corroborates the nucleotide sequence data (Table 3.2) and confirmed the presence of a 6xHis-tag on CTX-S2.

All CTX-MMP2 interaction studies (Section 3.3) were conducted with CTX-S2. For purposes of this research, no additional purification was done to ensure endotoxin removal. Endotoxin has not been shown to directly interact with MMP2 (EC 3.4.24.24, www.brenda.koeln.de). Furthermore, *in vitro* assay applications of CTX-S2 will be done on fixed cells and no live cell experiments will be conducted.

3.2 Matrix Metalloproteinase 2 (MMP2)
3.2.1 Introduction
Total crude cell lysates are typically used for MMP2 based zymography and the presence of interfering proteins such as other matrix metalloproteinases (MMPs) could influence the results. Further, zymography is a cumbersome and labour intensive technique. Qualitative and semi-quantitative confirmation of MMP2 and other MMPs in the sample still needs to be done by immuno-blotting techniques. As mentioned in Section 1.4.2, Annexin A2 was

reported as an alternative molecular target was for CTX. This made it necessary to evaluate the CTX-MMP2 interaction in an experimentally controlled manner. A C-terminal enhanced green fluorescent protein (EGFP) tagged MMP2 construct was designed for fluorescence microscopy co-localization studies (Section 3.3).

3.2.2 Cloning and Transfection of Matrix Metalloproteinase-2

3.2.2.1 Primer Design and PCR Amplification from pGEM-MMP2

A pGEM-T-Easy cDNA clone of MMP2, prepared from MCF-7 breast cancer cell line, was obtained from Miss Cleo Dodgen (Biotechnology Department, University of the Western Cape, Cape Town, South Africa) and the sequence was confirmed to be a perfect match for wild type full length pro-MMP2. This clone was named pGEM-T-MMP2 and was used as a template for PCR amplification (2.3.2.3). Primers (Table 3.5) were designed to amplify the full length pro-MMP2 (1983bp). The reverse primer (MMP2-R) was designed to include a fluorescent tag (Lumio-tag sequence, Life Technologies) on the C-terminal of MMP2. The forward primer included a *BamHI* restriction site and the reverse primer incorporated an *XhoI* restriction site to flank the 5' and 3' ends of the sequences respectively (Table 3.5).

Table 3.5: Primer Set Used for MMP2 PCR Amplification

MMP2-F (5')	5'-TGCT<u>GGATCC</u>ATGGAGGCGCTAATGGCCC-3'
MMP2-R (3')	5'-TATT<u>CTCGAG</u>*ACAACAACCAGGACAACA*AGGGCAGCCCAGTCG-3'

The BamHI and XhoI restriction sites respectively for the forward and reverse primers, respectively, are underlined. A Lumio-tag sequence is in red italics.

The PCR product was resolved on a 1% agarose gel (Figure 3.7) as described in Section 2.3.2.8. The expected PCR product size appeared to correspond to the expected size of 1983bp. Subsequent attempts to optimize the PCR yielded similar predicted amplicon sizes. A high fidelity hot-start Taq (HiFi™ Taq, Kapa Biosystems) was used for the large gene size (~2kb) as described in Section 2.3.2.3 and attempts with other Taq polymerases yielded non-specific bands at various conditions. The PCR amplicon band was excised and purified (2.3.2.4) for restriction digestion (2.3.2.5) with the Fermentas FastDigest® *BglII* and *SalI*. The pEGFP-N3 vector was linearized by restriction digestion with FastDigest® *BglII* and *SalI* (Section 2.3.2.5). The digested MMP2 PCR amplicon was ligated into the pEGFP-N3 vector (Section 2.3.2.6) which destroyed the restriction sites. *BglII* is an isoschizozyme of *BamHI* and *SalI* is an isoschizozyme of *XhoI*. The transformants (Section 2.3.1.4) were screened for

positive clones by colony PCR (Section 2.3.2.7) which identified five positive clones (lanes 1-5, Figure 3.8) which were sent for nucleotide sequence analysis (Section 2.3.2.10).
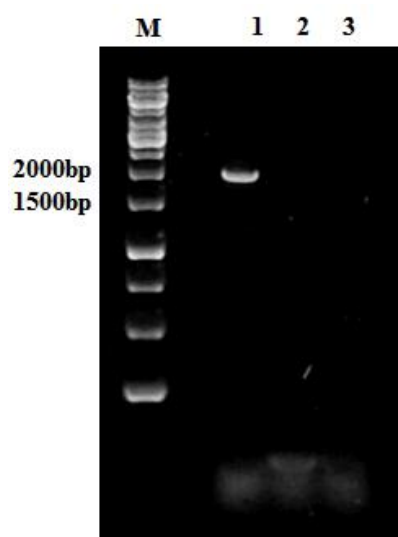
Figure 3.7: The PCR amplification product for MMP2. Lane 1 is the MMP2 amplicon; Lanes 2 and 3 are negative controls; M is molecular marker (Fermentas Generuler 1kb Ladder). GelRed was used to stain DNA on a 1% agarose gel.
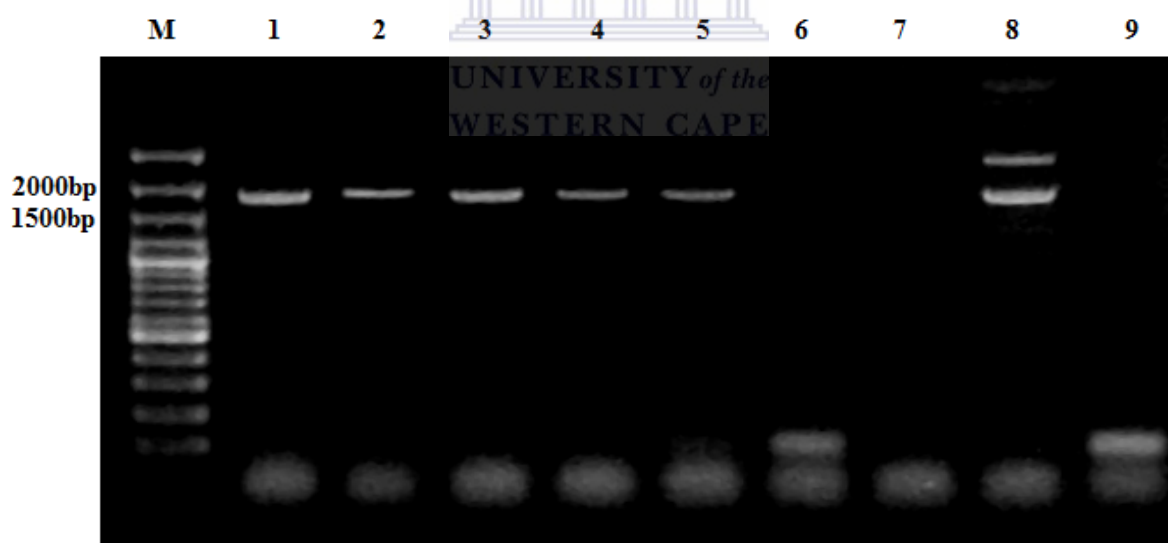
Figure 3.8: A colony PCR screen to detect positive clones for pEGFP-N3-MMP2. Lanes 1-5 contain positive clones, Lane 6 was a negative clone, Lane 9 is a duplicate of lane 6, Lane 7 is a negative control; Lane 8 is the vector template as a positive control. The marker (M) used was Fermentas O'Generuler 100bp Ladder. GelRed was used to stain DNA resolved on a 1% agarose gel.

3.2.2.2 Amino acid Residue Sequence Alignment of pEGFP-N3-MMP2

All clones sent for sequencing (Section 3.2.2.1, Figure 3.8) yielded identical results and a clone was selected at random. The reconstructed amino acid residue sequence (Table 3.6) indicates full length pro-MMP2 is truncated in the hemopexin domain at residue 599 (Table

3.6 and Figure 3.9). The 599 amino acids residues which were identified to be present correspond to a nucleotide sequence which is 1797bp in size. The predicted amplicon size was 1983bp (Section 3.2.2.1). There are 61 amino acid residues which correspond to 183bp nucleotides, absent from the C-terminal hemopexin domain of MMP2 in the pEGFP-N3-MMP2 construct. The MMP2 gene sequence truncation was probably the results of *BamHI* or *XhoI* digestion, yet no recognition sites for these two enzymes were found in the template cDNA sequences. The wild type MMP2 DNA sequence however does contain a *BamHI* restriction site (Table A11, Appendix). This error was most probably attributed to incorrect base calling during cDNA sequence analysis. MMP2 reverse primer miss-priming may have taken place for the nucleotide region 1625-1680 (Table 3.7), which does not correspond to the verified nucleotide sequence of 1797bp, which would deliver a protein product 541-556 amino acid residues in length. Further, the sequence alignment showed full length EGFP (green text, Table 3.6) was attached to the truncated C-terminal hemopexin domain at the 3' *SalI* restriction site (Figure 2.2, 2.3.2.5) of the pEGFP-N3-MMP2 construct starting at amino acid residue 599 (blue text, Table 3.6). The truncated protein product will be called tMMP2-EGFP for the remainder of the text. The Lumio-tag (Table 3.5, Section 3.2.2.1) which was designed for insertion at the end of the hemopexin domain of MMP2 was lost due to this C-terminal truncation.
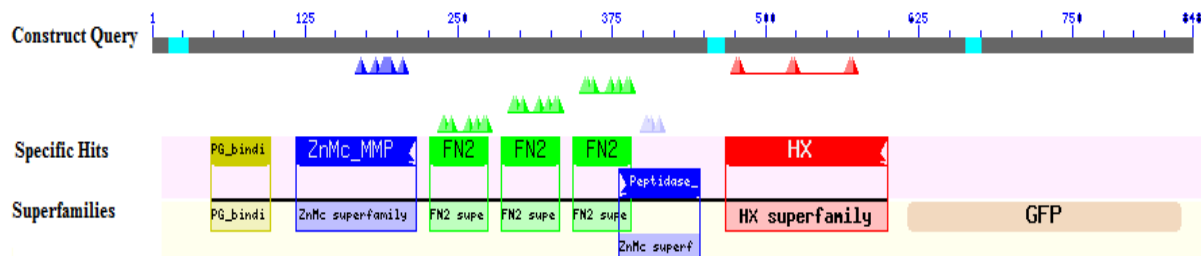
Figure 3.9: The conserved domains found for reconstruction of pEGFP-N3-MMP2 from sequencing data. PG_bindi – putative gelatin binding site; ZnMc_MMP – Conserved zinc binding pocket for matrix metalloproteinases; FN2 – conserved fibronectin type II domains; Peptidase – conserved peptidase zinc binding pocket; HX – conserved hemopexin domain; GFP – enhanced green fluorescent protein conserved domain.

The methionine at residue locus 598 (M598) is mutated to an isoleucine (I598) (Table 3.6) which would not affect the hydrophobicity of the position embedded in the hemopexin domain. However the substrate specificity could be affected as the hemopexin domain has been implicated in substrate binding (Section 1.3.1). A mutation at I582 to T582 (isoleucine to tryptophan) in the hemopexin domain changes the residue from an aliphatic hydrophobic residue to an aromatic basic residue which could also affect substrate binding. The mutation

F80 to L80 (phenylalanine to a leucine) conserves the hydrophobicity of the position, although the sterical hindrance at this particular position is decreased. Mutations from aliphatic to aromatic residues and vice versa affects the sterical aspects of the position, as aromatic residues have a tendency to be physically more bulky than aliphatic residues, which in turn potentially changes substrate binding as well as substrate specificity.

Table 3.6: Amino acid residue sequence alignment of pEGFP-N3-MMP2 with wild type pro-MMP2 (Genbank: NP_004521.1) sequence

```
Constr 1     MEALMARGALTGPLRALCLLGCLLSHAAAAPSPIIKFPGDVAPKTDKELAVQYLNTFYGC   60
WT           MEALMARGALTGPLRALCLLGCLLSHAAAAPSPIIKFPGDVAPKTDKELAVQYLNTFYGC

Constr 61    PKESCNLFVLKDTLKKMQKLFGLPQTGDLDQNTIETMRKPRCGNPDVANYNFFPRKPKWD   120
WT           PKESCNLFVLKDTLKKMQKFFGLPQTGDLDQNTIETMRKPRCGNPDVANYNFFPRKPKWD

Constr 121   KNQITYRIIGYTPDLDPETVDDAFARAFQVWSDVTPLRFSRIHDGEADIMINFGRWEHGD   180
WT           KNQITYRIIGYTPDLDPETVDDAFARAFQVWSDVTPLRFSRIHDGEADIMINFGRWEHGD

Constr 181   GYPFDGKDGLLAHAFAPGTGVGGDSHFDDDELWTLGEGQVVRVKYGNADGEYCKFPFLFN   240
WT           GYPFDGKDGLLAHAFAPGTGVGGDSHFDDDELWTLGEGQVVRVKYGNADGEYCKFPFLFN

Constr 241   GKEYNSCTDTGRSDGFLWCSTTYNFEKDGKYGFCPHEALFTMGGNAEGQPCKFPFRFQGT   300
WT           GKEYNSCTDTGRSDGFLWCSTTYNFEKDGKYGFCPHEALFTMGGNAEGQPCKFPFRFQGT

Constr 301   SYDSCTTEGRTDGYRWCGTTEDYDRDKKYGFCPETAMSTVGGNSEGAPCVFPFTFLGNKY   360
WT           SYDSCTTEGRTDGYRWCGTTEDYDRDKKYGFCPETAMSTVGGNSEGAPCVFPFTFLGNKY

Constr 361   ESCTSAGRSDGKMWCATTANYDDDRKWGFCPDQGYSLFLVAAHEFGHAMGLEHSQDPGAL   420
WT           ESCTSAGRSDGKMWCATTANYDDDRKWGFCPDQGYSLFLVAAHEFGHAMGLEHSQDPGAL

Constr 421   MAPIYTYTKNFRLSQDDIKGIQELYGASPDIDLGTGPTPTLGPVTPEICKQDIVFDGIAQ   480
WT           MAPIYTYTKNFRLSQDDIKGIQELYGASPDIDLGTGPTPTLGPVTPEICKQDIVFDGIAQ

Constr 481   IRGEIFFFKDRFIWRTVTPRDKPMGPLLVATFWPELPEKIDAVYEAPQEEKAVFFAGNEY   540
WT           IRGEIFFFKDRFIWRTVTPRDKPMGPLLVATFWPELPEKIDAVYEAPQEEKAVFFAGNEY

Constr 541   WIYSASTLERGYPKPLTSLGLPPDVQRVDAAFNWSKNKKTYIFAGDKFWRYNEVKKKIDG   600
WT           WIYSASTLERGYPKPLTSLGLPPDVQRVDAAFNWSKNKKTYIFAGDKFWRYNEVKKKM

Constr 601   TAGPGSIATMVSKGEELFTGVVPILVELDGDVNGHKFSVSG...........................
WT
```

*Constr – Reconstructed The start of the pEGFP-N3 sequence at the C-terminal of the truncated pro-MMP2 is in blue font. The sequence in green indicates the first fragment of EGFP as per pEGFP-N3 prediction.

Table 3.7: Potential Site of Miss-priming of the Reverse Primer

```
                    1625                                                    1680
MMP-2 (WT)          ACTGGATCTACTCAGCCAGCACCCTGGAGCGAGGGTACCCCAAGCCACTGACCAGC
                         |  |  |||        |    |    |  |         |            |
3' Primer (5' to 3')     TATTCTCGAGACAACAACCAGGACAACAAGGGCAGCCCAGTCG
```

3.2.3 Discussion

Sequence analysis of tMMP2-EGFP shows the presence of 3 mutations and a 173bp (61 amino acid) truncation. The truncation of MMP2 (Sections 3.2.2.1 and 3.2.2.2) in the C-terminal pEGFP-N3-MMP2 construct was not due to restriction enzyme recognition sites within the gene nucleotide sequence as the truncation occurred during PCR amplification. Miss-priming of the reverse primer (Table 3.7) by binding to this site would have generated a truncated protein product (541-556 amino acid residues) which did not correspond with the verified truncated sequence of 599 amino acid residues (Section 3.2.2.2). Currently, the cDNA sequences which served as template for MMP2 amplification are being verified to determine the cause of the *BamHI* restriction site occlusion. The mutation for amino acid residue 598 (Table 3.6) is most probably due to the truncation of the MMP2 PCR amplicon and subsequent ligation into the *SalI* restriction site of the pEGFP-N3 vector which altered the codon. The mutation for residue 80 was attributed to a single base mutation in the codon triplet, TTT (phenylalanine) to TTA (leucine) during PCR amplification. This mutation is not in the catalytic domain of MMP2 and is found in the putative gelatin binding domain of the protein. A codon change from ATC (isoleucine) to ACC (threonine) on residue position 582 was due to a single base mutation in the hemopexin domain of MMP2 and was most probably introduced during PCR amplification. The hemopexin domain is orientated in a transmembrane position in the event MMP2 is localized to the cytoplasmic membrane. The rest of the pro-MMP2 protein sequence was a good match for the wild type pro-MMP2.

MMP2 has been shown to retain catalytic activity for different splice variants [307, 308] and the pEGFP-N3-MMP2 construct was used to create a transfected drug responsive A2780 cell line (Section 5.2) which expressed tMMP2-EGFP in a stable manner which will be discussed in Section 3.3.

3.3 The Interaction between Chlorotoxin (CTX) and Matrix Metalloproteinase-2 (MMP2)

3.3.1 Introduction

Zymography techniques are typically employed for the detection of MMP2 in biological samples. This technique was also used by Deshane *et al* to demonstrate that CTX had a specific and inhibitory effect on MMP2 but offered no insight with regards to the interaction

mechanism between these two proteins. The direct interaction between CTX and MMP2 was brought into question in 2011 when Annexin A2 (Section 1.4.2) was identified as a potential molecular target for CTX. The interaction between CTX and MMP2 will be investigated using Michaelis-Menton enzyme kinetics as well as wide field fluorescence microscopy.

3.3.2 Michaelis-Menton Enzyme Kinetics

Enzyme kinetic studies were conducted in a similar manner as done by Weingarten *et al* [81], who reported MMP2 displaying Michaelis-Menton kinetics for the designed chromogenic peptide substrate, by using three different colorimetric peptide concentrations (Section 2.5.1.2) to obtain the Michaelis-Menton graph (Figure 3.10a). Pro-MMP2 activation to mature MMP2 by organomercurial APMA was described in Section 2.5.1.1. The assay was developed and conducted as described in Section 2.5.1.2 (Table 2.7) with the following inhibitors: commercial competitive inhibitor BiPS and recombinant CTX (CTX-S2, Sections 3.1.1.1-3.1.1.2). The assay was developed as a novel one-step realtime high-throughput kinetics assay. The Michaelis-Menton graph for three different chromogenic peptide concentrations can be seen in Figure 3.10a and was obtained as described in Section 2.5.1.2. The corresponding Lineweaver-Burke graph (Figure 3.10b) was obtained as described in Section 2.5.1.2. The kinetic parameters determined from the Lineweaver-Burke graph can be seen in Table 3.8.

MMP2 enzyme activity (Table 3.8) delivered a K_m (1.07 $\pm$ 0.01mM), V_{max} (2.75 $\pm$ 0.07µM/min) and k_{cat} (1.38 $\pm$ 0.04) in the absence of any inhibitors. In the presence of BiPS (MMP2+BiPS, Figure 3.11b; Table 3.8, MMP2+I2) there is no statistical change in the V_{max} compared to the control (MMP2, Figure 3.10 and Table 3.8). There was a statistical significant change in the K_m value compared to the control and subsequently a change in the turnover number (Table 3.8). The value for MMP2+I1 was aberrant and corresponds to ~35nM BiPS, twice the IC_{50} concentration. There was a statistical significant change for the V_{max} and K_m for both CTX-S2 (MMP2+CTX-S2, Figure 3.11b; Table 3.8, MMP2+CTX2) concentrations compared to the control. The turnover number for both concentrations of CTX-S2 used was significantly lower compared to control.

Table 3.8: Experimentally obtained kinetic parameters for the investigation of MMP2 activity in the presence of a commercial inhibitor and CTX.

	V_{max} (µM/min)	K_m (mM)	Turnover (k_{cat}; M/s/mg active MMP-2)
MMP2	2.75 ± 0.07	1.07 ± 0.01	1.38 ± 0.04
MMP2 + I_1	4.06 ± 2.80	1.65 ± 1.46	2.04 ± 1.40
MMP2 + I_2	2.78 ± 0.43	$0.94 \pm 0.21^{\dagger}$	1.39 ± 0.22
MMP2 + CTX_1	$1.90 \pm 0.10^{\dagger}$	$0.62 \pm 0.03^{\dagger}$	$0.95 \pm 0.05^{\dagger}$
MMP2 + CTX_2	$2.15 \pm 0.15^{\dagger}$	$0.67 \pm 0.08^{\dagger}$	$1.08 \pm 0.07^{\dagger}$

All averages are the average of experimental triplicates. An amount of ~2ng active MMP2 was used in all kinetic experiments (MMP2 – Matrix metalloproteinase-2; I_1 – Inhibitor concentration 1 (35nM); I_2 – Inhibitor concentration 2 (17.5nM); CTX_1 – Chlorotoxin (CTX-S2) concentration 1 (200nM) and CTX_2 – Chlorotoxin (CTX-S2) concentration 2 (100nM)). All units and values are expressed as per modern convention (Mike Danson Lecture, 2009). $\dagger$ Indicates statistical significance from the corresponding value for MMP2. Table A1 (Appendix) shows p-values, where $p < 0.05$ was statistically significant.

In seminal work Weingarten and Feder [81] developed a colorimetric assay for the global detection of collagenase activity in 1985. The substrate was designed as a global screen for collagenase activity from total crude cell lysates. As such, the cleavage site in the peptide was designed to be a universal matrix metalloproteinase substrate. The kinetic parameters reported for this thio-ester peptide was a $K_m = 4mM$ and a $k_{cat} = 370\,000h^{-1}$ ($103s^{-1}$). The K_m value is an indication of the binding of an enzyme to the substrate, where a large value indicates slow dissociation and as such a low affinity for the substrate (Rogers and Gibon, 2009) [309]. V_{max} is the theoretical maximal catalytic velocity an enzyme can achieve when the substrate affinity is high (small K_m) and k_{cat} is the turnover number of the enzyme, or how much substrate will be converted to product per unit of time per unit of enzyme [309]. Large values for V_{max} or k_{cat}, predicts high theoretical catalytic velocity [309]. In comparison, the values experimentally obtained for the K_m is 4-fold lower (Table 3.8) and the k_{cat} value (Table 3.8) is a hundred fold lower than reported by Weingarten for this chromogenic peptide substrate. This is attributed to the complex mixture of collagenase enzymes Weingarten used in the experimental work, compared to the pure recombinant mature MMP2 used for the enzyme kinetics in this study. A complex cell lysate can have many enzymes which could simultaneously utilize the chromogenic peptide substrate.
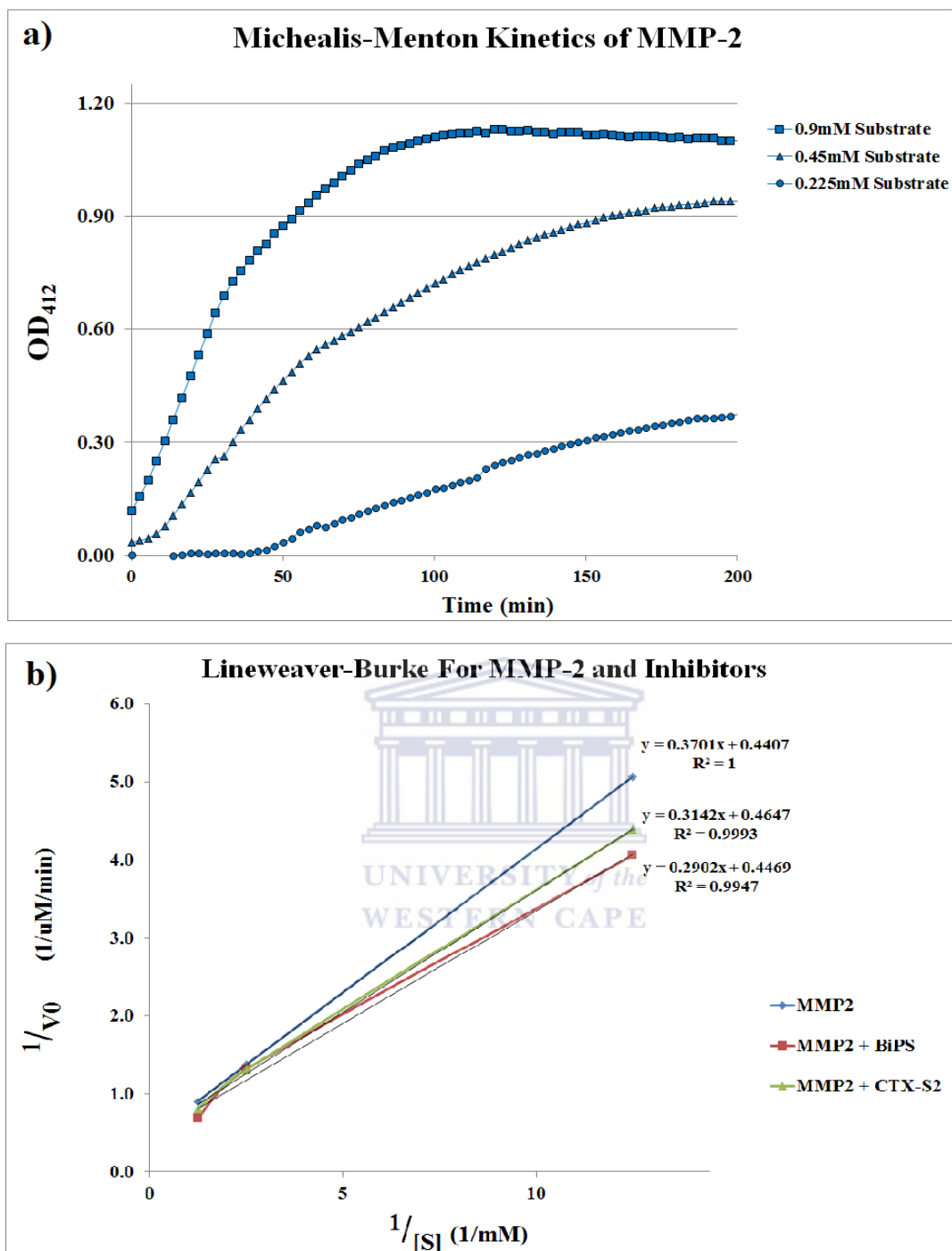
Figure 3.10: An example of the enzyme kinetic evaluation of the interaction of MMP2, BiPS and CTX-S2. The Michealis-Menton graph for time-dependent increase in optical density (OD) for MMP2 in the absence of inhibitors can be seen in (a). The Lineweaver-Burke graph (b) demonstrates the change in the intercept as well as gradient of the linear line in the absence and presence of inhibitors. The graphs are for the literature IC_{50} values for BiPS (17nM) and CTX-S2 (100nM). The experiment was done in technical triplicates on two different days.

The assay developed is novel and as such can also have an effect on the kinetic parameters. The IC_{50} value for the commercial inhibitor (MMP2 + I2, Table 3.8) shows no alteration in the V_{max} or k_{cat} but the K_m value was statistically different which indicates a change in the affinity of the enzyme for the chromogenic peptide substrate in the presence of the inhibitor.

This is indicative of competitive inhibition [309], as the inhibitor will compete with the chromogenic substrate to bind to the catalytic pocket of MMP2. This corresponds to the designed function of the inhibitor as per manufacturer information. The 35nM concentration of commercial inhibitor (MMP2 + I1, Table 3.8) gave aberrant values which may suggest oversaturation of the substrate binding pocket because the inhibitor was used at a too high concentration [309, 310]. Lowered V_{max}, K_m and k_{cat} values for both concentrations of CTX, acting as an unknown inhibitor, was obtained as opposed to the corresponding values for MMP2 in the absence of any inhibitors (Table 3.8). The inhibition mechanism could not be determined based on the kinetic data as the inhibitor curve lies above the no inhibitor curve [309, 310]. No crystallographic- or NMR data was obtained to indicate where CTX is located during the CTX-MMP2 interaction and as such the locus of CTX is left to speculation.

3.3.3 Wide Field Fluorescence Microscopy Co-localization Studies of MMP2

3.3.3.1 Differential tMMP2-EGFP *In Vitro* Translocation in Response To Various Biochemical Stimuli

The pEGFP-N3-MMP2 construct with the truncated hemopexin domain (tMMP2-EGFP, Section 3.2.2.2) was transfected (Section 2.4.4) into the drug sensitive A2780 cell line (Section 5.1.2) for stable fusion protein expression. All transfection attempts into the A2780cis (drug resistant) cell line were unsuccessful. Different biochemical stimuli, known to induce MMP2 membrane localization and zymogen maturation, were used to determine whether the EGFP fluorescence signal was specific to MMP2 intracellular localization. Biochemical stimulants of MMP2 maturation and subsequent translocation were used to determine if the translocation of EGFP was associated with MMP2 translocation, which would indicate whether tMMP2-EGFP was intact, as MMP2 is known to be autocatalytic (Section 1.3). The wide field fluorescence micrographs, obtained as described in Section 2.5.2.5, of the pEGFP-N3-MMP2 transfected A2780 cells under different biochemical stimuli (Section 2.5.2.2) can be seen in Figure 3.11. The different fluorescence channels are denoted DAPI (nuclear stain), EGFP (EGFP associated green fluorescence) and the composite overlay (DAPI + EGFP).

Control cells were untreated over the 24h period (Figure 3.11, Control) and showed green fluorescence distributed throughout the cell cytoplasm as well as in the nucleus. Cisplatin (Figure 3.11, 2µM cis) and PMA (Figure 3.11, 100ng/mL PMA) treated cells showed a decrease in overall adherent cell number as well as an observable translocation of the EGFP

(green) associated fluorescence emission from the cytoplasm to a cytoplasmic membrane compared to the control in the composite overlays. The composite overlay of the DAPI (blue) and EGFP (green) channels show no quenching of blue fluorescence emission (DAPI) for cisplatin and PMA treatment compared to the control which is suggestive of tMMP2-EGFP nuclear to cytoplasm/membrane translocation. Lipopolysaccharide treated cells (Figure 3.11, 100ng/mL LPS) showed an overall increase in the adherent cell number compared to the control, however the translocation of the EGFP associated fluorescence emission from the nucleus and cytoplasm to the cell membrane was not as significant as for cisplatin and PMA.

The transfected A2780 cells displayed EGFP associated fluorescence emission (Control, Figure 3.11) distributed throughout the cytoplasm as well as nucleus, where the green fluorescence was not attributed to auto-fluorescence as background subtraction was done pre- and post-image acquisition (2.5.2.5). The cytoplasmic and nuclear tMMP2-EGFP (Control, Figure 3.11) localization is attributed to the sequestration of pro-MMP2, where localization will be induced upon zymogen maturation (pro-MMP2 → MMP2). The EGFP associated fluorescence emission was confirmed to be associated with MMP2 translocation by utilizing biochemical stimuli reported to influence MMP2 expression levels *in vitro*. Sequence analysis (3.2.2.2) indicated that the C-terminal EGFP tagged MMP2 was truncated in the hemopexin domain and it was necessary to determine whether the protein product, tMMP2-EGFP, was intact as a fusion protein. Lipopolysaccharide (LPS) (Figure 3.11, LPS) stimulation induces a cellular immune response by the NF-κB pro-inflammatory pathway to induce global matrix metalloproteinase, including MMP2, expression in cancerous and non-cancerous cell lines [90, 102, 116, 311]. Increased cell number following LPS (a mitogen) treatment has been reported for mouse B cells were an increase in XBP-1 protein expression and alternate XPB-1 splicing was directly correlated with increased cell differentiation by MAPK associated kinases [312].

A decrease in adherent cell numbers was observed for the cisplatin and PMA treatment (Figure 3.11) with an increase in cytoplasmic volume as well as abnormal nuclear morphology. This is attributed to the known genotoxicity of the above mentioned compounds and the resultant cytoprotective response, where cisplatin chelates with DNA (1.2.3.2.1) and PMA is a known mutagenic carcinogen [3, 90, 116]. Roomi and co-workers demonstrated that PMA stimulation influences MMP9 and MMP2 expression dependent on the cell type [90]. Cisplatin treatment of the A2780 cell line has been reported to increase maturation of pro-

MMP2 which is associated with acquired multi-drug resistance as well as tumour malignancy [53, 115, 313, 314]. The observed translocation of tMMP2-EGFP to the cytoplasmic membrane under these different biochemical stimuli is indicative of increased activation of MMP2 from the zymogen form to a mature protease.
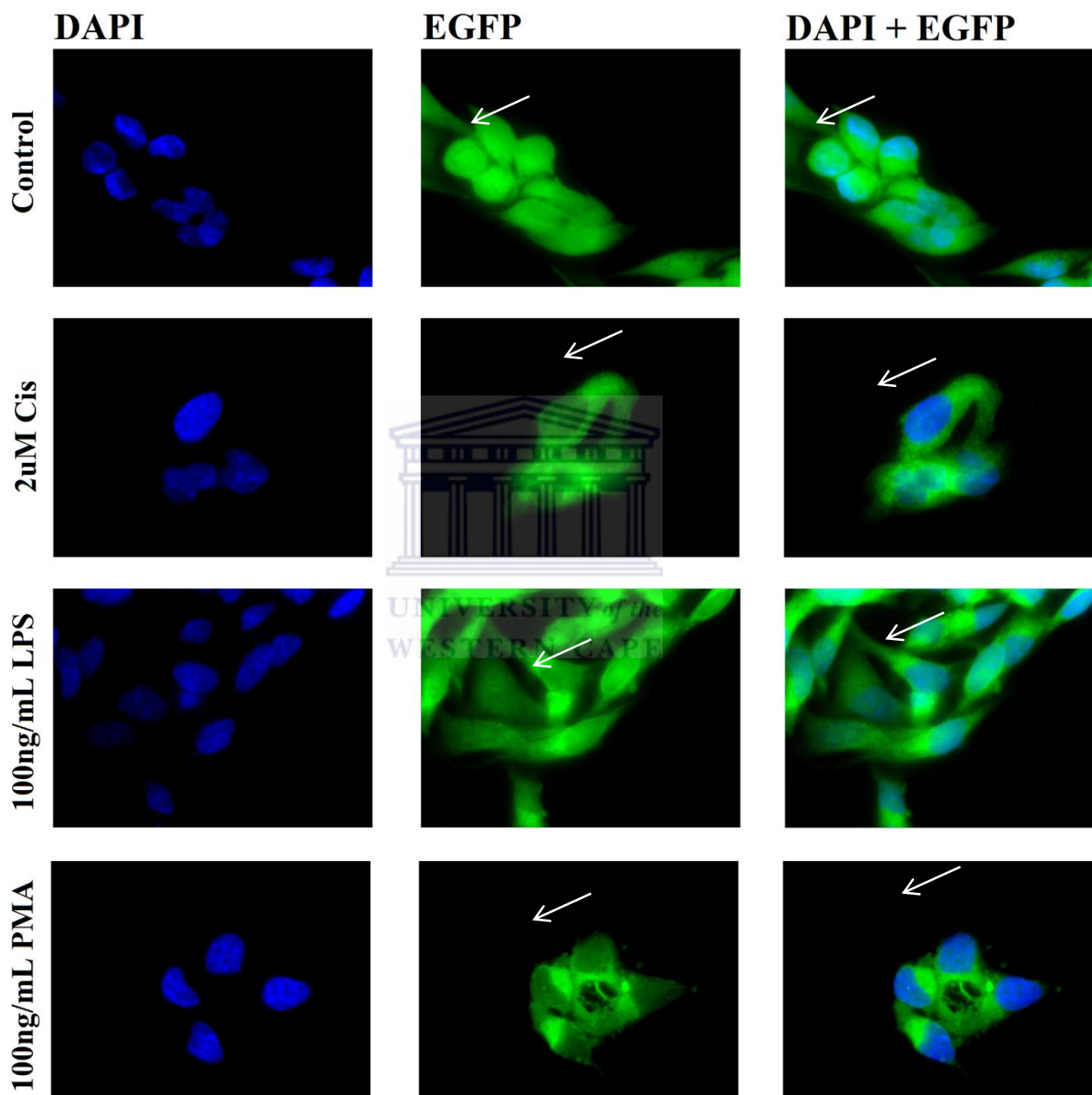
Figure 3.11: Wide field fluorescence micrographs of pEGFP-N3-MMP2 transfected A2780 cells under different biochemical stimuli. The blue colour is the nuclear stain DAPI and the green colour is enhanced green fluorescent protein (EGFP) associated green fluorescence emission. Control cells received no stimulus. The magnification is x100.

The microscopy was qualitative to specifically detect tMMP2-EGFP localization as well as translocation and as such no account could be given for native pro-MMP2 and active MMP2

in the cells. The above mentioned treatments resulted in translocation of EGFP associated green fluorescence emission to the cytoplasmic membrane compared to the untreated control. This implied that (i) the expression and localization of EGFP appeared to be responsive to MMP2 associated biochemical stimuli, (ii) EGFP was tethered to tMMP2 and (iii) tMMP2-EGFP displayed MMP2-like biological activity. The assumption can be made that the tMMP2 is tethered to EGFP in tMMP2-EGFP as predicted by sequence analysis. Further, the truncated hemopexin domain of tMMP2-EGFP appeared to have no effect on the cell membrane localization of the fusion protein. As mentioned in an earlier paragraph, MMP2 retains catalytic activity for different splice variants [308, 309] where the hemopexin domain was absent which served as support for the localization and translocation of tMMP2-EGFP observed under various biochemical stimuli.

The CTX-MMP2 interaction will be investigated in Section 3.3.3.2 with the transfected A2780 cells under 2μM cisplatin pre-treatment. The use of cisplatin would enable the pEGFP-N3-MMP2 cells to acquire drug resistance as well as to facilitate translocation of tMMP2-EGFP to the cell membrane. The membrane localization of tMMP2-EGFP was used to mimic MMP-2 associated malignancy [53, 115, 313, 314] of the A2780(c) cells as well as to demonstrate the therapeutic and diagnostic potential of the CTX-MMP2 interaction for cancer specific targeting (Section 3.3.3.2).

3.3.3.2 Wide Field Fluorescence Microscopy Co-localization Study of the CTX-(MMP-2) Interaction

The pEGFP-N3-MMP2 transfected A2780 cell line showed stable expression of tMMP2-EGFP (Section 3.3.3.1) and was kept under 2μM cisplatin treatment to keep the cell line multidrug resistant and have MMP2 associated malignancy (Sections 2.5.2.1 and 2.5.2.2). Quantum dots (QD$_{625}$), peak fluorescence emission 625nm, functionalized with thiolated polyethyleneimine (Section 2.2.4.1) and CTX (CTX-S2) bio-conjugated on the surface (Section 2.2.4.2) were prepared for the investigation of co-localization of CTX with tMMP2-EGFP to study the CTX-MMP2 interaction. Confirmation of the CTX-MMP2 co-localization was done by using two control experiments: (i) a goat polyclonal anti-MMP2 antibody (Pierce) bio-conjugated to the dansyl chloride (Sigma), as described in Section 2.5.2.3, for fluorescent labelling of MMP2 in untransfected A2780cis cells; and (ii) QD-PEI without CTX-S2 bio-conjugated to the nanoparticle surface. For ease of reading, CTX-S2 will be referred to as CTX in the remainder of this chapter. The cells were propagated as described in

Section 2.5.2.1 and stained with the fluorescent stains as described in Section 2.5.2.4. Micrographs were obtained as described in Section 2.5.2.5.

The DAPI stain (blue) indicates the nuclei (Figure 3.12a and Figure 3.12b, DAPI) and the green tMMP2-EGFP (Figure 3.12a and Figure 3.12b, EGFP) appears to be localized to the cellular membrane with fluorescence being observed in the cytoplasm. QD_{625} unconjugated with CTX was localized in a peri-nuclear region within the cells (DAPI+QD_{625}, Figure 3.12a) and no co-localization of QD_{625} with the MMP2-EGFP (EGFP+ QD_{625}, Figure 3.12) fluorescence. A composite overlay of all the channels (DAPI+EGFP+QD_{625}) showed the distinct localization of QD_{625}, tMMP2-EGFP and the nucleus (DAPI). QD_{625} conjugated with CTX showed co-localization to a similar locus as tMMP2-EGFP (EGFP, QD_{625}, EGFP+ QD_{625}; Figure 3.12b). There was little to no localization of QD_{625} with the DAPI nuclear stain (DAPI+QD_{625}; Figure 3.12b). An overlay of all the channels can be seen in DAPI+EGFP+QD_{625} in Figure 3.12b. CTX conjugated quantum dots (QD_{625}) appear to alter the localization of QD_{625} from a peri-nuclear region to a cytoplasmic membrane locus, which suggested an interaction between CTX conjugated QD_{625} and tMMP2-EGFP.

Dansylated anti-MMP2 antibody showed membrane specific localization (Dansyl, Figure 3.13a and Figure 3.13b) in A2780cis cells, which did not express tMMP2-EGFP, with less dansyl associated fluorescence emission was observed in the cytosolic regions of the cells. The DAPI stained the nuclei of the cells in Figure 3.13 (DAPI, a+b). QD_{625} unconjugated with CTX was localized in a peri-nuclear region (QD_{625}; DAPI+ QD_{625}; Figure 3.13a) with minimal co-localization of the QD_{625} with dansyl associated fluorescence emission (QD_{625}, Dansyl+QD_{625}; Figure 3.13a). Co-localization of QD_{625} conjugated with CTX (Figure 3.13b; QD_{625}, Dansyl+ QD_{625}) showed co-localization to the same cellular membrane associated region as the dansylated anti-MMP2 antibody (DAPI+Dansyl+QD_{625}; Figure 3.13b). The co-localization of the CTX conjugated quantum dots with the dansylated anti-MMP2 antibody suggested that the peptide as well as the antibody both had similar molecular targets.

The co-localization of CTX conjugated QD_{625} with tMMP2-EGFP (Figure 3.12b) as well as dansyl anti-MMP2 (Figure 3.13b) in a cellular membrane loci suggested there was a CTX-MMP2 interaction. In the absence of CTX the QD_{625} localization was peri-nuclear for tMMP2-EGFP expressing A2780cis cells (Figure 3.12a) as well as untransfected A2780cis cells (Figure 3.13a).
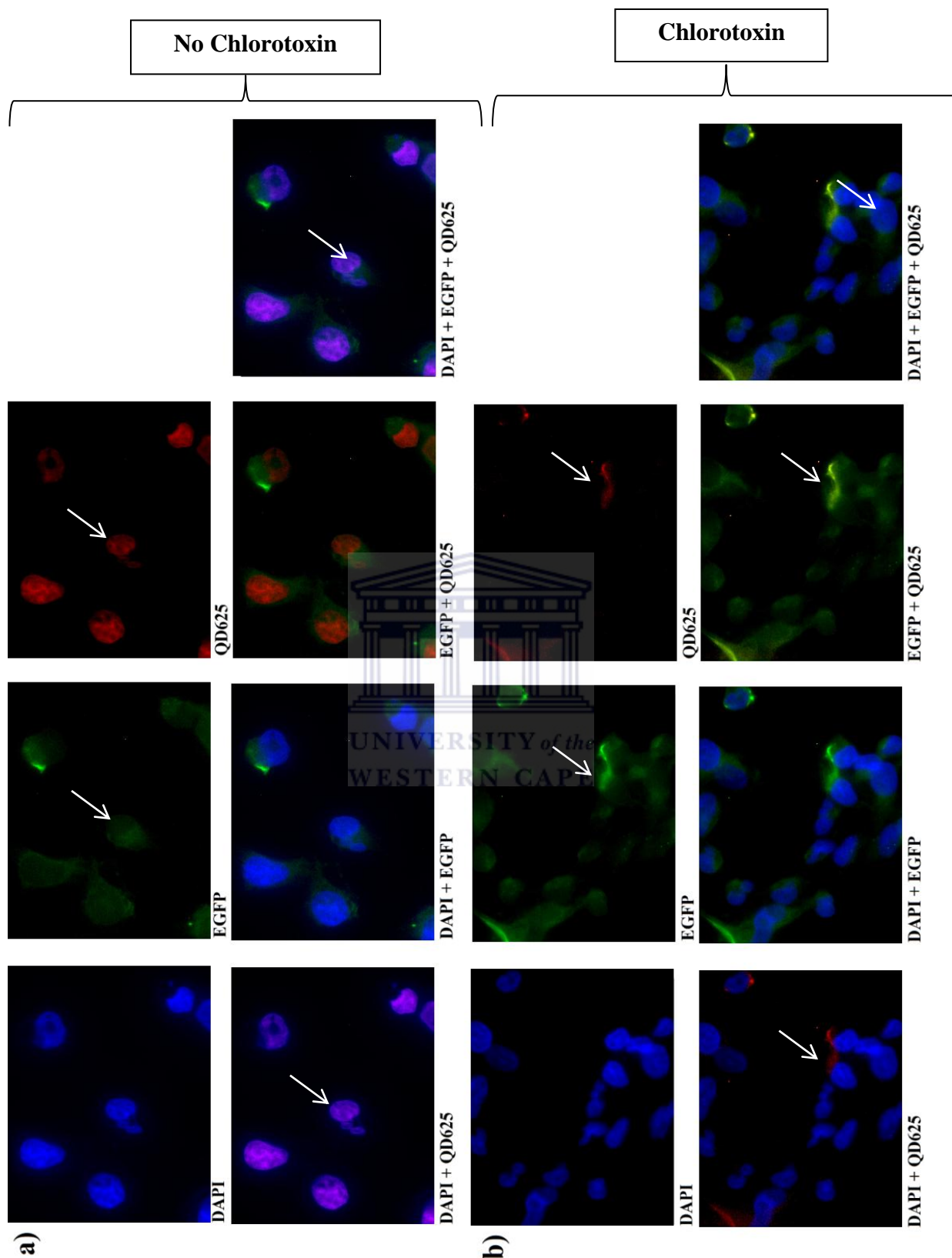
Figure 3.12: Wide field fluorescence microscopy of co-localization of CTX conjugated quantum dots with tMMP2-EGFP expressing A2780cis cells. The quantum dots without CTX can be seen in (a) and CTX conjugated quantum dots can be seen in (b). DAPI – Nuclear stain; EGFP – MMP2 tagged Enhanced Green Fluorescent Protein tagged with; QD_{625} – Quantum dots (peak emission 625nm). Micrographs were obtained at x100 magnification.
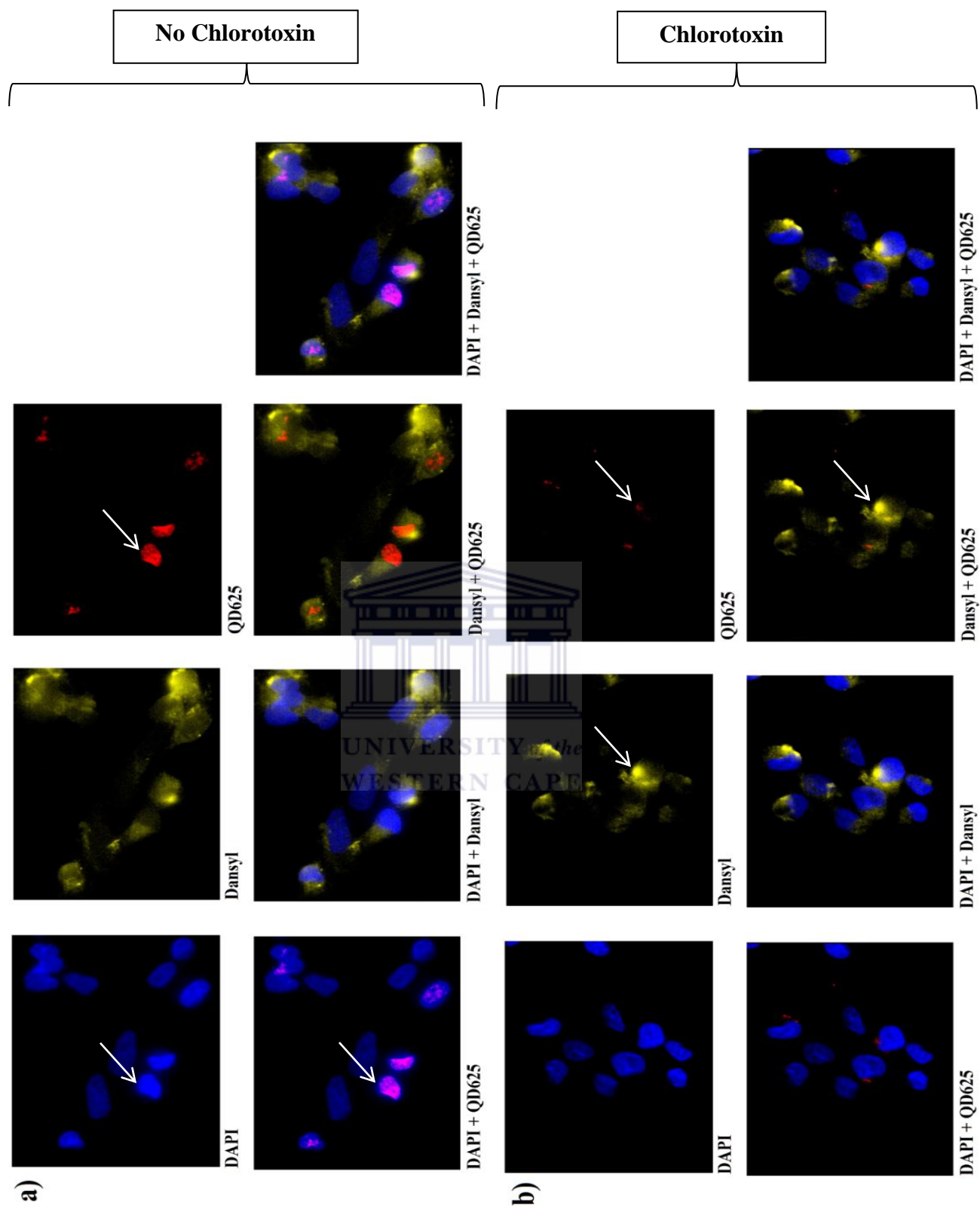
Figure 3.13: Wide field fluorescence microscopy of co-localization of CTX conjugated quantum dots with dansylated anti-MMP2 in A2780cis cells. The quantum dots without CTX can be seen in (a) and CTX conjugated quantum dots can be seen in (b). DAPI – Nuclear stain; Dansyl – Dansylated polyclonal anti-MMP2 antibody; QD$_{625}$ – Quantum dots (peak emission 625nm). Micrographs were obtained at x100 magnification.

Dansyl chloride labelling of antibodies (Section 2.5.2.4) was used due to instrumental limitations where there was significant spectral overlap for available wide-field fluorescence microscopy emission filters (blue, green, red) as well as commercially available fluorophores. Dansyl chloride fluorescence emission occurs at the same spectral window as EGFP and was arbitrarily depicted as yellow to avoid confusion in the micrographs. Typical organic fluorophores with fluorescence emission below 625nm would be quenched by QD_{625} (Section 1.6.3.2, Figure 1.18). Co-localization studies suggested that the CTX-MMP2 interaction took place and was independent of the truncated hemopexin domain of tMMP2-EGFP for the transfected A2780cis cells, where CTX labelled QD_{625} co-localized to the cell membrane with tMMP2-EGFP. The CTX-MMP2 interaction gained further support with the co-localization of dansylated anti-MMP2 with CTX conjugated QD_{625} at a cellular membrane locus in untransfected A2780cis cells. The QD_{625} which were unconjugated with CTX appeared to have a peri-nuclear localization which was attributed to the PEI polymer surface coating which has well known transfection and penetrative capabilities *in vitro* [280-283].

3.3.3.3 Discussion

The reported interaction of CTX with Annexin A2 called the interaction of CTX with MMP2 into question, but this study provided evidence that MMP2 was a viable molecular target for CTX [132]. The enzyme kinetic data of the interaction of CTX-S2 with recombinant full length MMP2 (Merck) provided no evidence for the CTX-MMP2 interaction. Further, recombinant pro-MMP2 was activated with APMA which cleaved the pro-peptide of the zymogen for mature MMP2 activation which ruled out the CTX-MMP2 kinetic interaction occurred with the pro-peptide. The hemopexin domain of mature MMP2 has been implicated in substrate/inhibitor binding and specificity [315] where tMMP2-EGFP was utilized for wide field fluorescence co-localization studies (Section 3.3.3.2). A fluorescence emission co-localization for red QD_{625} (CTX conjugated) and green tMMP2-EGFP was observed which showed CTX-S2 interacting with MMP2. The interaction of CTX and MMP2 for this study was not dependent on the truncated region of the hemopexin domain of MMP2, which excludes amino acid residue 600-660 from interaction with CTX. A process of elimination ruled out the pro-peptide, catalytic site as well as the latter 61 amino acid residues of the hemopexin domain of MMP2. The truncation of MMP2 in the fusion construct tMMP2-EGFP was a "happy accident" as it provided an essential piece of information which full length MMP2 would not have provided.

MMP2 is expressed in epithelial cells during tissue remodelling, especially for the case of aggressive metastatic cancers (Section 1.3.1, Table 1.1). The interaction of CTX with MMP2 could be used as a diagnostic tool (Section 1.4.2) and as well as a targeting moiety to deliver therapeutic payloads *in vivo* (Section 1.4.2). It was also demonstrated that CTX was directionally attached to gold nanoparticles (Section 3.1.4) which demonstrated the potential application of using the targeted nanoparticles as drug delivery vehicles (Section 1.5, Table 1.2). Undirected carbodiimide bioconjugation of CTX to fluorescent quantum dots (QD_{625}) was demonstrated as a sensitive diagnostic tool with 10pM QD_{625} conjugated with CTX showing detectable fluorescent *in vitro* labelling. The QD_{625} surface chemistry, PEI, is similar to the gold nanoparticles synthesized and discussed in Chapter 4 which will was utilized in Chapter 5 as drug delivery vehicles. The diagnostic cancer specific targeting modality of CTX for nanoparticles has been demonstrated. The drug delivery modality will be discussed in Chapter 5. Chapter 4 will discuss the synthesis of the gold nanoparticles as well as the chemistries used in this chapter.

Chapter 4: Synthesis, Characterization and Bioconjugation of Gold Nanoparticles and Quantum Dots

4.1 Introduction

Various synthetic routes exist for the synthesis of gold nanoparticles and quantum dots as well as tailoring of their respective surface functionalization (Sections 1.6.2 and 1.6.3). Gold nanoparticles (AuNPs) were synthesized in an adapted one-pot synthesis for theranostic applications. Different AuNP synthesis conditions were evaluated such as the addition tempo of the reducing agent as well as the ratio of the reducing agent to gold ions in solution and different passivation ligands (Section 4.3). The AuNPs were evaluated for physical and chemical stability in solution and the most stable AuNPs were evaluated for cellular penetrative ability (Section 5.2.3.6) and drug delivery applications (Sections 5.2.3.2-5.2.3.5) after drug loading and drug release studies (Section 4.4). Further applications of the AuNPs were to allow for the attachment of hexa-histidine (6xHis) tagged recombinant proteins through nickel (Ni^{2+}) affinity chromatography (Section 3.1.4). The ligands utilized for passivation of the AuNPs were commercially purchased and chemically altered to include required functional groups or freshly synthesized. The locally proprietary produced indium phosphide quantum dots (QDs) were functionalized with a similar surface functionality as the AuNPs (Section 4.5). This was done to determine if nanoparticle cellular localization was dependent on the nanoparticle composition or surface chemistry. A recombinant peptide was also evaluated as a potential cancer targeting vector with the use of the QDs (Chapter 3). Ligands synthesis and modification was done by utilizing basic chemistries (Section 4.2).

All syntheses and chemical modification reactions were carried out at ambient atmosphere. This was done to evaluate the reproducibility, labour intensity, difficulty of learning and cost effectiveness for applications in a developing country. Specialized laboratory equipment is not always readily available due to economic as well as logistic factors and it was necessary to determine whether the synthesis of gold nanoparticles as well as the ligands was possible with basic laboratory equipment to yield sufficiently pure products. The synthesis conditions were optimized to be as minimalistic as possible and still yield sufficiently pure drug delivery nanoparticles. Purity of the gold nanoparticles were assessed with energy-dispersive X-ray spectroscopy (EDX). Cost-effective and reproducible synthesis conditions would enable large-scale synthesis if so desired.

4.2 Ligand Synthesis and Characterization

4.2.1 Introduction

The chemical modified high molecular weight hyper branched polyethyleneimine (PEI-SH, 15kDa) was used in the one-pot synthesis of AuNPs as well as modification of quantum dot surfaces by ligand exchange. The synthesis of SH-NTA enabled the surface modification of PEI-SH functionalized AuNPs for the attachment of recombinant proteins on the nanoparticle surface (Section 3.1.4). Techniques used for characterization of the ligands were nuclear magnetic resonance (NMR, Section 2.2.1.2), electron spray ionization mass spectrometry (ESI-MS, Section 2.2.1.8) and attenuated total reflectance infrared spectroscopy (ATR, Section 2.2.1.3).

4.2.2 Synthesis of 6-*N*-2-(*N*-bis(carboxymethyl))-hexanoic acid (NH$_2$-NTA)

6-*N*-2-(*N*-bis(carboxymethyl))-hexanoic acid (Scheme 1, compound 3) was synthesized as described in Section 2.2.2.1 from N^6-Cbz-L-Lysine (Scheme 1, compound 1). The reaction can be seen in Scheme 1. The molecular formula is $C_{10}H_{18}N_2O_6$. The exact mass was predicted to be 262.12g.mol^{-1}. The product is white flocculate with a yield of 2.15g (65%). Characterization of 6-*N*-2-(*N*-bis(carboxymethyl))-hexanoic acid (NH$_2$-NTA) gave the following:

^{1}H-NMR (D$_2$O):δ 1.07 (m, C-4), 1.56 (m, C-3), 3.38 (m, C-2, C-5, CH$_2$), 3.54 (q, *J* = 14.1Hz, C-6), 7.31 (s, NH$_3^+$, 3H), 8.34 (s, OH, 3H)

MS (ESI): (M^{+1}) 263.13

ATR (ZnSe): $\upsilon_{(N-H)}$ 825.4 (sh), $\upsilon_{(C=O)}$ 1600.7 (s), $\upsilon_{(C=OH)}$ 1627.7 (sh), $\upsilon_{(C-H)}$ 2821.4 (w), $\upsilon_{(O-H)}$ 2890.8 (w), $\upsilon_{(O-H)}$ 2937.1 (w).

Proton resonances were not observed for all peaks due to spectral resonance overlap as observed for C-2/C-5. Mass spectrometry however showed an M^{+1} peak of 263.13Da gave a determined mass of 262.12g.mol^{-1} which confirmed the molecule was present.
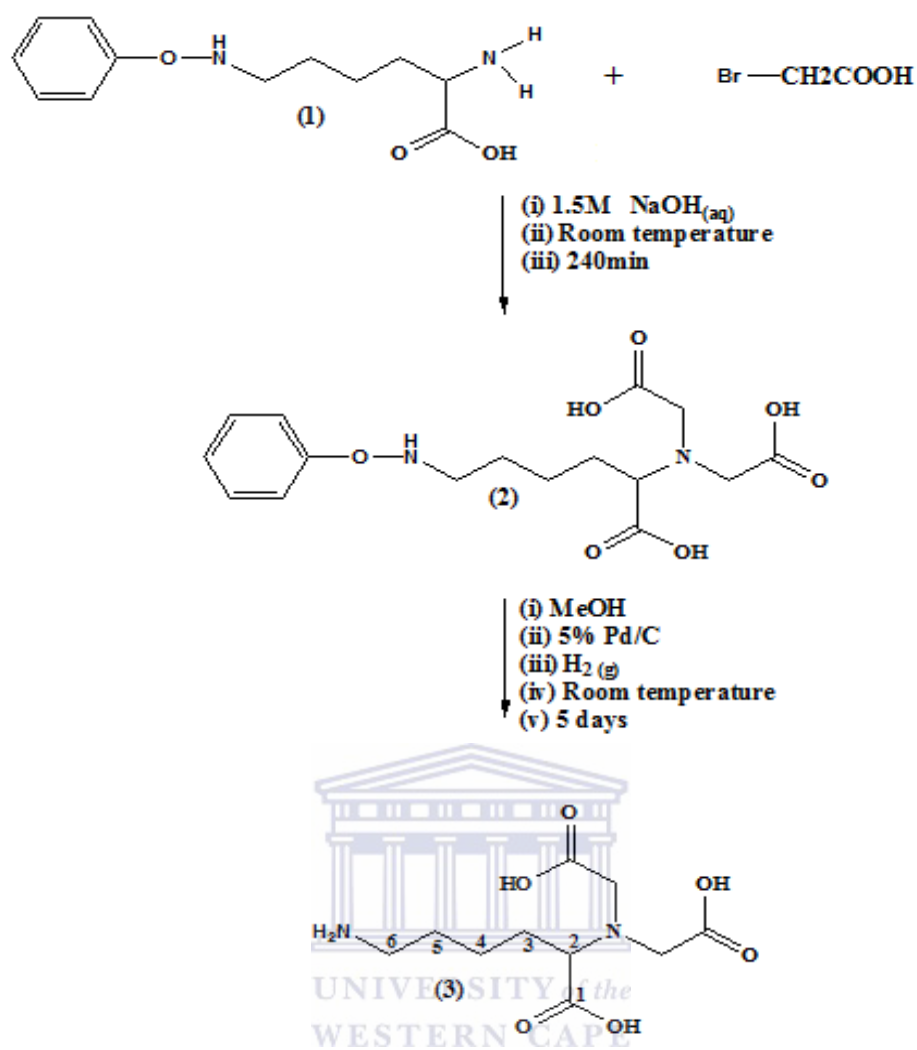
Scheme 1: The synthesis of 6-*N*-2-(*N*-bis(carboxymethyl))-hexanoic acid (NH₂-NTA)
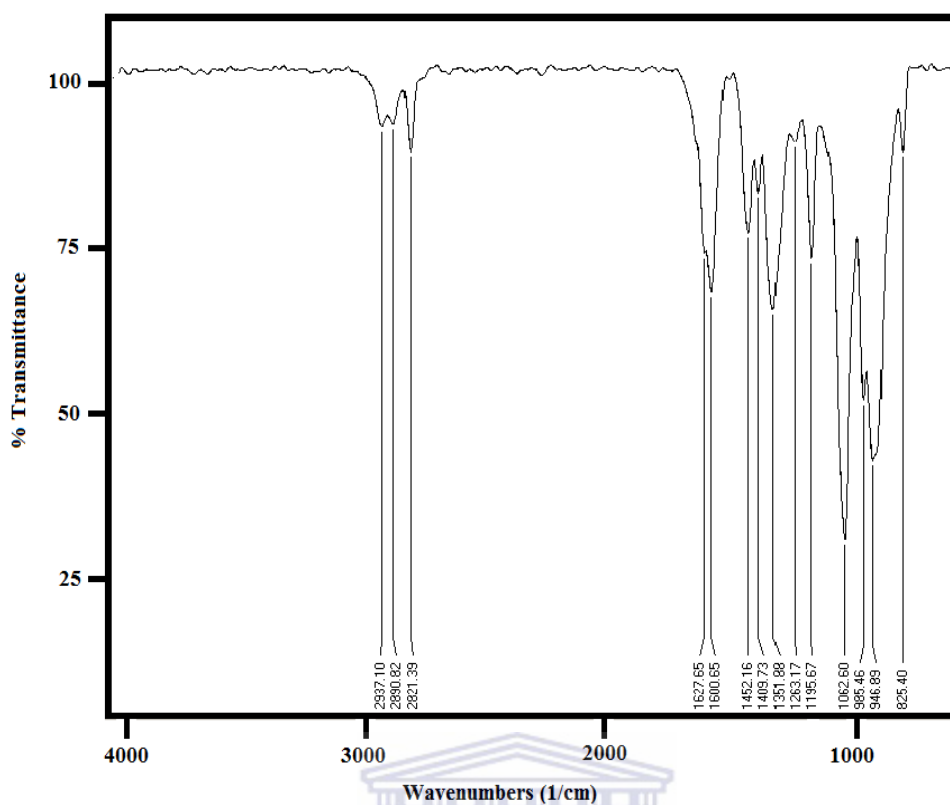
Figure 4.1: ATR infrared spectrum of 6-*N*-2-(*N*-bis(carboxymethyl))-hexanoic acid (NH₂-NTA)
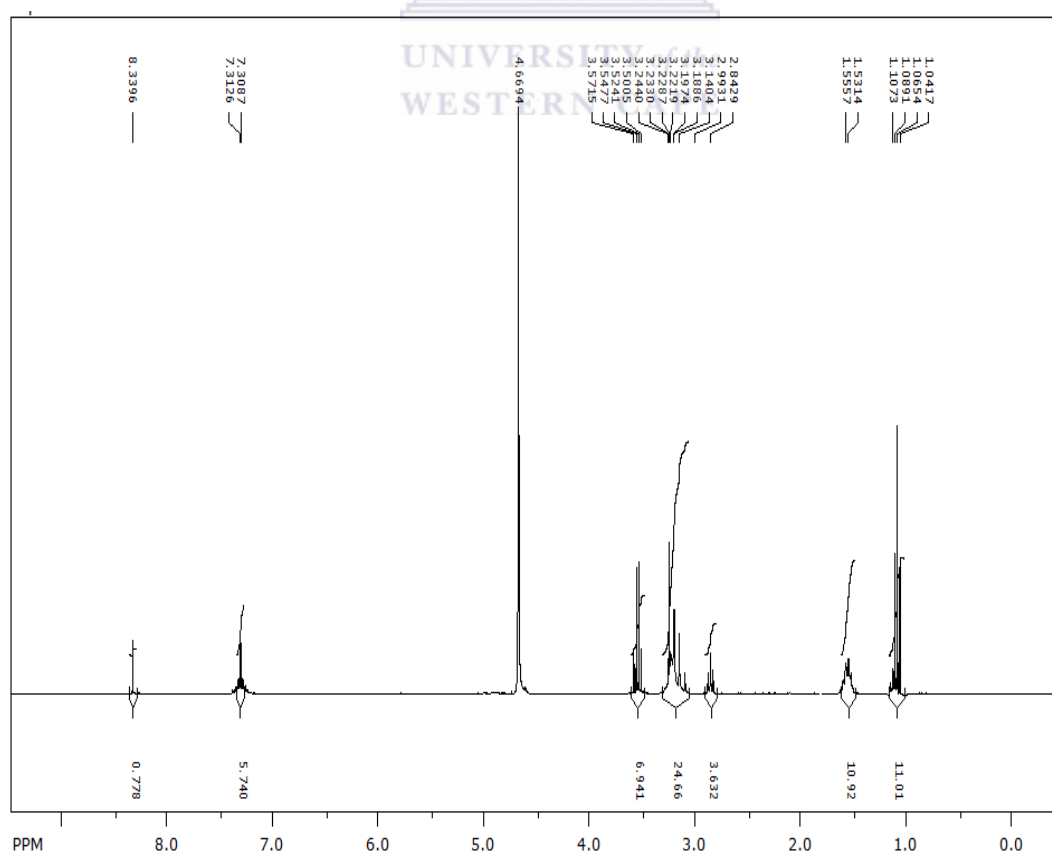
Figure 4.2: ¹H-NMR spectrum of 6-*N*-2-(*N*-bis(carboxymethyl))-hexanoic acid (NH₂-NTA)

4.2.3 Synthesis of 6-*N*-Thiobutyro-2-(*N*-bis(carboxymethyl))-hexanoic acid (SH-NTA)
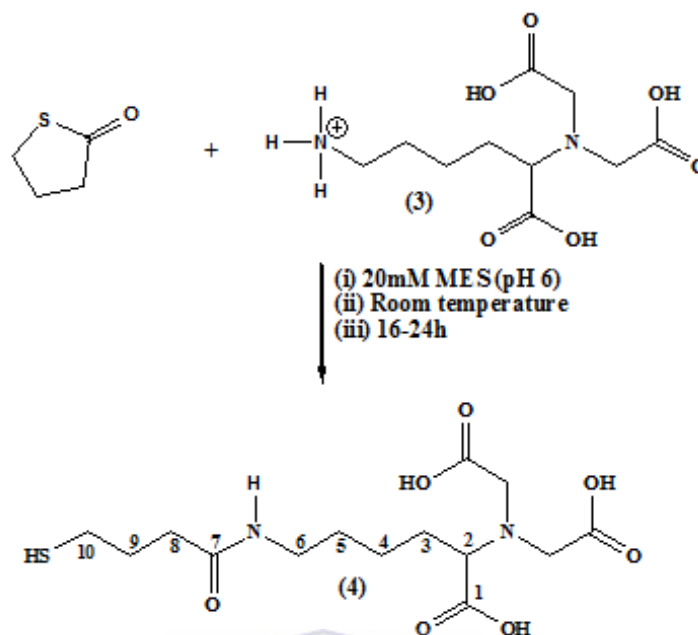
Scheme 2: Synthesis of 6-*N*-Thiobutyro-2-(*N*-bis(carboxymethyl))-hexanoic acid (SH-NTA)

Compound 4 was synthesized as described in Section 2.2.2.2. The product was a fine yellow powder of 1.23g (85%) yield. The molecular formula was $C_{14}H_{24}N_2O_7S$ with a predicted exact mass of 364.13g.mol^{-1}. The characterizations gave the following results:

^{1}H-NMR (D$_2$O):δ 1.11 (m, C-4), 1.43 (m, C-2 / C-5 / SH / CH$_2$), 1.68 (m, C-3), 1.84 (m, C-9), 2.20 (m, C-8), 2.64 (t, J = 7.5Hz , C-2), 3.01 (m, C-6), 3.05 (m, C-10 / NH), 8.34 (s, OH, 3H)

MS (ESI): (M^{+1}) 365.14

ATR (ZnSe): $\upsilon_{(C=O)}$ 1579.4 (s), $\upsilon_{(C=O)}$ 1662.4 (sh), $\upsilon_{(C-H)}$ 2856.1 (w), $\upsilon_{(O-H)}$ 2917.8 (w).

The presence of a thiol group was not indicated by H^1-NMR due to proton resonance overlap at 1.43ppm as well as at 3.01ppm. ATR also failed to indicate the presence of a thiol group due to instrumental limitation at 650cm^{-1} attributed to the ZnSe optical lens (Section 2.2.1.3). Ellman's reagent (Section 2.2.1.1) was used to confirm the presence of a thiol group. The molecular weight was determined to be 364.13g.mol^{-1} from the M^{+1} mass spectrometry peak.
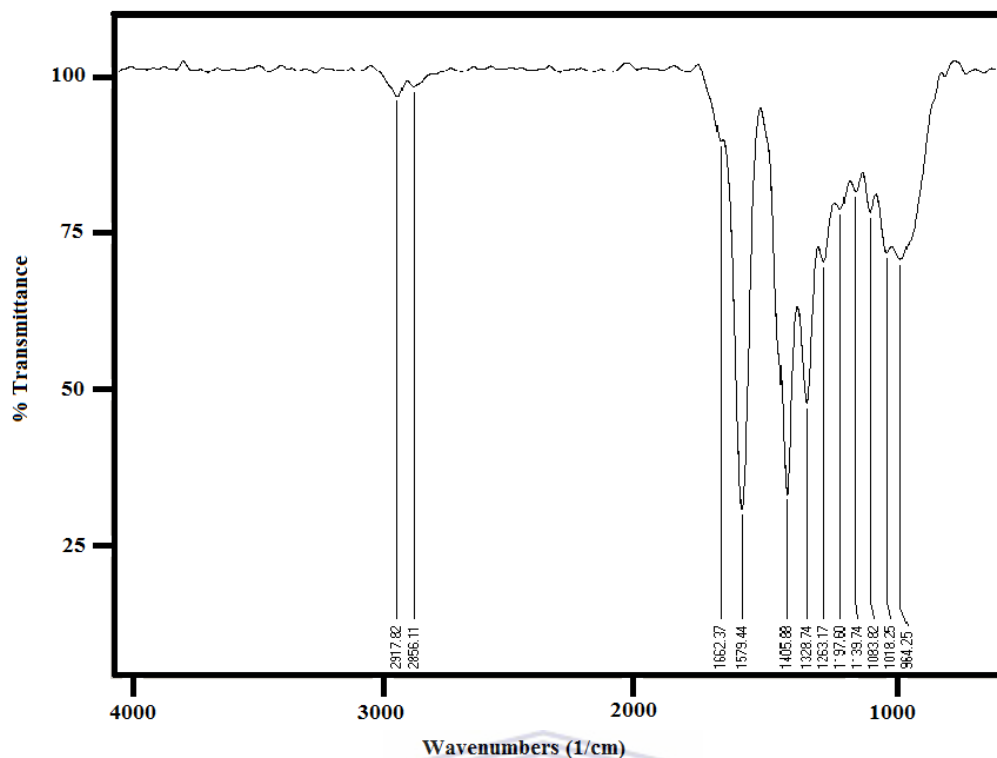
Figure 4.3: ATR Infrared spectrum of 6-*N*-Thiobutyro-2-(*N*-bis(carboxymethyl))-hexanoic acid (SH-NTA).
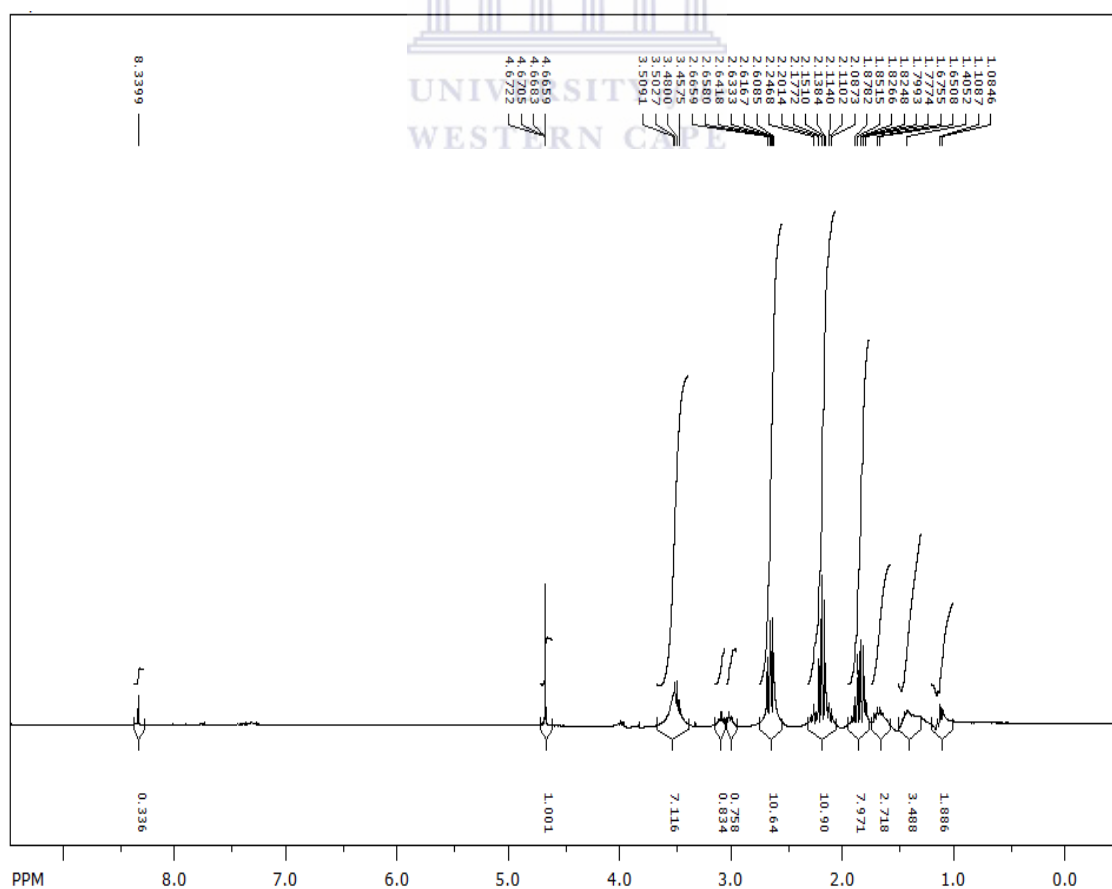
Figure 4.4: ^{1}H-NMR of 6-*N*-Thiobutyro-2-(*N*-bis(carboxymethyl))-hexanoic acid (SH-NTA).

4.2.4 Synthesis of *N*-Thiobutyro-polyethyleneimine (PEI-SH)

Commercial PEI (2kDa) was purchased from sigma and a thiol group was introduced on the PEI molecule at random to modify one primary amine (-NH$_2$) as described in Section 2.2.2.3 and shown in Scheme 3 to create compound 6. The ATR infrared spectrum of PEI and PEI-SH can be seen in Figure 4.6. A characteristic C-S stretch (green circle, Figure 4.6) appeared in the infrared spectrum of PEI-SH (red, Figure 4.6) and which is absent from PEI (black, Figure 4.6). An S-H stretch was not observed due to instrumental limitations of the ZnSe crystal having maxima of absorption at 650cm^{-1}. Confirmation of the presence of a thiol group was done by utilizing Ellman's reagent (Section 2.2.1.1). A 10mM of PEI solution contained 9.81±0.03mM thiol groups, which indicated for 1mol of PEI there is ~0.98mol thiol (SH). The value is representative of three different PEI-SH preparations. The estimation made in an earlier paragraph can now be modified to the following: For each mole of PEI-SH there will be on average 1mol thiol, 149mol primary amines, 90mol secondary amines and 120mol tertiary amines.
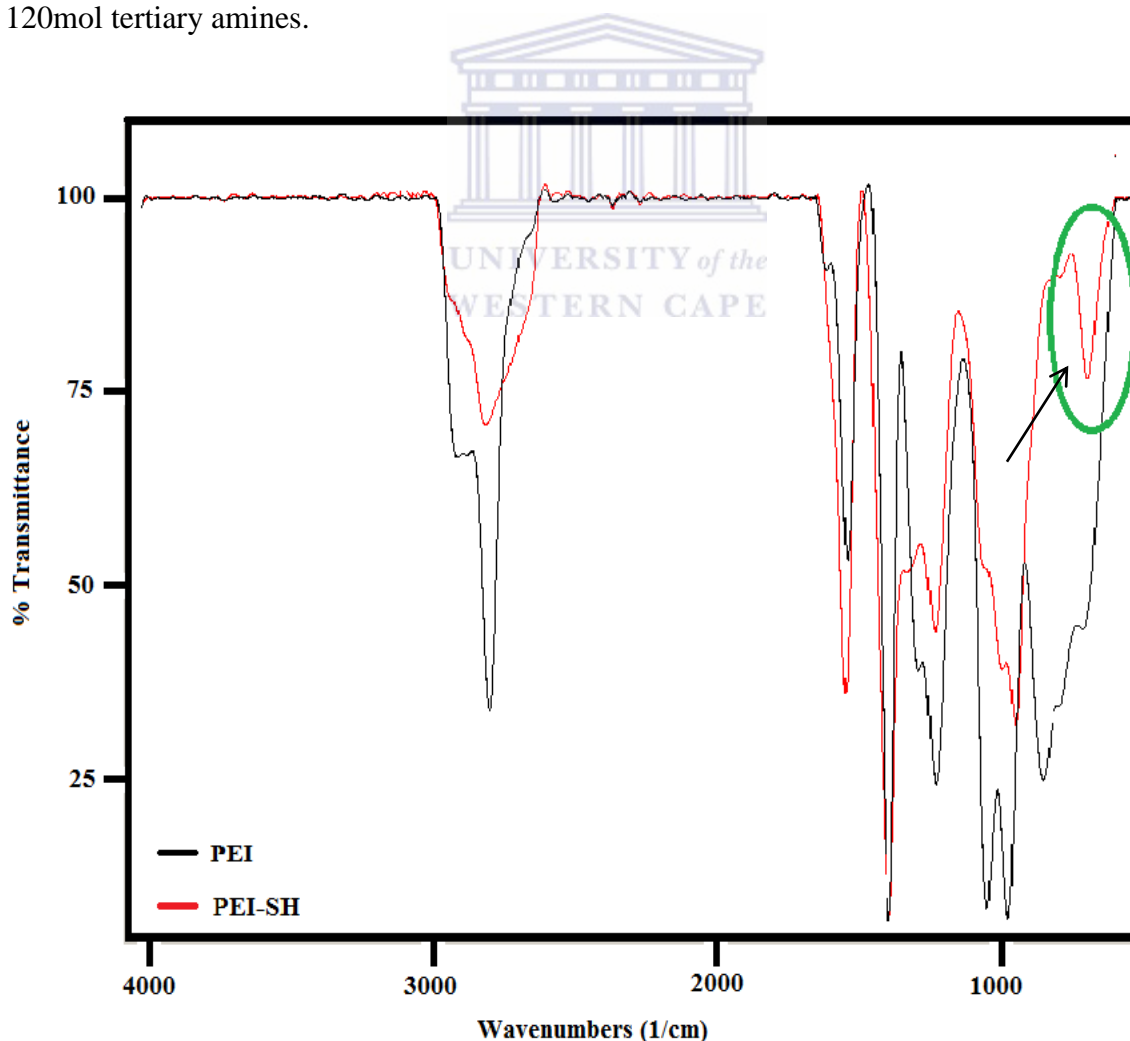
Figure 4.6: The superimposed ATR infrared spectra of PEI (black) and SH-PEI (red). A characteristic C-S stretch is highlighted with a green circle.
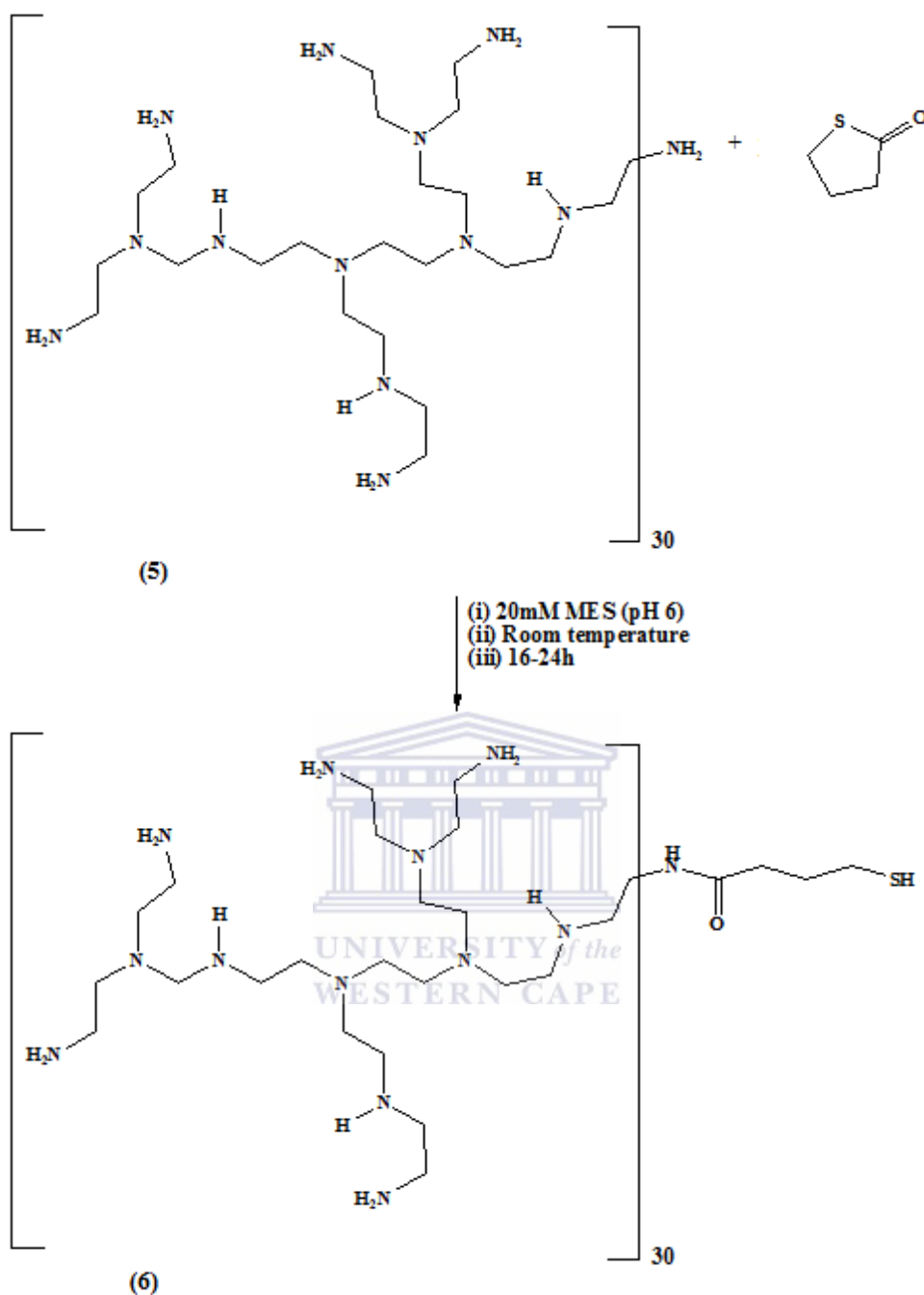
Scheme 3: The thiolation of high molecular weight hyper branched polyethyleneimine (5) to produce PEI-SH (6).

4.2.5 Discussion

The synthesis of the nitrilotriacetic acid derivatives, NH_2-NTA (Section 4.2.2) and SH-NTA (Section 4.2.3), gave good overall yields. The ^{1}H-NMR and ATR infrared data could not conclusively enable confirmation of the structures of the compounds. The ESI-MS gave perfect matches for the M^{+1} peak compared to the predicted mass of each compound. The synthesis of these two compounds was deemed successful. SH-NTA was used for the

modification of AuNP surfaces to facilitate the attachment of recombinant peptides with a 6xHis-tag for nickel affinity chromatography (Section 3.1.4).

The suggested mechanism of the synthesis of NH_2-NTA can be seen in Scheme 4. The nucleophilic attack of the lone pair of electrons on the primary amine on the carbocation of the 2-bromo acetic acid generated a nitrilotriacetic acid analogue. Nucleophilic substitution of the acetic acid groups onto the primary amine is a S_{N1} reaction. The reaction time was decreased with increased amounts of 2-bromo acetic acid and the reaction took place in a polar protic solvent (H_2O) at a slow rate (3h) [316]. The hydrogenation reaction took 5 days to complete under atmospheric conditions utilizing a palladium on carbon (5% Pd/C) catalyst. The mechanism for the synthesis of 6-*N*-Thiobutyro-2-(*N*-bis(carboxymethyl))-hexanoic acid (SH-NTA) from 6-*N*-2-(*N*-bis(carboxymethyl))-hexanoic acid (NH_2-NTA) can be seen in Scheme 5. The suggested mechanism of nucleophilic substitution is a S_{N1} mechanism as dictated by the polar protic solvent (H_2O) and a reaction tempo of 16-24h [316].
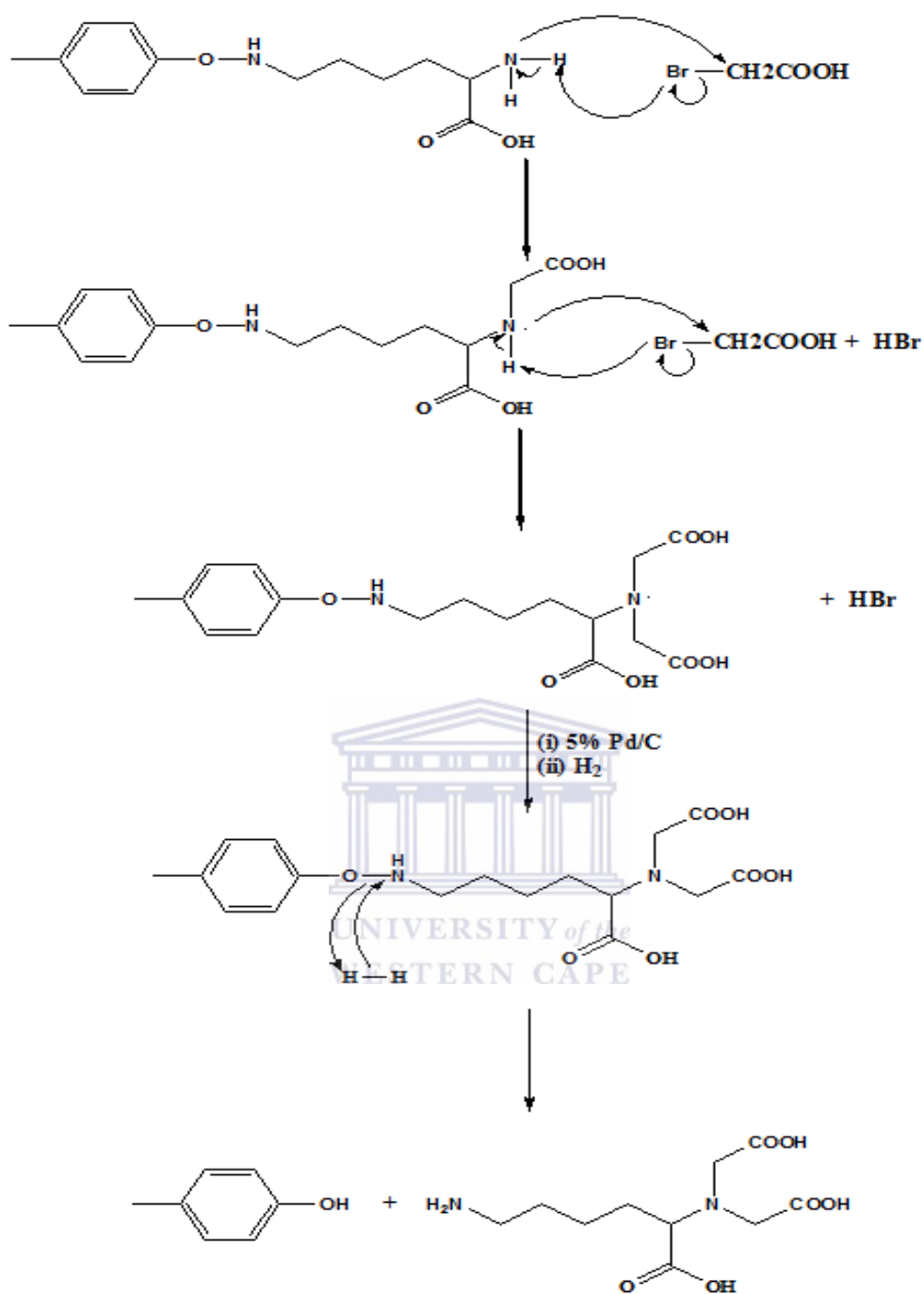
Scheme 4: The mechanism of the synthesis of 6-*N*-2-(*N*-bis(carboxymethyl))-hexanoic acid (NH$_2$-NTA).
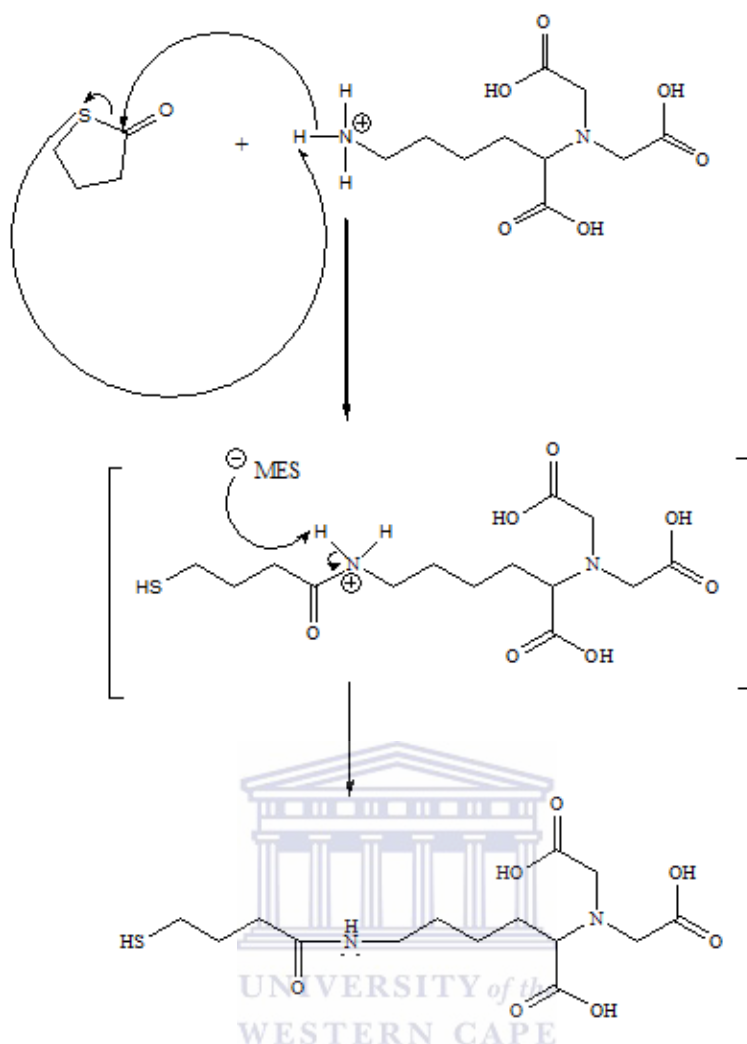
Scheme 5: The mechanism of the synthesis of 6-*N*-Thiobutyro-2-(*N*-bis(carboxymethyl))-hexanoic acid (SH-NTA).

The addition of a thiol group on the PEI to create PEI-SH was confirmed by Ellman's reagent as well as ATR. ESI-MS analysis could not confirm the presence of the addition of a thiobutyric acid molecule due to the low relative abundance of the thiobutyro group to the other constituents of the PEI molecule upon fragmentation. It was estimated for 1mol thiolated hyperbranched polymer PEI-SH had on average 1mol thiol, 149mol primary amines, 91mol secondary amines and 120mol tertiary amines. The relative intensities of the peaks in the mass spectra will suppress the presence of the thiobutyric acid group as well as from NMR analysis for detection of the SH-group. The mechanism for introducing the thiol group onto PEI is similar to the mechanism seen in Scheme 5. The PEI-SH will be used for the one-pot synthesis of PEI passivated AuNPs. Synthesis and chemical modification of the ligands was successful and was used for various applications in AuNP synthesis (4.3), quantum dot (QD) aqueous functionalization (4.5) as well as generate attachment points for peptides (3.1.4).

4.3 Gold Nanoparticle Synthesis and Physico-chemical Characterization

4.3.1 Introduction

The AuNP synthesis was an adaptation of a method published by Zheng *et al* in 2004 [287]. In their work they demonstrated the possibility of synthesizing one-pot water soluble AuNPs. The synthesis was standardised to produce AuNPs with a very narrow size distribution, typically 6-8nm in diameter, with a water soluble ligand passivated on the surface of the nanoparticle. These AuNPs could readily be applied for biological applications with minimal chemical modifications of the surface chemistry. In this synthesis they used reduced glutathione (GSH) and tiopronin as model ligands for their system. The synthesis was adapted to produce polydisperse AuNPs diameters with different surface passivation ligands. Larger AuNP diameters have larger surface areas for ligand passivation and subsequent higher drug loading capacity. Gold nanoparticle (AuNPs) intracellular distribution is dependent on the size as well as surface chemistry (Section 1.6.5). An AuNP preparation with a wide size distribution of nanoparticles would potentially act as drug delivery vehicles for doxorubicin distribution to multiple sites intracellular in a simultaneous manner and was investigated in Section 5.2.3. A drug, such as doxorubicin, which has multiple intracellular loci (nuclear, cytoplasmic and mitochondria) of biochemical interactions, would potentially have a more potent effect if it was delivered to all these interaction sites in a near simultaneous manner. In this adaptation of the Zheng *et al* synthesis reduced glutathione (GSH) was used as a comparative ligand for PEI-SH (Section 4.2.4) to test whether the size and charge of the ligand will have an effect on the AuNPs synthesis with regards to nanoparticle size and shape distribution. The high nitrogen content of PEI facilitated the investigation of charge dependent cellular localization (Section 5.2.3.6) and the primary amines ($-NH_2$) provided a high drug loading capacity (Section 4.4). The nanoparticles were also evaluated under various conditions for chemical stability in solution. The AuNPs which display the best overall stability was used for assays in Chapter 3 and Chapter 5. Techniques used for the characterization of the nanoparticles included ultraviolet-visible (UV-Vis, Section 2.2.1.6) spectrometry, high resolution transmission microscopy (HR-TEM, Section 2.2.1.4) and attenuated total reflectance infrared spectroscopy (ATR spectroscopy, Section 2.2.1.3).

4.3.2 Gold Nanoparticle Synthesis: The addition tempo of the reducing agent NaBH$_4$

The effect of the addition tempo of the reducing agent, NaBH$_4$, was investigated. The solution colour in the reaction vessel had a clear rich yellow colour which was attributed to presence of the gold ions (Au^{3+}) from the dissolved aurate salt. The synthesis was described in Section 2.2.3.1. Upon addition of the ligand the solution colour went from a clear rich yellow colour to a lighter hue of yellow within 20 minutes. Addition of the NaBH$_4$ (aq) made the solution change to a black and then a tea brown colour. The development of a deep wine red colour took place within 5 minutes. Purification of the AuNPs is described in Section 2.2.3.1. The AuNPs were unstable in de-ionised H$_2$O but showed stability in phospho buffered saline (PBS x1, pH 7.4). The AuNPs was freeze (Section 2.3.4) dried to a black-grey powder and readily resuspended as needed.

The solution colour for Slow A-C was variations of deep wine red. A red-brown solution colour was observed for Fast A-C. UV-Vis spectra were obtained as in Section 2.2.1.6. Fast addition of the reducing agent implies immediate addition of all of the NaBH$_4$, while slow addition of the reducing agent was drop-wise addition over 30 seconds. No change was observed for the surface plasmon resonance band (Figure 4.7, $\lambda_{SPR} = \lambda_{max} = 518nm$). Slow addition (Figure 4.7, Slow A-C) of the reducing agent delivered an overall increase in optical density for the AuNPs in comparison with the fast addition of the reducing agent (Figure 4.7, Fast A-C). UV-Vis spectroscopy indicated that the slow addition of the reducing agent yields differed significantly for different preparations (Figure 4.7, Table 4.1). Fast addition of the reducing agent showed no significant change in yields for different batch preparations (Figure 4.7, Table 4.1).

The average diameter per AuNP preparation was calculated as described in Section 1.6.2.2 as determined by Hais et al [218]. The diameters for Slow A-C were determined to be 4nm (Table 4.1). The Fast preparations each had a different average diameter (Table 4.1). Quantitative EDX analysis (Section 2.2.1.5) showed no significant differences in the elemental composition difference between the fast addition of the reducing agent (Table 4.1, Fast-A / Fast-B / Fast-C) and the slow addition of the reducing agent (Table 4.1, Slow-A / Slow-B / Slow-C). The average dry weight for the samples produced by slow addition of reducing agent was significantly higher than for the fast addition of the reducing agent. The average gold content (% mass) of the fast addition of the reducing agent was 52.55±2.10%

(60.78±4.81mg) per dry weight of sample and slow addition 43.79±7.88% (57.70±7.61mg) per dry weight of sample. This indicates no statistical significance in the amount of gold incorporated into the AuNPs for the different synthesis conditions. The other elements that contribute to the sample dry weight are carbon (C), nitrogen (N), oxygen (O), sodium (Na), phosphorus (P) and chlorine (Cl). These elements are attributed to the surface ligand as well as to the phospho-saline buffer (pH 7.4). The amount of gold in the aurate salt used per preparation was 92mg. The amount of gold utilized per AuNP preparation was calculated based on the dry weight % of Au (Table 4.1).
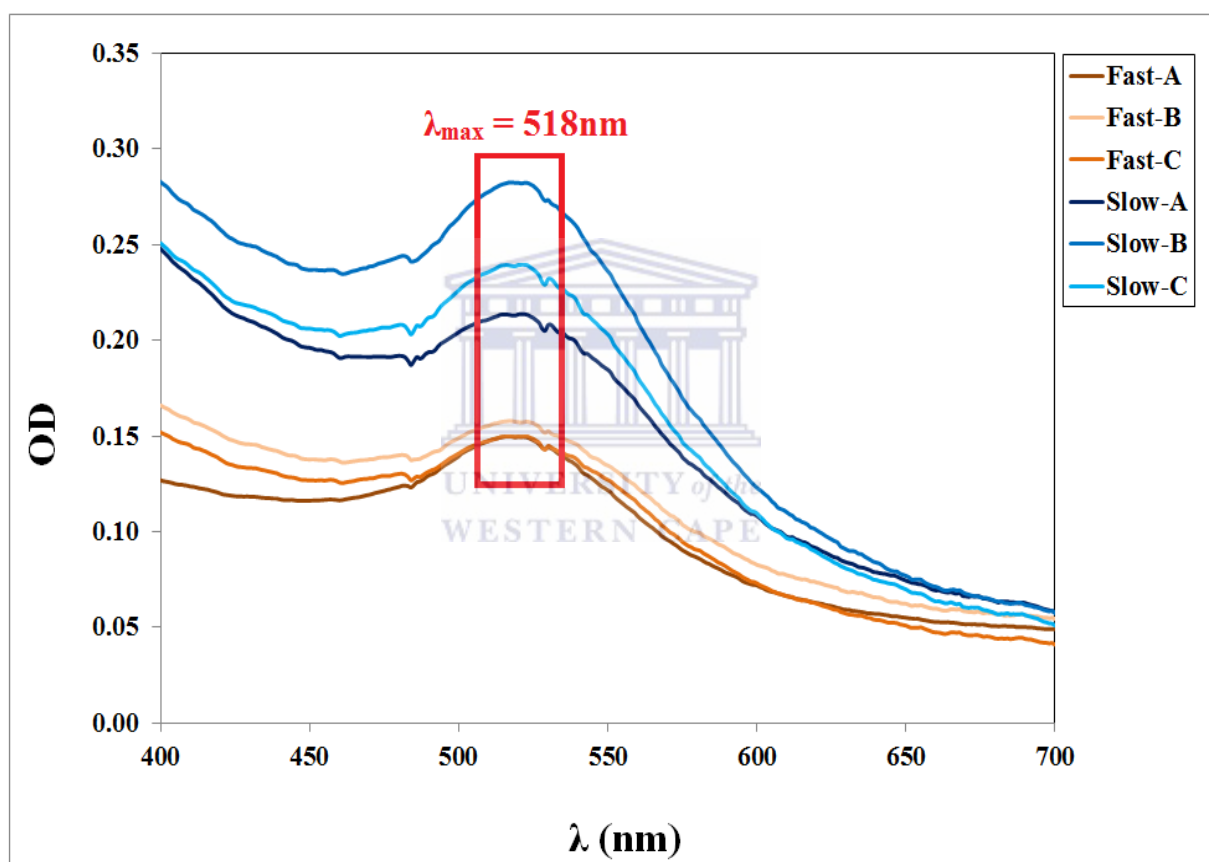
Figure 4.7: One-pot synthesized reduced glutathione (GSH) passivated AuNPs with variation in the tempo of NaBH$_4$ addition. The surface plasmon resonance (SPR) band (λ_{max} = λ_{SPR}) is highlighted in the red rectangle. Optical density (OD) is directly proportional to the concentration of AuNPs in solution. The synthesis was done in technical triplicates for each set of experimental conditions and repeated in duplicate on a different day. Table A2 (Appendix) provides p-values obtained where statistical significance was where p < 0.05.

Table 4.1: AuNP diameters, dry weight and energy dispersive X-ray spectroscopy (quantitative EDX, 2.2.1.5) elemental analysis of AuNPs Synthesized with Differential Addition Tempo of NaBH$_4$

Sample	A_{SPR}/A_{450}[†]	Diameter (nm)		Dry Weight (mg)	C	N	O	Na	P	Au	Cl
								Weight % (EDAX)			
Fast A	1.29	5		125	5.07	4.96	30.69	2.10	3.12	51.76	2.30
Fast B	1.15	4		113	4.01	2.63	26.78	2.13	6.89	55.07	2.48
Fast C	1.09	3		109	6.99	3.27	28.28	1.69	6.60	50.83	2.34
			Ave	115.67	5.36	3.62	28.58	1.97	5.54	52.55	2.37
			Std	8.33	1.51	1.20	1.97	0.25	2.10	2.23	0.09
Slow A	1.18	4		135	2.75	8.26	32.97	4.39	3.59	46.35	1.70
Slow B	1.19	4		123	2.80	4.69	26.41	4.44	6.93	50.07	4.66
Slow C	1.16	4		140	4.22	13.62	27.62	7.27	8.59	34.95	3.73
			Ave	132.67	3.26	8.86	29.00	5.37	6.37	43.79	3.36
			Std	8.74	0.83	4.49	3.49	1.65	2.55	7.88	1.52

*p-Values can be found in Table A3 in the Appendix. †Calculated according to Hais et al [218].

There was no statistical significant difference in the utilization of gold for the fast addition as well as slow addition of the reducing agent (Table 4.2). The average gold utilized for the fast addition of reducing agent was 60.78±4.81mg (66.06±5.23%) and for the slow addition of reducing agent was 57.70±7.61mg (62.71±8.27%).

Table 4.2: Aurate salt utilized during AuNP synthesis (based on quantitative EDX, 2.2.1.5)

Samples		Au^{3+} used (%)	Au^{3+} used (mg)	Au^{3+} unused (%)	Au^{3+} unused (mg)
Total Au^{3+} utilized in synthesis: 92mg / reaction					
Fast A		70.33	64.70	29.67	27.30
Fast B		67.64	62.33	32.36	29.77
Fast C		60.22	55.40	39.78	36.60
	Ave	66.06	60.78	33.94	31.22
	Std	5.23	4.81	5.23	4.81
Slow A		68.01	62.57	31.99	29.43
Slow B		66.94	61.59	33.06	30.41
Slow C		53.18	48.93	46.82	43.07
	Ave	62.71	57.70	37.29	34.30
	Std	8.27	7.61	8.27	7.61

*p-Values can be found in Table A4 in the Appendix. There was no statistical difference in the average amount of Au^{3+} used for synthesis of AuNPs.

AuNPs synthesized with fast addition of the reducing agent yielded amorphous AuNPs with varying sizes with observed aggregation of some of the AuNPs (Figure 4.8a). Numerous sub-1nm gold clusters were observed in the micrograph. The size distribution histogram showed a skewed bell-curve distribution with bias to the smaller AuNPs (Figure 4.8c). Contribution to the mean AuNP diameter was set at a 3.5% cut off contribution as well as a minimum contribution size of ≥ 1nm for the histogram. The mean diameter of the AuNPs was

calculated to be 5.32±2.98nm from 2352 nanoparticle counts with ImageJ (Section 2.2.1.4b), which indicates ~56% variation in size distribution thus classifying the AuNPs as polydisperse. The numerous sub 1nm gold clusters were confirmed to contain elemental gold by qualitative HR-TEM EDX line-scan analysis (Figure 4.8b, red) as described in Section 2.2.1.4a. The peaks observed for copper (Cu) and carbon (C) were attributed to the holey carbon copper grid. Slow drop wise addition of $NaBH_4$ yielded near spherical AuNPs without any sub 1nm gold clusters observable in the micrograph (Figure 4.9a). The AuNPs do not appear to show any aggregation and are well dispersed from each other. The AuNP size distribution histogram (Figure 4.9c) indicates the mean diameters of the particles were 12.35±4.33nm. This is a ~35% size distribution. The size distribution histogram shows a near perfect bell-curve distribution in AuNP size. Qualitative HR-TEM EDX line-scan (Section 2.2.1.4b) analysis (Figure 4.9b) confirmed the elemental composition of particles was gold.

UV-Vis based Beer-Lambert calculations for the determination of AuNP concentration in solution was not a feasible technique as discrepancies between the average diameters obtained from UV-Vis calculations (Table 4.1, Section 1.6.6.2) compared to the HR-TEM micrographs and size distribution histograms (Figure 4.8 and Figure 4.9). When the UV-Vis predicted diameter for Slow A-C of 4nm (Table 4.1) is compared to the size distribution histogram mean diameter of 12.35±4.33nm (Figure 4.9c) a distinct difference is observed. The Fast A-C preparations UV-Vis predicted diameter of 3-5nm (Table 4.1) diameter falls closer within the physical counted size distribution range of 5.32±2.98 nm (Figure 4.8c). Comparison of the mean diameters for the preparations predicts a redshift in the surface plasmon band for the Slow preparations but this was not observed. In Table 4.3 the optical density of the AuNPs at 450nm, the molar extinction coefficients and the corresponding AuNP concentrations for each AuNP preparation can be seen. The extinction coefficients are based on the mean diameter of the AuNPs. The concentration values (Table 4.3) for the Slow (A-C) preparations are lower than for the Fast (A-C) preparations, even though the optical density (OD) values are higher (Figure 4.7). This is however explained by taking the extinction coefficients into account. Comparison of the respective molar extinction coefficients (Table 4.3) indicate that Slow (A-C) has a higher molar extinction coefficient than for Fast (A-C). This corresponds to the size of the AuNPs where a larger diameter AuNP will have a larger extinction coefficient. As concentration is a measure of units per volume, it can be argued that less large diameter AuNPs are needed to have the same OD as for smaller diameter AuNPs.
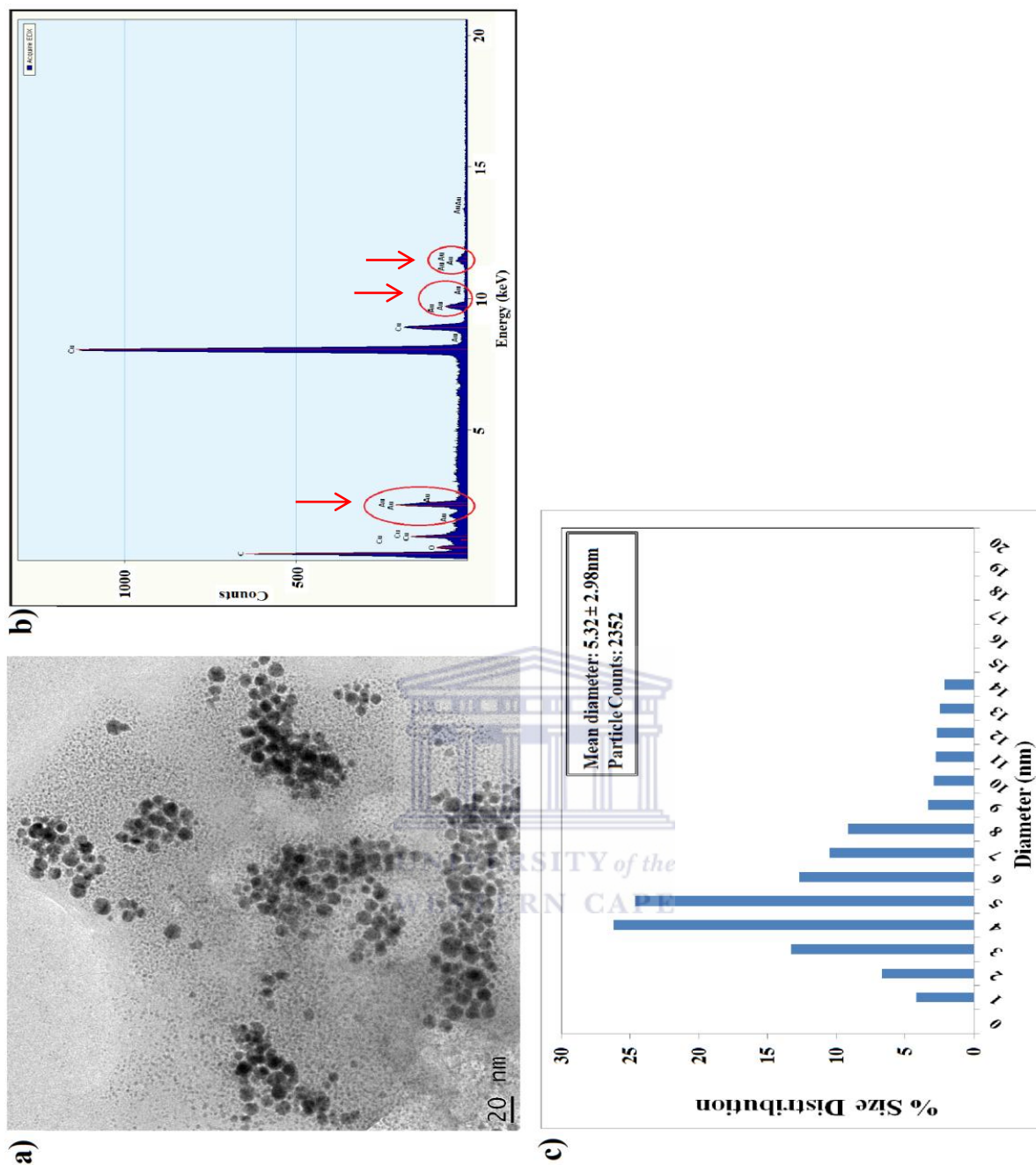
Figure 4.8: Gold nanoparticle characterization data for fast addition of NaBH$_4$ yields sub 1nm gold clusters as well as amorphous AuNPs with a poly-disperse size distribution. The HR-TEM micrograph can be seen in (a) with the corresponding EDX analysis in (b) with the gold peaks encircled in red. The size distribution histogram (c) shows a polydisperse size distribution (ImageJ). The data is representative for all AuNP preparations for this set of conditions.
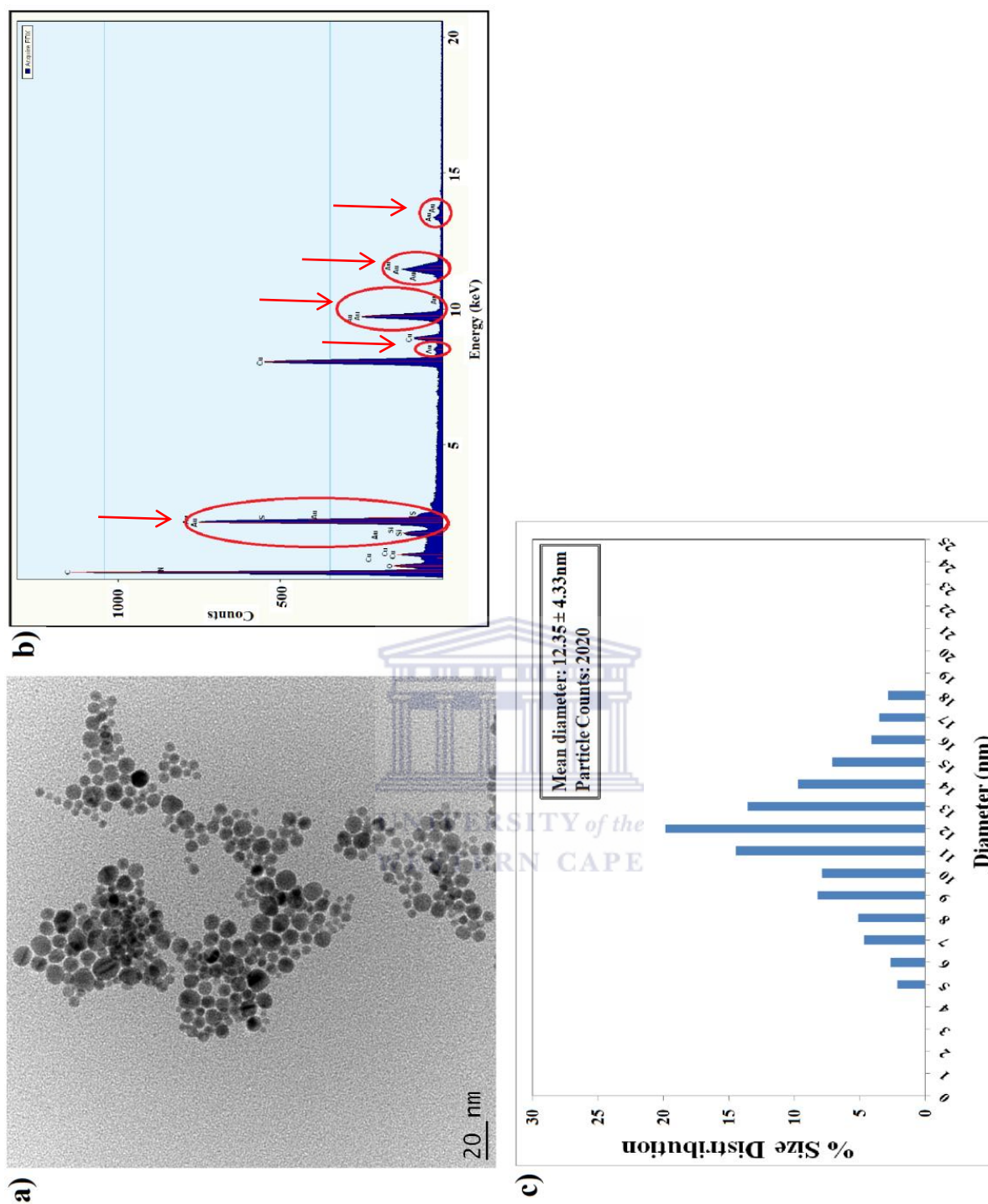
Figure 4.9: Gold nanoparticle characterization data for slow addition of NaBH₄ yields AuNPs with a polydisperse size distribution and no visible sub 1nm gold clusters. The HR-TEM micrograph can be seen in (a) with the corresponding EDX analysis in (b) with the gold peaks encircled in red. The size distribution histogram (c) shows a polydisperse size distribution (ImageJ). The data is representative for all AuNP preparations for this set of conditions.

Table 4.3: Concentrations for the prepared AuNPs based on the physical diameter counts from size distribution histograms (Figure 4.8c and Figure 4.9c).

Sample	Optical Density (450nm)	Average Diameter (nm)	$\varepsilon^\dagger$ $(Mol^{-1}.cm^{-1})$	[ ] (nM)
Slow A	0.127			0.91
Slow B	0.237	12.34 ± 4.33	1.39×10^8	1.71
Slow C	0.206			1.48
Fast A	0.116			16.11
Fast B	0.138	5.32 ± 2.98	7.20×10^6	19.17
Fast C	0.196			27.22

†Obtained from Hais et al [218] and calculated as in Section 1.6.2.2.

4.3.3 Gold nanoparticle synthesis: Different ligands with constant $NaBH_4:Au^{3+}$

The effect of the ligand on AuNP formation was investigated with slow addition of the reducing agent at a constant ratio $NaBH_4:Au^{3+}$ (Section 4.3.2). The ligands chosen were reduced glutathione (GSH) and thiolated polyethyleneimine (PEI-SH). The optimal ratio for GSH was determined to be 0.5:1 and for PEI-SH the ratio was 0.25:1 (Figure 4.10). For all ratios of PEI-SH:Au^{3+} above 0.25:1 the solution didn't change colour within 5h. Ratios of PEI-SH:Au^{3+} below 0.25:1 was not investigated. All GSH:Au^{3+} ratios below 0.5:1 had AuNPs aggregation within a short time frame (~10min) after addition of the reducing agent. GSH:Au^{3+} ratios above 0.5:1 made the reaction solution turn turbid yellow with no AuNP formation within 5h after addition of the reducing agent. An increase in optical density was observed for PEI-SH passivated AuNPs with a redshift in λ_{SPR} (Figure 4.10, $\lambda_{max} = 530nm$) than for GSH passivated AuNPs (Figure 4.10, $\lambda_{max} = 518nm$) under similar synthesis conditions.
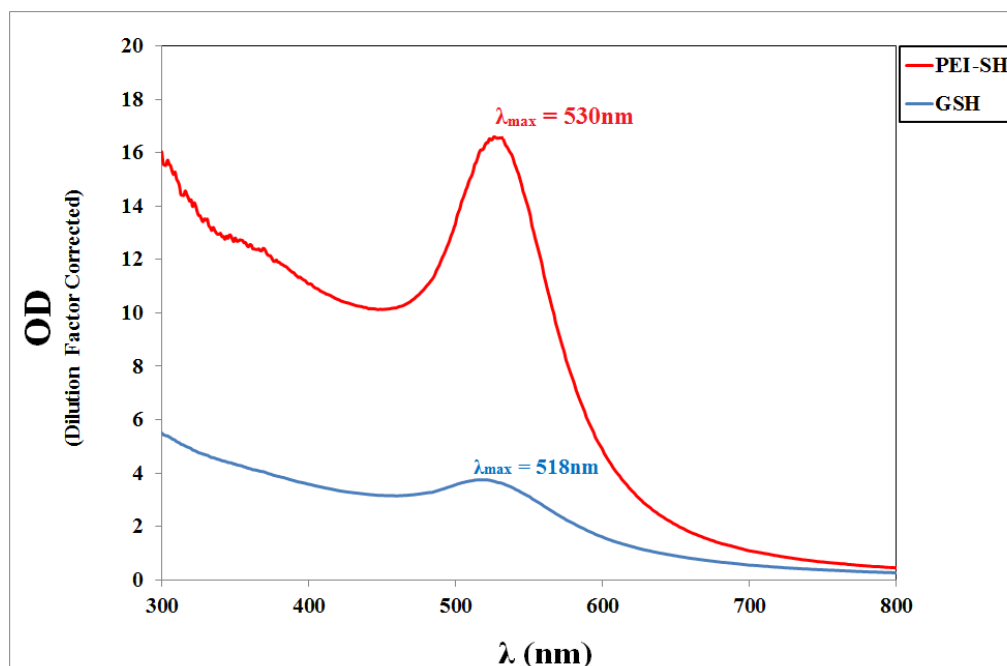
Figure 4.10: Comparative UV-Vis spectra of AuNPs synthesized with a constant NaBH$_4$:Au^{3+} (1:1) using GSH and PEI-SH. Identical synthesis conditions were used for both ligands. Optical density (OD) is directly proportional to AuNP concentration. The data is representative of technical triplicates and the synthesis was repeated on twice on different days.

4.3.4 Gold nanoparticle synthesis: Differential ratios of NaBH$_4$:Au^{3+} and constant ligand:Au^{3+} ratios

4.3.4.1 Synthesis and quantitative EDX analysis

AuNPs were synthesized (Section 2.2.4.1) with a constant ratio of ligand:Au^{3+} (AuNP-GSH and AuNP-PEI, Table 4.4) and varying ratios of NaBH$_4$:Au^{3+} (Table 4.4). The solution colour changes observed in Section 4.3.2 was also observed for AuNPs synthesized with differential amounts of NaBH$_4$ for a constant ratio of ligand:Au^{3+}. It should be noted that addition of PEI to the Au^{3+} solution, the solution colour changed from a rich yellow colour to a very light yellow, fainter than for the equivalent colour change observed for addition of GSH. This suggested PEI-SH reduced the gold cations in solution to a greater extent than GSH. The solution colour progressively turned a shade of red, dependent on the batch preparation conditions, within 5min post NaBH$_4$ addition for AuNP-GSH. A near immediate wine-red colour was observed for all AuNP-PEI preparations upon addition of NaBH$_4$. AuNP-GSH particles all displayed absorption onto the surfaces of containers made of polypropylene, borosilicate glass as well as silanol treated glassware. All attempts to recover the absorbed AuNPs were unsuccessful. Surface absorption of AuNP-PEI particles was not observed. All

AuNP preparations was readily lyophilized and resuspended for assays except AuNP-GSH A and AuNP-GSH B.

AuNP-PEI particles had a significant increase in overall dry weight when compared to AuNP-GSH as observed in Table 4.4. There was no statistical significant change in the dry weight of the different AuNP-PEI preparations except for AuNP-PEI A and AuNP-PEI D. AuNP-GSH preparations showed a statistical difference between AuNP-GSH B and AuNP-GSH D. There was a significant difference in the average dry weight of AuNP-PEI preparations compared to AuNP-GSH preparations. The AuNP-PEI particles elemental composition (Table 4.4) showed that carbon (C) contributed the most to the dry weight followed by gold (Au), chlorine (Cl) and nitrogen (N). The elemental composition of AuNP-GSH (Table 4.4) showed that gold (Au) contributed nearly half the dry weight percentage with oxygen (O) contributing ~20% per preparation. The oxygen content for both AuNP-PEI- and AuNP-GSH preparations are attributed to synthesis under atmospheric exposure, but the significant contribution of oxygen to the dry weight of the AuNP-PEI preparations can be partly attributed to the carboxylic groups of GSH which was used in the synthesis.

Table 4.4: Synthesis parameters for the preparation of AuNPs with a constant ligand:Au^{3+} and a varying $NaBH_4$:Au^{3+} as well as the corresponding quantitative EDX (Section 2.2.1.5) elemental analysis of differential AuNP preparations

Samples	$NaBH_4$: Au^{3+}	Ligand: Au^{3+}		Dry Weight (mg)	C	N	O	Na	P	Au	Cl
								Weight %			
AuNP-PEI A	0.25:1		Ave	329.33	29.74	4.29	6.08	9.64	6.84	21.21	21.87
			Std	12.99	6.16	2.64	4.16	2.37	5.77	3.58	7.74
AuNP-PEI B	0.50:1		Ave	319.33	35.43	11.94	10.57	5.28	5.76	18.97	12.05
		0.25:1	Std	21.20	4.43	1.18	1.62	0.95	1.63	1.55	0.31
AuNP-PEI C	0.75:1		Ave	287.33	37.51	11.56	9.25	1.92	3.15	17.91	10.23
			Std	24.50	3.95	1.94	1.78	0.81	1.89	4.52	5.30
AuNP-PEI D	1:1		Ave	286.67	44.20	12.15	11.12	4.29	5.64	11.72	10.90
			Std	10.41	1.16	0.30	0.49	0.95	0.23	1.34	0.92
AuNP-GSH A	0.25:1		Ave	100.33	4.05	4.86	25.94	12.50	5.50	27.60	19.12
			Std	12.10	1.78	0.77	6.92	0.71	0.47	2.56	5.23
AuNP-GSH B	0.50:1		Ave	114.00	4.36	3.94	30.48	2.80	5.78	49.56	3.09
		0.50:1	Std	8.89	1.16	1.04	0.21	1.50	1.53	0.86	1.55
AuNP-GSH C	0.75:1		Ave	100.00	3.23	3.16	28.18	2.12	9.26	48.48	5.57
			Std	16.09	0.59	0.91	3.30	0.08	6.65	4.13	2.05
AuNP-GSH D	1:1		Ave	93.67	3.26	6.55	21.86	5.47	5.54	49.83	7.49
			Std	6.43	0.43	8.60	3.61	7.39	1.34	8.67	7.02

*p-Values can be found in Table A3 in the Appendix. Statistical significance was for p < 0.05.

Table 4.5 summarizes the amount of gold from the aurate salt utilized for the differential synthesis of AuNPs, determined in a similar manner as for Table 4.1 and Table 4.2 based on the elemental composition of the dry weight. The AuNP-PEI D preparation utilized significant less gold for AuNP synthesis than the AuNP-PEI A-C preparations. AuNP-GSH A (Table 4.5) had significantly reduced utilization of gold when compared to preparation AuNP-GSH B-D. AuNP-PEI A-C and AuNP-GSH B-D did not differ statistically significant with gold utilization. When Table 4.4 and Table 4.5 are compared it becomes apparent that the contribution of gold to the dry weight of the AuNP-GSH preparations was higher than for the AuNP-PEI preparations. Further, the high carbon (C) contribution in dry weight for the AuNP-PEI preparations was attributed to the high molecular weight hyper-branched PEI (2kDa) which was significantly larger than GSH (307.32Da).

Table 4.5: Aurate salt utilized during the synthesis of gold nanoparticles based on EDX analysis from Table 4.3.

Total Au^{3+} utilized in synthesis: 92mg / reaction					
Samples		Au^{3+} used (%)	Au^{3+} used (mg)	Au^{3+} unused (%)	Au^{3+} unused (mg)
AuNP-PEI A	Ave	75.61	69.56	24.39	22.44
	Std	9.79	9.01	9.79	9.01
AuNP-PEI B	Ave	65.82	60.55	34.18	31.35
	Std	6.54	6.02	6.54	6.02
AuNP-PEI C	Ave	55.27	50.85	44.73	41.15
	Std	11.20	10.30	11.20	10.30
AuNP-PEI D	Ave	36.50	33.58	63.50	58.42
	Std	4.26	3.92	4.26	3.92
AuNP-GSH A	Ave	30.32	27.89	69.68	64.11
	Std	6.53	6.00	6.52	6.00
AuNP-GSH B	Ave	61.40	56.49	38.60	35.51
	Std	4.78	4.40	4.78	4.40
AuNP-GSH C	Ave	52.55	48.34	47.45	43.66
	Std	7.91	7.28	7.91	7.28
AuNP-GSH D	Ave	51.04	46.95	48.96	45.05
	Std	11.66	10.73	11.66	10.73

*p-Values can be found in Table A4 in the Appendix. Statistical significance was for $p < 0.05$.

4.3.4.2 Physicochemical Characterizations for Differentially Prepared AuNPs

The ATR infrared (Section 2.2.1.3) comparative spectra for the AuNP-PEI and AuNP-GSH preparations can be seen in Figure 4.11. AuNP-PEI (A-D) can be seen in Figure 4.11a and AuNP-GSH (A-D) can be seen in Figure 4.11b. Both AuNP preparations indicate the disappearance of a characteristic C-S stretch for PEI-SH (Figure 4.11a, blue) and GSH to AuNP-GSH (Figure 4.11b, blue). Peaks of the ligands that are found on the AuNP surface is highlighted in red. New peaks which appeared in the spectra for the AuNPs are highlighted in

green. A new peak was observed in the AuNP-PEI prepared AuNP spectra below $1000cm^{-1}$ (Figure 4.11a, green) which was attributed to the C-S peak observed for PEI-SH (Figure 4.11a, blue) shifting in the spectra due to proximity to the AuNP surface. The AuNP-PEI spectra corresponded very well with the spectra of PEI-SH (Figure 4.11a). Changes were observed for all the AuNP-GSH preparations compared to GSH (Figure 4.11b) as expected. The spectra for AuNP-GSH B indicated a distinctive difference from the other AuNP-GSH preparations with the appearance of additional peaks lower than $1000cm^{-1}$ (Figure 4.11b, AuNP-GSH B). However, the AuNP-GSH spectra did not correspond well with the GSH spectra. The altered spectra were attributed to the proximity of the GSH, which is a small ligand, to the AuNP surface which influenced the vibrational states of the small ligand [318, 319].

Figure 4.12 showed the comparative UV-Vis spectra (Section 2.2.1.6) of the differentially prepared AuNP-PEI (Figure 4.12a) and AuNP-GSH (Figure 4.12c) nanoparticles. The optical density was greatly increased of AuNP-PEI nanoparticles compared to the optical density for AuNP-GSH particles, being at least twice the value for AuNP-PEI as for AuNP-GSH. The proposed structures of the AuNPs can be seen for AuNP-PEI (Figure 4.12b) with the high molecular weight hyper-branched polymer on the surface and AuNP-GSH (Figure 4.12d) with the small zwitter ionic tri-peptide (GSH) on the surface. The structures were not drawn to scale. AuNP-PEI B (Figure 4.12a, red) showed a lower optical density at an equal dilution than the other AuNP-PEI preparations. AuNP-PEI A (Figure 4.12a, blue), AuNP-PEI B (Figure 4.12a, red) and AuNP-PEI D (Figure 4.12a, purple) had $\lambda_{max} = 530nm$ and AuNP-PEI C (Figure 4.12a, green) had $\lambda_{max} = 521nm$. There was no clear correlation between the surface plasmon resonance band ($\lambda_{SPR} = \lambda_{max}$) shift and the ratio of reducing agent used for synthesis of AuNP-PEI. AuNP-GSH A (Figure 4.12c, blue) AuNP-GSH B (Figure 4.12c, red) both displayed colloidal instability in solution within 30 minutes of re-suspension into solution. AuNP-GSH A/B had a $\lambda_{max} = 518nm$ and AuNP-GSH C/D had a $\lambda_{max} = 516nm$, indicating a blueshift in the electromagnetic spectrum which appears to be correlated with increased amounts of reducing agent. An increase in optical density was also directly correlated to increased ratios of $NaBH_4$ for AuNP-GSH (Figure 4.12c). When Table 4.5 is compared to the UV-Vis spectra (Figure 4.12) there appears to be a discrepancy between the optical density (OD) and the amount of gold utilized per AuNP preparation.
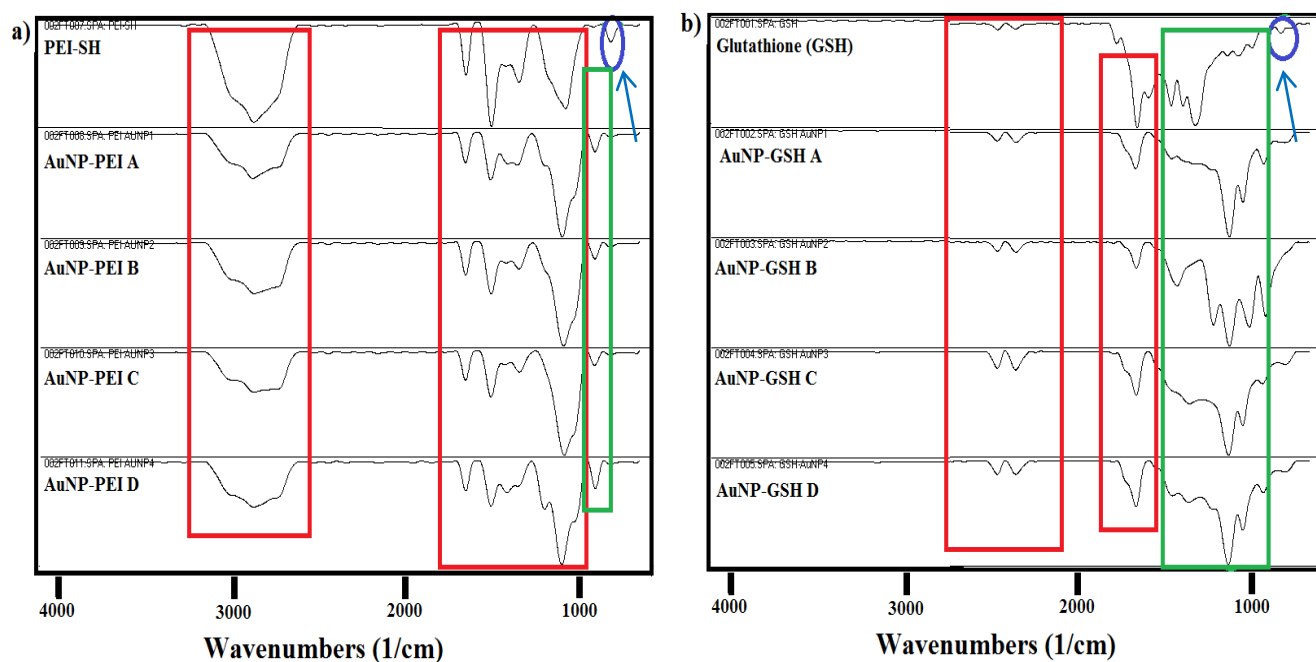
Figure 4.11: ATR infrared fingerprint spectra of AuNPs synthesized with PEI (a) and GSH (b) as capping agents. Peaks for AuNPs corresponding with ligand spectra are highlighted in red, novel peaks are highlighted in green. Fingerprint peaks are highlighted with red and peak variance is indicated in green.

Optical density of gold nanoparticles in solution is directly correlated to the amount of gold nanoparticles in solution as determined by the Beer-Lambert law. The same amount of aurate salt was used for AuNP synthesis for different ligands, GSH and PEI, as well as differential amounts of reducing agent used. It would then be expected that the optical density of AuNP-GSH and AuNP-PEI preparations would be similar in magnitude, however the optical density of the AuNP-PEI prepared nanoparticles was 2-3 fold more increased compared to AuNP-GSH. This suggested that the optical density, as well as the surface plasmon resonance (SPR) band maximum (λ_{SPR}) was being affected by the ligand on the surface of the AuNPs. PEI is an amine rich molecule (Scheme 3) where the lone pair of electrons on the nitrogen atoms could significantly affect the electronic properties of the SPR and alter it.
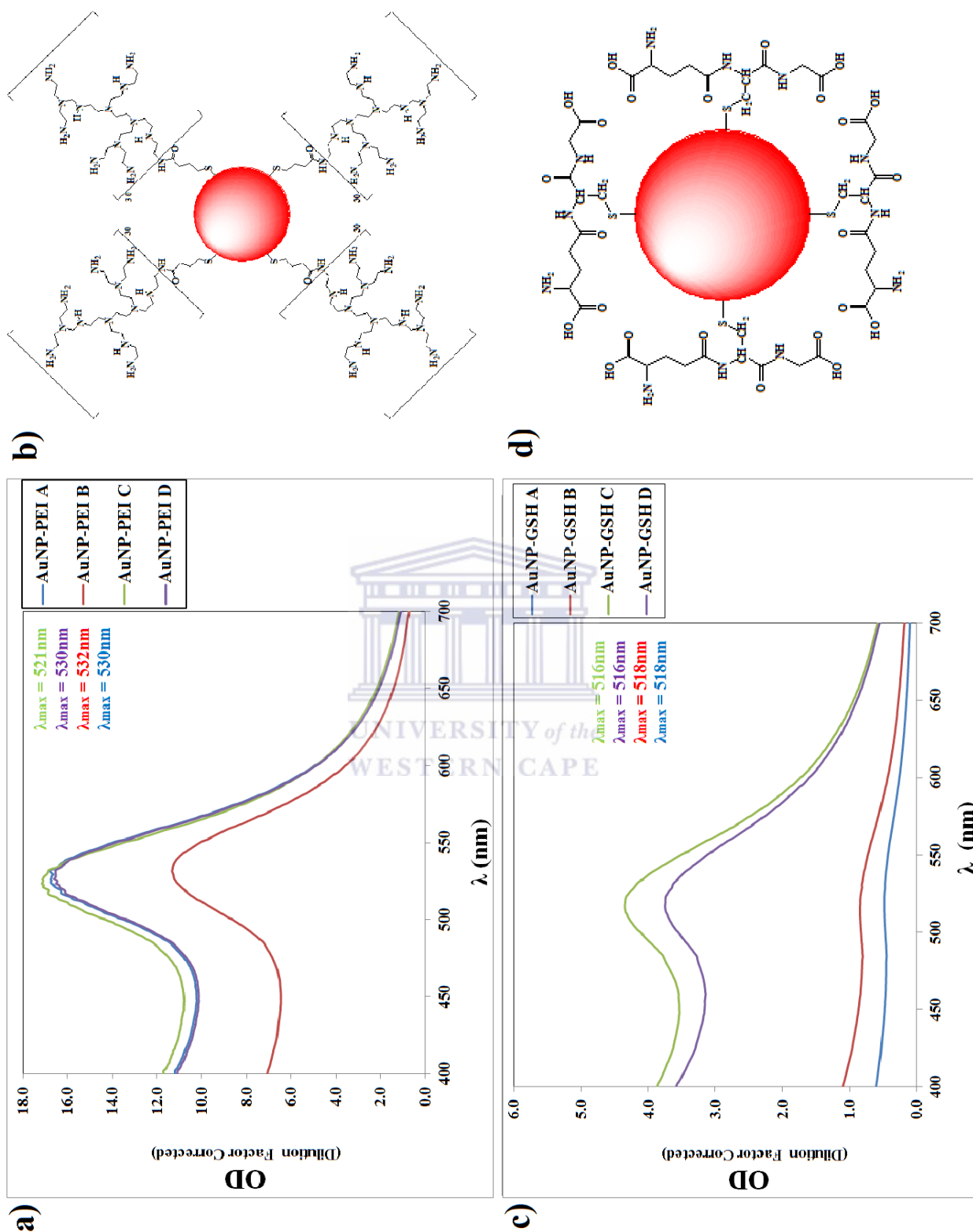
Figure 4.12: Comparative UV-Vis spectra of differentially prepared AuNPs and their corresponding proposed structures. The UV-Vis spectra for GSH capped (a) and PEI capped (b) AuNPs show distinct differences for the different synthesis conditions. The proposed structure for the one-pot synthesized AuNPs can be seen for PEI-SH (b) and GSH (d) respectively and are not drawn to scale. The data is representative of technical triplicates and was repeated twice on different days.

The overall surface charge of the AuNPs was investigated by agarose gel electrophoresis as described in Section 2.2.19. The migration of the AuNPs on an agarose gel can be seen in Figure 4.15. The AuNP-PEI preparations migrated towards the anode (Figure 4.13, Lanes 7-12 and 7-22) which indicated an overall positive surface charge. The AuNP-PEI particles displayed reduced electrophoretic mobility when compared to the AuNP-GSH preparations which indicated increased molecular mass. An experimental preparation for AuNP-PEI C (Figure 4.13, Lane 19) and AuNP-PEI D (Figure 4.13, Lane 21) both showed anomalous behaviour compared to the same experimentally prepared AuNP-PEI, migrating to the cathode and displaying similar electrophoretic mobility as for AuNP-GSH. Lane 21 (AuNP-PEI D) had a very diffuse band moving towards the anode indicating the presence of a high molecular mass AuNP as well. AuNP-GSH A and AuNP-GSH B both displayed colloidal instability and disintegrated during the assay (Figure 4.13, lanes 1-6, green circle). AuNP-GSH C and AuNP-GSH D showed the same electrophoretic ability in migration distance towards the cathode (Figure 4.13, Lanes 11-16) indicated an overall negative surface charge. The electrophoretic migration distance for the AuNP-GSH nanoparticles appeared to vary between different preparations and this was also observed for AuNP-PEI nanoparticles which suggested possible variations in the AuNP size distributions per batch.
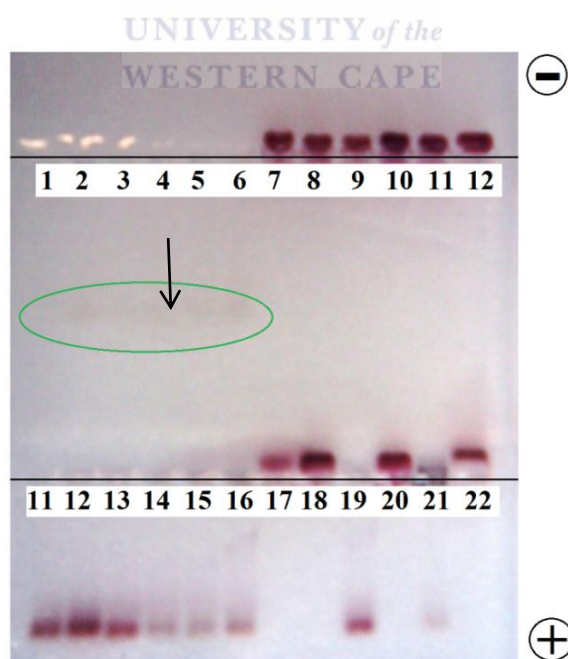
Figure 4.13: Electrophoretic mobility assay of differentially prepared AuNPs for qualitative charge and size distribution. The AuNPs were resolved on a 0.35% agarose gel for 40min at 50V. Each well represents an experimental preparation of the corresponding AuNPs. The anode (-) and cathode (+) is indicated on the gel and the centre of the wells are indicated by a black line. The green circle indicates AuNPs which disintegrated during electrophoresis. Lanes 1-3: AuNP-GSH A, Lanes 4-6: AuNP-GSH B, Lanes 11-13: AuNP-GSH C, Lanes 14-16: AuNP-GSH D, Lanes 7-9: AuNP-PEI A, Lanes 10-12: AuNP-PEI B, Lanes 17-19: AuNP-PEI C and Lanes 20-22: AuNP-PEI D. The data is representative for all preparations and was repeated in technical triplicates twice on different days.

4.3.4.3 HR-TEM and Qualitative EDX Analysis of Selected AuNP-GSH and AuNP-PEI preparations

The conditions for synthesis of the AuNPs can be found in Table 4.4. AuNP-GSH A and AuNP-GSH B (Section 4.3.2.3) both displayed colloidal instability making further physicochemical characterizations challenging. High resolution transmission electron microscopy (HR-TEM) and qualitative EDX analysis was done on selected prepared gold nanoparticle samples as described in Section 2.2.1.4.

AuNP-GSH D was synthesized under the exact conditions as in Section 4.3.2.1 for the slow addition of the reducing agent (Table 4.1, Table 4.2, Figure 4.7 and Figure 4.9) yielded similar results. Preparation AuNP-GSH C showed near spherical AuNPs which are well dispersed from each other (Figure 4.14a) with an average size distribution of 7.32±3.90nm for 2049 particle counts (Figure 4.14c). This is a ~53% variation in size distribution. These AuNPs can be considered polydisperse in size distribution. The EDX (Figure 4.14b) confirms the presence of gold in the sample.

AuNP-PEI A showed very well dispersed nanoparticles (Figure 4.15a) with a polydisperse size distribution (Figure 4.15a, c). AuNP shape discrimination and contribution to the sample was determined as described in 2.2.1.4. The AuNPs display mostly near spherical shapes with a low incidence (< 0.5%) of amorphous morphologies. The size distribution histogram (Figure 4.15c) indicates that AuNP-PEI A has a mean diameter of 17.38±9.05nm which is a ~52% variation in size distribution. The size distribution was calculated by counting 2516 particles with a cut off contribution to mean diameter of 3.5%.

AuNP-PEI B showed well dispersed AuNPs with a 7%, 172 of the 2457 particles counted, incidence of tetrahedral shaped AuNPs (Figure 4.16a). Also, near spherical AuNPs presented with hexagonal shaped facets. The mean diameter was determined to be 18.19±13.30nm (Figure 4.16c) which is a ~73% variation in size distribution. Tetrahedral shapes did not contribute to the mean diameter calculation. AuNP-PEI D showed all the AuNPs were well dispersed from one another (Figure 4.17a) and polydisperse in size distribution (Figure 4.17c) with a mean diameter of 16.48±7.72nm. This is ~47% variation in size distribution for 1994 particle counts. AuNP-PEI D showed a 42% incidence of tetrahedral AuNPs (Figure 4.17a and c). Tetrahedral AuNPs did not contribute to the mean diameter calculation.
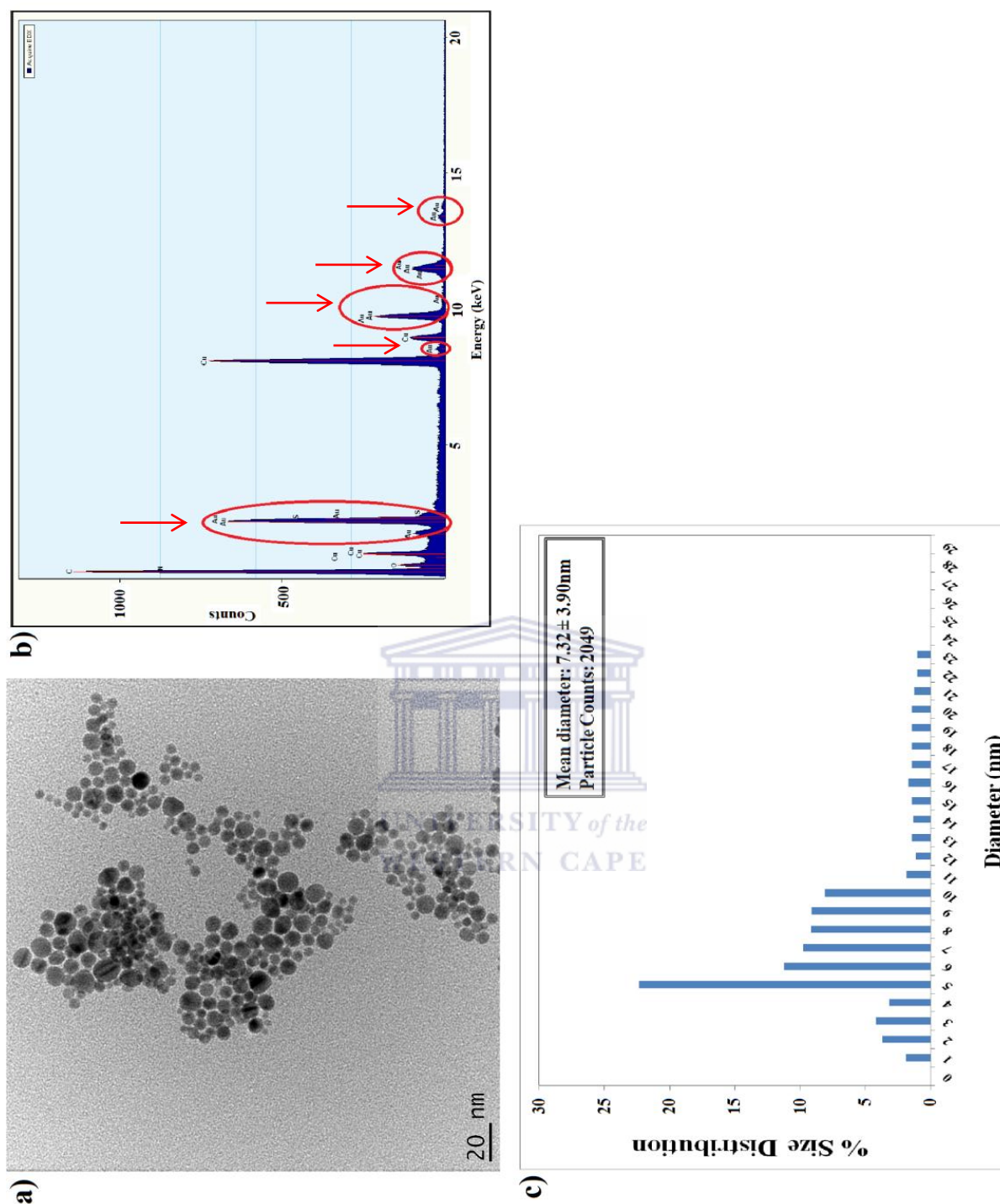
Figure 4.14: The HR-TEM and EDX results for AuNP-GSH C. The HR-TEM micrograph (a) and size distribution histogram (c) (ImageJ) and indicated polydisperse GSH capped near spherical AuNPs. Only AuNPs which contributed 3.5% to the size distribution and spherical in shape was used for mean diameter calculation. The EDX (b) confirms the gold content of the AuNPs where the gold peaks are indicated by red circles. The data is representative for all AuNP preparations for this set of conditions.
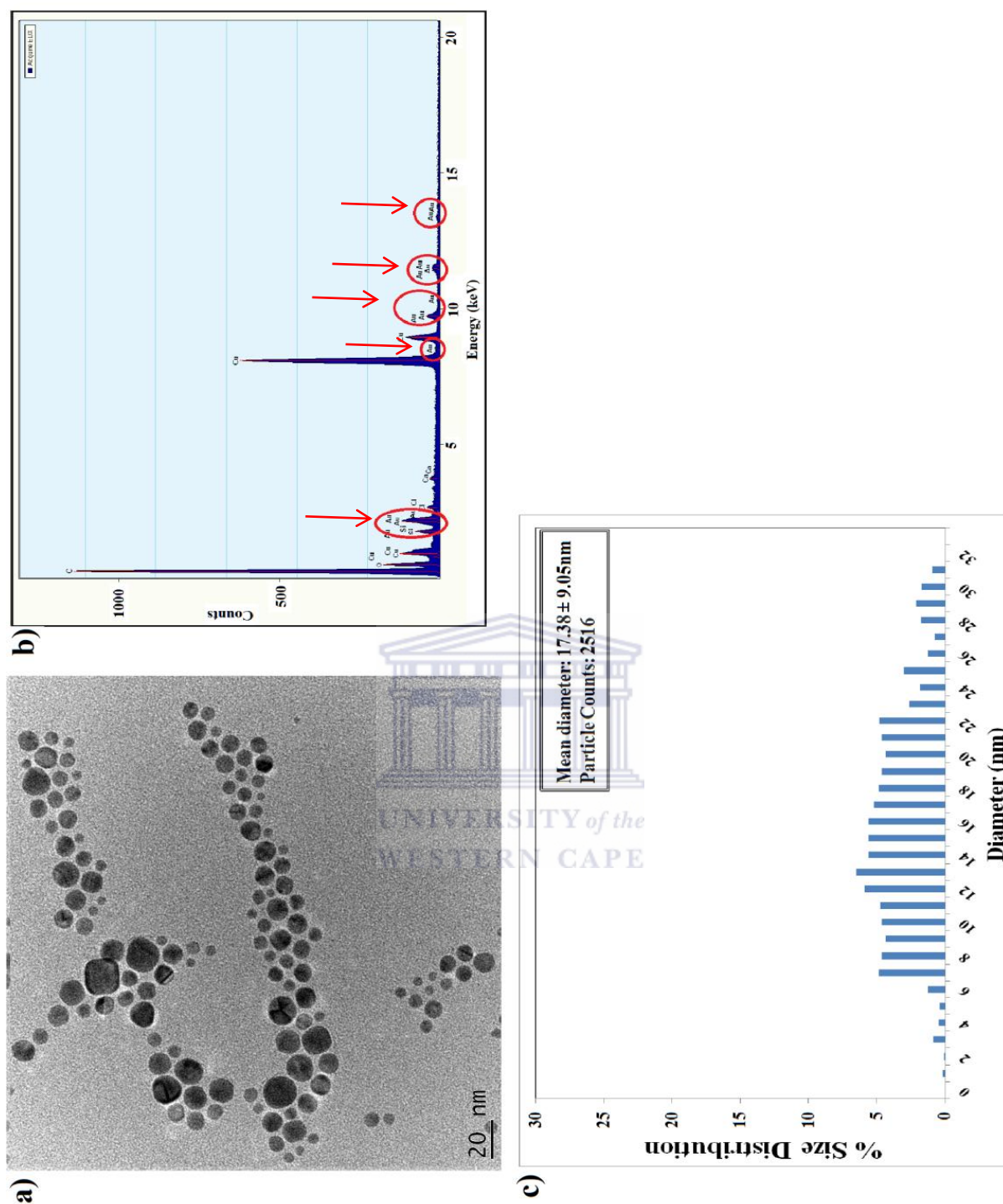
Figure 4.15: The HR-TEM and EDX results for AuNP-PEI A. The HR-TEM micrograph (a) and size distribution plot (b) (ImageJ) indicated polydisperse PEI capped AuNPs. Only AuNPs which contributed 3.5% to the size distribution was used for mean diameter calculation. The EDX (c) indicates the presence of gold confirming the composition of the AuNPs where the gold peaks are indicated with red circles. AuNP-PEI A and AuNP-PEI C showed highly similar AuNP properties in size and shape distribution. The data is representative for all AuNP preparations for this set of conditions.
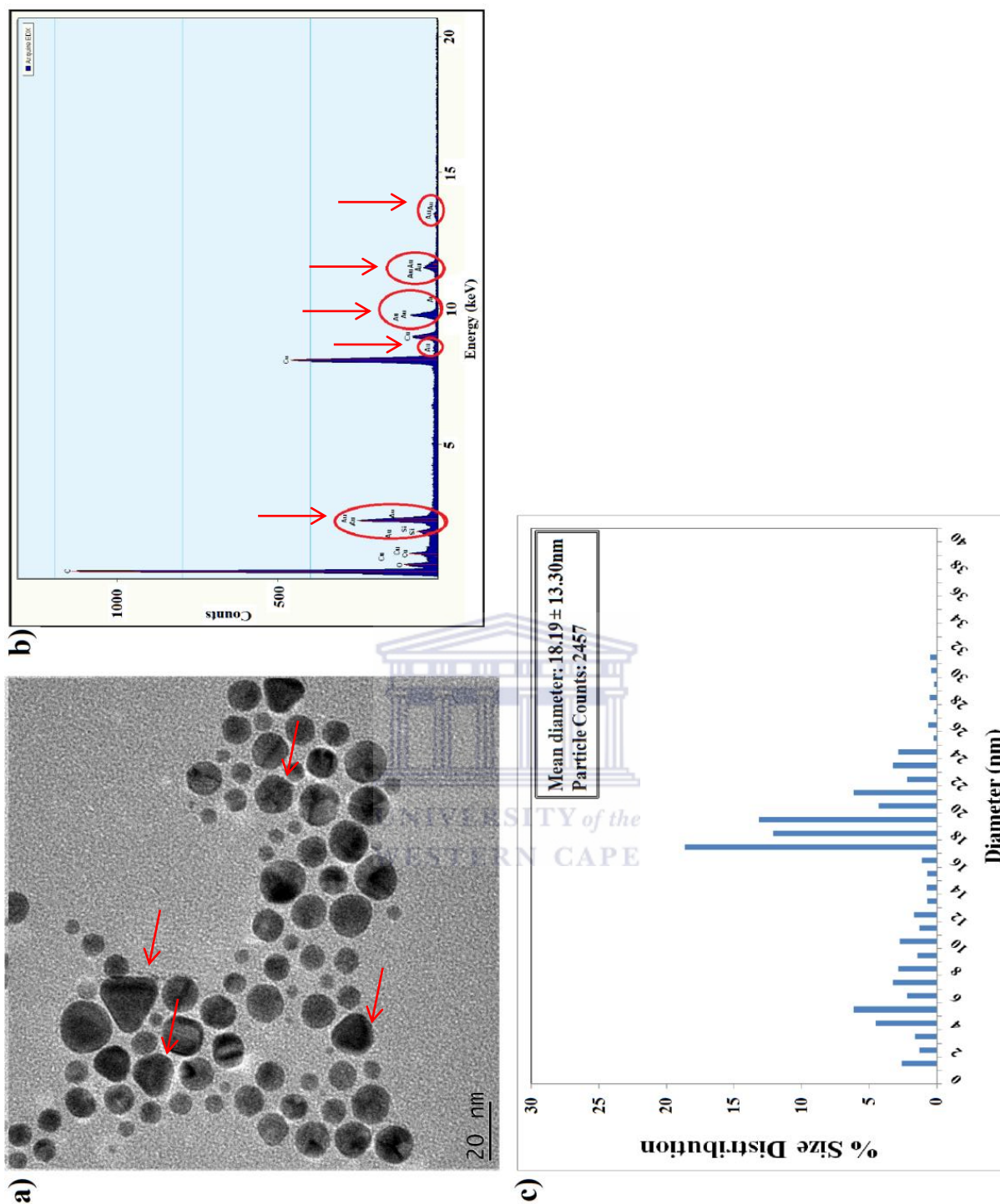
Figure 4.16: HR-TEM and qualitative EDX results for AuNP-PEI B. The HR-TEM micrograph (a) and size distribution plot (c) (ImageJ) indicated polydisperse PEI capped AuNPs. Only AuNPs which contributed 3.5% to the size distribution and which were spherical in shape was used for mean diameter calculation. The EDX (c) indicates the presence of gold confirming the composition of the AuNPs where the gold peaks was indicated with red circles. The data is representative for all AuNP preparations for this set of conditions.
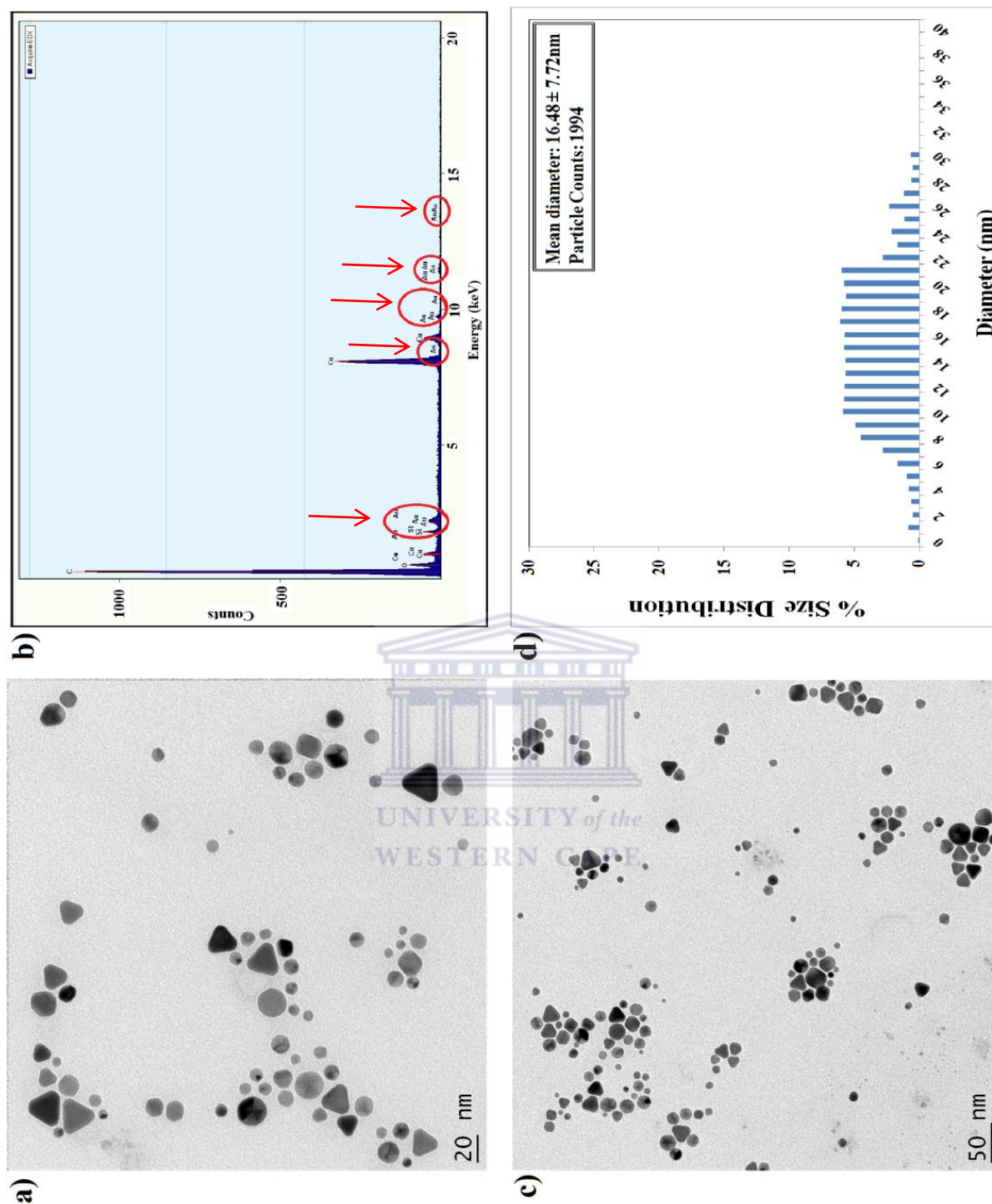
Figure 4.17: Physical parameters of the preparation of AuNP-PEI D. The HR-TEM micrographs (a, c) and size distribution plot (c) indicate polydisperse PEI capped AuNPs. Only AuNPs which contributed 3.5% to the size distribution and which were spherical in shape was used for mean diameter calculation. The EDX (c) indicates the presence of gold confirming the composition of the AuNPs. The data is representative for all AuNP preparations for this set of conditions.

Table 4.6 draws a comparison between the UV-Vis predicted nanoparticle diameters and the mean diameters calculated by ImageJ assisted AuNP diameter calculations from HR-TEM micrographs. The diameter of the AuNPs determines the molar extinction coefficient (ε) which is used to calculate the concentration of the nanoparticles in solution. Differences in the extinction coefficients as well as the concentrations can be seen when the UV-Vis predicted data is compared to the ImageJ counts. AuNP-GSH A and AuNP-GSH B shows concentrations values magnitudes greater for the UV-Vis prediction than obtained for the ImageJ counts. A similar trend was observed for AuNP-GSH C, AuNP-GSH D and all the AuNP-PEI preparations but to a lesser extent.

Table 4.6: AuNP-GSH and AuNP-PEI mean diameters and concentrations.

Sample	UV-Vis predicted values				ImageJ values (Physical counts)		
	A_{SPR}/A_{450}†	Diameter (nm)	ε† ($M^{-1}.cm^{-1}$)	[ ] (nm)	Diameter (nm)	ε† ($M^{-1}.cm^{-1}$)	[ ] (nm)
AuNP-GSH A	1.01	< 3	1.49×10^5	3260	6.18 ± 4.53	1.26×10^7	38.5
AuNP-GSH B	0.97	< 3	1.49×10^5	5850	6.60 ± 5.54	2.03×10^7	43.0
AuNP-GSH C	1.23	5	7.20×10^6	491	7.32 ± 3.90	2.03×10^7	174.0
AuNP-GSH D	1.19	4	3.62×10^6	873	8.34 ± 3.04	3.07×10^7	103.0
AuNP-PEI A	1.63	15	2.18×10^8	46.90	17.38 ± 9.05	3.23×10^8	31.6
AuNP-PEI B	1.75	22	7.31×10^8	88.50	18.19 ± 13.30	3.87×10^8	16.7
AuNP-PEI C	1.58	13	1.39×10^8	77.70	13.70 ± 7.52	1.76×10^8	61.3
AuNP-PEI D	1.63	15	2.18×10^8	46.50	16.48 ± 7.72	2.67×10^8	37.9

†Calculated from Hais et al [218] and described in Section 1.6.2.2.

4.3.4.4 Evaluation of AuNP-GSH C- and AuNP-PEI A aqueous chemical stability

The biological milieu is a complex mixture of metabolites, biochemicals and macromolecules where each has different chemical reactivity. It was necessary to evaluate the aqueous stability of the prepared AuNPs for aqueous chemical stability in a wide range of buffer systems where the ionic strength, pH as well as chemical reactivity towards the AuNP surface were investigated. Selected data will be represented for NaCl and β-mercaptoethanol to highlight the stability in these solutions. AuNP-GSH C was representative for the AuNP-GSH preparations and AuNP-PEI A was representative for the AuNP-PEI preparations, as similar results were obtained for all the AuNP-PEI particles. The stability assay evaluation was done as described in Section 2.2.3.2.

AuNP-GSH C showed a trend in decreasing optical density associated with increased ionic strength of the NaCl solution with a blueshift of the surface plasmon band (Figure 4.18a,

λ_{max}). The time-course stability was evaluated at an ionic strength of 1000mM NaCl for duration of 4 months. The data represented in Figure 4.18b showed no change in the UV-Vis spectra past 12h and was not included on the graph. AuNP-PEI A showed a similar decreasing trend in the optical density in associated with an increase in the ionic strength of NaCl (Figure 4.18c), however no change in the λ_{max} was observed. As for AuNP-GSH C, the time course stability showed similar results (Figure 4.18d).

β-mercaptethanol (BME) as a competing thiol induced colloidal instability in AuNP-GSH C (Figure 4.19c). There is a decrease in the optical density from 0.25mM BME without a shift in the λ_{max}. At increased concentrations of BME complete colloidal instability was observed for AuNP-GSH C in a concentration dependent manner. The aggregation was a near immediate effect of suspension in the BME solution and a time-course assay was not done. AuNP-PEI A showed superior stability compared to AuNP-GSH C (Figure 4.19a) with no observable shift for λ_{max} and a decrease in optical density. The UV-Vis spectra showed changes on the downward slope of the spectra ($\lambda > \lambda_{max}$). It appears that the stability of AuNP-PEI A has a correlation to threshold concentrations of BME: for 0.25mM-1mM the UV-Vis spectra overlap near perfect before a perceptible decrease in optical density takes place. Another threshold region appears to be attained at 5mM-10mM BME.
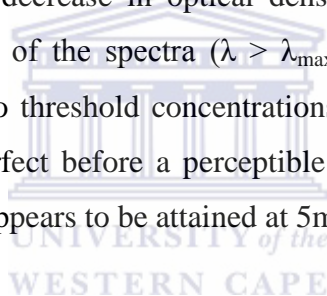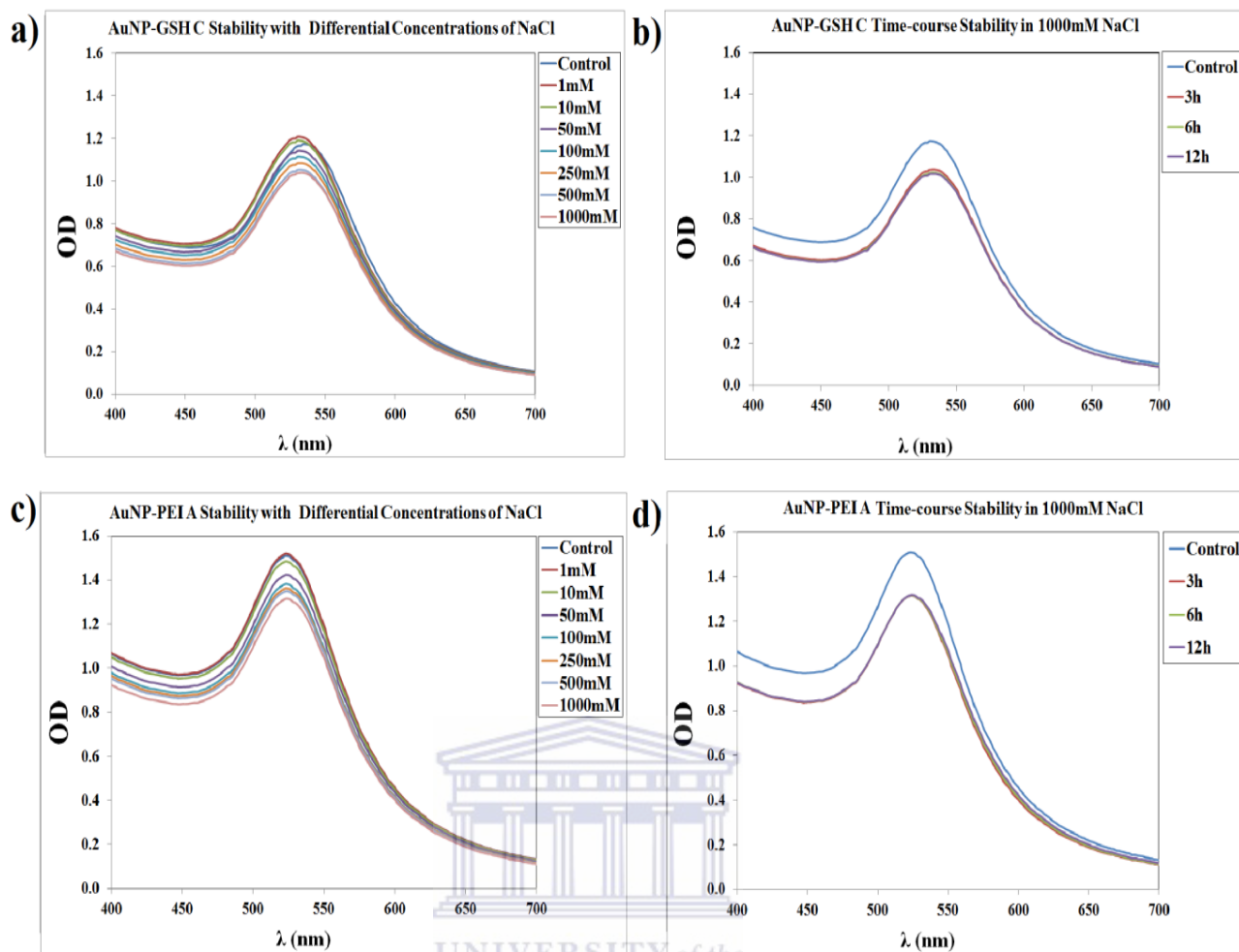
Figure 4.18: Stability of selected synthesized AuNPs in NaCl solutions. Both AuNP-GSH (a) and AuNP-PEI A (c) show very good stability up to an ionic strength of 1000mM NaCl. The time-course stability in 1000mM NaCl This stability was observed for 8 weeks and the UV-Vis spectra can be seen up to 12h for both AuNPs in b and d. There was no observed difference in the UV-Vis spectra for either AuNPs past 12h. The assay was done in triplicate and is representative for all results obtained for this assay.
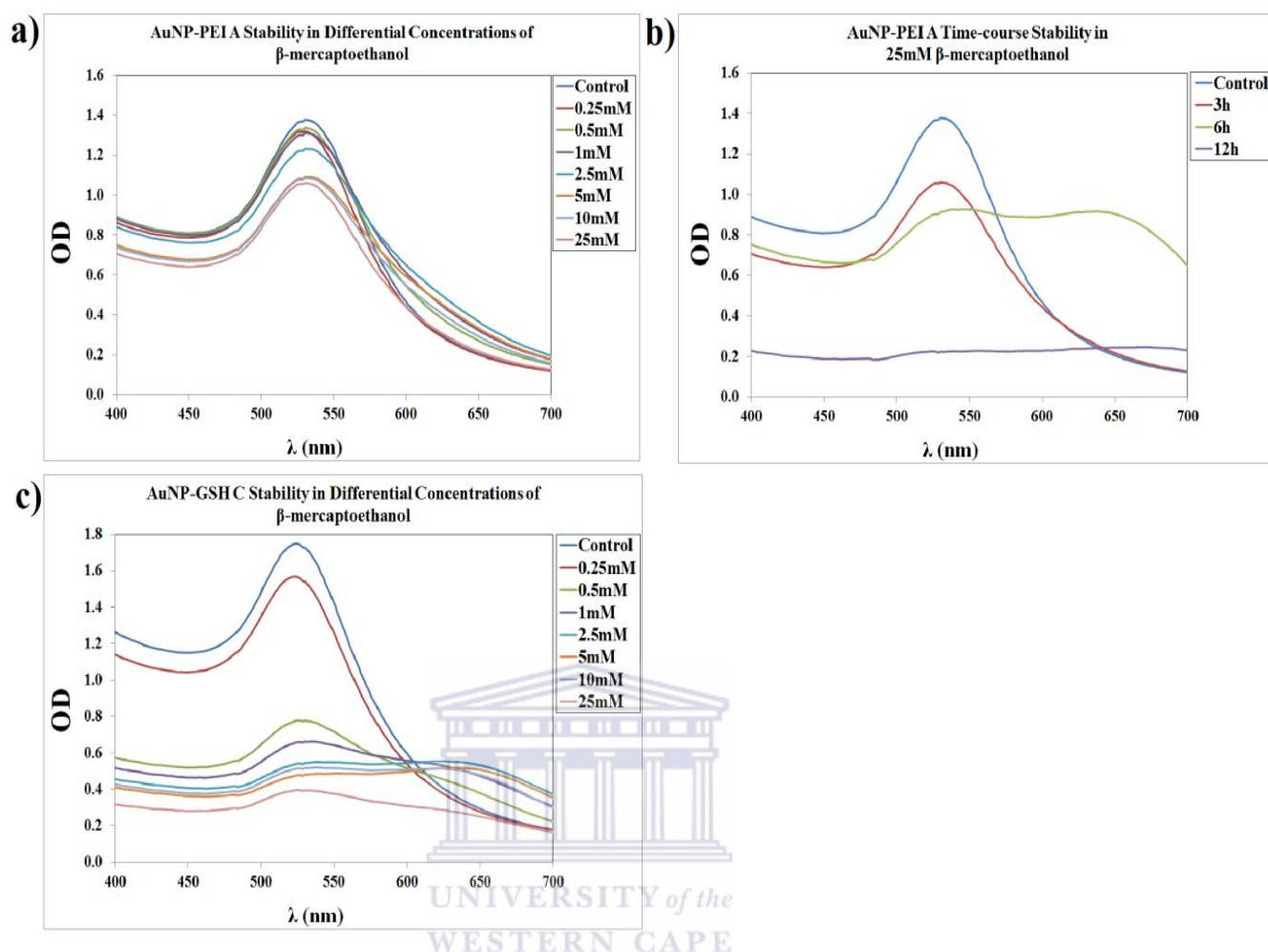
Figure 4.19: Stability of selected synthesized AuNPs in differential concentrations of β-mercaptethanol (BME). The assay was done in triplicate and is representative for all for results obtained for this assay

All the AuNP-PEI preparations showed colloidal instability in citrate solutions. The effect of ionic strength as well as time-course stability was investigated at two different pH values. Upon suspension of the AuNPs in the citrate solutions, at all the different concentrations, the solution colour went from clear wine-red to a turbid pink colour. AuNP-PEI A showed immediate colloidal instability for the whole range of citrate concentrations 1mM-100mM at pH 5 and pH 6 (Figure 4.20a and Figure 4.21a respectively). The time course stability of the nanoparticle was investigated at both pH values for 50mM (Figure 4.20b and Figure 4.21b) and 100mM (Figure 4.20c and Figure 4.21c). The colloidal instability did not result in loss of the characteristic UV-Vis spectra for citrate pH 5 (Figure 4.20) and citrate pH 6 (Figure 4.21) presenting with a redshift from 3h-12h compared to the surface plasmon band of the control. A comparative blueshift was observed from 12h to 24h (Figure 4.20 and Figure 4.21) which was still a redshift compared to the control surface plasmon band. The colloidal instability of the AuNP-PEI nanoparticles appears to be a function of ionic strength and not of pH.
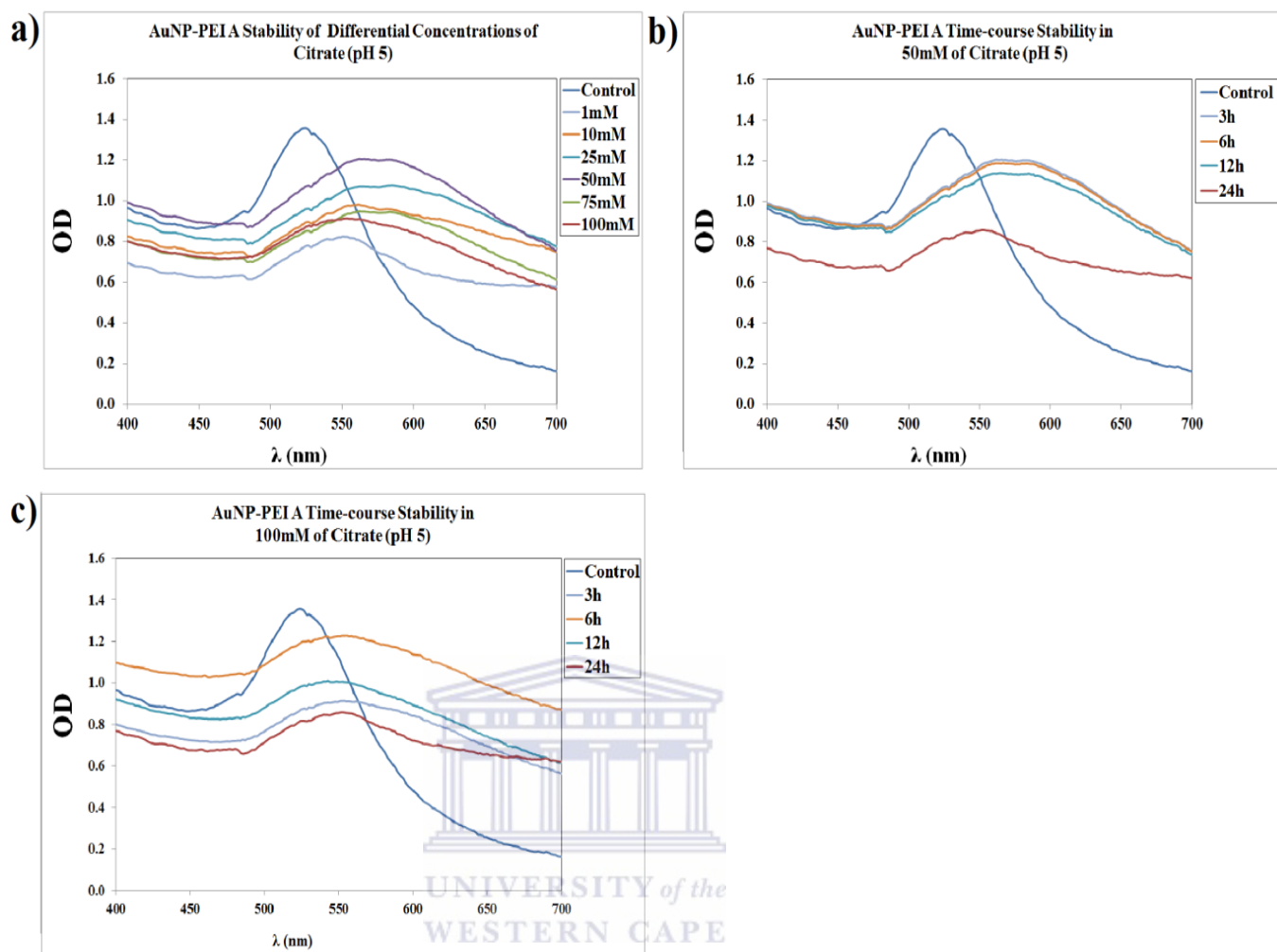
Figure 4:20: Stability of AuNP-PEI A in differential concentrations of citrate (pH 5). AuNP-PEI A showed a redshift in the UV-Vis spectrum (a) which was dependent on the ionic strength of the citrate in solution. The time course stability was evaluated for 24h in 50mM citrate (b) and 100mM citrate (c). The assay was done in triplicate and is representative for all results obtained for this assay.
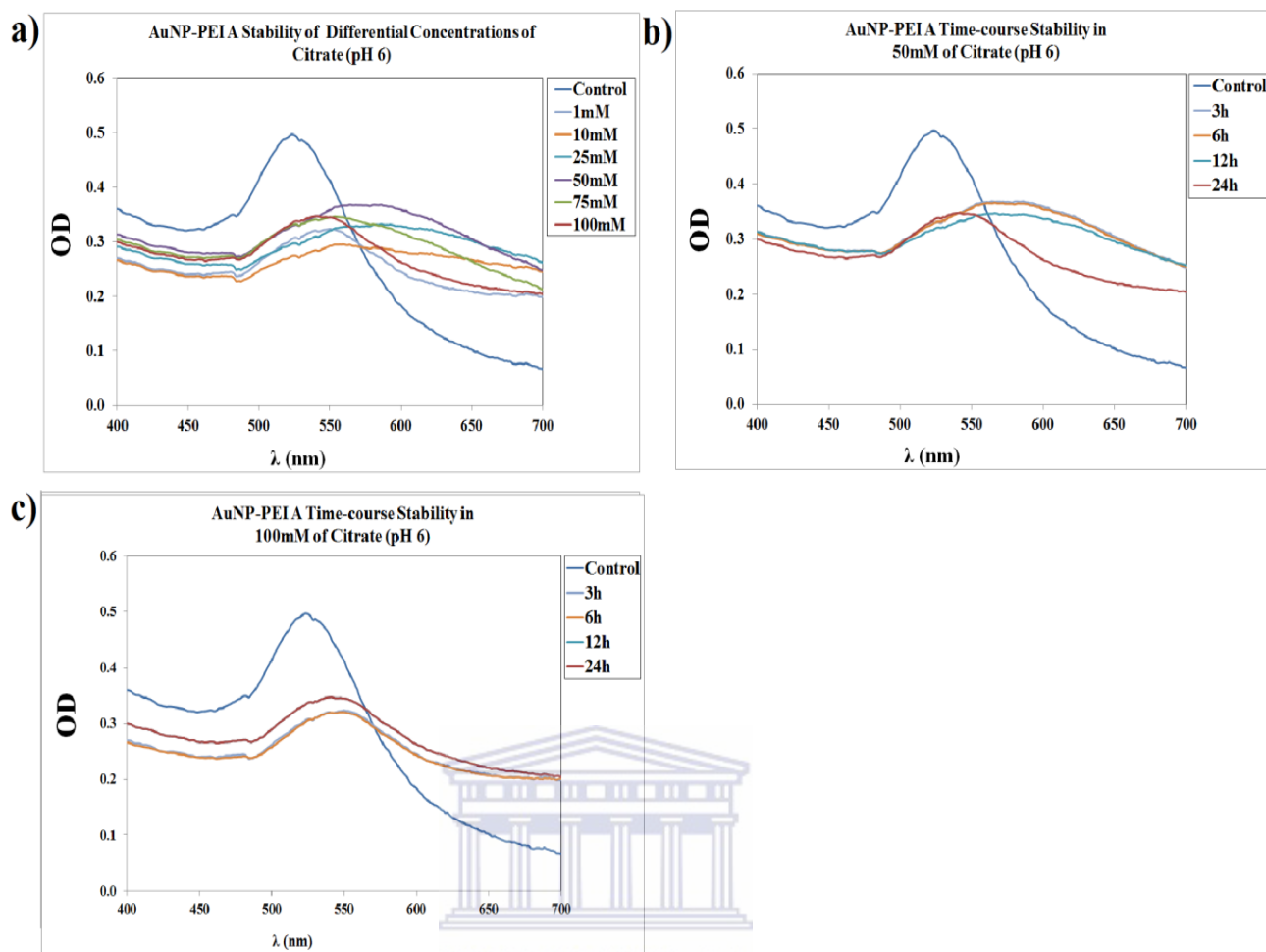
Figure 4:21: Stability of AuNP-PEI A in differential concentrations of citrate (pH 6). AuNP-PEI A showed a redshift in the UV-Vis spectrum (a) which was dependent on the ionic strength of the citrate in solution. The time course stability was evaluated for 24h in 50mM citrate (b) and 100mM citrate (c). The assay was done in triplicate and is representative for all results obtained for this assay.

4.3.5 Discussion

Typically $NaBH_4$ reduction of aurate salts produce mono-disperse sub 10nm AuNPs. Depending on the size of the AuNPs required diameters of 2nm to 15nm [46, 203, 287, 320] can be synthesized based on the surface ligand chosen as well as the amount of $NaBH_4$ added. It has been reported before that using a low ratio of $NaBH_4:Au^{3+}$ produced larger (18nm-38nm) polydisperse aqueous AuNPs passivated by borate ions [203]. The changes in solution colour from dark yellow to light yellow within 10min of addition of the ligand indicated gold cations undergoing reduction from Au^{3+} to Au^{1+}. This reduction was caused by the thiolate (R-S⁻) ligands forming polymeric precursors with the Au^{3+}. Upon addition of the reducing agent, $NaBH_4$, the polymeric aurate-thiolate precursors will further reduce the Au(I) to Au^0 which induced AuNP formation with the ligand covalently attached on the surface. A

mechanism for this phenomenon was proposed by Brinas *et al* in 2007 using reduced glutathione (GSH) as a model ligand and is described below [213]:

(1) $Au^{3+} + 3GSH$ $\rightarrow$ $Au(I)SG + GSSG$

(2) $n[Au(I)SG]$ $\rightarrow$ $[Au(I)SG]_n$

(3) $[Au(I)SG]_n + NaBH_4$ $\rightarrow$ $Au^0[Au(I)SG]_{n-1} + GSH$

Where the cycles, m, is dependent on the amount of reducing agent added as well as the aurate cations in solution,

(4) m cycles $\rightarrow$ $Au^0[Au(I)SG]_{n-m} + mGSH$
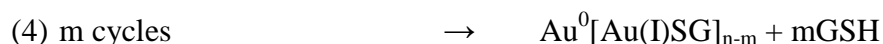
The GSH which was released per each cycle could covalently bind to the surface of Au^0, where the GSH had dual roles of promoting reduction mediated growth as well as surface passivation of the formed AuNP [213]. The colour change in the solution upon addition of the reducing agent was the stepwise nucleation, seeding and growth of the AuNPs during the formation process as discussed in Section 1.6.2.1. The tempo of addition of the reducing agent played a crucial role as drop-wise addition induced nucleation, where additional reducing agent will then induce seeding and growth of the AuNPs. Addition of the reducing agent all at once resulted in the nucleation and generation of many AuNP seeds which exhausted the reducing, preventing subsequent growth of the AuNPs. Earlier studies for various synthesis techniques demonstrated similar finding such as the classic 1994 two-phase AuNP synthesis developed by Brust *et al* [212]. This result was demonstrated for the adapted synthesis comparing the UV-Vis spectra (Figure 4.7) and the HR-TEM micrographs (Figure 4.8 and Figure 4.9). Fast addition of the reducing agent had significant amounts of sub 1nm gold clusters compared to the Slow addition of the reducing agent but no difference in the surface plasmon resonance band was detected as both preparations delivered a $\lambda_{SPR} = 518nm$. There was no significant difference in the mean diameter of the differentially prepared AuNPs but the phenomenon is attributed to the bathochromic shift phenomena observed for gold nanoparticles between the sizes of 8nm and 25nm (Section 1.5.2.2, Figure 1.22).

The study by Brinas *et* al [213] determined that the resulting AuNP diameters will be dependent on the pH of the solution, where a low pH preferentially favoured formation of larger AuNPs and a high pH preferentially favoured the formation of smaller AuNPs. A low pH facilitates a denser packing of the ligands and a high pH facilitates a less dense packing of

ligands. This was demonstrated by GSH spatial dimensions being dependent on the pH of the solution. It can be further extended by speculation that if the size of the AuNP is determined by the size of the precursor, that a physically bigger ligand will facilitate the formation of larger AuNPs. This was observed when PEI-SH was used as a ligand in 4.3.3 compared to GSH where a significant redshift and increase in optical density was observed (Figure 4.10). The optimal ratio of Ligand:Au^{3+} was experimentally determined by Zheng *et al* [287] to be 0.5:1, where the ligand can be a mono ligand or the sum of multiple ligands. In the seminal work done by Brust *et al* it was found that the ratio of thiol to gold is dependent on the reaction conditions [213]. This implied that for each type of solvent system and species of reducing agent, the ideal ratio of the thiol to gold would vary. If the ratio for GSH was < 0.5 there may not have been enough ligand to facilitate sufficient thiolate precursor formation and subsequent AuNP surface passivation. It has also been reported that thiolate ligands can also reduce the gold cations dependent on the reducing potential of the thiolate ligand [213, 287] which may well be the case for GSH ratios > 0.5 as well as PEI-SH ratios > 0.25.

For all AuNP preparation there was an overall increase in optical density for PEI-SH passivated AuNPs than for GSH (Figure 4.12), yet there was no significant difference in the amount of gold utilized for AuNP formation (Table 4.3). The increased optical density for the AuNP-PEI preparations is attributed to the high nitrogen content of PEI-SH. There are 360 lone-pair electrons for 360 nitrogen atoms per mer of PEI-SH which has 149mol primary amines, 91mol secondary amines and 120 tertiary amines. The surface plasmon resonance band is the effect of electrons washing over the surface of the AuNP (Chapter 1, Figure 1.21). Additional electrons introduced close to the surface of the AuNP affected the surface plasmon resonance and as a result alter the UV-Vis spectra. Further, the size poly-dispersity of the AuNPs for both the GSH and PEI-SH preparations influence the validity of the Beer-Lambert equation as one of the prerequisites for this equation is a homogenous distribution of an analyte species. A poly-disperse AuNP size distribution display spectroscopic properties which is a mean of the different molar extinction coefficients (ε), the more the variation in AuNP size the more inaccurate the equation will become. If the argument was extended to include a method, which uses the UV-Vis spectra by obtaining the ratio of the surface plasmon band (λ_{SPR}) to the absorption of the *d/f*-orbitals for noble metals at 450nm (λ_{450}), such as proposed by Hais *et al* [218] this same effect was observed. This concept is demonstrated by the UV-Vis predicted AuNP diameters and concentrations in contrast to the values obtained from ImageJ counts (Table 4.1, Table 4.3 and Table 4.6). These phenomena

as well as the bathochromic shift phenomena invalidated the use of the Beer-Lambert equation as well as the work done by Hais *et* al for determining mean diameter and concentration for AuNPs produced with this adapted AuNP synthesis. An adaptation of these methods to include a parameter(s) which described the electron density could compensate for the observed effect in this study.

The increase of the ratio of $NaBH_4$:Au^{3+} delivered more stable AuNP-GSH (C and D, λ_{SPR} = 516nm) which was more stable than the unstable AuNP-GSH (A and B, λ_{SPR} = 518nm) and also showed higher overall concentrations and decreased size distributions from the mean (Table 4.6). The surface plasmon band predicted the diameter for AuNP-GSH A and AuNP-GSH B was contradicted by the size distribution counts obtained from the micrographs (Table 4.6, ImageJ). The increased plasmon band for these mentioned AuNPs indicated the colloidal instability where smaller AuNPs were aggregating to appear larger. The ImageJ counts were done in the solid state and the UV-Vis spectra were done on the colloidal aqueous suspension. Dynamic light scattering would generate realtime data regarding colloidal instability under various parameters. The colloidal instability for AuNP-GSH A and AuNP-GSH B was indicative of inadequate quantities of $NaBH_4$ to ensure sufficient AuNP maturation which left the AuNP surfaces flawed which increased the mean surface area, leading to increased surface chemical reactivity and subsequent etching of the AuNPs. The surface imperfections were a plausible explanation for the disintegration of AuNP-GSH A and AuNP-GSH B during the electrophoretic mobility assay (lanes 1-6, Figure 4.13). Also, the AuNP-GSH preparations were unstable in ultrapure water (dH_2O, 18.2MΩ) and only displayed aqueous solubility in phospho buffered saline (PBS x1, pH 7.4) suggesting the need for adequate counter ions for AuNP solubility in water. AuNP-GSH C and AuNP-GSH D displayed good aqueous stability in differential concentrations of NaCl up to 1M but all the AuNP-GSH preparations showed absorption onto various glass and plasticware. The phosphate groups found in the component salts (K_2HPO_4, Na_2HPO_4 and NaH_2PO_4) could have facilitated the colloidal instability of the already unstable AuNP-GSH A and AuNP-GSH B [321]. AuNP-GSH C displayed near immediate colloidal instability in the presence of a competing thiol, BME. In a biological milieu there are many endogenous competitive thiol containing small molecules as well as macromolecules such as proteins. BME was used as an evaluation tool to determine how susceptible the AuNP-GSH will be to a competitive thiol. The effect of BME as a known competitive thiol which induces irreversible aggregation of

alkane thiolate passivated AuNPs for the conditions where the BME affinity for the AuNP surface is higher than the already present passivated thiol [322].

It is the first time that one-pot ligand passivated AuNPs have been synthesized using high molecular weight hyper branched PEI. The Au-NP PEI preparations showed no statistical significant difference in the mean particle diameters with increasing amounts of NaBH₄. A combinatorial effect of using PEI-SH and $NaBH_4:Au^{3+}$ (0.5:1 and 1:1) showed a trend in increased tetrahedral morphology AuNPs. This was seen as a combinatorial effect as for the corresponding ratios of $NaBH_4:Au^{3+}$ the AuNP-GSH particles were spherical and the other AuNP-PEI preparations also presented with near spherical particles. It is possible that the high molecular weight hyper branched PEI-SH could have acted as a growth template as well as generating a thiolate precursor, but this needs to be investigated further. Goon *et al* demonstrated the shape and size control effect which PEI (M_w = 25 000g.mol⁻¹) had on magnetite nanoparticles which were subsequently capped with a gold shell [323]. By variation of the stoichiometry between the different components in the above mentioned synthesis cube-, tetrahedral- as well as near spherical nanoparticles were produced. The tetrahedral AuNPs in this synthesis (Section 2.2.4.1) were passivated with PEI-SH in a covalent manner. Attempts were made to separate the different morphologies by using agarose electrophoresis but these attempts were unsuccessful. The AuNP-PEI particles showed minimal migration (Figure 4.13) from the loading wells even at agarose concentrations as low as 0.15%. The agarose gel was structurally unstable at such low agarose concentrations. Currently, two separation techniques are being standardized to enable shape and size enrichment of the AuNP-PEI preparations: Sucrose gradient centrifugation and denaturing gradient gel electrophoresis (DGGE), the latter which is a polyacrylamide based electrophoretic technique. Size and shape enrichment will enable further more in-depth physicochemical- as well as biological characterization of the AuNP-PEI prepared nanoparticles. The aberrant behaviour of AuNP-PEI C and AuNP-PEI D during the electrophoretic mobility assay, Figure 4.13, in lane 19 and lane 21 respectively is unknown. The AuNP-PEI preparations displayed similar high stability in NaCl as for AuNP-GSH C. However a superior stability in BME is attributed to one of two effects. The cationic hyper-branched PEI-SH shields the AuNP surface sterically as well as electrostatically, effectively hindering the BME from interacting with the AuNP surface. The other possibility was that the PEI-SH had higher affinity for the AuNP surface than the BME, requiring more BME to outcompete the PEI-SH from the AuNP surface. Both these options remain speculative until

electrochemical studies can be conducted. The AuNP-PEI preparations displayed significant pH independent colloidal instability in differential concentration of aqueous citrate solutions. This was first reported by Puntes *et al* in 2009 [302] where they described the interactions of citrate with cationic and anionic functionalized AuNPs. At acidic pH the amines were protonated and had a positive charge. The citrate (3 carboxylic acid groups) acted as a counter ion for the cationic moiety on the AuNP surface as well as an inter-particle bridge. This will induce particle to particle electrostatic crosslinking with a redshift in the surface plasmon band as well as a decrease in optical density. This aggregation will take place regardless of the presence of polyethylene glycol on the AuNP surface [302].

The AuNP synthesis yielded poly-dispersed nanoparticles with covalent attached ligand in a one-pot manner. The synthesis produced AuNPs which were more stable with a high molecular weight cationic ligand and displayed different particle morphologies dependant on the amount of reducing agent used. The reproducibility for a set of synthesis conditions showed no statistical variance but also no statistical variance was observed for the mean size distribution for different synthesis conditions for the same ligand. However, a trend in increased mean diameter was observed as well as the formation of anisotropic nanoparticles. Size- and shape enrichment techniques would enable separation of the desired morphologies as well as sizes. AuNP-PEI A was chosen for drug loading (Section 4.4) due to the overwhelming particle morphology being near spherical (Section 4.3.4, Figure 4.15), the superior chemical stability in solution (Section 4.3.4.4) as well as having the best overall toxicology response of all the AuNP-PEI preparations (Section 5.2.2.2). Near spherical morphology for the AuNPs was deemed important as inclusion criteria as to eliminate shape dependent effects in the drug delivery experiments.

4.4 AuNP-PEI A Surface Modification, Drug Loading and Drug Release
4.4.1 Introduction

The AuNP-PEI A gold nanoparticle preparation were covalently surface modified with different ratios of a commercial crosslinking polyethylene glycol (SM-PEG$_6$) as well as SH-NTA (Section 4.2.3) followed by covalent drug loading of doxorubicin by utilizing glutaraldehyde for amine-to-amine crosslinking. Total drug load as well as the *in situ* drug release was determined. The non-specific interaction of AuNP-PEI A, the PEG modified intermediates as well as the drug loaded variants were evaluated with isolated biomolecules

and complex solutions of biomolecules. The techniques utilized in this section were ATR, UV-Vis Spectroscopy and HPLC analysis.

4.4.2 AuNP-PEI A: Drug loading and the changes in surface chemistry

AuNP-PEI A was diluted, functionalized with differential concentrations of SM-PEG$_6$ (Section 2.2.3.3.1) and doxorubicin was covalently loading loaded onto the primary amines of the AuNP-PEI surface (Section 2.2.3.3.2). The AuNP-PEI A solution in the reaction vessel changed from a red-purple colour (OD ~ 0.5) to a turbid orange-red colour. Figure 4.22a showed a 23.8-fold increase in the optical density of the solution after doxorubicin covalent drug loading, as well as a significant blueshift in the λ_{max} from 530nm to 495nm. There was a change in the surface plasmon band from a characteristic gold nanoparticle band (510-550nm) to the maximum wavelength of absorption of doxorubicin (495nm). A comparison in the ATR "fingerprint" spectra (Figure 4.22c) for AuNP-PEI (blue), 30% PEG DOX (green) and DOX (red) showed that the spectra for 30% PEG DOX (green) had significant increased absorption for 1500-1000cm^{-1}. The doxorubicin loaded variant of AuNP-PEI A, 30% PEG DOX, was readily lyophilized and resuspended for later use. The intermediate functionalization of the AuNP-PEI A surface with SM-PEG$_6$ to create 30% PEG caused colloidal instability during the lyophilisation (Section 2.4.3) process. The 30% PEG particles showed aggregation within 72h after preparation (results not shown). The UV-Vis spectra showed a redshift for λ_{max} from 530nm (Figure 4.22b, blue) to 545nm (Figure 4.22b, black) after functionalization with 30% PEG. There was no perceptible change in the colour of the nanoparticle solution for AuNP-PEI A and the 30% PEG modified solution (Figure 4.22d). Covalent drug loading of doxorubicin onto 30% PEG caused a significant blueshift in λ_{max} from 545nm (Figure 4.22b, black) to 495nm (Figure 4.22b, green). 30% PEG (Figure 4.23a) as well as 30% PEG DOX (Figure 4.23b) displayed colloidal instability during HR-TEM analysis. The nanoparticles clustered and aggregated under the electron beam, losing their morphology. The proposed structures for the changes in the surface chemistry are given in Figure 4.24. The simplified structures indicate the shielding of the nanoparticle surface (dash circle) as well as the overall nanoparticle positive charge. AuNP-PEI A can be seen in Figure 4.24a. One-pot functionalization of AuNP-PEI with the bifunctional cross linker, SM-PEG$_6$, and with SH-NTA (Section 4.2.3) can be seen in Figure 4.24b. The drug loaded AuNP-PEI A, 30% PEG DOX, can be seen in Figure 4.24c. The proposed structure for the intermediate AuNP-PEI functionalization with 30% PEG (black spectra, Figure 4.22b; 30% PEG, Figure 4.22d and Figure 4.24b) was used for nickel (Ni^{2+}) titrations and subsequent surface plasmon

resonance (SPR) interactions with the recombinant peptide CTX-S2 in Chapter 3. This AuNP was referred to as AuNP-NTA for simplicity in Chapter 3 (Section 3.1.4).
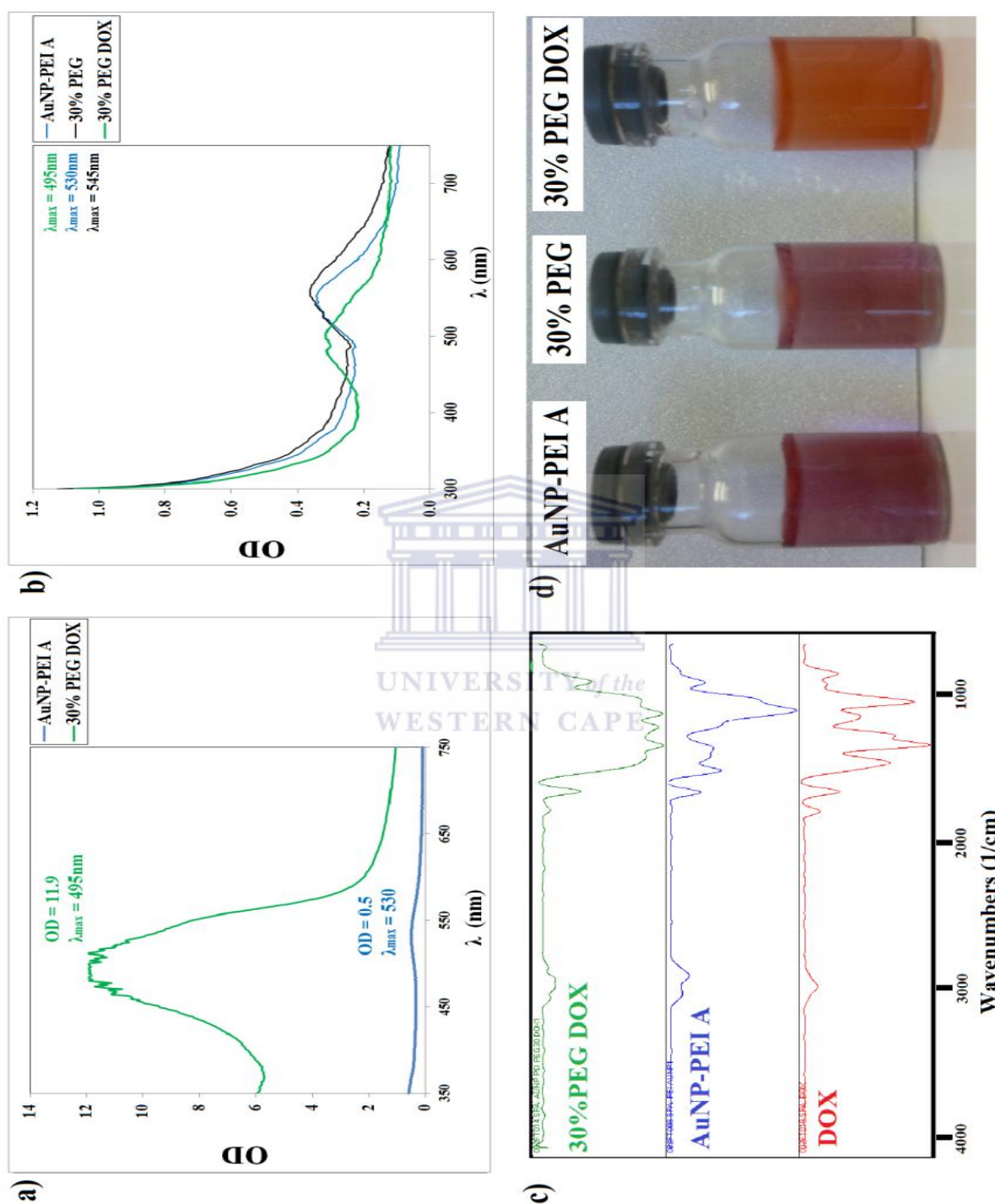
Figure 4:22: The surface modification of AuNP-PEI A with a bifunctional PEG crosslinker followed by drug loading of doxorubicin. Doxorubicin loading (green) onto the surface of AuNP-PEI A (blue) gave a significant increase in optical density as well as a blueshift in the spectrum (a). The ATR infrared fingerprint spectrum for AuNP-PEI A (blue) and the doxorubicin loaded 30%PEG DOX (green) can be seen in (c). Surface chemistry modification was monitored by UV-Vis spectroscopy (b) where shifts in λ$_{max}$ can be observed. The changes in the surface chemistry were observed in the AuNP solution colour as seen in (d). The data is representative for technical triplicates.
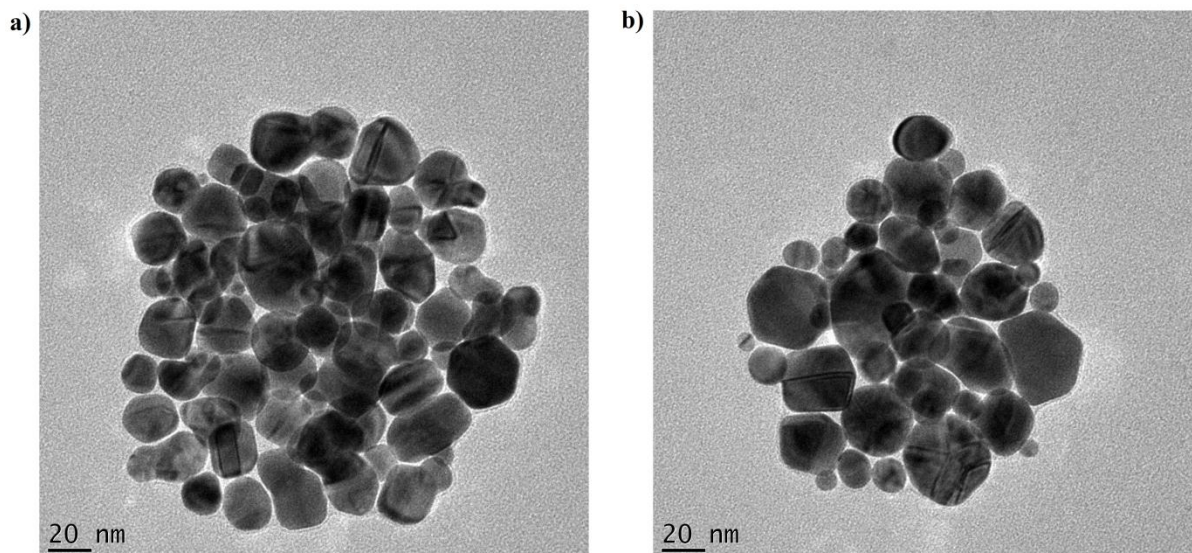
Figure 4.23: Colloidal instability for 30% PEG (a) and 30% PEG DOX (b) during HR-TEM analysis. The micrographs are representative for all preparations of nanoparticles with SM-PEG₆ and subsequent drug loading with doxorubicin.
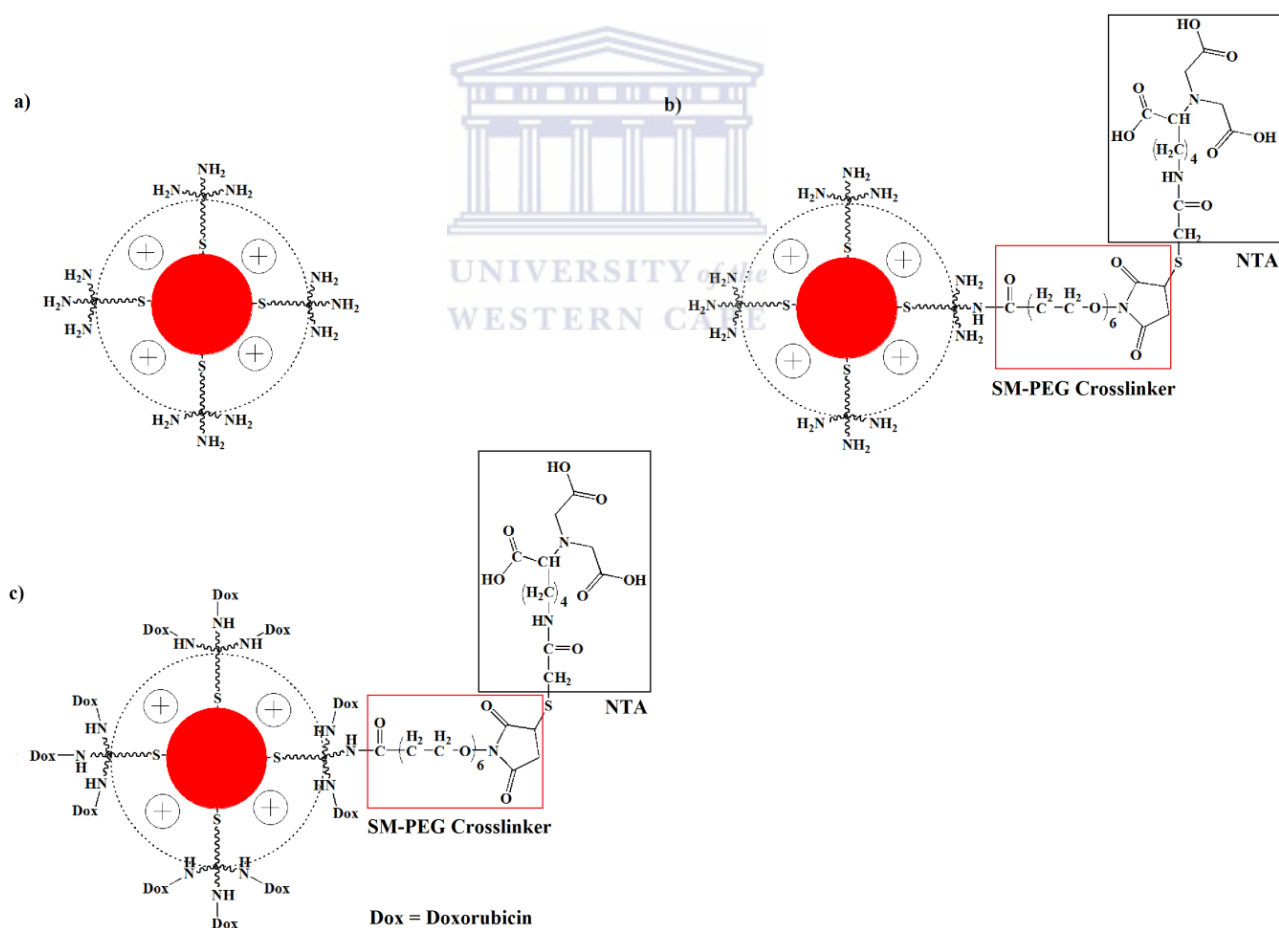
Figure 4.24: The stepwise alteration in the surface chemistry of AuNP-PEI A. A simplified proposed structure for AuNP-PEI A can be seen in (a). 30% PEG-NTA modification of the total primary amines is represented in (b). Doxorubicin primary amine to primary amine crosslinking is shown in (c).

4.4.3 Biomolecule interaction of AuNP-PEI A, 30% PEG and 30% PEG DOX

The interaction of the nanoparticles with biomolecules (Section 2.2.3.2) was to done to investigate possible non-specific surface interactions with the AuNPs, pre- and post-doxorubicin loading. The time-points displayed were representative for detectable changes in the UV-Vis spectra. The interaction with a common serum protein, bovine serum albumin (BSA) was shown in Figure 4.25. AuNP-PEI A showed interaction with BSA from the first time point (Figure 4.25a, 15min) with a gradual restoration of the UV-Vis spectra at 24h. The spectra remain unchanged from 24h to 48h with regards to the surface plasmon band, there was however significant differences in the spectra from 300-450nm. The surface plasmon band (λ_{max}) showed a blueshift from the control (530nm) to 24h (520nm). A similar trend was observed for 30% PEG with a more pronounced initial change in the spectra at 15min and a more rapid return to spectra which has a blueshift in the surface plasmon band at 24h. The 24h shift was from 545nm to 520nm (Figure 4.25b), compared to control and a redshift in the surface plasmon band, 520nm to 525nm, from 24h to 48h (Figure 4.25b). For the time points 15min to 180min, both AuNP-PEI A and 30% PEG solutions was observed to turn a turbid colour with the disappearance of the turbidity at 24h and 48h. The doxorubicin loaded nanoparticle, 30% PEG DOX (Figure 4.25c), however showed a different interaction at the corresponding time-points than AuNP-PEI A and 30% PEG as well as a change in the optical densities. No significant change was observed in the λ_{max} (495nm) for the time points for 30% PEG DOX (Figure 4.25c). A significant decrease in the optical density was observed at 24h and a significant increase in the optical density at 48h.

Tissue culture media aims to mimic the circulatory system of an organism by providing essential nutrients, proteins as well as growth factors for cells grown *in vitro* and as such is a complex mixture of biomolecules which could potentially interact with nanoparticles. The interaction of the nanoparticles with mammalian cell culture media, RPMI1640, is shown in Figure 4.26. For all the time points AuNP-PEI A (Figure 4.26a), 30% PEG (Figure 4.26b) and 30% PEG DOX (Figure 4.26c) showed interactions with the media with altered UV-Vis spectra, specifically significantly increased optical densities within 48h. A permanent redshift in the λ_{max}, associated with increased incubation time, was seen for all three nanoparticles. 30% PEG DOX showed the most resistance to change in the spectra during the assay. AuNP-PEI A had a redshift from 530nm to 545nm (Figure 4.26a), 30% PEG had a blueshift from 545nm to 542nm (Figure 4.26b) and 30% PEG DOX had a redshift from 495nm to 555nm (Figure 4.26c). The solution colour for AuNP-PEI A and 30% PEG developed turbidity as

well as an increase in optical density at 48h. The solution colour remained clear for 30% PEG DOX.
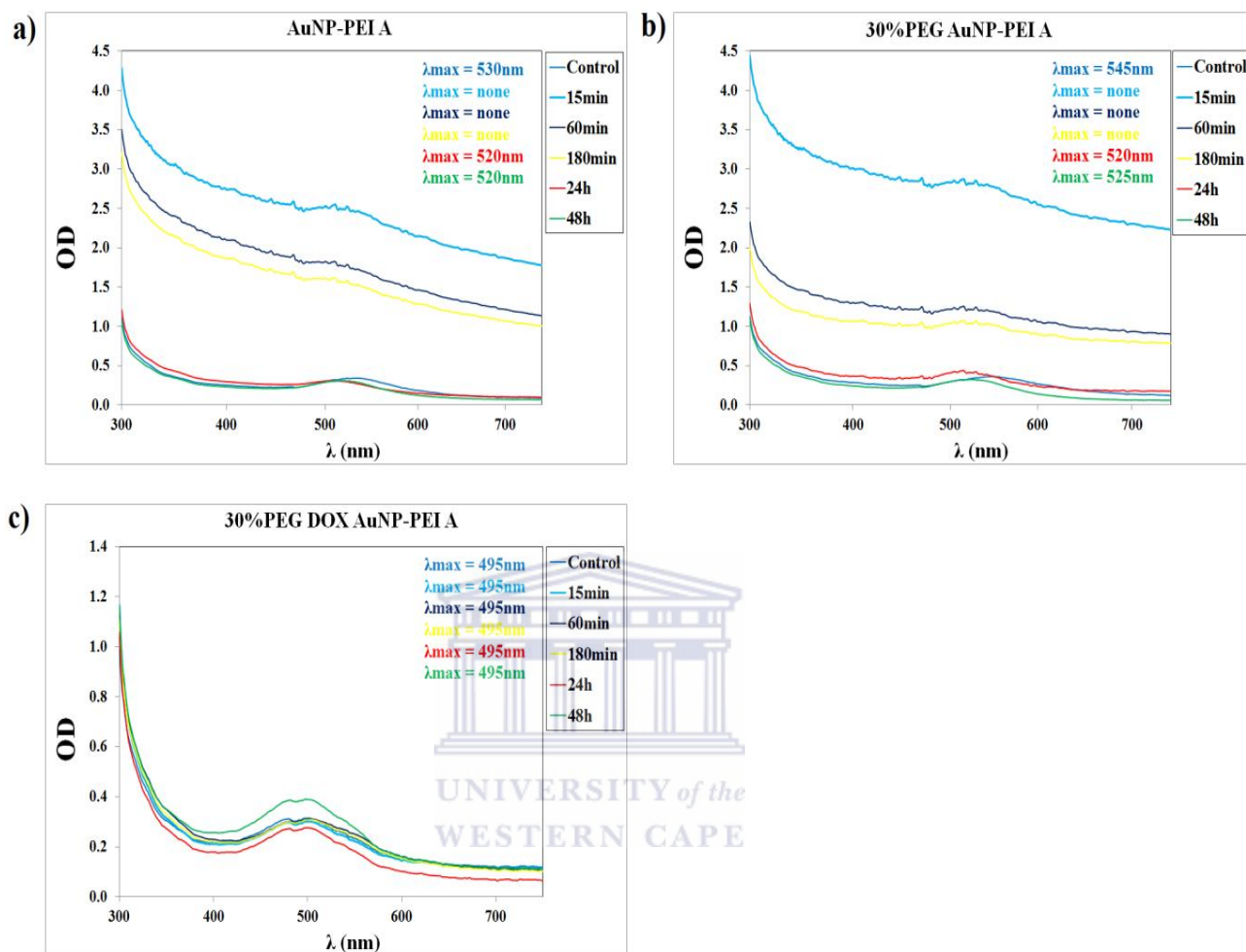
Figure 4.25: Time-course stability of AuNP-PEI A (a), 30% PEG (b) and 30% PEG DOX (c) in bovine serum albumin (BSA). 30%PEG DOX showed greater stability in a 1mg/mL BSA solution than its precursors over 48h. The data is representative for all results obtained for this assay done in triplicate.
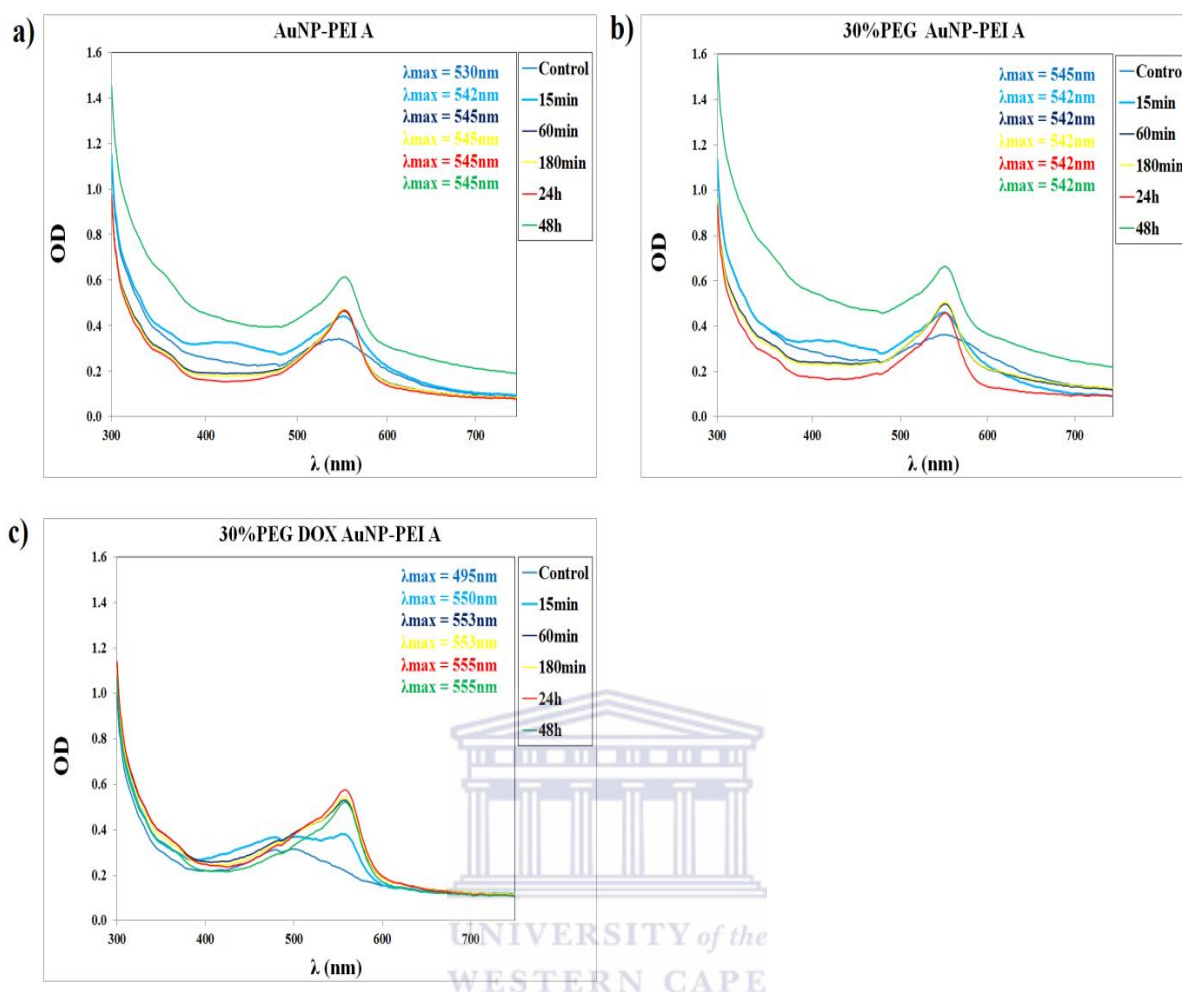
Figure 4.26: Time-course stability of AuNP-PEI A (a), 30% PEG (b) and 30% PEG DOX (c) in RPMI1640. 30% PEG DOX showed a lessened effect in the presence of a complex biological solution compared to its precursors. The data is representative for all results obtained for this assay done in triplicate.

The nanoparticle interactions with foetal bovine serum (FBS) supplemented RPMI1640 is shown in Figure 4.27. For all the nanoparticles there was a significant increase in the optical density in a time dependent manner. AuNP-PEI A showed a significant redshift from 530nm to 542nm within 15min (Figure 4.27a) with a further time dependent redshift to 546nm within 48h. 30% PEG (Figure 4.27b) showed a blueshift from 545nm to 537nm within 15min. A time dependent redshift resulted in a surface plasmon band at 544nm within 48h. A similar trend in UV-Vis spectra was seen for 30% PEG DOX (Figure 4.27c) with a redshift in the spectra from 495nm to 554nm within 15min. This redshift remained constant for the duration of the 48h.
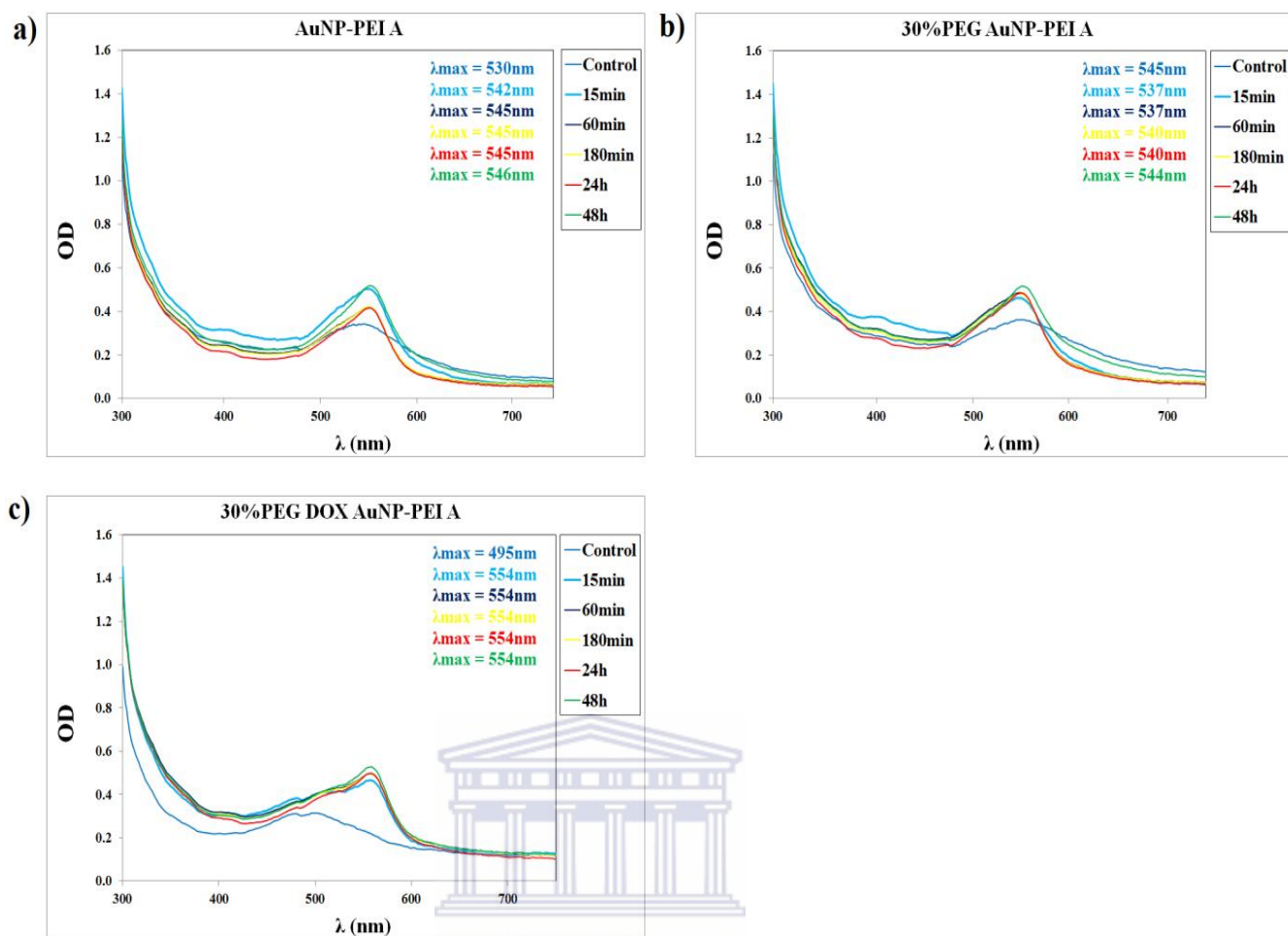
Figure 4.27: Time-course stability of AuNP-PEI A (a), 30% PEG (b) and 30% PEG DOX (c) in foetal bovine serum (FBS) supplemented RPMI1640. AuNP-PEI A showed less interaction with a complex biological solution than its chemical modified variants. The data is representative for all results obtained for this assay done in triplicate.

4.4.4 Drug release of doxorubicin from the 30% PEG DOX AuNP-PEI A surface

Doxorubicin release from the nanoparticle surface was done as described in Section 2.2.3.3.3a and subsequently analysed by HPLC analysis (Section 2.2.3.3.3b). The HPLC overlay chromatogram can be seen for the doxorubicin standard series (serial dilution) in Figure 4.28a. Doxorubicin was detected at a retention time of 6.10±1.10min. The linearity of the standard series can be seen in Figure 4.28b. The UV-Vis spectrum of the corresponding chromatogram peaks confirmed the identity of the compound as doxorubicin (Figure 4.28c). The retention times, integration for the area under the curve and concentrations for the corresponding peaks can be seen in Table 4.7.

As an example, the amount of doxorubicin hydrolysed after 30min of incubation in 0.1N HCl (Section 2.2.4.3.3a) can be seen in Figure 4.29. Four peaks were identified on the

chromatogram as doxorubicin associated peaks. The first identified peak (Figure 4.29a, Table 4.7) had a retention time of 6.20min, corresponding with the expected retention time for doxorubicin. The additional peaks had retention times of 8.98min (Figure 4.29b, Table 4.5 – Unknown #1), 11.28min (Figure 4.29c, Table 4.5 – Unknown #2) and 13.97min (Figure 4.29d, Table 4.7 – Unknown #3) respectively and where identified as doxorubicin metabolites by the comparing the UV-Vis spectra of the peaks with that of doxorubicin (Figure 4.29c). The total doxorubicin released was calculated to be 312.9nM (Table 4.7) and was the summation of all 4 peaks found to correspond to the UV-Vis spectra of doxorubicin. The peak at 11.28min contributed the most to the total doxorubicin released from the nanoparticle surface (129.36nM, Table 4.7 – Unknown #2). The doxorubicin peak at 6.20min had the second highest contribution to doxorubicin released from the nanoparticle surface (109.41nM, Table 4.7 – Doxorubicin).

Table 4.7: HPLC analyses of drug release from the AuNP-PEI A surface after 30min.

Peak		Retention Time (min)	Relative Area (mAu*min)	Concentration (nM)
Standard series (Serial dilution)	**Doxorubicin x1**	6.02	694.76	450
	Doxorubicin x2	6.11	362.65	225
	Doxorubicin x4	6.14	174.97	112.50
	Doxorubicin x8	6.17	114.78	56.25
Peak 1	**Doxorubicin**	6.20	168.92	109.41
Peak 2	**Unknown #1**	8.98	89.27	57.82
Peak 3	**Unknown #2**	11.28	199.72	129.36
Peak 4	**Unknown #3**	13.97	25.18	16.31
				312.90
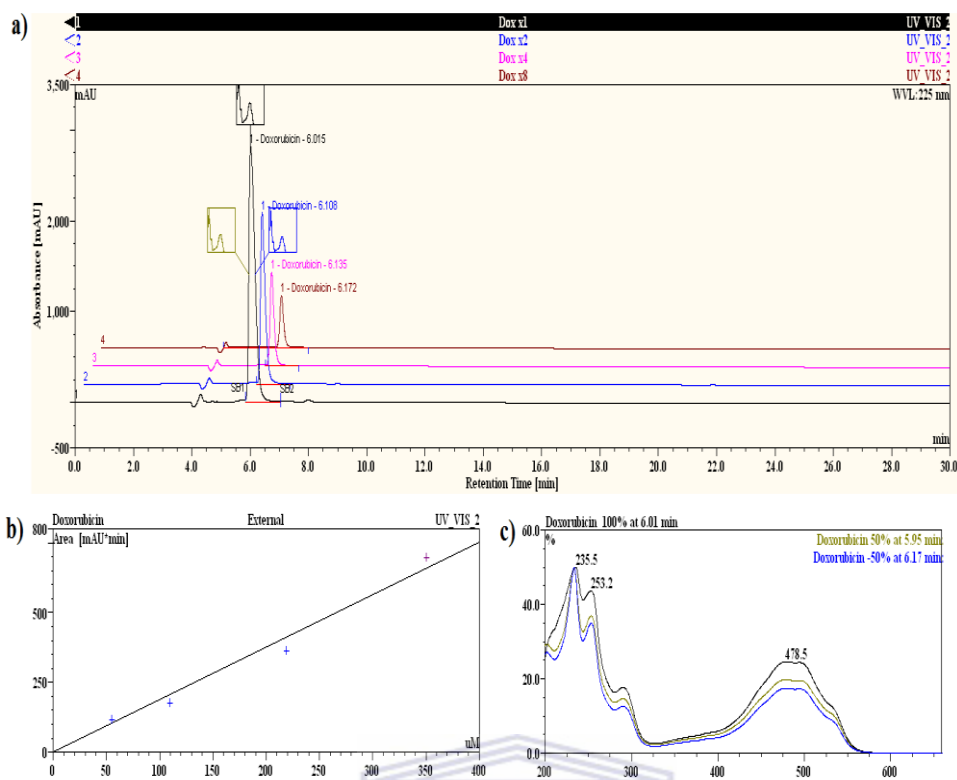
Figure 4.28: Doxorubicin standard series utilized for acid hydrolysis based drug release assay of doxorubicin from the AuNP-PEI A surface. The overlay chromatograms for the serial dilution standard series for doxorubicin can be seen in (a). The linearity of the standard series can be seen in (b). The UV-Vis spectrum for doxorubicin can be seen in (c). Retention times as well as integration can be seen in Table 4.5. The data is representative of technical triplicates and was repeated twice on different days.
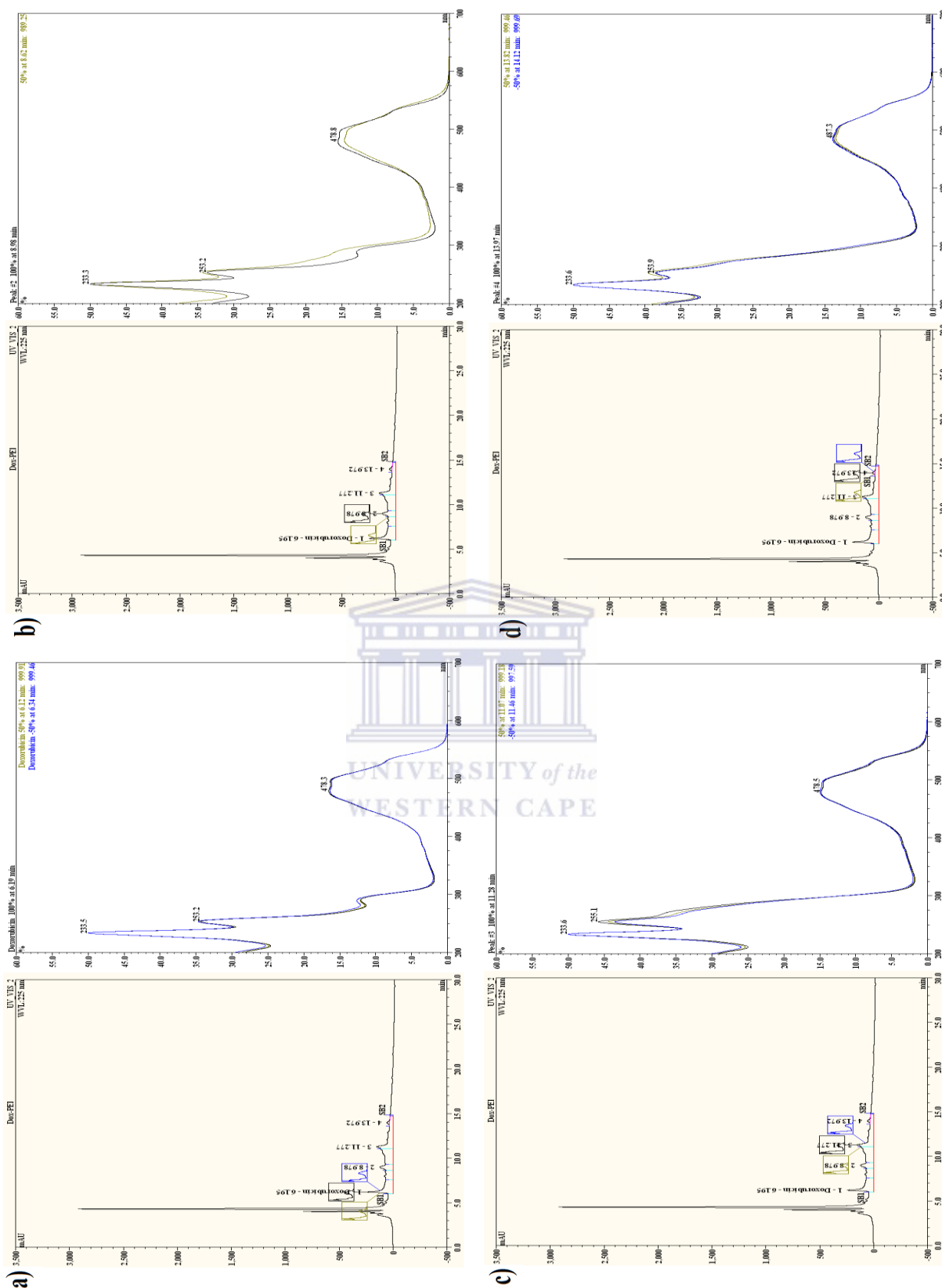
Figure 4.29: HPLC analysis of the acid hydrolysis (0.1 N HCl) of doxorubicin from the surface of AuNP-PEI A after 30min. Four peaks were identified which had the corresponding UV-Vis spectra for doxorubicin with increase in retention time (a-d). Retention times and integration can be seen in Table 4.5. The data is representative of technical triplicates.

The acid hydrolysis facilitated release of doxorubicin from the nanoparticle surface was monitored for 24h (Figure 4.30) by HPLC analysis. After 3 hours (180min) the total doxorubicin release was 402nM. At 12h (720min) the total doxorubicin released was 401nM and at 24h (1440min) it was 405nM. The estimated concentration of 30% PEG DOX used for the drug release assay was calculated to be 100pM AuNP according to the method of Haiss *et al* [218] (Sections 1.6.2.2 and 2.2.1.6a). An average of 400nM doxorubicin released per 100pM AuNP-PEI A indicates doxorubicin: AuNP-PEI A = 4000:1. On a mole to mole basis this means 1mmol of 30% PEG DOX AuNP-PEI A released 4mol doxorubicin.
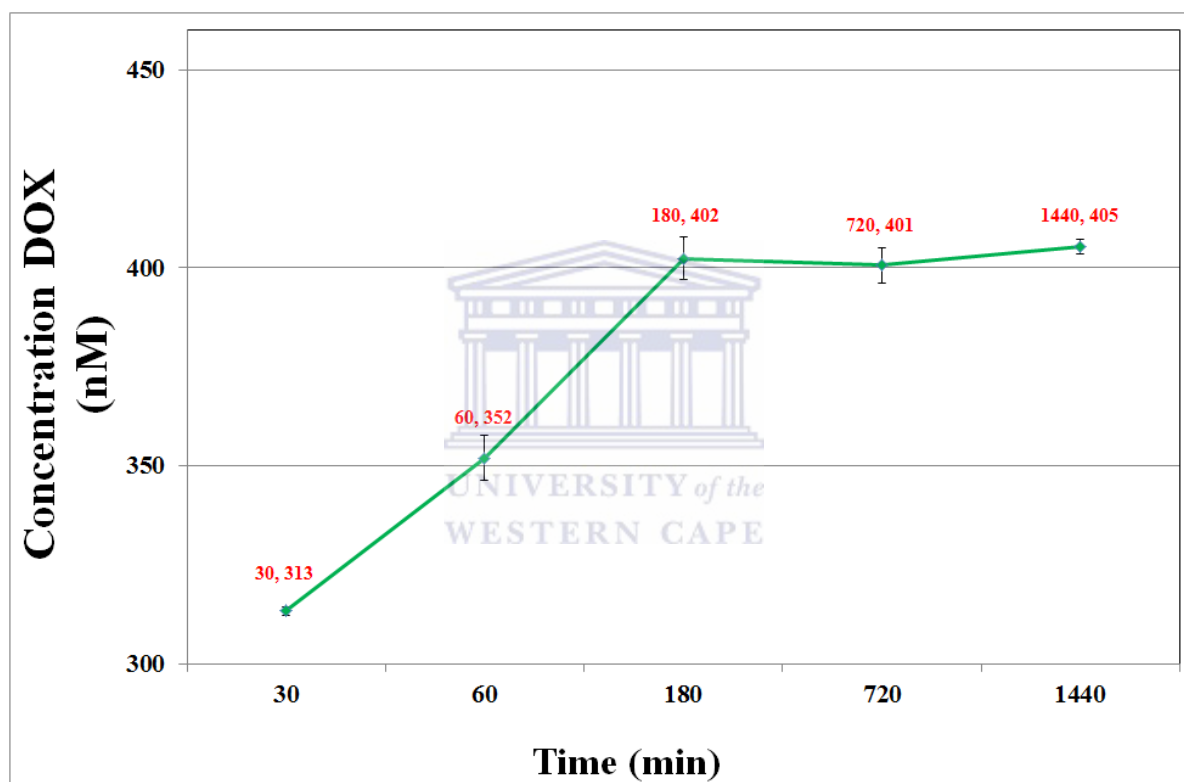
Figure 4:30: Time-course acid hydrolysis of doxorubicin from the AuNP-PEI A (30%PEG DOX) surface. The time points are indicated in coordinates (x (min), y (nM)). The data is representative for all assays. The p-values can be found in Table A5 in the Appendix.

In Section 4.2.4 the estimation was made that for each mol PEI-SH there will be 149mol primary amines. The covalent attachment of doxorubicin utilizes primary amine crosslinking (Section 2.2.4.3.2). If the assumption is made that all the remaining primary amines are utilized for crosslinking for a 30% PEG AuNP-PEI functionalization with 149mol primary amines per 1mol PEI-SH, this implies that (0.3)(149) = 44.7mol ≈ 45mol primary amines unavailable for covalent drug loading. Thus 149mol − 45mol = 104mol primary amines available for covalent drug loading. Then for 4000mol doxorubicin this means:

(4000mol doxorubicin)/(104mol primary amines)

= 38.46mol ($\approx$ 38.5mol) doxorubicin per 104mol PEI-SH, then x represents the amount of total PEI-SH per mol AuNP:

$$(38.5\text{mol}).(100\%) = (70\%)x$$

$$x = 55\text{mol PEI-SH per 1mol AuNP}$$

The estimation was made, as shown above, that there was 55mol PEI-SH for 1mol of AuNP-PEI. However the size poly-dispersity of the AuNPs will make this ratio vary significantly.

4.4.5 Discussion

The blueshift of the surface plasmon from 530nm to a wavelength which was not associated with the surface plasmon (λ_{max} = 495nm) as well as the 23.8-fold increase in optical density indicated the drug loading onto the AuNP surface was sufficient enough to completely destroy the typical UV-Vis spectra associated with AuNPs. This high drug loading potential was attributed to the large number of primary amines PEI-SH provided for amine-to-amine crosslinking. This type of crosslinking has been used previously to covalently load doxorubicin onto polymers [89-91]. The typical trend in the literature is to utilize carbodiimide chemistry to load doxorubicin onto carboxyl functionalized AuNPs [147, 324, 325]. Kumar *et al* demonstrated that 70-80 doxorubicin molecules were loaded per single AuNP, mediated by carbodiimide chemistry [147]. *In situ* drug release assays indicated that 1mol AuNP-PEI 30% PEG DOX will release 4000mol of doxorubicin within 3 hours. The *in situ* acid hydrolysis based drug release assay aims to mimic the acidic (4 < pH < 6) conditions found in endosomes and lysosomes [279, 326-328]. In the event of endosome of lysosome sequestration of drug delivery vehicles, such as gold nanoparticles, the chemotherapeutic payload would be degraded or exocytosed from the cell, thus decreasing the overall effectiveness of the formulation.

Physico-chemical characterizations of AuNP-PEI A as well as the changes in the surface chemistry proved challenging, with UV-Vis spectroscopy and ATR infrared spectroscopy the most facile methods. Electrophoretic mobility assays for qualitative evaluation of change in overall charge and molecular weight, per stepwise surface modification, was not be done due to the limitations of the current experimental setup, as mentioned in an earlier paragraph, for size and shape enrichment. HR-TEM analysis caused aggregation under the electron beam which suggests the 30%PEG and 30%PEG DOX functionalization may lower the melting

point of AuNP-PEI A. A similar phenomenon was reported where AuNPs aggregated under a 200keV beam which melted the AuNPs and induced solid state aggregation [329, 330]. Dynamic light scattering experiments may give better insight into the colloidal stability of 30%PEG and 30%PEG DOX and was considered as an essential component of the experimental workload, however this was not a feasible experiment due to logistical factors as well as agreement of non-disclosure which provided challenges in engaging other researchers.

Non-specific interactions with bovine serum albumin (BSA) showed that the doxorubicin loaded AuNP, 30%PEG DOX, had the least amount of interaction with this serum protein. BSA has an isoelectric point (pI) of 4.6 and would be negatively charged at pH 7 [331] which was the pH of the assay. The 30%PEG DOX AuNP (Figure 4.25c) was most stable during the BSA assay, most likely attributed to the doxorubicin shielding the AuNP-PEI from the negatively charged BSA. The cationic AuNP-PEI A had electrostatic interactions with the anionic BSA as seen in Figure 4.25a. The 30% PEG AuNP (Figure 4.25b) displayed non-specific interaction with the BSA and showed a UV-Vis spectra which returned to a near original state as well as a less pronounced change in the surface plasmon band which was attributed to the PEG functionalization reducing the non-specific interactions [156, 287]. Similar trends for 30%PEG was seen for all biomolecule interactions. Data generated in this study indicated that 30% surface functionalization with PEG_6 ($SM-PEG_6$) did not completely abolish non-specific interactions but decreased the biomolecule interactions. Complete abolishment of the non-specific biomolecule interactions were not seen in this study and were attributed to the strong cationic nature of the PEI-SH.

RPMI1640 (Figure 4.26) and foetal bovine serum (FBS) supplemented RPMI1640 (Figure 4.27) showed significant redshifts and changes in the optical density of AuNP-PEI interactions as well as for 30%PEG DOX. RPMI1640 is a complex biological solution which aims to mimic serum constituents for mammalian cell culture purposes. It contains a mixture of inorganic salts, vitamins and specifically reduced glutathione as indicated on the product information sheet provided by the supplier (Lonza). Reduced glutathione (GSH) can act as a competitive thiol in a similar manner to BME [332, 333] as well as act as an inter-particle particle-to-particle bridge by electrostatic- hydrogen bonding [334]. The addition of FBS further complicated the solution composition. Any number of small molecules, amino acids or peptides could be implicated in the reaction. Also, the pH indicator used in RPMI1640 is

phenol red which has a zwitter ionic charge bearing potential. Phenol red could have potential electrostatic interactions with the cationic AuNPs in a pH dependent manner since the assay conditions were done at pH 7.4, this is near the pH range (Figure 4.31) where the acid-base conjugate pair exists in equilibrium [335]. It has been shown for citrate capped AuNPs that the nanoparticles aggregated *in vitro* in the presence of cell culture media in a time dependent manner before cellular internalization occurred and as such inflicted mechanical injury to the cells [336]. It has not yet been reported to what extent PEG influences this interaction. The aggregates can cause mechanical injury to the cells or change the intrinsic composition of the media if vitamins or cofactors are binding to the surface of the AuNP leading to nutritional deficiencies for the cells.
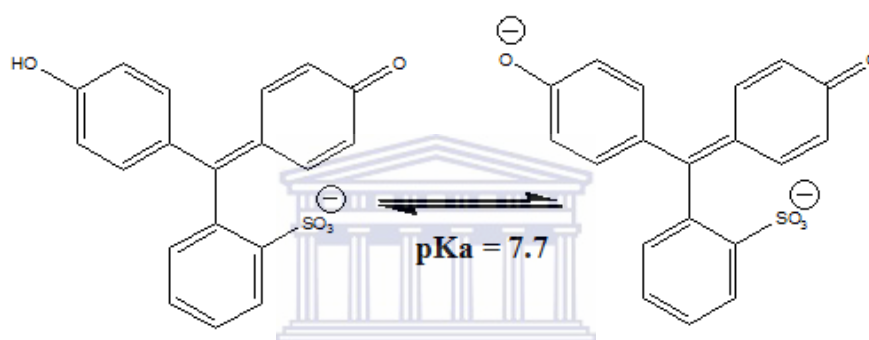
Figure 4.31: The protonation of phenol red

The AuNP-PEI A nanoparticle proved to have a high drug loading capacity on a comparative mole to mole basis. The colloidal instability of 30% PEG necessitated it to be freshly prepared on the day it was needed for an assay while 30% PEG DOX could be readily lyophilized and resuspended for later use. AuNP-PEI A and 30% PEG DOX was used to evaluate the drug delivery platform in multidrug sensitive- and multidrug resistant ovarian carcinoma cells *in vitro* cell based assays in Chapter 5. The proof of concept which utilized this PEI-SH drug delivery platform in a targeted manner was investigated by functionalizing nanoparticles with completely different physicochemical characteristics, namely quantum dots (Section 4.5), and then evaluating the nanoparticle cellular localization with the help of fluorescence microscopy (Section 3.3.3.2). The transfer of the PEI-SH drug delivery platform to quantum dots is discussed in Section 4.5.

4.5 Quantum Dot (QD) Surface Modification and Characterization

4.5.1 Introduction

The fluorescent semi-conductor quantum dots (QDs) are gaining popularity in cellular- and whole animal imaging applications. The intrinsic electronic semi-metallic properties of these nanoparticles make them superior high contrast materials for optical investigations. A major drawback is the inherent toxicity associated with the materials used in the synthesis of these nanoparticles. Propriety indium-phosphide based QDs were obtained from Mr Paul Mushonga [388] and these nanoparticles were investigated for the transferability of the PEI surface functionalization chemistry utilized for AuNP-PEI. The QDs were used to investigate the interaction between chlorotoxin and matrix metalloproteinase-2 in wide field fluorescence microscopy protein co-localization studies (Chapter 3).

4.5.2 Surface Modification of palmitic acid passivated QD_{625}

Palmitic acid passivated QD_{625} was ligand exchanged (Section 2.2.4.1) from a chloroform solution to an aqueous solution of PEI-SH (Section 4.2.4). This resulted in aqueous soluble QD_{625} which had thiol anchored covalent attached PEI-SH on the surface. A significant blueshift and increase in relative fluorescence intensity was observed for QD_{625} during the phase transfer from palmitic acid passivated to PEI-SH modified (QD_{625}-Palmitic acid to QD_{625}-PEI, Figure 4.33). The QD-PEI was further modified with SM-PEG_6 (Section 2.2.4.2a) which resulted in no observable changes in the emission maxima or in relative fluorescence intensity (QD_{625}-PEI 30%PEG, Figure 4.32). The MMP2 targeting peptide, Chlorotoxin was covalently coupled to the QD_{625}-PEI 30% PEG surface by carbodiimide chemistry (Section 2.2.4.2b) without changes were observed for the quantum dot emission maxima or the relative fluorescence intensity for the peptide functionalized QD_{625} (CTX-QD_{625}-PEI 30% PEG, Figure 4.32). An emission peak at 465nm was observed for QD-Palmitic acid for which the relative fluorescence emission intensity significantly decreased with subsequent functionalization with PEI and 30% PEG. There was a significant increase for this 465nm emission with the peptide functionalization (CTX-QD_{625}-PEI 30% PEG, Figure 4.32) but this was still significantly lower than for QD_{625}-Palmitic acid.
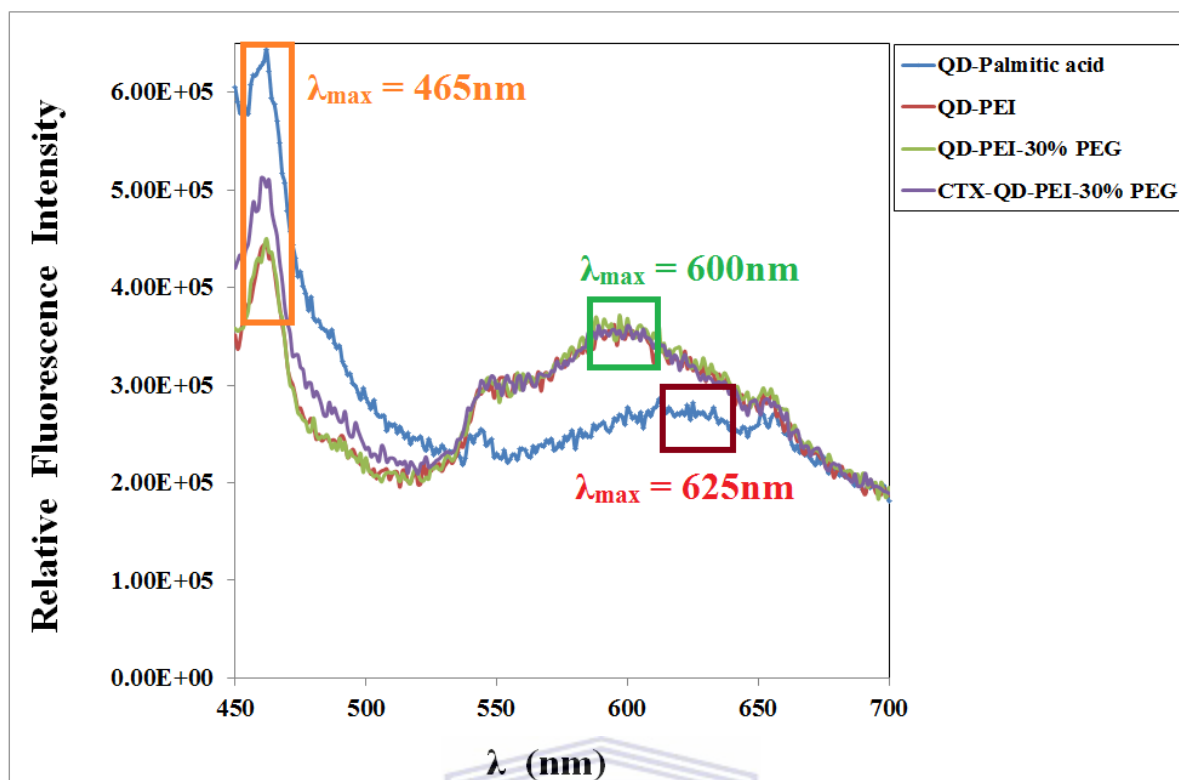
Figure 4.32: The fluorescence emission spectra of 100nM QD$_{625}$ during differential functionalization of the nanoparticle fluorescence.

The proposed change in surface chemistry is represented in Figure 4.32. The proposed structure for QD$_{625}$-Palmitic acid (Figure 4.33a), QD$_{625}$-PEI (Figure 4.33b), QD$_{625}$-PEI 30% PEG (Figure 4.33c) and peptide functionalized CTX- QD$_{625}$-PEI 30% PEG (Figure 4.33d) illustrates the changes in the surface chemistry of the quantum dots with modifications required for downstream biological fluorescence microscopy applications.
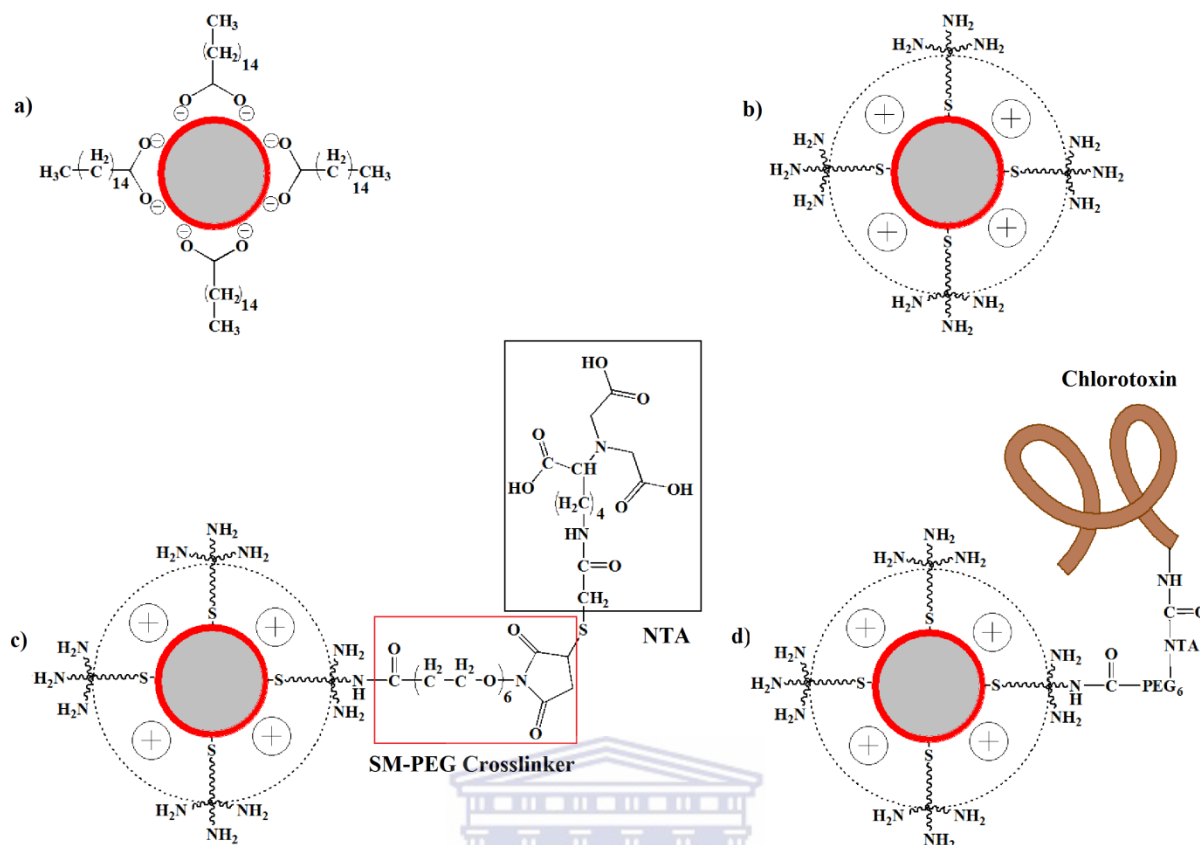
Figure 4.33: The proposed changes in surface chemistry of QD$_{625}$ with different surface functionalization.

4.5.3 Discussion

QD sample quantity was limited. All other physicochemical characterizations were done by Mr Paul Mushonga [388]. Fluorescence emission spectroscopy will be presented for the novel surface modifications done to this palmitic acid passivated QDs.

Ligand exchange (Section 2.2.4.1) of the QD$_{625}$-Palmitic acid was completed within 2 hours and the marked change in the emission profile was observed. The phase change of the QD$_{625}$ from the chloroform to the aqueous layer indicates a change in surface chemistry. The QD$_{625}$ is altered from being lipophilic palmitic acid chelated passivated (Figure 4.33a) to covalent passivated by PEI-SH (Figure 4.33b) with a thiol bond. The QD$_{625}$ is capped with a zinc-selenide (ZnSe) shell. Zinc has a preferential affinity for thiol groups over amines and is such is the most likely bond that PEI-SH will form with the QD shell [171, 174, 230, 233]. The blueshift from 625nm peak emission to 600nm peak emission was observed for- and attributed to the PEI-SH functionalization. The high nitrogen content of the polymer provides lone pair electrons which altered the electronic character (similar as discussed in Section 4.3.7) of the system and as such effected a significant change in the fluorescence character of

the system. The effect of amine (nitrogen) containing ligands was reported to induce a redshift in the fluorescence emission spectra of QDs post ligand exchange [233]. However, a blueshift was however observed for the indium-phosphide QDs as well as an increase in peak fluorescence emission intensity at 600nm, where the latter is indicative of an increased quantum yield which was not an effect of dilution error as all samples were at equal dilution during fluorescence emission spectroscopy (Section 2.2.4.1). A loss of quantum yield is typically predicted for QD ligand exchange reactions [161, 233, 255] from an organic solution to an aqueous solution due to surface imperfections created in the QD shell as atoms get stripped from the crystal lattice structure during ligand exchange and subsequently the core atoms can leak from the QD core structure [162, 292, 337]. 30% PEG showed no altered peak fluorescence emission maxima nor did the chemical conjugation of chlorotoxin (CTX). Another phenomenon was observed where a fluorescence emission peak was found at 465nm which differentially changed with surface functionalization. The latter phenomenon, the blueshift in peak emission as well as the increase in fluorescence intensity at the same QD_{625} concentration during surface functionalization needs to be investigated further as these are novel physicochemical observations. The new observed phenomena may be specifically a combination of noble metal doping of the indium based QD_{625} as well as the use of the hyperbranched high molecular weight PEI-SH which introduced novel electronics to the proprietary QD_{625} (personal communication with Dr Martin Onani, Nanotechnology Innovation Centre (NIC), Department Chemistry, University of the Western Cape, Cape Town, South Africa).

CTX was conjugated utilizing water soluble carbodiimide (EDC) chemistry as opposed to nickel affinity binding of the NTA to the recombinant 6xHis–tag on CTX due to the small sample quantity of QDs. The NTA group has 3 carboxyl acid groups (Figure 4.33c) which were used for EDC chemistry facilitated coupling of primary amine residues on CTX.

The success of the functionalization of the QD_{625} with PEI-SH and CTX was confirmed in Section 3.3.3.2 with protein co-localization fluorescence microscopy studies. Shuming Nie suggested that PEI can be used as an efficient endosome disruptive coating for QDs using smaller variants of hyper branched PEI as well as linear PEI [226, 236, 255, 279, 337]. The functionalization of QD_{625} with PEI deserves more in-depth research to determine the photo-physics as well as the electronic effects observed for this project.

Chapter 5: Interactive Studies of Gold Nanoparticles (AuNPs) with Paired Ovarian Carcinoma Cell Lines

5.1 Cellular Reversion from Multi-drug Resistance to Drug Responsive: Biomarker Assisted Evaluation of Malignancy

5.1.1 Introduction

The multi-drug resistant cell line (A2780cis) was reverted to the drug responsive (A2780) cell line. The purpose being two-fold: Firstly, is it possible to have an aggressive cancer revert back to a less malignant form *in vitro* and secondly can a selective drug response be observed between drug responsive and drug resistant variants of the cell line. The cell line reversion was confirmed with selected biomarkers. Cells were propagated as described in Section 2.4.2.

5.1.2 Reversion of A2780cis to A2780: Multi-Drug Resistant (MDR) to Drug Sensitive

The differences in cellular morphology between the cells cultured in the absence of cisplatin and presence of 2μM cisplatin (Section 2.4.3.1) can be seen in Figure 5.1a and Figure 5.1b respectively. Distinct white spots were visible in the cells that were under cisplatin treatment (Figure 5.1b) and were observed at different magnifications for the treated cells. A more epithelial morphology was seen for the untreated cells (Figure 5.1a) which were elongated and presented with larger cytoplasmic volumes. The A2780cis cells (Figure 5.1b) showed a more elongated morphology but some cells also presented with near-spherical or amorphous morphology. It was also found that the floating cells (Figure 5.1b) were still viable, since subculturing of these cells resulted in cellular attachment and growth. This cell line is derived from a very aggressive metastatic ovarian tumour. The A2780cis cells display all the molecular hallmarks of metastasis with increased expression of matrix metalloproteinases, adhesion molecules and angiogenesis associated proteins [53]. The morphological changes observed for the cells prompted confirmation of A2780cis reversion with immunoblotting.
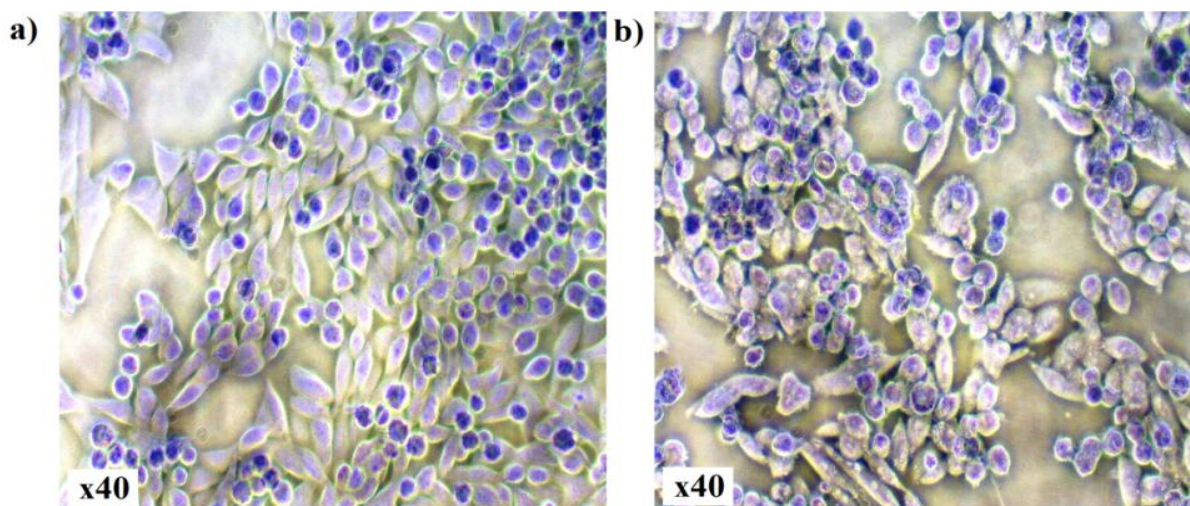
Figure 5.1: Cellular morphology of the cisplatin responsive A2780 (a) and the resistant A2780cis cells.

The protein expression patterns from passage 7 to passage 8 appeared to not have distinct differences (Figure 5.2a) for both cisplatin treated and untreated cells. However, passage 9 (Figure 5.2a, p9 and p9c) showed altered protein expression for both cell types with the presentation of a distinctive high molecular weight protein band < 100kDa (red rectangle, Figure5.2a). This high molecular weight band was not the result of cisplatin treatment as it was present in the untreated (p9) as well as the cisplatin treated (p9c) lanes. The high molecular weight protein band may be associated with the duration and conditions of continuous sub-culturing. High passage number can result in altered protein expression and may not always be indicative of the disease stage as well as associated molecular events which have prompted the World Health Organization (WHO) to define criteria for biomarkers [14]. This has been a hot-topic of debate in biomarker discovery in the past few years. Immunoblotting (Figure 5.2b) was done to confirm the reversion of A2780cis to A2780. Biomarkers from different subcellular loci were chosen for this purpose.

A membrane associated death receptor-death receptor ligand (CD27-CD27L) interaction [338-340], a mitochondrial anti-apoptotic heatshock protein (HSP60) [341-343] and a nuclear housekeeping protein (MLH1) [57, 344, 345] were chosen. β-actin was chosen as the housekeeping reference gene. Immunoblots and densiometric analysis were done as described in Section 2.4.3.2. The mitochondrial heatshock protein (HSP60) showed relative increased expression in the cisplatin treated cells for each passage compared to the untreated cells with regards to the immunoblot (Figure 5.2b) and the corresponding densiometric analysis (Figure 5.2c). HSP60 is a mitochondrial chaperone protein which is predominantly found in the mitochondrial matrix but can also be found in the cytoplasm [342]. HSP60 plays an anti-

apoptotic role in the mitochondria associated apoptosis pathway where it interacts with Bax (pro-apoptotic member of the Bcl-2 family) to prevent pore formation in the mitochondrial inner membrane which prevents cytochrome C release to the cytoplasm [346]. The role of HSP60 in acquired multi-drug resistance in ovarian cancer is still a controversial topic with conflicting reports in the literature. Up regulated expression of HSP60 desensitizes the cells to the pro-apoptotic signal and is associated with acquired drug resistance [342, 347]. Conversely, in the absence of cisplatin the cells displayed decreased HSP60 expression. This was observed at p7 to p9, indicating altered molecular pathways between the treated and untreated cells. MLH1 expression showed relative increased protein expression for the cisplatin untreated cells (Figure 5.2b and Figure 5.2c). Acquired multi-drug resistance presents with decreased expression of MLH1, a mismatch repair gene, for various cancers as well as ovarian cancers of epithelial origin [57, 348]. No direct link has yet been established between multi-drug resistance and altered mRNA expression of MLH1 [56] which suggests that MLH1 regulation is on a translational level. Evidence indicates that MLH1 is epigenetically repressed by methylation with acquired multidrug resistance where decreased expression of MLH1 results in resistance to apoptosis [55, 348, 349]. Conversely, increased expression of MLH1 sensitizes the cells to pro-apoptotic signals. The epigenetic silencing will decrease MLH1, making this an invaluable biomarker for determining cancer cell malignancy. Two intracellular biomarkers confirmed the reversion of the multidrug resistant cell line A2780cis to a drug responsive cell line, referred to as A2780.

Reversion was also confirmed by flow cytometry using a third biomarker, CD27. CD27 is a tumour necrosis factor associated death receptor with CD70/CD27L being the binding ligand [340]. Qualitative flow cytometry analysis (Section 2.4.3.3) of the fluoroisothiocyanite (FITC) labelled CD27L ligand was evaluated for the cisplatin treated and untreated cells (Figure 5.3). The fluorescence shift for A2780 as compared to control (Figure 5.3, A2780) was not as pronounced as for A2780cis (Figure 5.3, A2780cis). It may appear contradictory that a multi-drug resistant cancer cell line showed increased expression of a death receptor, but this receptor has been shown to have immuno-modulation functionalities. CD27 is crucial in maintaining T-cell immunity [340], B-cell activation [350], NF-κB signal transduction and MAPK/JNK activation [350] as well as acting as a decoy receptor [339]. It is clear that CD27 can modulate the overall inflammatory response. These characteristics make CD27 a significant contributor to avoidance of apoptosis as well as acquired multi-drug resistance.
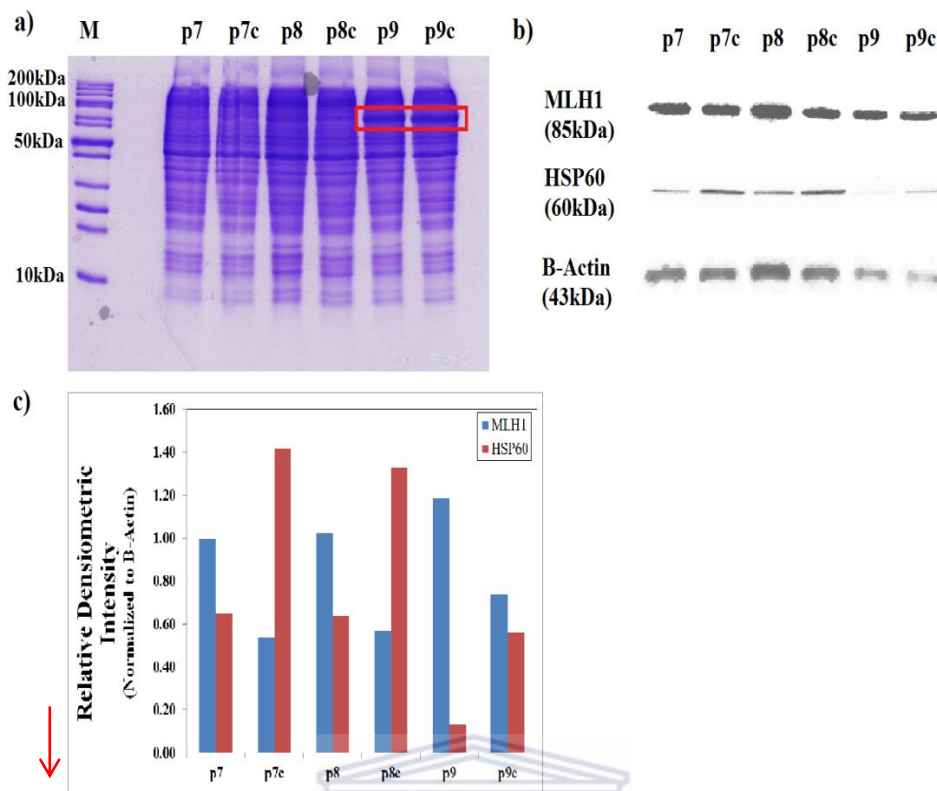
Figure 5.2: The change in relative protein expression in A2780cis cells during reversion from drug resistant to drug responsive. The SDS-PAGE gel for whole cell lysates can be seen in (a) with the corresponding immunoblots for selected biomarkers MLH1 and HSP60. The densiometric analysis of the immunoblot was normalized to β-actin (c). Passage 7, 8 and 9 of A2780cis cells in the absence of cisplatin are in lanes 7, 8 and 9 respectively. Passage 7, 8 and 9 of A2780cis cell treated with 2μM cisplatin are in lanes 7c, 8c and 9c respectively. The cell lysates were resolved on a 14% SDS-PAGE gel using Thermo PageRuler Unstained Protein Ladder (M). Densiometric analysis was done with ImageJ®.
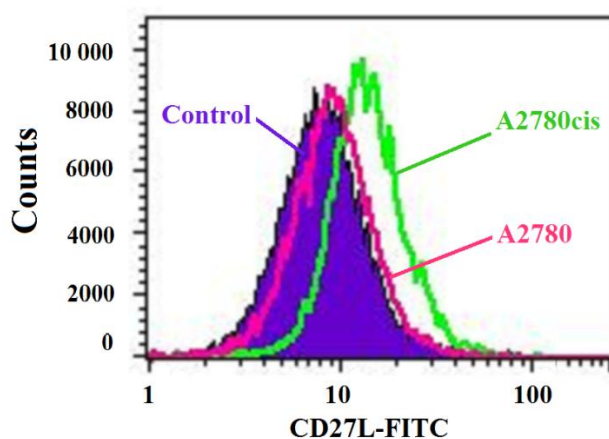
Figure 5.3: Qualitative flow cytometric analysis of the reversion of the multi-drug resistant A2780cis at p9. The multidrug resistant A2780cis (green) cell line shows a shift to the right compared to control. No shift was observed for the drug responsive A2780 cell line. The control was unlabelled cells. A2780cis – cells treated with 2μM cisplatin and A2780 – cells untreated with cisplatin. A total of 10 000 cells were counted.

Reversion of the multi-drug resistant A2780cis to the drug responsive A2780 cell line was successful. The immuno-blotting (Figure 5.2b) and flow cytometry (Figure 5.3) for known

biomarkers indicated molecular differences between the two cell lines. There were also distinct morphological differences between the two cell lines (Figure 5.1). The passive reversion of the cell line in the absence of cisplatin suggested that the cellular cytoprotective response pathways were not essential anymore which is indicative of epigenetic gene regulation. Epigenetic gene regulation has been suggested as the governing factor in ovarian carcinoma malignancy [12, 14, 16, 63], as well as for *in vitro* models such as the A2780/A2780cis paired cell lines [63, 349, 351]. The reversion of A2780cis to A2780 was to generate a genetic identical paired cell line for comparative analysis of cytotoxicity of AuNPs. A2780 and A2780cis cell lines were cultured to passage 9 for all cell based assays in further experiments.

5.2 Gold Nanoparticle (AuNP) Interactions with A2780 / A2780cis Cells

5.2.1 Introduction

Nanotoxicology is a controversial topic in the current literature as new nanotechnology devices are being approved by the FDA for applications in human diagnostics and therapeutics. Environmental concerns have also been raised. It has become necessary to evaluate how nanoparticles interact with biological molecules as well as within living cells *in vitro* and *in vivo*. As such, the paired cell lines A2780/A2780cis were used to determine differential response of the cell lines to AuNPs and their drug loaded variants. The objective was to determine whether a drug delivery system could be developed at ultralow dosages, compared to current *in vitro* drug delivery models, which could overcome multidrug resistance.

Tetrazolium salt cell viability and cytotoxicity assays such as the (3-(4,5-Dimethylthiazol-2-yl)-2,5-diphenyltetrazolium bromide (MTT) assay have fallen out of favour for the evaluation of nanotechnology based treatments as a wide range of nanoparticles were reported to have direct interactions with the cell permeable tetrazolium salts inside the cells [256, 352]. Further, AuNPs have spectral overlap with the MTT assay in the range of 450nm-560nm, dependent on the mean size distribution of the AuNPs. WST-1 (2-[4-iodophenyl]-3-[4-nitrophenyl]-5-[2,4-disulfophenyl]-2H-tetrazolium salt) was chosen as an alternative tetrazolium assay, with a maximum absorption wavelength at 450nm where AuNPs have a minimum absorption wavelength. WST-1 is impermeable to the cell membrane and interacts with a plasma membrane bound NADH-oxidase enzyme with superoxide being the main co-

factor for reduction of the tetrazolium salt [353, 354]. The WST-1 assay would potentially reduce the interference from the nanoparticles on tetrazolium assays, especially if the nanoparticles were internalized into the cells. Other assays that were utilized to evaluate the toxicity of the AuNPs determined the mechanism of cell death, oxidative stress and sub-cellular localization associated with the nanoparticles. The assays used were based on colorimetric detection, luminometric detection and immunoblotting as well as electron microscopy techniques. In general, a time point of 24h post treatment was chosen for analysis as this is a commonly used exposure time for *in vitro* cell based assays for doxorubicin (DOX).

5.2.2 Cytotoxicity Evaluation of the Surface Ligands and Synthesized AuNPs

5.2.2.1   Doxorubicin (DOX) and Polyethyleneimine (PEI)

The cytotoxicity of doxorubicin (DOX) and high molecular weight hyper branched polyethyleneimine (PEI, 15.4kDa) were examined on the cell lines A2780 and A2780cis (Figure 5.4). DOX is a known chemotherapeutic compound and was used to determine if the cell lines had a differential cytotoxicity response. A differential toxicity response for DOX would demonstrate phenotypic differences in the cell lines that were established with biomarkers in Section 5.1.2. PEI of various molecular weights has been reported to have cytotoxic effects *in vitro* [355, 356]. AuNPs were synthesized in a one-pot manner with PEI as a surface ligand (Section 4.3) which made it necessary to determine how toxic PEI was to the cell lines as well as if there was a differential toxicological response between the cell lines. The WST-1 dose response assays were done as described in Section 2.4.5.1.

The A2780 cells (red, Figure 5.4a) showed high sensitivity to DOX with no statistical significant differences between the concentrations of DOX used. The A2780cis (red, Figure 5.4b) cells showed statistical significant differential response to DOX from concentrations of 32μM and lower, where no statistical significance was found between the concentrations of 32μM, 16μM, 8μM and 4μM. This supported the reversion of A2780cis to A2780 (Section 5.1.2), since A2780cis is expected to be resistant to DOX. Further investigation of the paired cell line response to DOX was not conducted at lower DOX concentrations. An approximate LD_{50} of 8μM DOX was chosen for the A2780cis cell line.

High molecular weight PEI (15.4kDa) was very toxic to A2780 (yellow, Figure 5.4a) with statistically significant lowered toxicity at 8μM and 4μM respectively. Comparatively, PEI

was more toxic to A2780cis (yellow, Figure 5.4b) at 4μM PEI than for A2780. However at higher dosages A2780cis displayed a lessened toxic effect than A2780. It appeared that the approximate LD_{50} of PEI for both A2780 and A2780cis was 8μM.
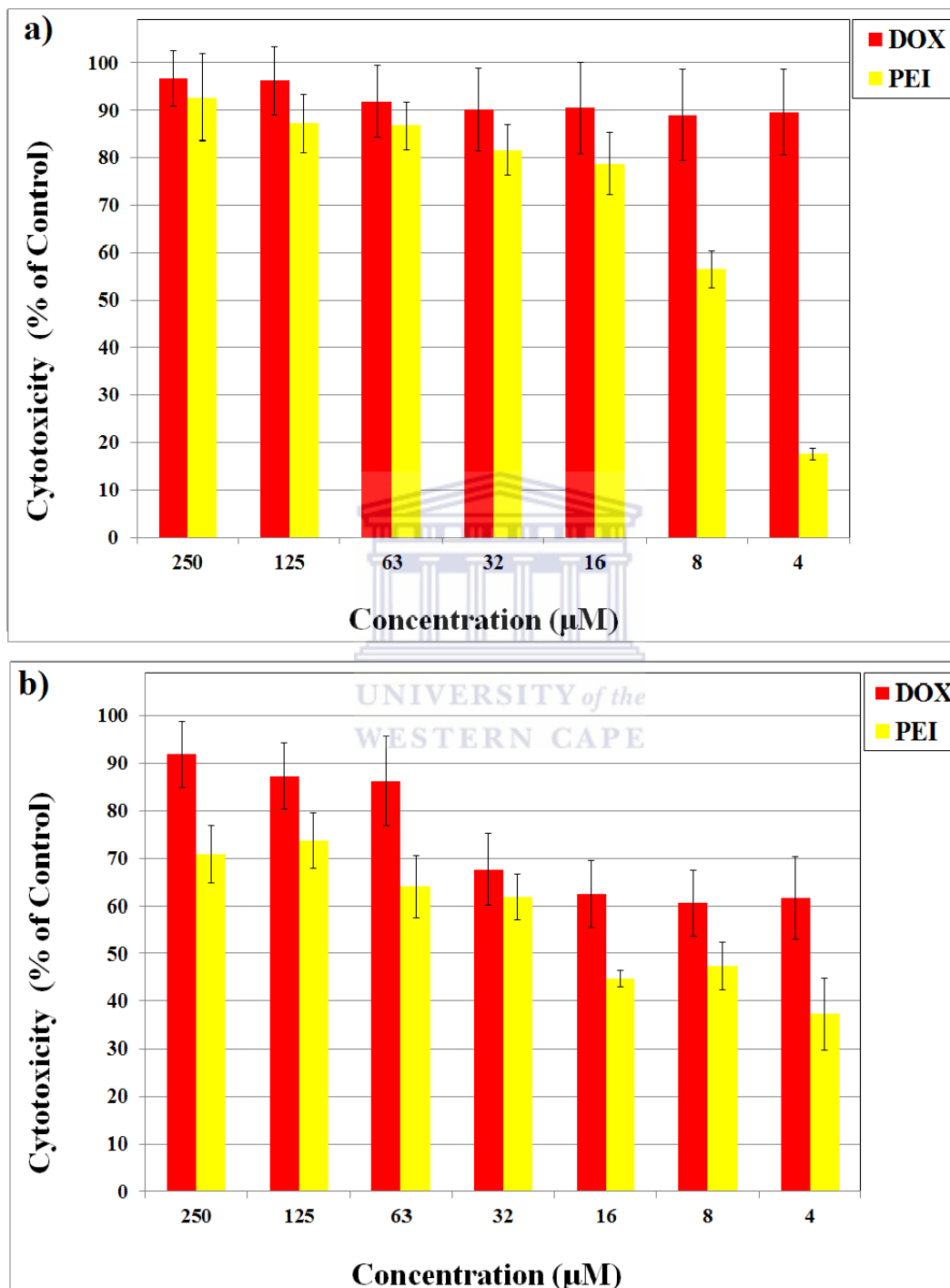
Figure 5.4: Cytotoxicity of Doxorubicin (DOX) and Polyethyleneimine (PEI, 15kDa) on paired ovarian carcinoma cell lines. The drug responsive A2780 (a) cell line is very sensitive to high levels of doxorubicin treatment as opposed to the drug resistant A2780cis cell line (b). The assay was done with WST-1 24h post-treatment and the optical density (OD) measured at 450nm. The assay was done in technical triplicates and biological duplicates. Table A6 shows p-values where $p < 0.05$ was statistical significant (Appendix).

5.2.2.2 Cytotoxicity of Differentially Synthesized One-pot Polyethyleneimine Functionalized Gold Nanoparticles (AuNP-PEI)

Polyethyleneimine (PEI) functionalized AuNPs were synthesized in a one-pot manner (Section 4.3) and evaluated for *in vitro* cytotoxicity (Section 2.4.5.1) on the A2780/A2780cis cell lines. The cytotoxicity for the AuNPs 24h post-treatment can be seen in Figure 5.5. DOX (8μM) was used as a negative control as well as to evaluate relative toxicity of the AuNPs. The AuNPs displayed increased cytotoxicity towards the multidrug resistant cell line (Figure 5.5b) compared to the drug responsive cell line (Figure 5.5a) on a dose-to-dose comparison. Comparison of the approximate LD_{50} values (Table 5.1) for the two cell lines showed overall that the AuNPs were at least twice as toxic for A2780cis than for A2780. AuNP-PEI A showed a trend in lowered cytotoxicity compared to the other AuNPs for both cell lines, where the approximate LD_{50} values were 500pM (Figure 5.5 and Table 5.1). AuNP-PEI A also showed statistical difference in decreasing concentrations from 1000pM to 125pM for both cell lines and was statistically significantly less toxic than the other AuNPs at 32pM for A2780 cells (Figure 5.5a) but only differed statistical significant at 32pM compared to AuNP-D for A2780cis cells (Figure 5.5b). AuNP-PEI B showed statistical significant lowered toxicity from 1000pM to 250pM for A2780 cells (Figure 5.5a) and statistical significant lowered toxicity from 1000pM to 125pM for A2780cis cells (Figure 5.5b). AuNP-PEI C showed aberrant toxicity with a statistical significant lowered toxicity from 1000pM to 125pM with a statistical significant increased toxicity at 63/32pM for A2780 cells. A statistical significant decrease in toxicity was observed for AuNP-PEI C from 100pM to 125pM for A2780cis cells (Figure 5.5b). Cytotoxicity for AuNP-PEI D was statistical significant lower from 500pM to 125pM for both A2780 and A2780cis cells. At 62pM of AuNP-PEI D for the A2780 cells (Figure 5.5a) there was a statistical significant difference compared to 125pM and 32pM. All AuNPs displayed a dose-dependent trend in toxicity. AuNP-PEI A had the overall lowest toxicity on a dose-to-dose comparison with the other AuNPs. AuNP-PEI B/C/D showed dose-dependent decreased toxicity with an increased toxicity from 62pM and lower concentrations, most likely attributed to the irregular shaped AuNPs present in these preparations. AuNP-PEI A/C both have spherical in morphology (Section 4.3.5) where AuNP-PEI B/D nanoparticles have rod-, rectangular- and tetrahedral morphologies (Section 4.3.5). Different aspects of the variation in toxicity of the AuNPs will be discussed in the following few paragraphs. Attention will be paid to AuNP size distribution, surface functionalization and morphology.
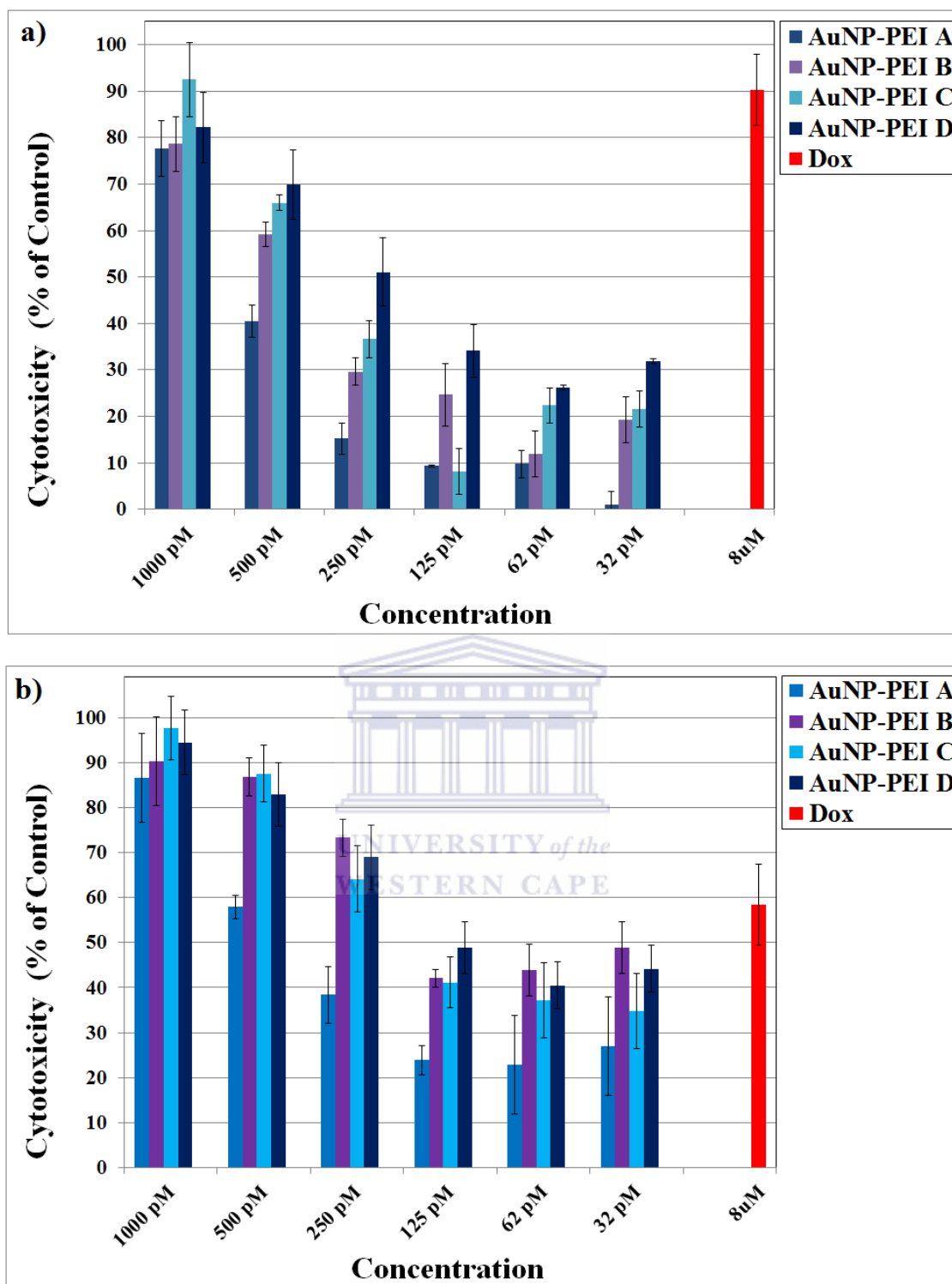
Figure 5.5: Cytotoxicity evaluation for differentially prepared AuNP-PEI nanoparticles in paired ovarian carcinoma cell lines. The drug responsive cell line A2780 (a) and drug resistant cell line A2780cis (b) have a dose-dependent response to the AuNPs. DOX – Doxorubicin. The assay was done with WST-1 24h post-treatment and the optical density (OD) read at 450nm. The assay was done in technical triplicates and biological duplicates. Doxorubicin (DOX) is the positive control. All AuNPs are in 1xPBS (pH 7.2) solution. Table A7 shows p-values where p < 0.05 was statistical significant (Appendix).

Table 5.1: Approximate LD$_{50}$ values chosen for differentially prepared AuNP-PEI and the variance in *in vitro* toxicity to paired ovarian carcinoma cell lines.

	A2780 (pM)	A2780cis (pM)	Fold Cytotoxicity Increase to A2780cis (A2780/A2780cis)
AuNP-PEI A	500	500	1
AuNP-PEI B	500	125	4
AuNP-PEI C	250	125	2
AuNP-PEI D	250	32 - 125	2 – 7.8

 ***Values were chosen based on the value closest to 50% cytotoxicity.**

5.2.2.3 Discussion

Doxorubicin (DOX) and Polyethyleneimine (PEI) are both known cytotoxic molecules. The LD$_{50}$ of 8μM for DOX was near the lower recommended DOX dosage (7μM) used for patient treatment (Section 1.2.3.2.2). This selected concentration of 8μM DOX was used as a reference for further cytotoxicity cell based assays to determine comparative cytotoxicity of the AuNPs. The fold increased cytotoxicity of doxorubicin for A2780 compared to A2780cis was not investigated further as it fell outside the scope of the study. High molecular weight PEI polymers are cytotoxic [355, 356] due to the cationic nature of the molecule which is directly correlated to the amount of amines (primary, secondary and tertiary) found in the molecule, which act as proton acceptors. Low molecular weight PEI (<2kDa) is typically utilized for its well-known transfection capability of DNA [281, 357] and it was expected that high molecular weight PEI (2kDa) would display similar qualities. Even with a wide range of commercial transfection reagents available, PEI is reported to have superior transfection efficiency [281, 357]. Low- and high molecular weight PEI is widely used in nanotechnology applications as a building block for block-co-polymer nanoparticles [282, 283] as well as coatings on metallic nanoparticles [279, 358]. In all these reported studies, PEI facilitated non-viral gene delivery into cells with a very high efficiency [357]. The proton sponge effect would come into effect and facilitate escape from the endosomes to the cytoplasm [255].

Comparative concentrations of citrate capped AuNPs used in the literature indicated dosages from the low nanomolar (nM) [274, 359] to mid micromolar (μM) range [274, 359] with values of up to up to 100μM [359] being reported. In comparison, the prepared AuNP-PEI appeared highly toxic (Table 5.1) with LD$_{50}$ values ranging from 32-500pM. AuNP-PEI A/C both have near spherical nanoparticle morphologies, where toxicity is assumed to be attributed to the polydisperse size distribution as well as the cationic surface functionalization. AuNP-PEI B/D has non-spherical nanoparticle morphologies (rectangular, tetrahedral, etc)

which may have contributed to the observed toxicity in Figure 5.5. The toxicity of AuNP-PEI is governed by the following factors: size; surface functionalization; morphology and other possible factors. These arguments will be raised and discussed in the next few paragraphs

Currently the effect of size on the toxicity of AuNPs towards cells has been investigated with the conclusion that smaller nanoparticles would localize towards a perinuclear region [267, 268, 271, 359] or for the case of ultrasmall AuNPs which can enter the nucleus [271, 359] and even cross the blood-brain barrier [360, 361]. Bigger nanoparticles will be sequestered in the cytoplasm or even be membrane bound to organelles or the plasma membrane itself [267, 268, 359]. A 2012 publication by Huang *et al* [268] demonstrated that smaller anionic AuNPs have deeper tumour penetration as well as sub-cellular penetration capabilities than larger anionic AuNPs. The larger AuNPs were sequestered in the cytoplasm. These AuNPs were functionalized with tiopronin which creates a carboxylic (-COOH) functionality on the AuNP surface, lending the AuNP an anionic charge. These anionic functionalized AuNPs managed to penetrate tumour cells and growths which have a net negative charge, demonstrating the ability of these nanoparticles to overcome potential electrostatic repulsion (Section 1.6.5). Citrate capped AuNPs have been reported to have genotoxicity [192, 275, 361, 362] and acting as pro-oxidants or free radical generators [193, 352, 363] which contributes to cytotoxicity in the cytoplasm. The AuNP-PEI nanoparticles have a polydisperse size distribution by design and as such the AuNPs would have various intracellular loci, ranging from intra-nuclear to plasma membrane bound. Cationic surface functionalized AuNPs showed more toxicity to cells than anionic functionalized AuNPs [210, 254, 273], but cationic surface functionalization for nanoparticles in general were reported to have superior cellular penetration, cellular retention and sub-cellular distribution [254, 255, 279]. A rough estimation determined that there is 55mol PEI per 1mol AuNP-PEI (Section 4.4.4). This means that at a concentration of 1000pM (1nM) AuNP-PEI there is 55nM (0.055μM) PEI, which is 72.7 fold lower than 4μM PEI (Figure 5.4). This suggested that the amount of PEI on the AuNP-PEI surface did not contribute significantly to the toxicity observed for AuNP-PEI A-D. The polydisperse size and cationic surface functionalization of the AuNP-PEI were considered to contribute synergistically towards the high toxicity reported in Figure 5.5 and Table 5.1. This may be true especially for AuNP-PEI A/C, where the nanoparticle morphologies were near spherical. Factors that may further contribute to the observed toxicity for AuNP-PEI B/D will be discussed in the next paragraph.

The exact role that the shapes of the AuNPs play within the cellular environment has not yet been clearly defined. Most studies are conducted done on rod shaped gold nanoparticles [274, 363, 354] and spherical nanoparticles [271, 274, 363, 364], with contradictory or ill-defined explanations. In most studies the gold nanoparticles are CTAB functionalized and as such this author proposes that the surface ligand contributes to the cellular toxicity than the AuNPs themselves [36, 185, 271]. From a catalytic chemistry viewpoint the increased surface area to volume ratio makes nanoparticles ideal as catalyst [141, 365, 366]. Anisotropic (tetrahedral, rods, rectangles, etc.) metal nanoparticles display differential catalytic activity over the spherical morphologies [141, 365, 366]. The heavy metals Au, Pt and Pd display similar catalytic activities but each has its own specific application. Rectangular shapes will have reduced catalytic activity and tetrahedral shapes will display increased catalytic activity [141, 366]. Numerous types of reactions can be catalysed by metallic nanoparticles are numerous and only a few will be mentioned [141, 367]: Hydrogenation, oxidation, reduction, amination and carbonylation. In the complex biological milieu there are many different micro- and macromolecules with unique chemical properties and the possibility exists that these above mentioned reactions could take place. Chemical modification of macromolecules such as nucleic acids (DNA or RNA) and proteins could alter the function of these molecules. In the case of DNA the nanoparticles may affect an epigenetic modification and silence a gene. For proteins the AuNPs could interact with the cysteine residues and bind to the thiol moiety, potentially impeding the protein function. This seemed to be the most reliable explanation why increased toxicity was found for AuNP-PEI B/D (Figure 5.5). As mentioned in Chapter 4 (Section 4.3.4), separation of the AuNPs based on different sizes and morphologies was unsuccessful and needs further investigation to determine the toxicity of different AuNP morphologies and size distributions on the ovarian carcinoma cells.

New evidence is emerging that citrate capped gold nanoparticles are not as biocompatible as previously assumed. Interactions with cellular thiols from small molecules as well as larger macromolecules have been identified (Section 1.6.5). Typically AuNPs evaluated for toxicity and reported in the literature get prepared by one of the following techniques: (i) Turkevich prepared AuNPs (Section 1.6.2.1); (ii) Brust one-pot thioalkane functionalized AuNPs (Section 1.6.2.1) and (iii) Inverse micelle CTAB passivated AuNPs [141]. Citrate or CTAB are electrostatically absorbed on the AuNP surface [141]. Bio-functionalization of these AuNPs requires ligand exchange (Section 1.6.2.1). When the ligand on the AuNP surface is electrostatically absorbed on the surface instead of attached by a covalent bond, the AuNPs

could display colloidal instability in the biological milieu. Electrostatic AuNP surface functionalization can be disrupted by NaCl or other inorganic salts such as $CaCl_2$. This is utilized in nanoparticle flocculation assays to determine whether biomolecules are covalently or electrostatically attached to the AuNP surface [331, 368, 369]. Tissue culture media contains a cocktail of salts at various ionic strengths. Also, human blood is rich in inorganic salts. These salts can displace the electrostatic absorbed surface ligands and induce nanoparticle aggregation. A question comes to mind: During the cell based assays, is cell death induced by unstable nanoparticles or by much larger aggregates? Aggregates are not as homogenously dispersed as the smaller nanoparticles. The aggregates could accumulate on top of the cells, piercing the cell membrane or rupture the cell membrane by sheer weight of mechanical force. The same argument can be made in the case where electrostatic absorption is utilized to functionalize the AuNPs with anticancer compounds or poly-phenolic compounds. This question is rarely addressed in biomedical nanotechnology publications to date. Mirza *et al* demonstrated in 2011 that electrostatically adsorbed DOX on Turkevich prepared AuNPs aggregated in PBS (pH 7.4), acetic acid (pH 2.4) as well as HCl (pH 1) [370]. The only solution the AuNPs were stable in was 2-(*N*-morpholino)ethanesulfonic acid (MES) at pH 6. The stability in MES was most probably due to the sulfonic acid moiety's affinity for AuNP surfaces [371] and no proof was provided that the DOX was not displaced from the AuNP surface by MES. AuNP-PEI A-D proved to be stable in a wide concentration range of NaCl (Section 4.3.6) but displayed colloidal instability in the presence of a strong counter-ion such as citrate (Section 4.3.6) as well as biomolecules such as bovine serum albumin (Section 4.4.3) and tissue culture media (Section 4.4.3). The surfaces of AuNP-PEI A-D was shown to not be exposed for biomolecule interactions, unlike citrate capped AuNPs, which was demonstrated by the high stability of the AuNP-PEI nanoparticles in the presence of a strong competing thiol namely β-mercaptoethanol (Section 4.3.6). Aggregation of AuNP-PEI A-D was not induced by β-mercaptoethanol as readily as for AuNP-GSH A-D. This suggested PEI shielded the AuNP surface better than GSH. The PEI on AuNP-PEI interacted with biomolecules, demonstrated for a strong counter-ion such as citrate (Section 4.3.6), bovine serum albumin (Section 4.4.3), and tissue culture media (Section 4.4.3). Aggregation associated toxicity or unfavourable interactions with biomolecules could be a possible reason for the observed cytotoxicity of AuNP-PEI A-D as well.

AuNP-PEI A was chosen for drug loading as it displayed the least cytotoxicity of all the AuNPs as well as the nanoparticles being near-spherical in morphology. This reduced the

factors which could influence cytotoxicity, where AuNP size distribution and surface functionalization was then assumed to be the main contributors. AuNP-PEI A as well as its drug loaded variants, 10-30% PEG, was evaluated to determine the possible causes of the toxicity.

5.2.3 Cytotoxicity and Mechanism of Cell Death for Doxorubicin Loaded AuNP-PEI A

5.2.3.1 Introduction

Covalent drug loading of doxorubicin (DOX) onto AuNP-PEI A was done as described in Section 2.2.4.3.2. AuNP-PEI A was modified with three polyethylene glycol concentrations (10-30%) as described in Section 2.2.4.3.1 and shown in Section 4.4.2. All AuNPs were in x1 PBS (pH 7.4). As a cytotoxicity reference 8μM DOX was used for all assays. The toxicity for AuNP-PEI A at its LD_{50} value (500pM; Table 5.1 and 5.2.2) was used to compare the cytotoxicity of its drug loaded variants. The mechanism of cell death will be investigated as well as a suggested induction mechanism. The subcellular distribution of the AuNPs was also investigated with transmission electron microscopy. For the purposes of this section, 10-30% PEG DOX from Section 4.4.2 will be referred to as 10-30% PEG.

5.2.3.2 Cytotoxicity of the DOX loaded AuNP-PEI A

Cytotoxicity was determined with the WST-1 assay (Section 2.4.5.1). The A2780cis cells (Figure 5.6b) showed increased sensitivity to the DOX loaded AuNP-PEI on a dose-to-dose basis when compared to the A2780 cells (Figure 5.6a). The lowest dose of 30% PEG, 5.3pM, for both the A2780 cells (Figure 5.6a) and A2780cis cells (Figure 5.6b) was statistically significant different from the higher concentrations of 30% PEG. The other DOX loaded AuNPs (10% / 20% PEG) showed colloidal instability in the presence of biomolecules (results not shown) and were not used for any other cell biology assays. 30% PEG showed the best stability (Section 4.4.2). A summation of Figure 5.6 can be seen in Table 5.2.
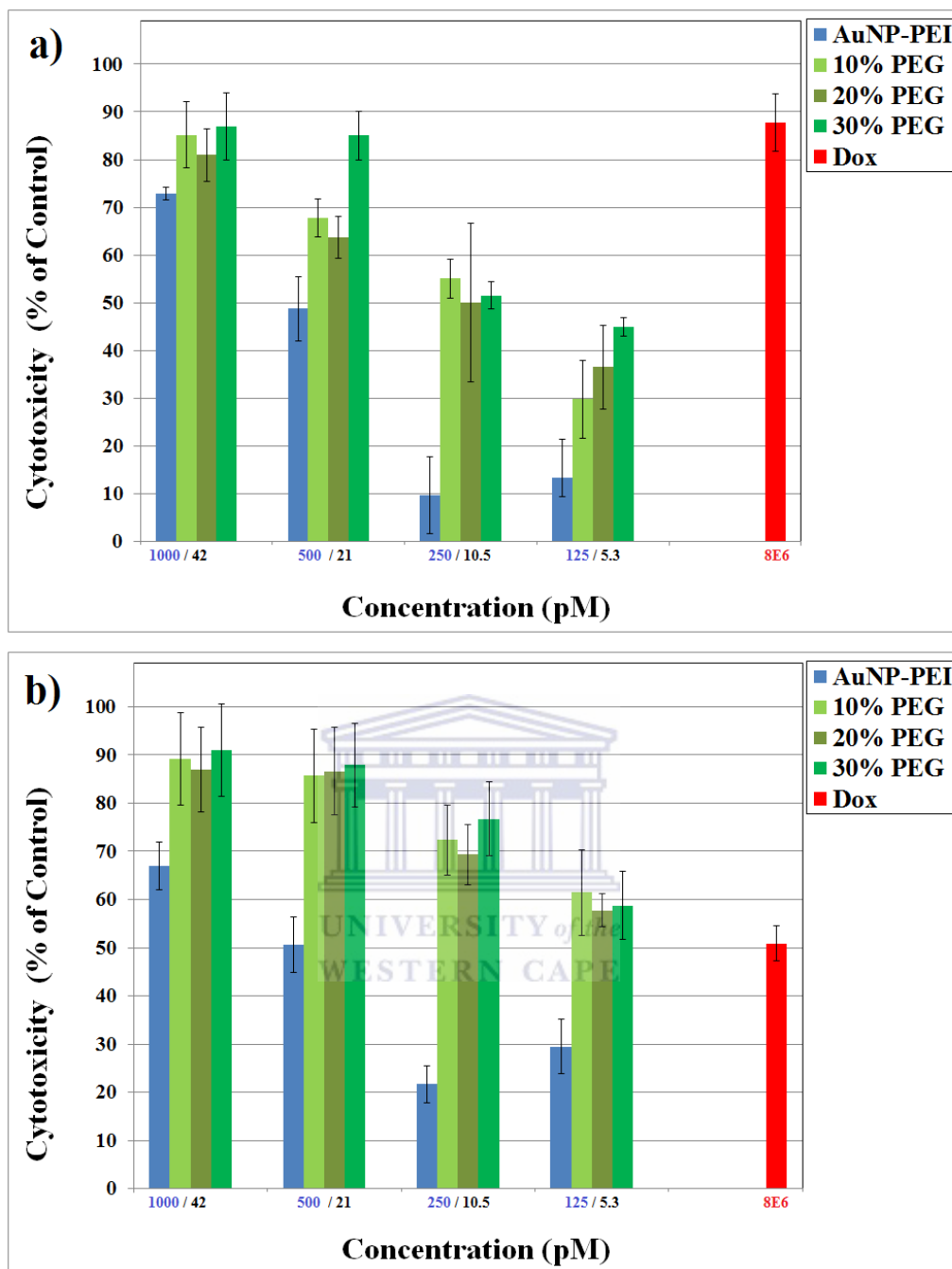
Figure 5.6: Cytotoxicity differentially surface modified-DOX loaded AuNPs. The cytotoxicity for A2780 can be seen in (a) and for A2780cis can be seen in (b). On the X-axis the value in blue is the non-drug loaded AuNP and the value in black indicates the concentration for DOX loaded AuNPs (PEG – Polyethylene glycol; DOX – Doxorubicin; 10% PEG – 10% PEG-DOX; 20% PEG – 20% PEG-DOX and 30% PEG – 30% PEG-DOX). The assay was done with WST-1 24h post-treatment and the optical density (OD) read at 450nm. The assay was done in technical triplicates and biological duplicates. Table A8 shows p-values where $p < 0.05$ was statistical significant (Appendix).

The fold increase in cytotoxicity of the drug loaded variants of AuNP-PEI (10-30% PEG) compared to DOX was calculated based on the *in situ* drug release assay (Section 4.4.2), where it was determined that 4000mol DOX was released per 1mol AuNP-PEI. The LD$_{50}$ values (Table 5.2) for the nanoparticles showed DOX loaded AuNPs had increased

cytotoxicity compared to AuNP-PEI. The drug loaded AuNPs (10-30% PEG, Figure 5.6) were 23.8-fold diluted in concentration compared to AuNP-PEI A at the same optical density (OD ~ 0.2) (Section 4.4.2). The LD_{50} of 5.3pM 30% PEG was ~94-fold less than the LD_{50} of 500pM AuNP-PEI for A2780cis and the LD_{50} of 10.5pM 30% PEG was ~48-fold less than the LD_{50} of 500pM AuNP-PEI for A2780 cells. The drug resistant A2780cis cells were ~2-fold more sensitive to the DOX loaded AuNPs than A2780 cells. The DOX loaded AuNPs were 190-fold more cytotoxic than 8μM DOX for the A2780 cells and 377-fold more cytotoxic than 8μM DOX for the A2780cis cells (Table 5.2). This fold increase in cytotoxicity was calculated based on the concentration of DOX on the AuNP surface where 42nM DOX is delivered for 10pM AuNP-PEI (A2780) and 21.2nM DOX is delivered for 5.3pM AuNP-PEI (A2780cis).

Table 5.2: Approximate LD_{50} values for DOX loaded surface functionalized AuNP-PEI (Calculated based on 4000mol DOX per 1mol AuNP-PEI as per Section 4.4.2).

Formulation	LD_{50} (pM)		Fold Cytotoxicity Increase				
	A2780	A2780cis	A2780/A2780cis	DOX / A2780	AuNP-PEI / A2780	DOX / A2780cis	AuNP-PEI / A2780cis
AuNP-PEI	500	500	1	-	-	-	-
10% PEG	10.5	< 5.3	1.98	190	47.62	377	94.34
20% PEG	10.5	< 5.3	1.98	190	47.62	377	94.34
30% PEG	10.5	< 5.3	1.98	190	47.62	377	94.34
DOX	8×10^6	8×10^6	-	-	-	-	-

*Values were chosen based on the value closest to 50% cytotoxicity.

Gu *et al* (2011) designed AuNP-DOX conjugates for overcoming multidrug resistance in HepG2 (liver carcinoma) cells [372]. The MTT assay was used to assess toxicity after a treatment period of 24h. DOX (20μM) and AuNP-DOX (8μM DOX equivalent) caused 50% of the cells to die 24h post-treatment. This is a fold increase in dosage efficacy of x2.5 for a 24h period. Similarities in this study indicated that the multidrug resistant cell line also displayed increased sensitivity towards the DOX nanoparticle conjugates. A study by Wang *et al* (2011) designed DOX tethered AuNPs to target multidrug resistant MCF7 (breast cancer)

cells [373]. The drug sensitive MCF7 cells showed an LD_{50} of 350μM 72h post-treatment. The multidrug resistant MCF7-AD displayed LD_{50} at two time points for two different nanoparticle-DOX conjugates. At 48h the corresponding dosage was 8.83μM DOX equivalents and at 72h the corresponding dosage was 3.13μM DOX equivalents. This represents an increase in dosage efficacy of x39.6 and x111.8 respectively. Both these cited studies were *in vitro* in nature with no direct translation to *in vivo*. Prabaharan *et al* synthesized folate targeted block-co-polymer passivated AuNP nanoconstructs and achieved a DOX load of 34μg/mL (62μM) per 10mg/mL nanoconstruct, where DOX release was facilitated by a pH sensitive linker [146]. The MTT assay was used to evaluate the toxicity of the above mentioned nanoconstruct in 4T1 (mouse mammary carcinoma) cells with disappointing results. DOX showed a dose-to-dose increased cytotoxicity to the cancer cells than the DOX loaded nanoconstruct. Further, microscopy indicated that the nanoconstructs were sequestered in endosomes. The labile nature of DOX makes it unstable in acidic environments [374] and as such endosome sequestration ($4 \leq pH \leq 6$) would release DOX prematurely to an acidic environment leading to drug degradation. Kim *et al* (2008) utilized pH sensitive micelles to deliver DOX to multidrug resistant A2780 cells *in vitro* as well as *in vivo* xenografted athymic nude mice and found the optimal dosage of DOX is ~17μM administered over a 24h period [375]. In this model 80% of the A2780 cells were still alive 24h post treatment.

All the above mentioned studies utilized the MTT assay as well as used monodisperse citrate capped AuNPs (except Kim *et al*) which were subsequently functionalized by ligand exchange and employment of further bioconjugation techniques. No reports were made for intracellular localization of the AuNPs (except Prabaharan *et al*) with cytotoxicity or cell viability being the only toxicity assays reported. Further, no indication was given what the mechanism of cell death was as DOX is known to induce topical necrosis [26, 34, 376]. DOX dosages delivered by the nanoparticles in the previous paragraph were all in the same range as the clinical dosage, 7μM to 330μM (Section 1.2.3.2.2) and although a direct comparison between *in vitro / in vivo* models and a clinically approved product cannot be drawn, the reported dosages were still high. DOX can present with severe cardiotoxicity, nephrotoxicity and hepatotoxicity at the clinical dosage (Section 1.2.3.2.2). The above mentioned studies showed some success with drug delivery to the drug resistant cells where 50% - 80 % of the cells were alive within 24h-72h of treatment. The high cellular viability 24h post-treatment implies that consecutive treatments were required to achieve complete cell death which could

lead to acquired drug resistance, especially for the ovarian carcinoma (Section 1.2.4.2) where consecutive treatments of doxorubicin is the prescribed treatment post-surgery (Section 1.2.3.2.2).

The DOX loaded AuNP-PEI (10%, 20% and 30%) appeared to overcome the inherent multidrug resistant cytoprotective mechanisms of the A2780cis cells at ultralow DOX concentrations with a single dosage within 24h. The A2780cis drug resistant cells were twice as sensitive to 30% PEG (5.3pM AuNP-PEI and 21.2nM DOX) than A2780 drug responsive cells (10.5pM AuNP-PEI and 42nM DOX) but the type of cell death as well as the induction time of cell death is unknown. The type of cell death as well as the induction time of cell death could potentially differ between the A2780 cell line and A2780cis cell line, but was not investigated due to logistical reasons. Mechanistic studies were limited to the A2780cis cell line. AuNP-PEI (no DOX loaded) and its drug loaded variant 30% PEG, at their respective LD_{50} values, was used to generate a model for cell death.

5.2.3.3 Apoptotic Cell Death is Induced by Gold Nanoparticles

Cytotoxicity only gives an estimate of how many cells are alive for a given time period post-treatment. It does not elucidate any mechanisms of cell death. Further investigation was required to determine how cell death occurred and to propose a model for the cell death observed with the WST-1 cytotoxicity assay. Figure 5.7 shows the qualitative ApoPercentage™ (BioColor) assay (Section 2.4.5.2) to determine if apoptosis was the mechanism of cell death 24h post-treatment treatment with AuNP-PEI (500pM) and 30% PEG (5.3pM)

The control cells (Figure 5.7a) show a few apoptotic cells. A significant number of cells treated with 8μM DOX (Figure 5.7b) stained positive for apoptosis. AuNP-PEI (Figure 5.7d) and 30% PEG (Figure 5.7e) treatment of the cells showed many cells stained positive for apoptosis. Treatment of the cells with 1mM H_2O_2 (Figure 5.7c) showed prominent staining compared to the other treatments as well as floating cells. The cellular morphology was also a qualitative indication of the stage of apoptosis the cells were in. The cells in Figure 5.7c indicated a potential early apoptotic event which ran its course over a 24h time period. Figure 5.7b, Figure 5.7d and Figure 5.7e showed cells which were in different stages of apoptosis. The stages of apoptosis and the time-points of apoptosis were dependent on the dosage of the compound used as well as the type of compound.

A qualitative colorimetric assessment of the amount of cells undergoing apoptosis can be seen in Figure 5.8. The qualitative colorimetric ApoPercentage™ assay (Section 2.4.5.2) was conducted on the same cells which were used to obtain the micrographs for Figure 5.7. The level of apoptosis in the various treatments showed a statistical significant difference compared to the control (Figure 5.8a). The AuNP-PEI and DOX treatments were not statistically different from each other but showed a fold increase in apoptosis of ~2 and ~2.5 compared to control (Figure 5.8b), respectively. The treatment with 30% PEG was similar to that of H_2O_2 (Figure 5.8a), displaying a fold increase in apoptosis of ~3.7 and ~3.2 compared to the control (Figure 5.8b), respectively. Comparison of the cellular morphology for the 30% PEG and H_2O_2 treatments showed the cells were in different stages of apoptosis, but that the level of induction for 30% PEG was increased compared to AuNP-PEI and DOX alone. It is possible that cells detached during the assay as the qualitative colorimetric assay used an alkaline lysis reagent to release the dye from the cells to give a homogenous colour distribution in the wells.
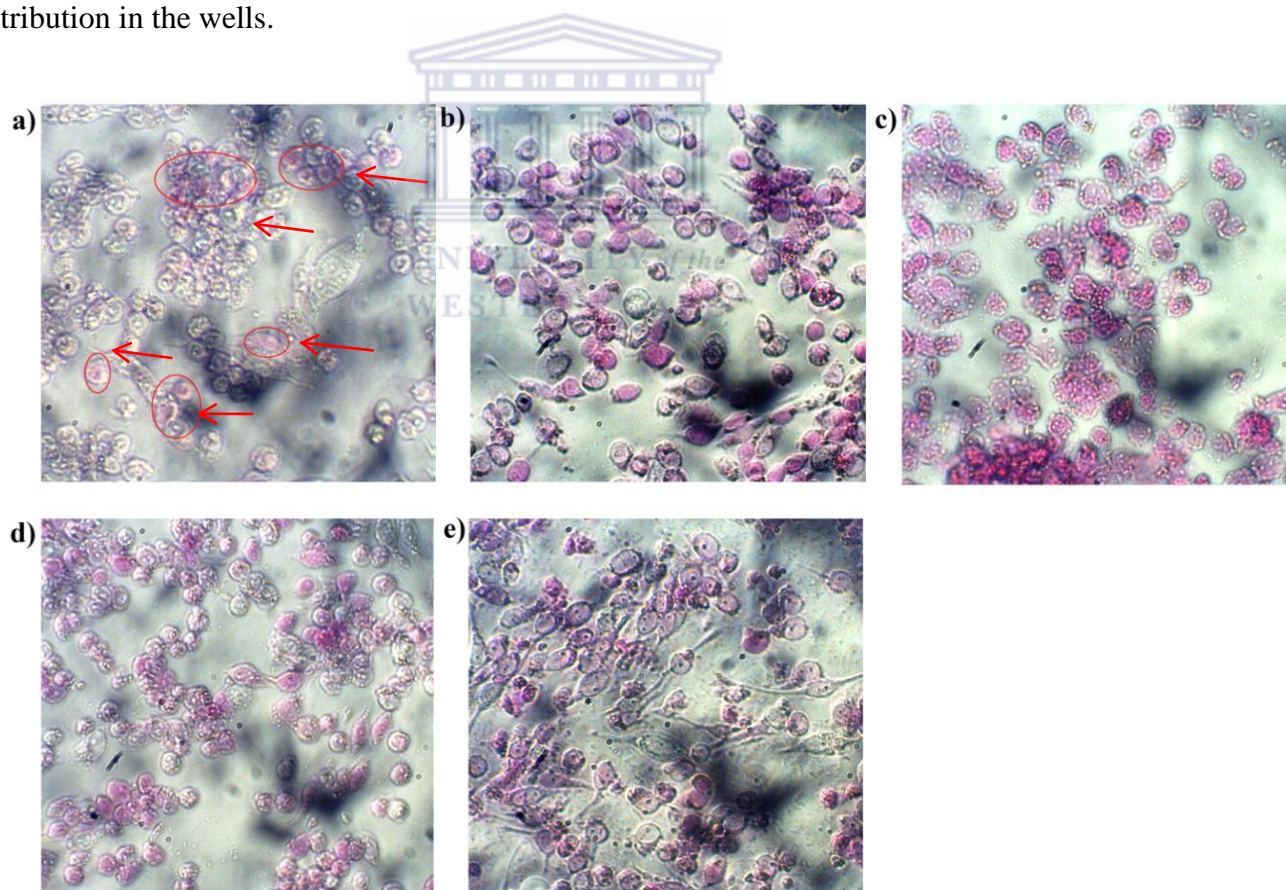
Figure 5.7: ApoPercentage™ (BioColor) assay for the qualitative colorimetric microscopy detection of apoptosis in A2780cis cells 24h post-treatment with AuNP-PEI and 30%PEG. A red-purple stain on the cells indicates apoptosis where: a) untreated control; b) 8µM Doxorubicin; c) 1mM H_2O_2; d) AuNP-PEI and e) 30%PEG. Micrographs are at x20 magnification and are representative of technical triplicates and biological duplicates.

The ApoPercentage™ dye will stain cells undergoing apoptosis by being internalized specifically into apoptotic cells [377, 378]. The assay will not stain for necrotic cell death due to cellular rupture and loss of plasma membrane integrity. The apoptotic cells found in untreated cells (Figure 5.7a) was expected as apoptosis is a normal cellular event to maintain tissue homeostasis [379]. DOX is known to induce cell death by apoptosis and necrosis by H_2O_2 generation [28, 29] in a 24h time window and has been demonstrated in Section 5.2.2.1. The H_2O_2 treatment caused significant loss of cellular morphology. The manufacturer recommends the use of H_2O_2 as a positive control for apoptosis mediated by an oxidative stress pathway within 3h for most cells [29, 377]. Further, 30% PEG (5.3pM AuNP-PEI and 21.2nM DOX) showed a similar level of apoptosis induction as H_2O_2 (1mM). This suggested 30% PEG was a very potent inducer of apoptosis considering this is a multidrug resistant cell line. Comparison of the micrographs for AuNP-PEI (Figure 5.7d) and 30% PEG (Figure 5.7e) with the cytotoxicity data (Figure 5.6) showed a discrepancy. The micrographs indicated more than 50-60% of the cells are undergoing apoptosis (red stains), compared to the 50-60% cytotoxicity reported with the WST-1 assay (Figure 5.6) which will be discussed after the next paragraph.

Apoptosis (Figure 5.9) is the preferred mechanism of cell death chemotherapeutic compounds used in cancer treatment as it is non-inflammatory to adjacent cells [380]. Apoptosis is mediated by the immune system [380, 381, 382] and an ATP-dependent [380, 381] process characterized by cell shrinkage [380, 382], membrane blebbing [380, 382], chromatin condensation [380, 382] and nuclear fragmentation [380, 381, 382]. Macrophages will absorb the cellular vesicle residue post-apoptosis [380, 382]. Necrosis (Figure 5.9) on the other hand is a pro-inflammatory process [383] which is an ATP-independent cellular event characterized by cellular and organelle swelling with no nuclear- or membrane condensation as well as leakage of cellular contents to the extracellular matrix with inflammation to nearby cells [383]. Apoptosis can be one of various pathways where the two most well established and studied are the intrinsic or mitochondrial pathway [380, 381] and the extrinsic or death-receptor mediated pathway [380, 381]. The intracellular pathway is induced by intracellular stress such as oxidative damage [380, 384, 385] or DNA damage [380, 384, 385]. The extrinsic pathway is mediated by extracellular signals to cellular receptors to induce apoptosis [380, 384, 385].
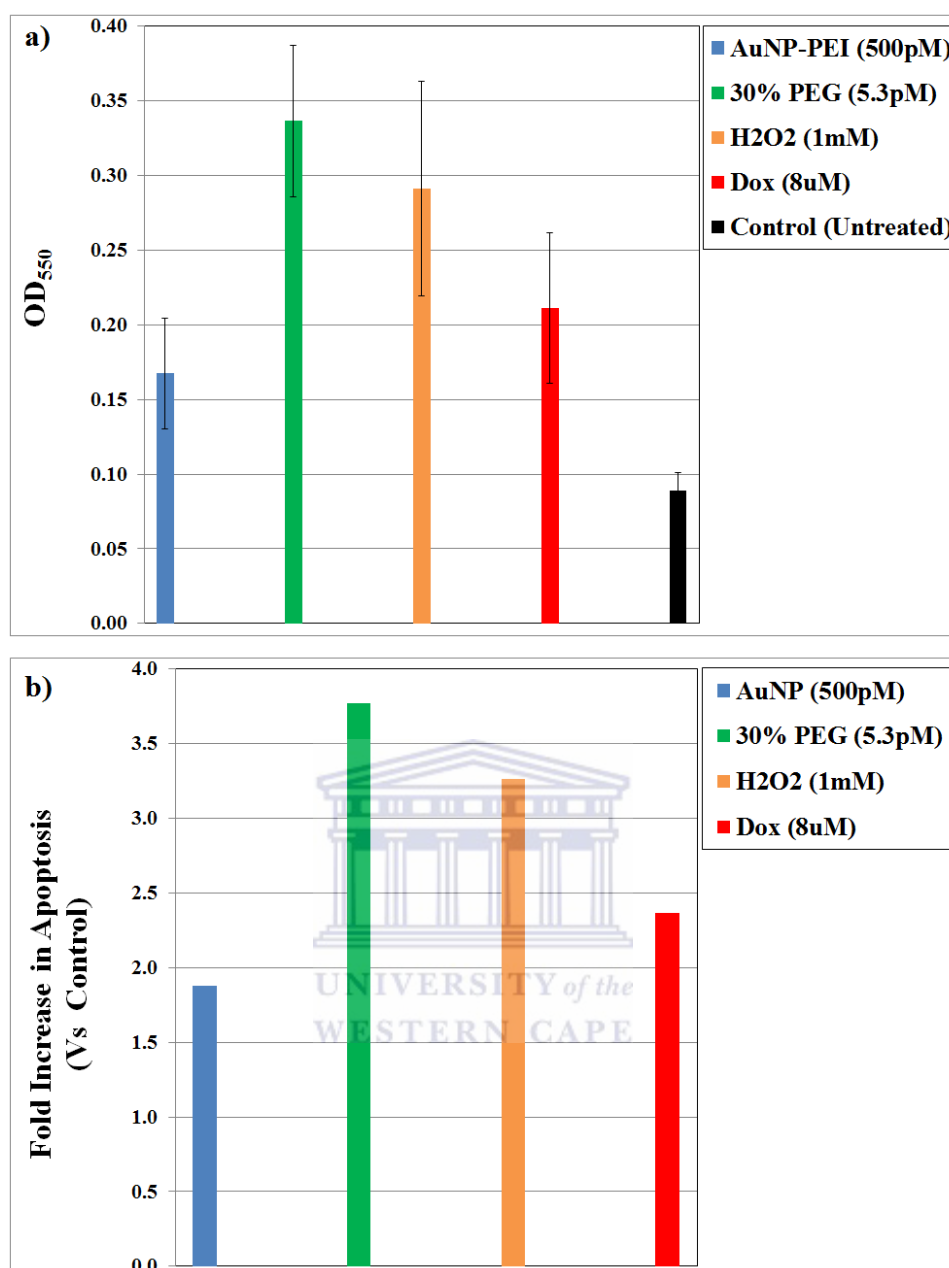
Figure 5.8: ApoPercentage™ (BioColor) assay for the qualitative colorimetric detection of apoptosis 24h post-treatment. The relative increase in apoptosis in the A2780cis cells 24h post-treatment with the selected inducers can be seen compared to the control (a). An increase in optical density is directly correlated to the extent of apoptosis activation. The fold increase in apoptosis relative to control can be seen in (b). The assay was done in technical triplicates and biological duplicates. The optical density (OD) was read at λ = 550nm. Table A9 shows p-values where p < 0.05 was statistical significant (Appendix).

The cell morphologies (Figure 5.7) display the morphological hallmarks of apoptosis with Figure 5.9 as a guideline. The energy requirement of apoptosis as an active cellular process requires active enzymes. Dehydrogenase enzymes contribute to the production of reduced energy carriers, such as NADH and $FADH_2$, which facilitate ATP production. WST-1 undergoes enzymatic conversion by a plasma membrane bound NADH-oxidase [353, 354], and this enzyme can potentially be influenced by altered intracellular concentrations of

reduced NADH/NAD$^+$. The NADH-oxidase enzyme could retain sufficient activity in the late stages of apoptosis and as such influence the colorimetric WST-1 reaction. It is unknown if the protein expression of this NADH-oxidase was altered during the apoptotic event for the different treatments used in this section.
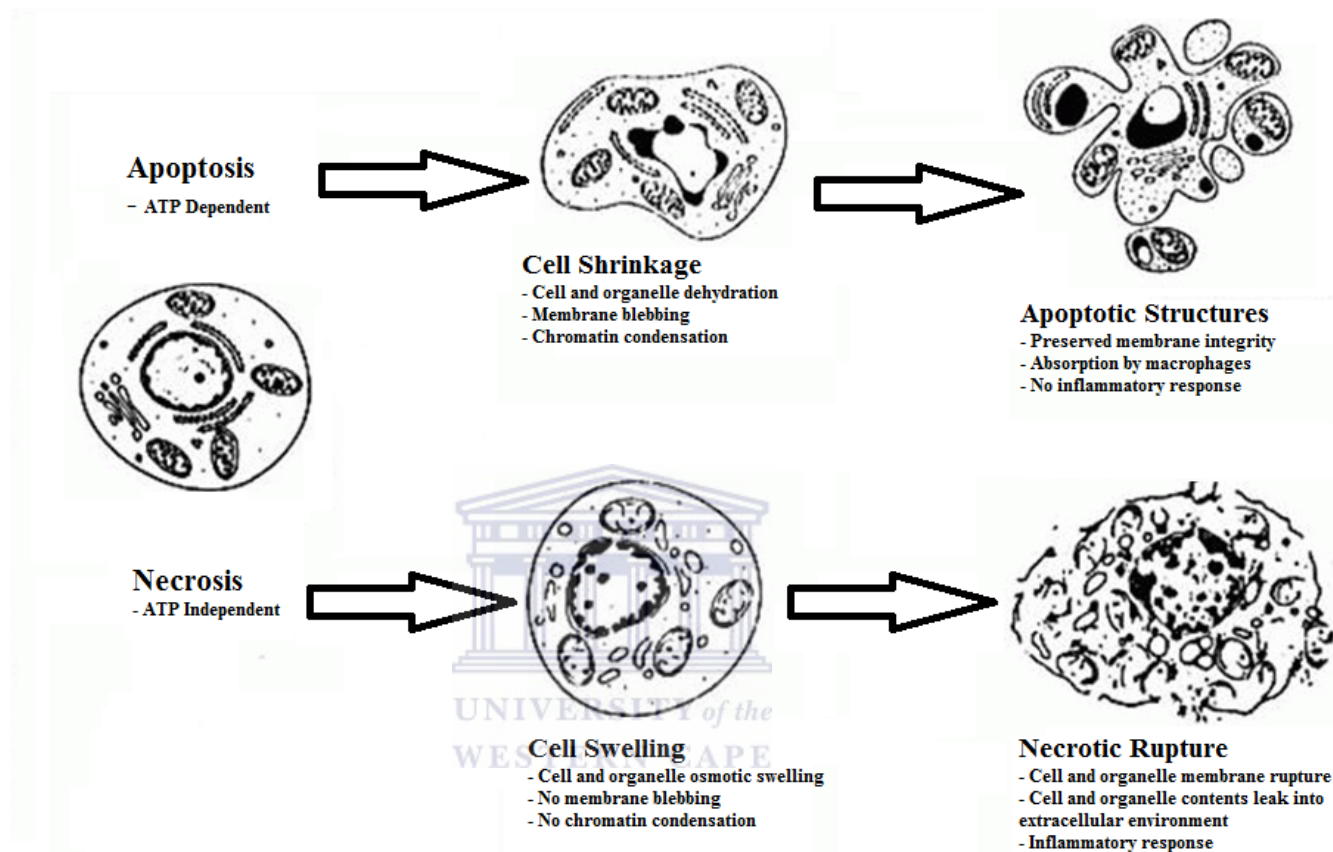
Figure 5.9: The two major forms of cell death: Apoptosis and necrosis. (Image obtained and adapted from http://www.icms.qmul.ac.uk/flowcytometry/uses/oncosis).

AuNP-PEI and 30% PEG induced apoptotic cell death in multidrug resistant ovarian carcinoma cells (A2780cis) at ultralow dosages of DOX within 24h. The pathway of induction of apoptosis as well as the time-point of induction is still unknown and will be investigated in the next few sections.

5.2.3.4 Caspase-3 as an Effector of Apoptosis Induced by Nanoparticle Cytotoxicity

An immunoblot (Section 2.4.5.3) for procaspase-3 was done 24h post-treatment with AuNP-PEI, 30% PEG and DOX to determine if apoptosis was induced by the mature effector caspase-3. The immunoblot can be seen in Figure 5.10a with the corresponding densiometric

analysis in Figure 5.10b. The relative expression levels of procaspase-3 showed a decreasing trend compared to control (Figure 5.10b) for AuNP-PEI, 30% PEG and DOX.

A decrease in procaspase-3 levels correlated to activation of mature caspase-3. The antibody utilized for the immunoblot (Figure 5.10a) is monoclonal specific to procaspase-3 and would not detect caspase-3. Apoptosis was induced by caspase-3 activation for AuNP-PEI, 30% PEG and DOX. The time-point of procaspase-3 activation to mature caspase-3 after treatment with 30% PEG was investigated with a 48h time-course study (Figure 5.11). The immunoblot (Figure 5.11a) and the densiometric analysis (Figure 5.11b) show a decrease in procaspase-3 compared to the control at the different time-points. The trend in decrease of procaspase-3 in the control cells at different time-points was expected as this is a normal cellular event with cells undergoing apoptosis, but was not to the same extent as for the 30% PEG treated cells (Figure 5.11a and Figure 5.11b). The time course activation indicated procaspase-3 was activated at 3h post treatment with 30% PEG in a time-dependent manner which showed decreased procaspase-3, with no procaspase-3 detected at 48h post treatment (Figure 5.11b).
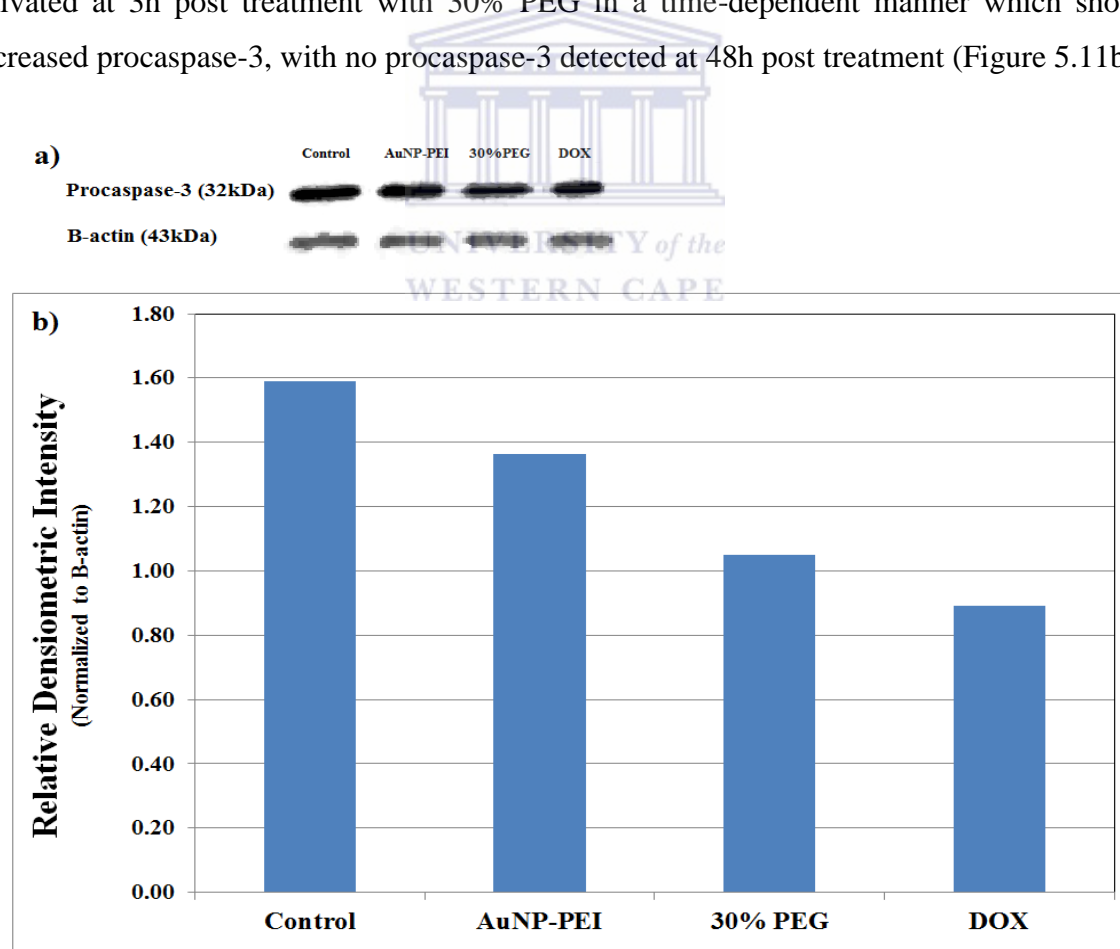
Figure 5.10: Immunoblot for the detection of procaspase-3 activation 24h post-treatment. The immunoblot can be seen in (a) and the relative normalized densiometric analysis (ImageJ) can be seen in (b). β-actin is the loading control for the immunoblot. Dosages used for treatment are the LD$_{50}$ values from Table 5.2. The control was untreated. The data is representative for all assays.
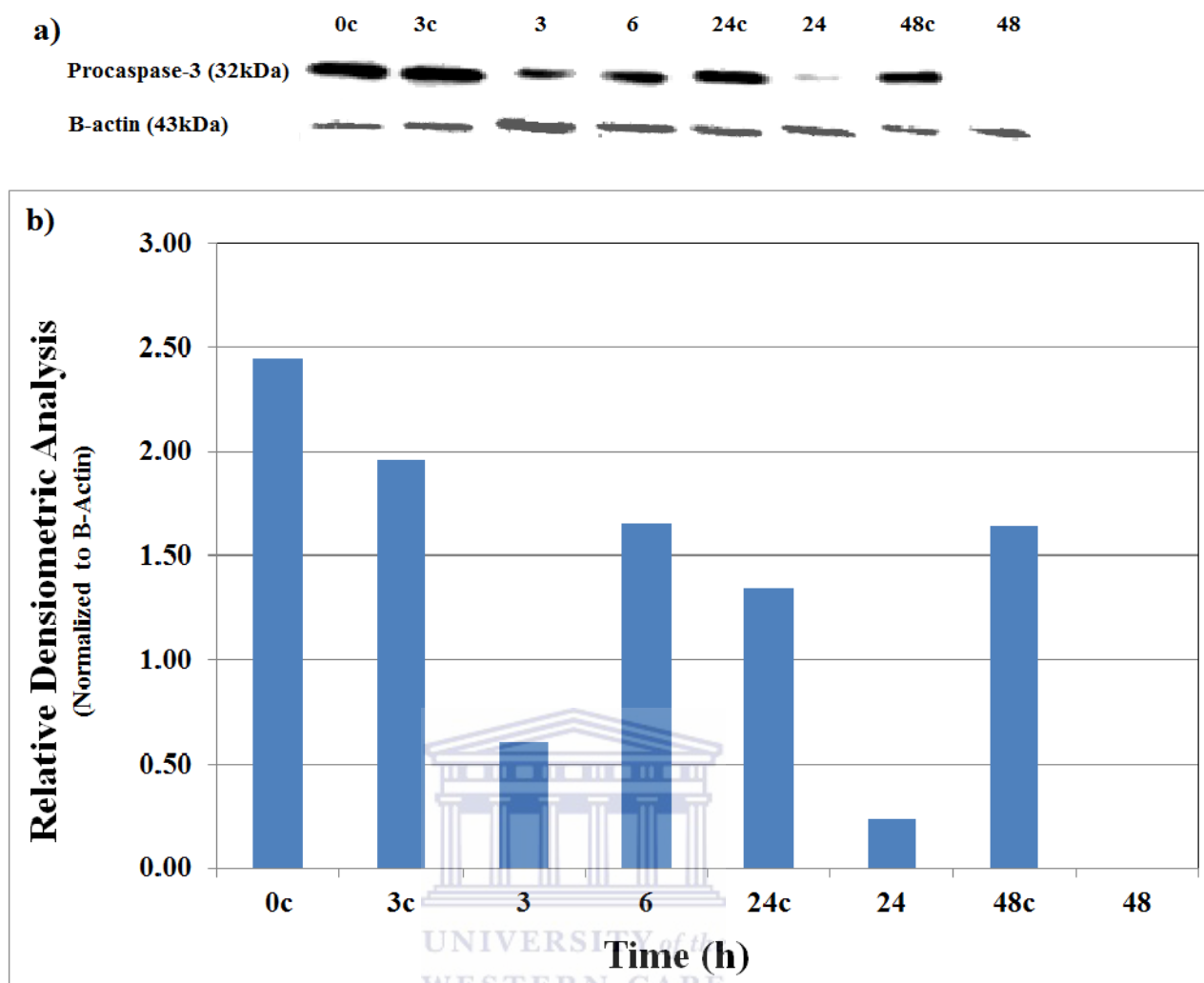
Figure 5.11: Immunoblot for the detection of caspase-3 activity in a time-course dependent manner over 48h. The immunoblot can be seen in (a) and the relative normalized densiometric analysis can be seen in (b). β-actin is the loading control for the immunoblot. Dosages used for treatment are the LD$_{50}$ values from Table 5.2. (3, 6, 24 and 48 are the respective hours post-treatment; 0C, 3C, 24C and 48C are the untreated controls at the respective time points. The data is representative for all assays.

Relative protein expression of procaspase-3 will decrease as it gets activated to mature caspase-3, the effector for the intrinsic pathway of apoptosis (Section 5.2.3.3). This suggested 30% PEG induced apoptosis by DNA damage or oxidative stress, which corresponds to expected mechanisms of cellular stress associated with DOX [28, 385] and caspase-3 was reported as the effector caspase for DOX [28, 385]. The pathway of apoptosis induction by AuNP-PEI, 30% PEG and DOX was mediated caspase-3. Further, the induction time-point of apoptosis after treatment with 30% PEG took place within 3h at ultralow dosages of a DOX (21.2nM). It is unknown however whether the activation of caspase-3 is in response to oxidative stress or nuclear associated toxicity. This will be investigated in Sections 5.2.3.5 and 5.2.3.6, respectively.

5.2.3.5 Oxidative Stress as a Cause of Apoptosis and Caspase-3 Activation Induced by Gold Nanoparticles

Glutathione (GSH) is a major significant intracellular antioxidant (Section 1.2.4.2.2) which also plays a role in drug efflux for drug resistant cancer (Section 1.2.4.2.3). Oxidative stress is an indicator of cytotoxicity and can be determined by monitoring intracellular GSH levels. A commercial luminescence assay (Section 2.4.5.4) was utilized to determine reduced glutathione (GSH) and oxidized glutathione (GSSG) 24h post treatment with AuNP-PEI, 30% PEG, DOX and H_2O_2 (Figure 5.12).

30% PEG showed statistically significant GSH (Figure 5.12a) and GSSG (Figure 5.12b) depletion compared to the untreated control, where the GSH/GSSG depletion was as extensive as observed for DOX or H_2O_2. The fold increase in GSH (Figure 5.12c) and GSSG (Figure 5.12d) depletion for 30% PEG is ~13.5-fold and ~15-fold compared to the control, respectively. The fold increase in GSH and GSSG depletion for AuNP-PEI is ~1.5-fold and ~1.6-fold compared to the control, respectively. The treatment with 30% PEG resulted in more extensive intracellular depletion of GSH and GSSG than AuNP-PEI. The fold increase in GSH depletion for DOX and H_2O_2 were ~86-fold and ~63-fold compared to control, respectively. Also, DOX and H_2O_2 resulted in GSSG depletion of ~51-fold and ~46-fold compared to control, respectively.

Reduced glutathione (GSH) plays an integral role in the cytoprotective mechanism for DOX induced oxidative stress [72]. The depletion of GSSG prevents the cell from recycling GSSG to GSH mediated glutathione reductase (GRx) [69, 387] as depicted in Figure 5.13. GSSG will be recycled to GSH which is dependent on reduced electron carrier NADH. The depletion of GSH as well as GSSG results in intracellular depletion of this antioxidant. The depletion of total glutathione in the cell indicates cellular efflux of GSH-conjugated electrophiles, catalysed by glutathione-S-transferase (GST) [69, 387]. Spontaneous nucleophilic attack of the thiol of GSH can also conjugate this tripeptide to reactive electrophilic species with subsequent cellular efflux [66]. Intracellular GSH depletion and disturbance of the GSH:GSSG homeostasis is known to be the major inducer of apoptosis [69]. The above mentioned mechanisms are reported for DOX and H_2O_2 [28, 29].
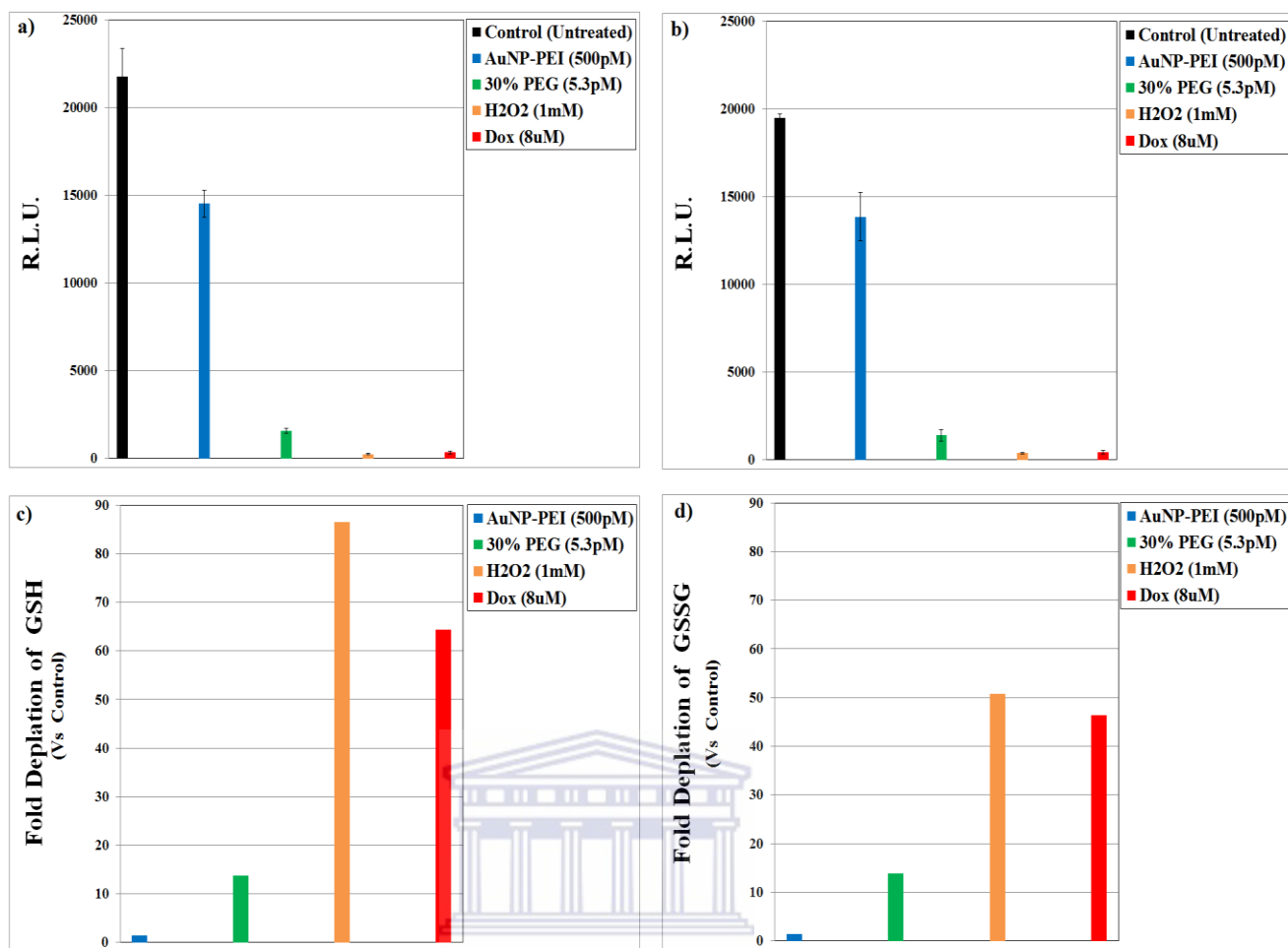
Figure 5.12: GSH/GSSG-Glo (Promega) assay for the qualitative detection of reduced glutathione (GSH) and oxidised glutathione (GSSG) levels. The relative luminescence units (R.L.U.) can be seen for reduced glutathione (GSH) in (a) and for oxidized glutathione (GSSG) in (b). The assay was done 24h post-treatment. The assays were done in technical triplicates and in biological duplicates. Table A10 shows p-values where p < 0.05 was statistical significant (Appendix).
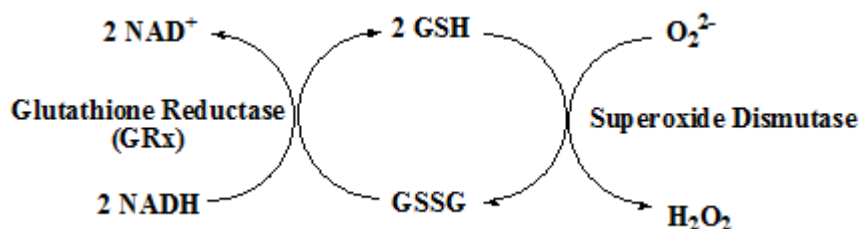
Figure 5.13: The glutathione recycling pathway

AuNP-PEI showed significant less total glutathione depletion compared to 30% PEG, DOX or H_2O_2. Induction of oxidative stress by intracellular depletion of total glutathione is a suggested pathway for the induction of apoptosis by AuNP-PEI and 30% PEG. This corresponded to the data in Section 5.2.3.4 as oxidative stress is a known pathway for caspase-3 activation. The depletion of total intracellular glutathione was significant as this

tripeptide has been implicated as a significant contributor to the cytoprotective mechanisms of multidrug resistance (Section 1.2.4.2.2). The tempo of GSH- as well as GSSG depletion is unknown as the assay was done 24h post-treatment with AuNP-PEI and 30% PEG. The activation of caspase-3 was within 3h of treatment which indicated that significant oxidative stress had already taken place for 30% PEG. This however needs to be confirmed with more directed time-course assays. Caspase-3 activation was determined to be by an oxidative stress pathway. In the next section the subcellular localization of AuNP-PEI and 30% PEG was investigated.

5.2.3.6 Subcellular Localization Of Gold Nanoparticles

The subcellular localization of AuNP-PEI (Figure 5.14) and 30% PEG (Figure 5.15) in A2780cis cells 24h post-treatment was investigated by biological transmission electron microscopy (TEM) (Section 2.4.5.5). The TEM analysis was done at 24h post-treatment to determine the sub-cellular localization of the above mentioned AuNPs.

The A2780cis cell cross sections (Figure 5.14) showed healthy cells as well as cells that were in various stages of apoptosis with fragmented and condensed nuclei as well as disrupted cytoplasmic structures. The areas in the cell cross sections which were of interest were highlighted in red (Figure 5.14a), blue (Figure 5.14b) and green (Figure 5.14c). In Figure 5.14a AuNP-PEI showed cytoplasmic localization with no organelle specific association observed. However, AuNP-PEI nanoparticles were not individually dispersed through the cytoplasm and displayed near circular patterns of localization with regards to each other. AuNP-PEI also showed perinuclear cytoplasmic localization (Figure 5.14b and 5.14c) without any apparent association with particular cellular organelles or structures. Once again the same arrangement patterns for AuNP-PEI were observed which suggested a possible association with an unobserved organelle. AuNP uptake was not observed for all cells, but uptake appeared to be associated with aberrant nuclear morphology and size as well as fragmented cytoplasmic structure. Cells which showed no AuNP-PEI content presented with intact nuclear and cytoplasmic structures (not highlighted).
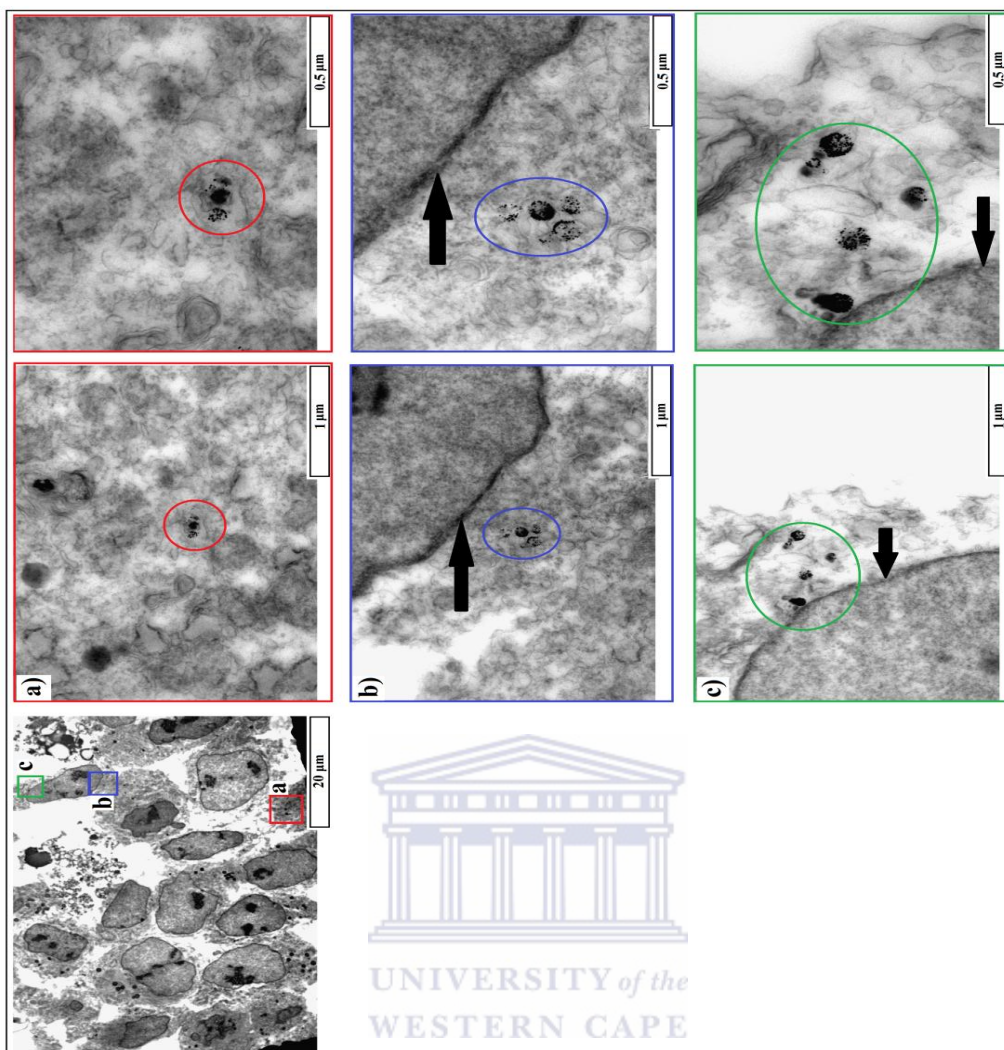
Figure 5.14: Biological HR-TEM micrograph of A2780cis cell cross sections 24h post-treatment with 500pM AuNP-PEI. AuNPs are cytoplasmic localized in a cell in the late stages of apoptosis and can be seen in (a) indicated by the red rectangle. AuNPs in perinuclear localization can be seen in (b), indicated by a blue rectangle, and in (c), indicated by a green rectangle. Nuclear membranes are indicated by black arrows (b, c).

The A2780cis cells treated with 30% PEG (Figure 5.15a and Figure 5.15b) showed a decrease in cell number, compared to AuNP-PEI treated cells, where most of the cells displayed a loss of nuclear- and cytoplasmic integrity. A significant amount of vesicles and cellular debris was found. The 30% PEG (Figure 5.15a, red) appear to be in a cytoplasmic region sequestered in organelles in close proximity to a condensed nucleus (Figure 5.15a, green). Figure 5.15b shows 30% PEG sequestered in organelles (Figure 5.15b, blue) in an extracellular localization with a fragmented plasma membrane in close proximity to a condensed nucleus (Figure5.15b, yellow). For Figure 5.15a and Figure 5.15b the morphologies of the condensed nuclei as well as the organelle specific sequestration of the AuNPs indicated intermediate to late stage apoptosis.
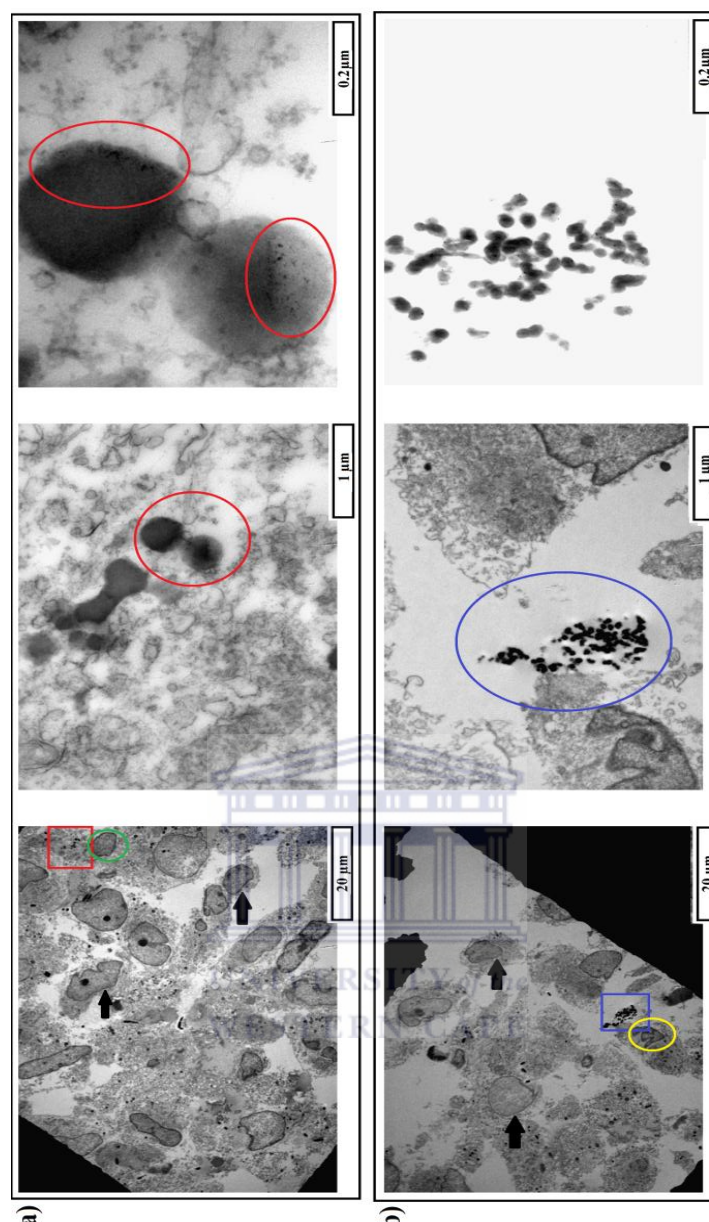
Figure 5.15: Biological HR-TEM micrograph of A2780cis cell cross sections 24h post-treatment with 5.3pM 30% PEG. Different sections of the TEM copper grid can be seen in (a) and (b). Black arrows indicate disrupted nuclei and disrupted cytoplasmic integrity. Green (a) and yellow (b) indicates condensed and fragmented nuclei. Red (a) and blue (b) indicates AuNPs.

AuNP-PEI demonstrated cellular retention as well as intracellular penetration in the A2780cis cells 24h post-treatment. This was however a qualitative assessment of the nanoparticle content of the cells and ICP-MS would be able to give a more quantitative answer. The AuNP-PEI showed cytoplasmic and nuclear localization with no observed organelle sequestration. This added merit to the study design where it was speculated that AuNPs polydisperse in size would have multiple subcellular loci. The toxicity also appeared to be associated with AuNP-PEI internalization, where cells which did not internalize AuNP-PEI appeared to present with normal morphology. The nuclear shrinkage as well as disturbed

cytoplasmic structures suggested that the stage of apoptosis for A2780cis cells, which internalized AuNP-PEI, was early to intermediate as no apoptotic vesicles were observed. The proximity of the AuNP-PEI to the nucleus also indicated possible nuclear toxicity but no AuNP-PEI was seen within the nuclei. The A2780cis cell cross-sections for 30% PEG treatment showed cells which were in intermediate to late stages of apoptosis 24h post-treatment with a large number of condensed and fragmented nuclei as well as apoptotic vesicles. It is unknown what the sub-cellular localization of 30% PEG was as the nanoparticles were sequestered in organelles within apoptotic cells / apoptotic vesicles. A time-course experiment will be ideal to investigate this above mentioned observed phenomena. The type of organelles in which 30% PEG was sequestered is unknown and would require organelle specific immunohistology to be identified. An assumption was made that the unknown organelles were lysosomes as this is an organelle which has been reported in the literature with a peri-nuclear localization during AuNP sequestration [154]. An assumption was made that the 30% PEG delivered the DOX payload because the A2780cis cell cross sections showed evidence of significant apoptosis. Nuclear toxicity could have contributed to induction of apoptosis for 30% PEG in the event where it was in a perinuclear loci, delivering DOX to the nuclei. The assumption would be valid if 30% PEG had similar cytoplasmic as well as perinuclear localization as observed for AuNP-PEI. This however needs further investigation.

5.3 Discussion

The ideal *in vitro* cell line panel to evaluate a novel therapeutic would include non-cancerous cell lines as well as cancerous cell lines. The two cell lines used for this study were both cancerous, A2780 a drug responsive cell line and A2780cis a multidrug resistant cell line. The A2780cis ovarian carcinoma cell line was isolated from a patient who had multidrug resistant epithelial ovarian cancer (ECACC, Section 2.4.1). The argument was made that multidrug resistance is dependent on a highly similar or identical genotype, where the phenotype was dependent on epigenetic changes and altered protein expression which altered the intracellular environment. The use of a non-cancerous cell line, such as fibroblasts, would not have contributed to data regarding overcoming multidrug resistance in epithelial ovarian carcinoma. Attempts were made to obtain ovarian biopsy tissue, cancerous and non-cancerous, to create *in vitro* subcultures but this was deemed logistically challenging. This study was conducted under an agreement of nondisclosure and created a challenge to engage other researchers.

The reversion of the multidrug resistant cell line (A2780cis) to the drug responsive cell line (A2780) was deemed successful as the cellular morphologies and biomarkers confirmed phenotypic differences in the cells. The cells were genetically identical. It is unknown if this above mentioned reversion can take place *in vivo*. Significant differences exist between an *in vitro* model of cancer and how cancer will behave in an *in vivo* environment and was demonstrated by the small amount of *in vitro* developed therapeutics which proceeds to clinical trials [176, 387]. This study provided strong evidence that the developed nanoparticle drug delivery system, AuNP-PEI (AuNP-PEI A) and 30% PEG overcame cytoprotective mechanisms of the A2780cis cells. Also, the drug resistant A2780cis cells were 2-fold more susceptible to AuNP-PEI and 30% PEG than the drug responsive A2780 cells. The significance becomes more apparent when it is considered that the nanoparticle concentration for 30% PEG (5.3pM) was ~94-fold dilute to AuNP-PEI (500pM). The 30% PEG delivered ~21nM DOX to the A2780cis cells and induced equal or increased cell death compared to other *in vitro* AuNP studies which reported micromolar concentrations of DOX (Section 5.2.3.2). Experimental data suggested 30% PEG induced apoptosis mediated by caspase-3 associated with increased oxidative stress in the A2780cis cells within 3h of treatment. Transmission electron microscopy of the A2780cis cell cross sections showed AuNP-PEI nanoparticles were localized in the cytoplasm as well as in peri-nuclear regions without any observable organelle sequestration and 30% PEG was sequestered in post-apoptotic vesicles (Section 5.2.3.6). A proposed mechanistic pathway for 30% PEG can be seen in Figure 5.16: Treatment of multidrug resistant ovarian carcinoma cells (A2780cis) with 30% PEG resulted in caspase-3 activation within 3h post-treatment by oxidative stress induced apoptosis.
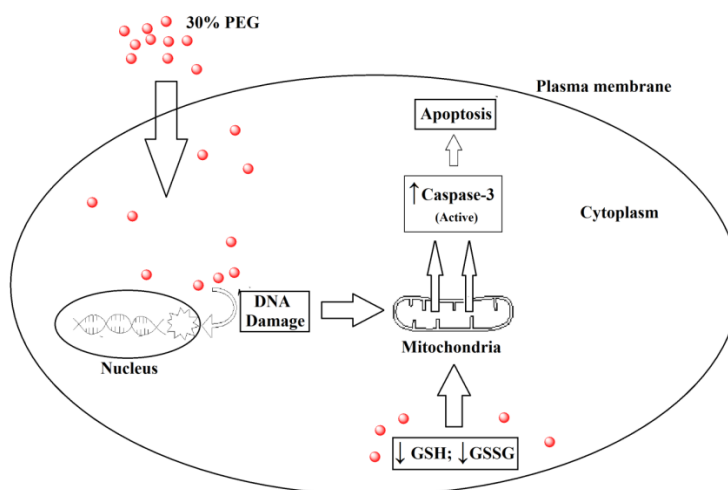
Figure 5.16: A suggested pathway for the induction of apoptosis by the intrinsic mitochondrial pathway.

Chapter 6: General Discussion, Conclusion and Future Work

6.1   General Discussion

Ovarian cancer is difficult to diagnose where a successful diagnosis typically occurs at advanced stages of the disease. Acquired drug resistance attributed to successive chemotherapy treatment (Section 1.2.3), a high rate of disease relapse (Section 1.2.2) and a high incidence of diagnosis to mortality rate (Section 1.2.1) is typically expected for ovarian cancer in advanced disease stages, where the disease can become incurable. The need for a cost-effective and robust chemotherapeutic formulation which could overcome the inherent multidrug resistance mechanisms of ovarian cancer in a target specific manner was needed where increased chemotherapeutic cellular internalization as well as cellular retention would prove beneficial. A chemotherapeutic formulation with a multimodal functionality would enable diagnosis and treatment to occur simultaneously in a theranostic manner. Theranostic based chemotherapy enables realtime monitoring of treatment progress. Nanotechnology was seen as a solution where gold nanoparticles as well as quantum dots were chosen to demonstrate *in vitro* drug delivery and *in vitro* cancer specific targeting to ovarian carcinoma cells, respectively.

Chlorotoxin (CTX) is assumed to be a matrix metalloproteinase-2 (MMP2) targeting peptide where the biomolecular interaction was called into question by recent publications in the literature [132]. The specific nature of the CTX-MMP2 interaction is still unknown as neither the kinetic data nor the fluorescence microscopy co-localization data could elucidate the CTX-MMP2 interaction. Kinetic data could not provide any useful information regarding the reported inhibition of MMP2 by CTX. There appears to be no interaction of CTX with the truncated region of the hemopexin domain (pEGFP-N3-MMP2, Section 3.3.3), based on wide field fluorescence microscopy. Further study is required to identify the residue-to-residue interaction for CTX-MMP2, to determine whether this peptide-protein interaction is transient or if the interaction locus is dependent on changes in the biological milieu. The presence of MMP2 in serum is directly correlated with the stage- and metastatic potential as well as a poor prognosis for many types of cancers (Table 1.1, Section 1.3.1). A general diagnostic screen which can detect these cancers could potentially improve the patient's prognostic outcome. The stage of the cancer can be potentially estimated, in a similar manner to the

latest commercial pregnancy tests, which can improve the diagnosis of cancer. The need for such a type of diagnosis becomes more apparent for hard to diagnose cancers, such as ovarian cancer, which typically is diagnosed in late stages of the disease. The drug delivery applications for using CTX as a targeting moiety for gold nanoparticles was demonstrated with the surface plasmon resonance affinity experiment where nitrilotriacetic acid (NTA) functionalized gold nanoparticles displayed directionality of attachment to 6xHis-tag CTX (Section 3.1.4). In an undirected bioconjugation of CTX to quantum dots (Section 3.3.3), through the use of water soluble carbodiimide, the specificity of CTX for MMP2 appears to have remained unaffected. The above mentioned gold nanoparticles and quantum dots had similar surface chemistries as the gold nanoparticles which were used for drug delivery (Sections 4.4.2 and 4.5.2). Potential *in vivo* diagnostic techniques can exploit fluorescence emission, surface enhanced Raman spectroscopy (SERS) as well as X-ray imaging for CTX targeted nanoparticles.

The one-pot polyethyleneimine (PEI) synthesized gold nanoparticles (AuNP) proved to be very efficient in cellular internalization and distribution to multiple subcellular loci (5.2.3.6). The drug loaded AuNP-PEI proved to be 2-fold more cytotoxic to drug resistant ovarian carcinoma cells than to the drug responsive ovarian carcinoma cells. The drug resistant ovarian carcinoma cells (A2780cis) are melphalan, cisplatin and doxorubicin as well as irradiation resistant. The increased sensitivity of A2780cis cells may be attributed to the PEI on the AuNP-PEI being able to overcome the multidrug resistance mechanisms where cellular accumulation and decreased cellular efflux is suggested to cause depletion of total glutathione levels. Immunodetection of procaspase-3 levels indicates that programmed cell death is initiated within 3h post treatment for the doxorubicin loaded AuNP-PEI (Figure 5.11, Section 5.2.3.4) and within 24h for non-doxorubicin loaded AuNP-PEI (Figure 5.10, Section 5.2.3.4). The exact mechanism is unknown but a suggested global pathway was introduced in Section 5.3 which are based on two known mechanisms of doxorubicin induced cell death as well as experimental data. The doxorubicin loaded AuNP-PEI achieved programmed cell death within 3h at ultralow concentrations (~21nM) of doxorubicin loaded onto 5.3pM AuNP-PEI (Sections 5.2.3.2-5.2.3.5). No similar nanoparticle based drug delivery studies have reported similar findings for achieving cell death at ultralow concentrations of a chemotherapeutic drug up to date. Further investigation of the A2780cis cell line drug resistance related molecular- and cell biology is needed to understand exactly how the above

mentioned nanoparticles overcome the cytoprotective mechanisms as well as induce programmed cell death in such a fast manner.

The toxicity of AuNP-PEI to non-cancerous cells is unknown as it fell outside the scope of this study, but needs to be investigated. Also, the efficacy of this developed drug delivery platform to overcome multidrug resistance as well as its cytotoxicity needs to be investigated with an *in vivo* model. The argument can be made that drug loaded AuNP-PEI functionalized with CTX would only target MMP2 expressing cancer cells. However the inherent toxicity of the AuNP-PEI, drug loaded and non-drug loaded, is an important parameter for non-cancerous cells as to determine organ distribution and potential organ specific associated toxicity such as nephrotoxicity or cardiotoxicity.

The synthesis of one-pot functionalized gold nanoparticles (Section 4.3) proved to be facile and provided size polydisperse nanoparticles which had stability based on the surface ligand (Section 4.3.6). Different nanoparticle shapes raised an interesting question: would anisotropic nanoparticles have a different *in vitro* toxicity profile than near spherical nanoparticles? The nanoparticle preparations which contained the anisotropic nanoparticles did display a trend in increased cytotoxicity compared to near spherical nanoparticles Sections (4.3.4 and 5.2.2.2). Polyethylene glycol (PEG) functionalization of the gold nanoparticles did display altered biomolecule interaction but this interaction was not completely abolished (Sections 4.4.3). Covalent drug loading of doxorubicin and subsequent acid hydrolysis proved to be facile and showed that 1mmol AuNP-PEI delivered 4mol doxorubicin (Sections 4.4.2). The gold nanoparticles, drug loaded and non-drug loaded, proved to be stable during the freeze-drying process and stable for long periods of time in lyophilized form. Further, the timeframe required for the synthesis, purification and drug loading of AuNPs is less than 72h. The synthesis of the gold nanoparticles proved to be cost effective for the development of a drug delivery vehicle. This is an important consideration for developing countries such as South Africa where the majority of the population live in rural areas with limited access to health care facilities.

Ovarian cancer is typically detected in the late stages of the disease where treatments are either ineffective with a high rate of disease relapse or development of acquired drug resistance and ultimately an incurable cancer. Diagnosis and treatment can be invasive, expensive as well as ineffective and have to be repeated on a regular basis to monitor the

disease. This study demonstrated in an *in vitro* model the ability of nanotechnology to overcome the cytoprotective mechanisms of a multidrug resistant ovarian carcinoma (A2780cis) by delivering ultralow concentrations doxorubicin to the cells. Cell death initiation appears to be within 3h with only 40-50% of the cells viable after 24h with a single dose. The implication is a potential successful cost-effective treatment of an incurable cancer without the need for excessive multiple follow-up treatments which necessitates the need to evaluate the doxorubicin loaded AuNPs with *in vivo* studies. Chemotherapy associated symptoms such as vomiting; hair loss and lethargy can also be potentially avoided with ultralow dosages of doxorubicin. The inherent metallic nature of gold nanoparticles will make visualization of the cancer possible with X-ray imaging, and as such *in vivo* localization of the gold nanoparticles with their drug payload can be determined. Systemic toxicity can be overcome by targeting the drug delivery vehicle (gold nanoparticles) to cancer cells specifically with CTX. The drug loading can also be done for fluorescent quantum dots as the same surface chemistry is present as for gold nanoparticles, generating another theranostic nanoparticle. Quantum dots are viewed as too toxic to be utilized for diagnostics, but an argument can be made that current chemotherapy treatments are known to be toxic and as such acceptable levels of intrinsic toxicity is acceptable for a diagnostic tool which will result in localized cancer tissue toxicity. The question is raised: "Does the toxicity of quantum dots matter for the scenario where cancer specific targeting is employed to deliver a chemotherapeutic payload?" The case where chlorotoxin is utilized as a cancer targeting moiety for quantum dots (Section 3.3.3.2) serves as an illustrative consideration.

6.2 Conclusion

Gold nanoparticles and quantum dots proved useful for *in vitro* therapeutic- and diagnostic tools, showing potential multimodal properties. Gold nanoparticles were synthesized in a one-pot manner with a readily adaptable surface chemistry which overcame the cytoprotective mechanisms of a multidrug resistant cell line to deliver a doxorubicin payload and induced programmed cell death. This was achieved with ultralow dosages of doxorubicin compared to the typical *in vitro* and *in vivo* dosages in a comparative short time frame. The gold nanoparticles proved to be colloidal stable pre- and post-drug loading and cost effective to produce. The primary objective of the study was met in full.

Full length C-terminal EGFP tagged MMP2 was not successfully produced, presenting with a truncation in the hemopexin domain of MMP2 yet proved to be an informative mistake, acting as supportive evidence for the interaction of CTX-MMP2. Recombinant affinity tagged (6xHis-tag) chlorotoxin was successfully produced for the proof of concept for MMP2 specific cancer targeting of multimodal nanoparticles (gold nanoparticles and quantum dots) which can serve as therapeutic delivery vehicles as well as high contrast imaging reagents. The secondary objective of the study was satisfactorily met.

Nanotechnology applied in this study shows promise for the treatment and diagnosis of multidrug resistant ovarian cancer.

6.3 Outputs and Future Work

The work in this study was conducted under an agreement of non-disclosure. Aspects of the work, which is not in violation of the above mentioned agreement, will be submitted to peer-reviewed journals for publication.

Aspects of the research will be followed up for publication purposes. The following topics will receive attention:

(i) Gold nanoparticle synthesis and characterization:

- Physicochemical characterizations such as dynamic light scattering (DLS) to monitor changes in the nanoparticle surface chemistry during drug loading as well as in stability assays (BSA, RPMI1640, NaCl, etc.)
- Investigation of the effect of other polyethyleneimine polymers and similar dendrimers on the size and shape distribution of the nanoparticles;
- Size- and shape enrichment of the nanoparticles for more specific physicochemical as well as biological characterization;
- Covalent drug loading of other chemotherapeutic agents.

(ii) The CTX-MMP2 interaction:

- Cloning and expression of full length C-terminal EGFP tagged MMP2 for fluorescence co-localization studies;
- Cloning and expression of C-terminal EGFP tagged subdomains of MMP2 for fluorescence co-localization studies;

- Cloning and expression of subdomains of MMP2 for NMR as well as crystallography studies of the CTX-MMP2 interaction.

(iii) Molecular mechanisms of how the gold nanoparticles overcome multidrug resistance:

- Elucidate the proposed oxidative stress pathway by immunodetection techniques as well as quantitative PCR;
- Determine genotoxicity as well as potential epigenetic changes;
- Biochemical investigation for metabolic changes in the cells.

(iv) Evaluation of the developed drug delivery platform in other *in vitro* cancerous and non-cancerous cell lines;

(v) Evaluation of the developed drug delivery platform *in vivo*.

UNIVERSITY *of the*
WESTERN CAPE

REFERENCES

1.   Blagoskony, M.V. 2005. Molecular Theory of Cancer, *Cancer Biology & Therapy*, 4(6):621-627. June.

2.   Chen, Y. and Hunter, D.J. 2005. Molecular Epidemiology of Cancer, *CA Cancer J Clin*, 55:45-54.

3.   Loeb, L.A. and Harris, C.C. 2008. Advances in Chemical Carcinogenesis – A Historical Review and Prospective, *Cancer. Res.*, 68(17):6863-6872, Sept.

4.   Wogan, G.N., Hecht, S.S., Felton, J.S., Conney, A.H. and Loeb, L.A. 2004. Environmental and Chemical Carcinogenesis, *J. Sem. Cancer*, 473-486, Jun.

5.   Stoner, G.D., Morse, M.A. and Kelloff, G.J. 1997. Perspectives in Cancer Chemoprevention, *Environmental Health Perspectives*, 105(4):945-954.

6.   Lee, J.T. and Herlyn, M. 2007. Old Disease, New Culprit: Tumor Stem Cells in Cancer, *J. Cell. Physiol*, 213:603-609.

7.   Center, M., Siegel, R. and Jemal, A. 2011. Global Cancer Facts & Figures, 2nd Ed, American Cancer Society Inc, Atlanta.

8.   World Healgth Organization (WHO) – Cancer, http://www.who.int/cancer/en/ (Accessed: 06-04-2012).

9.   North American Centre for Disease Control (CDC) – Cancer, http://www.cdc.gov/cancer (Accessed: 06-04-2012).

10.   Cvetkovic, D., Connolly, D.C. and Hamilton, T.C. 2004. Chapter 28: Molecular Biology and Molecular Genetics of Ovarian, Fallopian Tube, and Primary Peritoneal Cancer, Gynaecologic Cancer: Controversies in Management, Elsevier Science, 385-398.

11.   Balkwill, F., Bast, R.C., Berek, J., Chenevix-Trench, G., Gore, M., Hamilton, T., Jacobs, I., Mills, G., Souhami, R., Urban, N., Ursulic, S. and Smyth, J. 2003. Current Research and Treatment for Epithelial Ovarian Cancer – A Position Paper from the Helen Harris Memorial Trust, *European Journal of Cancer*, 39:1818-1827.

12.   Auersperg, N., Wong, A.S.T., Choi, K.C., Kang, S.K. and Leung, P.C.K. 2001. Ovarian Surface Epithelium: Biology, Endocrinology and Pathology, *Endocrine Reviews*, 22(2):255-288.

13. Riman, T., Persson, I. and Nilsson, S. 1998. Hormonal Aspects of Epithelial Ovarian Cancer: Review of Epidemiological Evidence, *Clinical Endocrinology*, 49:695-707, May.

14. Williams, T.I., Toups, K.L., Saggese, D.A., Kalli, K.R., Cliby, W.A. and Muddiman, D.C. 2007. Epithelial Ovarian Cancer: Disease Etiology, Treatment, Detection and Investigational Gene, Metabolite and Protein Biomarkers, *Journal of Proteome Research*, 6:2936-2962, Jan.

15. Fathalla, M.F. 1971. Incessant Ovulation – A Factor in Ovarian Neoplasia?, *The Lancet*, 7716(298):163.

16. Tonin, P. 2009. Thematic Issue on the Molecular Biology of Hereditary Ovarian Cancer, *Molecular Oncology*, 3:94-96, Feb.

17. Gentry-Maharay, A. and Menon, U. 2011. Screening for Ovarian Cancer in the General Population, *Best Practise & Research Clinical Obstetrics and Gynaecology*, 26:243-256, Nov.

18. Van der Burg, M.E.L., Van Lent, M., Buyse, M., Kobierska, A., Colombo, N., Favalli, G., Lacave, A.J., Nardi, M., Renard, J. and Pecorelli, S. 1995. The Effect of Debulking Surgery After Induction Chemotherapy on the Prognosis in Advanced Epithelial Ovarian Cancer, *N. Engl. J. Med.*, 332(10): 629-634.

19. Morrison, J., Swanton, A., Collins, S. and Kehoe, S. 2009. Chemotherapy Versus Surgery for Initial Treatment in Advanced Ovarian Epithelial Cancer, *The Cochrane Library (Wiley & Sons)*, 3:1-19.

20. McGuire, W.P. and Markman, M. 2003. Primary Ovarian Cancer Chemotherapy: Current Standards of Care, *British Journal of Cancer*, 89(3):3-8.

21. Harries, M. and Gore, M. 2002. Chemotherapy for Recurrent Ovarian Cancer Part II: Chemotherapy for Epithelial Ovarian Cancer – Treatment of Recurrent Disease, *Lancet Oncol.*, 3:537-545. Sept.

22. Hall, M.D. and Hambley, T.W. 2002. Platinum-(IV) Anti-tumour Compounds: Their Bioinorganic Chemistry, *Coordination Chemistry Reviews*, 232:49-67.

23. Hall, M.D., Okabe, M., Shen, D.W., Liang, X.J. and Gottesman, M.M. 2007. The Role of Cellular Accumulation in Determining Sensitivity to Platinum-Based Chemotherapy, *Ann. Rev. Pharmacol. Toxicol.*, 48:495-535.

24. Siddik, Z.H. 2003. Cisplatin: Mode of Cytotoxic Action and Molecular Basis of Resistance, *Oncogene*, 22:7265-7279.

25.   Haxton, K.J. and Burt, H.M. 2009. Polymeric Drug Delivery of Platinum-based Anticancer Agents, *Journal of Pharmaceutical Sciences*, 98(7):2299-2316.

26.   Pfizer Doxorubicin CCO Formulary – Revised October 2009.

27.   Preobrazhenskaya, M.N., Tevyashova, A.N., Olsufyeva, E.N., Huang, K.F. and Huang, H.S. 2006. Second Generation Drugs-derivatives of Natural Antitumour Anthracycline Antibiotics Daunorubicin, Doxorubicin and Carminomycin, *J. Med. Sci.*, 26(4):119-128, Mar.

28.   Thorn, C.F., Oshiro, C., Marsh, S., Hernandez-Boussard, T., McLeoad, H., Klein, T.E. and Altman, R.B. 2011. Doxorubicin Pathways: Pharmacodynamics and Adverse Effects, *Pharmacogenet. Genomics*, 21(7):440-446, Jul.

29.   Mizutani, H., Tada-Oiakowa, S.H., Hiraku, Y., Kojima, M. and Kawanishi, S. 2005. Mechanism of Apoptosis Induced by Doxorubicin through Generation of Hydrogen Peroxide, *Life Sciences*, 76:1439-1453.

30.   Kostoryz, E.L. and Yourtee, D.M. 2001. Oxidative Mutagenesis of Doxorubicin-Fe(III)-Complex, *Mutation Research*, 490:131-139.

31.   Drummond, J.T., Anthoney, A., Brown, R. and Modrich, P. 1996. Cisplatin and Adriamycin Resistant are Associated with MutLα and Mismatch Repair Deficiency in an Ovarian Tumor Cell Line, *The Journal of Biological Chemistry*, 271(33):19645-19648.

32.   Mohamed, H.E., El-Swefy, S.E. and Hagar, H. H. 2000. The Protective Effect of Glutathione Administration on Adriamycin-induced Acute Cardiac Toxicity in Rats, *Pharmacological Research*, 42(2): 115-121.

33.   Sayed-Ahmed, M.M., Salman, T.M., Gaballah, H.E., El-Naga, S.A.A., Nicolai, R. and Calvani, M. 2001. Propionyl-L-carnitine as Protector against Adriamycin-induced Cardiomyopathy, *Pharmcological Research*, 43(6):513-520.

34.   Boonsanit, D., Kanchanapangka, S. and Buranakarl, C. 2006. L-Carnitine Ameliorates Doxorubicin-induced Nephrotoxicity Syndrome in Rats, *Nephrology*, 11:313-320.

35.   Wang, G.W. and Kang, Y.J. 1999. Inhibition of Doxorubicin Toxicity in Cultured Neonatal Cardiomyocytes with Elevated Metallothionein Levels, *The Journal of Pharmacology and Experimental Therapeutics*, 288(3):938-944.

36.   Dobrovolskala, M.A., Aggarwal, P., Hall, J.B. and McNeil, S.E. 2008. Preclinical Studies to Understand Nanoparticle Interaction with the Immune System

and Its Potential Effect on Nanoparticle Biodistribution, *Molecular Pharmaceutics*, 5(4):487-495.

37. Li, S.D. and Huang, L. 2008. Pharmacokinetics and Bio-distribution of Nanoparticles, *Molecular Pharmaceutics*, 5(4):496-504.

38. Rowinsky, E.K. 1997. The Development and Clinical Utility of the Taxane Class of Antimicrotubule Chemotherapy Agents, *Ann. Rev. Med.*, 48:353-374.

39. Dean, E., El-Helw, L. and Hasan, J. 2010. Targeted Therapies in Epithelial Ovarian Cancer, *Cancers*, 2:88-113.

40. Steeg, P.S. 2006. Tumor Metastasis: Mechanistic Insights and Clinical Challenges, *Nature Medicine*, 12:895-904, Aug.

41. Yang, J., Mani, S.A. and Weinberg, R.A. 2006. Exploring a New Twist on Tumor Metastasis, *Cancer Res.*, 66(9): 4549-4552, May.

42. Schaner, M.E., Ross, D.T., Ciaravina, G., Sorlie, T., Troyanskaya. O., Diehn, M., Wang, Y.C., Duran, G.E., Sikic, T.L., Caldeira, S., Skomedal, H., Tu, I.P., Hernandez-Boussard, T., Johnson, S.W., O'Dwyer, P.J., Fero, M.J., Kristensen, G.B., Borresen-Dale, A.L., Hastie, T., Tibshirani, R., Van de Rijn, M., Teng, N.N., Longacre, T.A., Bolstein, D., Brown, P.O. and Sikic, B.L. 2003. Gene Expression Patterns in Ovarian Carcinomas, *Molecular Biology of the Cell*, 14:4376-4386.

43. Albini, A., Mirisola, V. and Pfeffer, U. 2008. Metastasis Signatures: Genes Regulating the Tumor-microenvironment Interactions Predict Metastatic Behaviour, *Cancer Metastasis Rev.*, 27:75-83.

44. Rinker-Schaeffer, C.W., O'Keefe, J.P., Welch, D.R. and Theodorescu, D. 2006. Metastasis Suppressor Proteins: Discovery, Molecular Mechanisms and Clinical Application, *Clin. Cancer Res.*, 12(13):3882-2889, Jul.

45. Feki, A., Berardi, P., Bellingan, G., Major, A., Krause, K.H., Petignat, P., Zehra, R., Pervaiz, S. and Irminger-Finger, I. 2009. Dissemination of Intraperitoneal Ovarian Cancer: Discussion of Mechanisms and Demonstration of Lymphatic Spreading in Ovarian Cancer Model, *Critical Reviews in Oncology/Hematology*, 72:1-9.

46. Shield, K., Ackland, M.L., Ahmed, N. and Rice, G.E. 2009. Multicellular Spheroids in Ovarian Cancer Metastases: Biology and pathology, *Gynecologic Oncology*, 113:143-148.

47. Yoneda, J., Kuniyasu, H., Crispens, M.A., Price, J.E., Bucana, C.D. and Fidler, I.J. 1998. Expression of Angiogenesis-Related Genes and Progression of

Human Ovarian Carcinomas in Nude Mice, *Journal of the National Cancer Institute*, 90(6):447-454, Mar.

48. Kenny, H.A., Kaur, S., Coussens, L.M. and Lengyel, E. 2008. The Initial Steps of Ovarian Cancer Metastasis are Mediated by MMP-2 Cleavage of Vitronectin and Fibronectin, *The Journal of Clinical Investigation*, 118(4):1367-1379, Apr.

49. Zhang, L., Conejo-Garcia, J.R., Katsaros, D., Gimotty, P.A., Massobrio, M., Regnani, G., Makrigiannakis, A., Gray, H., Schlienger, K., Liebman, M.N., Rubin, S.C. and Coukos, G. 2003. Intratumoral T Cells, Recurrence and Survival in Epithelial Ovarian Cancer, *N. Engl. J. Med.*, 348:203-213.

50. Weihong, D., Yanhua, X. and Zehua, W. 2005. Apoptosis Rate and Objective Diagnosis of Drug Resistance of Ovarian Cancer Cell Lines, *The Chinese-German Journal of Clinical Oncology*, 4(5):304-308.

51. Hamaguchi, K., Godwin, A.K., Yakushiji, M., O'Dwyer, P.J., Ozols, R.F. and Hamilton, T.C. 1993. Cross-Resistance to Diverse Drugs is Associated with Cisplatin Resistance in Ovarian Cancer Cell Lines, *Cancer Res.*, 53:5225-5232.

52. Kunjachan, S., Blauz, A., Mockel, D., Theek, B., Kiessling, F., Etrych, T., Ulbrich, K., Van Bloois, L., Storm, G., Bartosz, G., Rychlik, B. and Lammers, T. 2011. Overcoming Cellular Multidrug Resistance using Classical Nanomedicine Formulations, *European Journal of Pharmaceutical Science*, 2011, Aug.

53. Solar, P. and Sytkowski, A.J. 2011. Differentially Expressed Genes Associated with Cisplatin Resistance in Human Ovarian Adenocarcinoma Cell Line A2780, *Cancer Letters*, 309:11-18, May.

54. Drummond, J.T., Anthony, A., Brown, R.B. and Modrich, P. 1996. Cisplatin and Adriamycin Resistance Are Associated with MutLα and Mismatch Repair Deficiency in an Ovarian Tumour Cell Line, *The Journal of Biological Chemistry*, 271(33):19645-19648, Aug.

55. Massey, A., Offman, J., Macpherson, P. and Karran, P. 2003. DNA Mismatch Repair and Acquired Cisplatin Resistance in *E.coli* and Human Ovarian Carcinoma Cells, *DNA Repair*, 2:73-89, Sept.

56. Helleman, J., Van Staveren, I.L., Dinjens, W.N.M., Van Kuijk, P.F., Ritstier, K., Ewing, P.C., Van der Burg, M.E.L., Stoter, G. and Berns, E.M.J.J. 2006. Mismatch Repair and Treatment Resistance in Ovarian Cancer, *BMC Cancer*, 6:201.

57.   Selvakumaran, M., Pisarcik, D.A., Bao, R., Yeung, A.T. and Hamilton, T.C. 2003. Enhanced Cisplatin Cytotoxicity by Disturbing the Nucleotide Excision Repair Pathway in Ovarian Cancer Cell Lines, *Cancer Res.*, 63:1311-1316.

58.   Juin, P, Geneste, O., Raimbaud, E. and Hickman, J.A. 2004. Shooting at Survivors: Bcl-2 Family Members as Drug Targets for Cancer, *Biochimica et Biophysica Acta*, 1644:251-260.

59.   Preston, T.J., Abadi, A., Wilson, L. and Singh, G. 2001. Mitocondrial Contributions to Cancer Cell Physiology: Potential for Drug Development, *Advanced Drug Delivery Reviews*, 49:45-61.

60.   Ghavami, S., Hashemi, M., Yeganeh, B., Xiao, W. Eshragi, M., Bus, C.J., Kadkhoda, K., Wiechec, E., Halayko, A.J. and Los, M. 2009. Apoptosis and Cancer: Mutations within Caspase Genes, *J. Med. Genet.*, 46:497-510.

61.   Sasaki, H., Sheng, Y.L., Kotsuji, F. and Tsang, B.K. 2000. Down-Regulation of X-linker Inhibitor of Apoptosis Protein Induces Apoptosis in Chemiresistant Human Ovarian Cancer Cells, *Cancer Res.*, 60:5659-5666.

62.   Asselin, E., Mills, G.B. and Tsang, B.K. 2001. XIAP Regulates Akt Activity and Caspase-3-dependent Cleavage during Cisplatin-induced Apoptosis in Human Ovarian Epithelial Cancer Cells, *Cancer Res.*, 61:1862-1868.

63.   Roy, G., Horton, J.K., Roy, R., Denning, T., Mitra, S. and Boldogh, I. 2000. Acquired Alkylating Drug Resistance is Unaffected by Altered Levels of Pro- and Anti-Apoptotic Proteins, *Oncogene*, 19:141-150.

64.   Vazquez, A., Bond, E.E., Levine, A.J. and Bond, G.L. The Genetics of the p53 Pathway, Apoptosis and Cancer Therapy, *Nature Drug. Disc.*, 7:979-987.

65.   Reles, A., Wen, H.W., Schimder, A., Gee, C., Runnebaum, I.B., Kilian, U., Jones, L.A., El-Nagger, A., Minguillon, C., Schonborn, I., Reich, O., Kreienberg, R., Lichtenegger, W. andPress, M.F. 2001. Correlation of p53 Mutations with Resistance to Platinum-based Chemotherapy and Shortened Survival in Ovarian Cancer, *Clin. Cancer Res.*, 7:2984-2997, Oct.

66.   Townsend, D.M., Tew, K.D. and Tapiero, H. 2003. The Importance of Glutathione in Human Disease, *Biomedicine & Pharmacotherapy*, 57:145-155.

67.   Mistry, P., Kelland, L.R., Abel, G., Sidhar, S. and Harrap, K.R. 1991. The Relationships between Glutathione, Glutathione-S-transferase and Cytotoxicity of Platinum Drugs and Melphalan in Eight Human Ovarian Carcinoma Cell Lines, *Br. J. Cancer*, 64:215-220.

68. Godwin, A.K., Meister, A., O'Dwyer, P.J., Huang, C.S., Hamilton, T.C. and Anderson, M. 1991. High Resistance to Cisplatin in Human Ovarian Cancer Cell Lines is Associated with Marked Increase of Glutathione Synthesis, *Proc. Natl. Acad. Sci.*, 89:3070-3074, Apr.

69. Cho, H.Y., Reddy, S.P., DeBiase, A., Yamamoto, M. and Kleeberger, S.R. 2005. Gene Expression Profiling of NRF2-Mediated Protection against Oxidative Injury, *Free Radical Biology & Medicine*, 38:325-343, Jan.

70. Hayes, J.D. and McMahon, M. 2009. NRF2 and KEAP1 Mutations: Permanent Activation of an Adaptive Response in Cancer, *Trends in Biochemical Sciences*, 34(4):175-188, March.

71. Lau, A., Villeneuve, N.F., Sun, Z., Wong, P.K. and Zhang, D.D. 2008. Dual Roles of Nrf2 in Cancer, *Pharmacological Research*, 58:262-270, Sept.

72. Shim, G., Manandhar, S., Shin, D., Kim, T.H. and Kwak, M.K. 2009. Acquisition of Doxorubicin Resistance in Ovarian Carcinoma Cells Accompanies Activation of the NRF2 Pathway, *Free Radical Biology & Medicine*, 47:1619-1631, Sept.

73. Harvey, C.J., Thimmulappa, R.K., Singh, A., Blake, D.J., Ling, G., Wakabayashi, N., Myers, A. and Biswal, S. 2009. Nrf2-Regulated Glutathione Recycling Independent of Biosynthesis Survival during Oxidative Stress, *Free Radical Biology & Medicine*, 46:443-453, Jan.

74. Helleman, J., Burger, H., Hamelers, I.H.L., Boersma, A.W.M., De Kroon, A.I.P.M., Stoter, G. and Nooter, K. 2006. Impaired Cisplatin Influx in an A2780 Mutant Cell line, *Cancer Biology & Therapy*, 5(8):943-949, Aug.

75. Gottesman, M.M., Fojo, T. and Bates, S.E. 2002. Multidrug Resistance in Cancer: Role of ATP-Dependent Transporters, *Nature Reviews*, 2:48-58, Jan.

76. Meijerman, I., Beijnen, J.H. and Schellens, J.H.M. 2008. Combined Action and Regulation of Phase II and Multidrug Resistance Proteins in Multidrug Resistance in Cancer, *Cancer Treatment Reviews*, 34:505-520, March.

77. Zisowsky, J., Koegel, S., Leyers, S., Devarakonda, K., Kassack, M.U., Osmak, M. and Jaehde, U. 2007. Relevance of Drug Uptake and Efflux for Cisplatin Sensitivity of Tumor Cells, *Biochemical Pharmacology*, 73:298-307.

78. Pakunlu, R.I., Cook, T.J. and Minko, T. 2003. Simultaneous Modulation of Multidrug Resistance and Anti-apoptotic Cellular Defence by MDR1 and BCL-2

Targeted Antisense Oligonucleotides Enhances the Anticancer Efficacy of Doxorubicin, *Pharmaceutical Research*, 20(3):351-359, March.

79. Yan, X., Yin, J., Tao, H., Mao, N., Yang, Y. and Pan, L. 2010. Increased Expression of Annexin A3 is a Mechanism of Platinum Resistance in Ovarian Cancer, *Cancer Res.*, 70(4):OF1-OF9, Feb.

80. Morgunova, E., Tuuttila, A., Bergmann, U., Isupov, M., Lindqvist, Y., Scheinder, G. and Tryggvason, K. 1999. Structure of Human Pro-Matrix Metalloproteinase-2: Activation Mechanism Revealed, *Science*, 284:1667-1679, Jun.

81. Weingarten, H., Martin, R. and Feder, J. 1985. Synthetic Substrates of Vertebrate Collagenase, *Biochemistry*, 24:6730-6734, Mar.

82. Xia, T., Akers, K., Eisen, A.Z. and Seltzer, J.L. 1996. Comparison of Cleavage Site Specificity of Gelatinases A and B using Collagenous Peptides, *Biochimica et Biophysica Acta*, 1293:259-266.

83. Banyai, L., Tordai, H. and Patthy, L. 1994. The Gelatin-Binding Site of Human 72 kDa Type IV Collagenase, *Biochem. J.*, 298:403-407.

84. Egeblad, M. and Werb, Z. 2002. New functions for the matrix metalloproteinases in cancer progression, *Cancer*, 2:161-174, Mar.

85. Wu, X., Li, H., Kang, L., Li, L., Wang, W. and Shan, B. 2002. Matrix Metalloproteinase-2 – A Potential Marker of Prognosis for Epithelial Ovarian Cancer, *Gynecologic Oncology*, 84:126-134.

86. Turpeenniemie-Hujanen, T. 2005. Gelatinases (MMP-2 and -9) and their Natural Inhibitors as Prognostic Indicators in Solid Cancers, *Biochimie*, 87:287-297, Jan.

87. Hofmann, U.B., Westphal, J.R., Van Muijen, G.N.P. and Ruiter, D.J. 2000. Matrix Metalloproteinases in Human Melanoma, *J. Invest. Dermatol*., 115:337-344, May.

88. Smyth-Templeton, N. and Stetler-Stevenson, W.G. 1991. Identification of a basal promotor for the Human Mr 72 000 Type IV Collagenase Gene and Enhanced Expression in a Highly Metastatic Cell Line, *Cancer Res.*, 51:6190-6193, Nov.

89. Yamamoto, M., Mohanam, S., Sawaya, R., Fuller, G.N., Seiki, M., Sato, H., Gokaslan, Z.L., Liotta, L.A., Nicolson, G.L. and Rao, J.S. 1996. Differential Expression of Membrane-Type Matrix Metalloproteinase and Its Correlation with Gelatinase A Activation in Human Malignant Brain Tumors *In Vivo* and *In Vitro*, *Cancer Res.*, 56:384-392, Jan.

90.   Roomi, M.W., Monterrey, J.C., Kalinovsky, T., Rath, M. and Niedzwiecki, A. 2009. Patterns of MMP-2 and MMP-9 Expression in Human Cancer Cell Lines, *Oncology Reports*, 21:1323-1333, Feb.

91.   Jones, J.L., Glynn, P. and Walker, R.A. 1999. Expression of MMP-2 and MMP-2, Their Inhibitors and the Activator MT1-MMP in Breast Carcinomas, *J. Pathol.*, 189:161-168, Mar.

92.   Sehgal, I. and Thompson, T.C. 1999. Novel Regulation of Type IV collagenase (Matrix Metalloproteinase-9 and -2) Activities by Transforming Growth Factor-β1 in Human Prostate Cancer Cell Lines, *Molecular Biology of the Cell*, 10:407-416, Feb.

93.   Brown, P.D., Levy, A.T., Margulies, I.M.K., Liotta, L.A. and Stetler-Stevenson, W.G. 1990. Independent Expression and Cellular Processing of Mr 72000 type IV Collagenase and Interstitial Collagenase in Human Tumorigenic Cell Lines, *Cancer Res.*, 50:6184-6191, Jun.

94.   Emmert-Buck, M.R., Roth, M.J., Zhuang, Z., Campo, E., Rozhin, J., Sloane, B.F., Liotta, L.A. and Stetler-Stevenson, W.G. 1994. Increased Gelatinase A (MMP-2) and Cathepsin B Activity in Invasive Tumor Regions of Human Colon Cancer Samples, *Am. J. Pathol.*, 145:1285-1290, Dec.

95.   Giambernardi, T.A., Grant, G.M., Taylor, G.P., Hay, R.J., Maher, V.M., McCormick, J.J. and Klebe, R.J. 1997. Overview of Matrix Metalloproteinase Expression in Cultured Human Cells, *Matrix Biology*, 16:483-496.

96.   Cheung, P.Y., Sawicki, G., Wozniak, M., Wang, W., Radomski, M.W. and Schulz, R. 2000. Matrix Metalloproteinase-2 Contributes to Ischemia-Reperfusion Injury in the Heart, *Circulation*, 101:1833-1839, Jan.

97.   Kwan, J.A., Schulze, C.J., Wang, W., Leon, H., Sariahmetoglu, M., Sung, M., Sawicka, J., Sims, D.E., Sawicki, G., and Schulz, R. 2004. Matrix metalloproteinase-2 (MMP-2) is present in the nucleus of cardiac myocytes and is capable of cleaving poly(ADP-ribose) polymerase (PARP) *in vitro*, *FASEB J.*, 18:690-692.

98.   Elkington, P.T.G., O'Kane, C.M. and Friedland, J.S. 2005. The Paradox of Matrix Metalloproteinases in Infectious Disease, *Clinical and Experimental Immunology*, 142:12-20, Apr.

99. Rumbaugh, J., Turchan-Cholewo, J., Galey, D., St Hillaire, C., Anderson, C., Conant, K. and Nath, A. 2006. Interaction of HIV Tat and Matrix Metalloproteinase in HIV Neuropathogenesis: A New Host Defense Mechanism, *FASEB J.*, 20:E1114-E1123.

100. Fridman, R., Fuerst, T.R., Bird, R.E., Hoyhtya, M., Oelkuct, M., Kraus, S., Komarek, D., Liotta, L.A., Berman, M.L. and Stetler-Stevenson, W.G. 1992. Domain Structure of Human 72-kDa Gelatinase/Type IV Collagenase, *The Journal of Biological Chemistry*, 257(22):15398-15405, Aug.

101. Bernardo, M.M. and Fridman, R. 2003. TIMP-2 (Tissue Inhibitor of Matrix Metalloproteinase-2) Regulates MMP-2 (Matrix Metalloproteinase-2) Activity in the Extracellular Environment after pro-MMP-2 activation by MT1 (Membrane Type 1)-MMP, *Biochem J.*, 374: 739-745.

102. Brooks, P.C., Stromblad, S., Sanders, L.C., Von Schalscha, T., Aimes, R.T., Stetler-Stevenson, W.G., Quigley, J.P. and Cheresh, D.A. 1996. Localization of Matrix Metalloproteinase-2 (MMP-2) to the Surface of Invasive Cells by Interaction with Integrin $\alpha_v\beta_3$, *Cell*, 85:683-693, May.

103. Howard, E.W. and Banda, M.J. 1991. Binding of Tissue Inhibitor of Metalloproteinase 2 to Two Distinct Sites on Human 72-kDa Gelatinase, *The Journal of Biological Chemistry*, 266(27):17972-17977, May.

104. Hernandez-Barrantes, S., Toth, M., Bernardo, M.M., Yurkova, M., Gervasi, D.C., Raz, Y., Sang, Q.X.A. and Fridman, R. 2000. Binding of Active (57kDa) Membrane Type 1-Matrix Metalloproteinase (MT1-MMP) to Tissue Inhibitor of Metalloproteinase (TIMP)-2 Regulates MT1-MMP Processing and Pro-MMP2 Activation, *The Journal of Biological Chemistry*, 275(16):12080-12089, Jan.

105. Sariahmetoglu, M., Crawford, B.D., Leon, H., Sawicka, J., Li, L., Ballerman, B.J., Holmes, C., Berthiaume, L.G., Holt, A., Sawicki, G. and Schulz, R. 2007. Regulation of Matrix Metalloproteinase-2 (MMP-2) Activity by Phosphorylation, *FASEB, J.*, 21:2486-2495, Jul.

106. Munshi, H.G., Wu, Y.I., Mukhopadhyay, S., Ottaviano, A.J., Sassano, A., Koblinski, J.E., Platanias, L.C. and Stack, M.S. 2004. Differential Regulation of Membrane Type-1 Matrix Metalloproteinase Activity by ERK 1/2 − and p38 MAPK-modulated Tissue Inhibitor of Metalloproteinase 2 Expression Controls Transforming Growth Factor-β_1-induced Pericellular Collagenolysis, *The Journal of Biological Chemistry*, 279(37):39042-39050, Jul.

107. Nelson, K.K., Ranganatham, A.C., Mansouri, J., Rodriguez, A.M., Providence, K.M., Rutter, J.L., Pumiglia, K., Bennett, J.A. and Melendez, J.A. 2003. Elevated *Sod2* Activity Augments Matrix Metalloproteinase Expression: Evidence for the Involvement of Endogenous Hydrogen Peroxide in Regulating Metastasis, <u>*Clin. Cancer Res.*</u>, 9:424-432, Jan.

108. Van de Wiele, C. and Oltenfreiter, R. 2006. Imaging Probes Targeting Matrix Metalloproteinases, <u>*Cancer Biotheraphy & Radiopharmaceuticals*</u>, 21:409-417, Nov.

109. Cai, W., Rao, J., Gambhir, S.S. and Chen, X. 2006. How Molecular Imaging is Speeding up Antiangiogenic Drug Development, <u>*Mol. Cancer Ther.*</u>, 5:2624-2633, Nov.

110. Pirila, E., Maisi, P., Salo, T., Koivunen, E. and Sorsa, T. 2001. *In Vivo* Localization of Gelatinases (MMP-2 and -9) by *In Situ* Zymography with a Selective Gelatinase Inhibitor, <u>*Biochemical and Biophysical Research Communications*</u>, 287:766-774, Aug.

111. Snoek-van Beurden, P.A.M. and Von den Hoff, J.W. 2005. Zymographic Techniques for the Analysis of Matrix Metalloproteinases and their Inhibitors, <u>*Biotechniques*</u>, 38:73-83, Jan.

112. Leber, T.M. and Balkwill, F.R. 1997. Zymography: A Single-step Staining Method for Quantification of Proteolytic Activity on Substrate Gels, <u>*Anal. Biochem.*</u>, 249:24-28, Jan.

113. Medina, O.P., Haikola, M., Tahtinen, M., Simpura, I., Kaukinen, S., Valtanen, H., Zhu, Y., Kuosmanen, S., Cao, W., Reunanen, J., Nurminen, T., Saris, P.E.J., Smith-Jones, P., Bradbury, M., Larson, S. and Kairemo, K. 2011. Liposomal Tumor Targeting in Drug Delivery Utilizing MMP-2- and MMP-9-Binding Ligands, <u>*Journal of Drug Delivery*</u>, 2011:1-9, Jan.

114. Medina, O.P., Soderlund, T., Laakkonen, L.J., Tuominen, E.K.J., Koivunen, E. and Kinnunen, P.K.J. 2001. Binding of Novel Peptide Inhibitors of Type IV Collagenases to Phospholipid Membranes and Use in Liposome Targeting to Tumor Cells *In Vitro*, <u>*Cancer Res.*</u>, 61:3978-3985, May.

115. Davidson, B., Goldberg, I., Gotlieb, W.H., Kopolovic, J., Ben-Baruch, G., Nesland, J.M., Berner, A., Bryne, M. and Reich, R. 2000. High Levels of MMP-2,

MMP-9, MT1-MMP and TIMP-2 mRNA correlate with Poor Survival in Ovarian Carcinoma, *Clinical & Experimental Metastasis*, 17:799-808, Feb.

116.   Shen, S.C., Lin, C.W., Lee, H.M., Chien, L.L. and Chen, Y.C. 2006. Lipopolysaccharide Plus 12-O-Tetradecanoylphorbol-13-acetate Induction of Migration and Invasion of Glioma Cells *In Vitro* and *In Vivo*, *Neuroscience*, 140:477-489, Feb.

117.   Konstantinopoulos, P.A., Spentzos, D., Fountzilas, E., Francoeut, N., Sanisetty, S., Grammatikos, A.P., Hecht, J.L. and Cannistra, S.A. 2011. Keap1 Mutations and Nrf2 Pathway Activation in Epithelial Ovarian Cancer, *Cancer Res.*, OnlineFirst:1-9, Jun.

118.   DeBin, J. A., and Strichartz, G. R. 1991. Chloride Channel Inhibition by the Venom of the Scorpion *Leiurus quinqeustriatus*, *Toxicon*, 29**:**1403–1408.

119.   Lippens, G., Najib, J., Wodsk, S.J. and Tartar, A. 1995. NMR Sequential Assignments and Solution Structure of Chlorotoxin, a Small Scorpion Toxin That Blocks Chloride Channels, *Biochemistry*, 34:13-21, Sept.

120.   Landon, C., Cornet, B., Bonmatin, J.M., Kopeyan, C., Rochat, H., Vovelle, F. and Ptak, M. 1996. ^{1}H-NMR-derived Secondary Structure and the Overall Fold of the Potent Anti-mammal Anti-insect toxin III from the Scorpion *Leiurus quinqeustriatus quinquestriatus*, *Eur. J. Biochem.*, 236:395-404, Sept.

121.   Tamaoki, H., Miura, R., Kusunoki, M., Kyogoku, Y., Kobayashi, Y. and Moroder, L. 1998. Folding Motifs Induced and Stabilized by Distinct Cysteine Frameworks, *Protein Engineering*, 11(8):649-659.

122.   Deshane, J., Garner, C.C. and Sontheimer, H. 2002. Chlorotoxin Inhibits Glioma Cell Invasion via Matrix Metalloproteinase-2, *Journal of Biological Chemistry*, 278:4136-4144, Feb.

123.   Sontheimer, H. 2008. An Unexpected Role for Ion Channels in Brain Tumor Metastasis, *Exp. Biol. Med.*, 233:779-791.

124.   Wiranowska, M., Colina, L.O.and Johnson, J.O. 2011. Clathrin-mediated Entry and Cellular Localization of Chlorotoxin in Human Glioma, *Cancer Cell International*, 11:27-40.

125.   Akcan, M., Stroud, M.R., Hansen, S.J., Clark, R.J., Daly, N.L., Craik, D.J. and Olson, J.M. 2010. Chemical Re-engineering of Chlorotoxin Improves Bioconjugation Properties for Tumor Imaging and Targeted Therapy, *J. Med. Chem.*, 54:782-787, Aug.

126. Yu, X.F., Sun, Z., Li, M., Xiang, Y., Wang, Q.Q., Tang, F., Wu, Y., Cao, Z. and Li, W. 2010. Neurotoxin-conjugated Upconversion Nanoprobes for Direct Visualization of Tumors Under Near-infrared Irradiation, *Biomaterials*, 31:8724-8731, Aug.

127. Veiseh, O., Kievit, F.M., Gunn, J.W., Ratner, B.D. and Zhang, M. 2009. A Ligand-mediated Nanovector for Targeted Gene Delivery and Transfection in Cancer Cells, *Biomaterials*, 30:649-667, Nov.

128. Veiseh, M., Gabikian, P., Bahrami, S.B., Veiseh, O., Zhang, M., Hackman, R.C., Ravanpay, A.C., Stroud, M.R., Kusuma, Y., Hansen, S.J., Kwok, D., Munoz, N.M., Sze, R.W., Grady, W.M., Greenberg, N.M., Ellenbogen, R.G. and Olson, J. 2007. Tumor Paint: A Chlorotoxin:Cy5.5 Bioconjugate for Intraoperative Visualization of Cancer Foci, *Cancer Res.*, 67(14):6882-6888, Jul.

129. Mamelak A.N., Rosenfeld S., Bucholz R., Raubitschek A., Nabors L.B., Fiveash J.B., Shen S., Khazaeli M.B., Colcher D., Liu A., Osman M., Guthrie B., Schade-Bijur S., Hablitz D.M., Alvarez V.L. and Gonda M.A. 2006. Phase I Single-Dose Study of Intracavitary-Administered Iodine-131-TM-601 in Adults with Recurrent High-Grade Glioma, *J. Clin. Oncol.*, 24(22):3644–50.

130. Lyons, S.A., O'Neal, J. and Sontheimer, H. 2002. Chlorotoxin, A Scorpion Derived Peptide, Specifically Binds to Gliomas and Tumors of Neuroectodermal Origin, *Glia*, 39:162-173.

131. Jacoby, D.B., Dyskin, E., Yalcin, M., Kesavan, K., Dahlberg, W., Ratliff, J., Johnson, E.W. and Mousa, S.A. 2010. Potent Pleiotropic Anti-angiogenic Effects of TM601, a Synthetic Chlorotoxin Peptide, *Anticancer Research*, 30:39-46.

132. Kesavan , K., Ratliff, J., Johnson, E.W., Dahlberg, W., Asara, J.M., Misra. P., Frangioni, J.V. and Jacoby, D.B. 2010. Annexin A2 is a Molecular Target for TM601, a Peptide with Tumor-targeting and Anti-angiogenic Effects, *The Journal of Biological Chemistry*, 285(7):4366-4374, Jan.

133. Veiseh, O., Sun, C., Gunn, J., Kohler, N., Gabikian, P., Lee, D., Bhattarai, N., Ellenbogen, R., Sze, R., Hallahan, R., Olson, J. and Zhang, M. 2005. Optical and MRI Multifunctional Nanoprobe for Targeting Gliomas, *Nano Lett.*, 5(6):1003-1008, Mar.

134.   Kievit, F.M., Veiseh, O., Fang, C., Bhattarai, N., Lee, D., Ellenbogen, R.G. and Zhang, M.   2010. Chlorotoxin Labeled Magnetic Nanovectors for Targeted Gene Delivery to Glioma, *ACS Nano*, 4(8):4587-4594, Aug.

135.   Fu, Y., An, N., Li, K., Zheng, Y. and Liang, A.   2012. Chlorotoxin-conjugated nanoparticles as potential glioma-targeted drugs, *J. Neurooncol.*, 107:457-462, Jan.

136.   Veiseh, O., Kieivt, F.M., Ellenbogen, R.G. and Zhang, M.   2011. Cancer Cell Invasion: Treatment and Monitoring Opportunities in Nanomedicine, *Advanced Drug Delivery Reviews*, 63:582-596.

137.   Lee, S., Xie, J. and Chen, X.   2010. Peptide-Based Probes for Targeted Molecular Imaging, *Biochemistry*, 49:1364-1376, Jan.

138.   Chandrawati, R., Hosta-Rigau, L., Vanderstraaten, D., Lokuliyana, S.A., Stadler, B., Albericio, F. and Caruso, F. 2010. Engineering Advanced Capsosomes: Maximizing the Number of Subcompartments, Cargo Retention and Temperature-Triggered Reaction, *ACSNano*, 4(3):1351-1361.

139.   Rodriguez-Lorenzo, L., De la Rica, R., Alvarez-Puebla, R.A., Liz-Marzan, L.M. and Stevens, M.M. 2012. Plasmonic Nanosensors with Inverse Sensitivity by Means of Enzyme-Guided Crystal Growth, *Nature Materials*, 11:604-607.

140.   Ghosh, S.K. and Pal, T.   2007. Interparticle Coupling Effect on the Surface Plasmon Resonance of Gold Nanoparticles: From Theory to Applications, *Chem. Rev.*, 107:4797-4862, Jan.

141.   Daniel, M.C. and Astruc, D.   2004. Gold Nanoparticles: Assembly, Supramolecular Chemistry, Quantum-Size-Related Properties, and Applications towards Biology, Catalysis and Nanotechnology, *Chem. Rev.*, 104:293-346, Jan.

142.   Cao. C. and Sim, S.J.   2006. Signal Enhancement of the Surface Plasmon Resonance Immunoassay using Enzyme Precipitation-Functionalized Gold Nanoparticles: A Femto-molar Level Measurement of Anti-glutamic acid Decarboxylase Antibody, *Biosensors & Bioelectronics*, 22:1874-1880, Aug.

143.   Kneipp, J., Kenipp, H., McLaughlin, M., Brown, D. and Kneipp, K.   2006. *In Vivo* Molecular Probing of Cellular Compartments with Gold Nanoparticles and Nanoaggregates, *Nano Lett.*, 6(10):2225-2231, Sept.

144.   Xie, J., Zhang, Q., Lee, J.Y. and Wang, D.I.C.   2008. The Synthesis of SERS-Active Gold Nanoflower Tags for *In Vivo* Applications, *ACSNano*, 2(12):2473-2480.

145. Hainfeld, J.F., Slatkin, D.N., Focella, T.M. and Smilowitz, H.M. 2006. Gold Nanoparticles: A New X-Ray Contrast Agent, *The British Journal of Radiology*, 79:248-253, Mar.

146. Prabaharan, M., Grailer, J.J., Pilla, S., Steeber, D.A. and Gong, S. 2009. Gold Nanoparticles with a Monolayer of Doxorubicin-conjugated Amphiphilic Block Copolymer for Tumor-targeted Drug Delivery, *Biomaterials*, 30:6065-6075, Aug.

147. Kumar, S.A., Peter, Y.A., Nadeau, J.L. 2008. Facile Biosynthesis, Separation and Conjugation of Gold Nanoparticles to Doxorubicin, *Nanotechnology*, 19:495101, Nov.

148. Chanda, N., Kattumuri, V., Shukla, R., Zambra, A., Katti, K., Upendran, A., Kulkarni, R.R., Kan, P., Fent, G.M., Casteel, S.W., Smith, C.J., Boote, E., Robertson, J.D., Cutler, C., Lever, J.R., Katti, K.V. and Kannan, R. 2009. Bombesin Functionalized Gold Nanoparticles Show *In vitro* and *In vivo* Cancer Receptor Specificity, *Proc. Natl. Acad. Sci.*, 1072(10):1-6, Nov.

149. Cheng, Y., Samia, A.C., Meyers, J.D., Panagopoulos, I., Fei, B. and Burda, C. 2008. Highly Efficient Drug Delivery with Gold Nanoparticle Vectors for *In Vivo* Photodynamic Therapy of Cancer, *J. Am. Chem. Soc.*, 130:10643-10647, Jul.

150. Agasti, S.S., Chompoosor, A., You, C.C., Ghosh, P., Kim, C.K. and Rotello, V.M. 2009. Photoregulated Release of Caged Anticancer Drugs from Gold Nanoparticles, *J. Am. Chem. Soc.*, 131:5728-5729, Jan.

151. Gibson, J.D., Khanal, B.P. and Zubarev, E.R. 2007. Paclitaxel-Functionalized Gold Nanoparticles, *J. Am. Chem.*, 129:11653-11661, Aug.

152. Lee. S., Cha, E.J., Park, K., Lee, S.Y., Hong, J.K., Sun, I.C., Kim, S.Y., Choi, K., Kwon, I.C., Kim, K. and Ahn, C.H. 2008. A Near-Infrared-Fluorescence-Quenched Gold Nanoparticle Imaging Probe for *In Vivo* Drug Screening and Protease Activity Determination, *Angew. Chem. Int. Ed.*, 47:2804-2807, May.

153. Craig, G.E., Brown, S.D., Lamprou, D.A., Graham, D. and Wheate, N.J. 2012. Cisplatin-Tethered Gold Nanoparticles That Exhibit Enhanced Reproducibility, Drug Loading and Stability: A Step Closer to Pharmaceutical Approval?, *J. Am. Chem. Soc.*, 51(6):3490-3497, Mar.

154. Brown, S.D., Nativo, P., Smith, J.A., Stirling, D., Edwards, P.R., Venugopal, B., Flint, D.J., Plumb, J.A., Graham, D. and Wheate, N.J. 2010. Gold Nanoparticles for the Improved Anticancer Drug Delivery of the Active Component of Oxaliplatin, *J. Am. Chem. Soc.*, 132:4678-4684, Mar.

155. Weston, S.D., Daniel, W.L., Giljohann, D.A., Mirkin, C. A., Lippard, S.J. 2009. Polyvalent Oligonucleotide Gold Nanoparticle Conjugates as Delivery Vehicles for Platinum(IV) Warheads, *J. Am. Chem. Soc.*, 131:14652-14653, Aug.

156. Shenoy, D., Fu, W., Li, J., Crasto, C., Jones, G., DiMarzio, C., Sridhar, S. and Amiji, M. 2006. Surface Functionalization of Gold Nanoparticles using Hetero-bifunctional Polyethylene Glycol Spacer for Intracellular Tracking and Delivery, *International Journal of Nanomedicine*, 1(1):51-57.

157. Yigit, M.V. and Medarova. 2012. *In Vivo and Ex Vivo* Applications of Gold Nanoparticles for Biomedical SERS Imaging, *Am. J. Nucl. Med. Mol. Imaging*, 2(2):232-241, Apr.

158. Kemp, M.M., Kumar, A., Mousa, S., Dyskin, E., Yalcin, M., Ajayan, P., Linhardt, R.J. and Mousa, S.A. 2009. Gold and Silver Nanoparticles Conjugated with Heparin Derivative Possess Anti-angiogenic Properties, *Nanotechnology*, 20:455104.

159. Ghosh, P.S., Kim, C.K., Forbes, N.S. and Rotello, V.M. 2008. Efficient Gene Delivery Vectors by Tuning the Surface Charge Density of Amino Acid-Functionalized Gold Nanoparticles, *ACSNano*, 2(11):2213-2218.

160. Han, G., Ghosh, P. and Rotello, V.M. 2007. Functionalized Gold Nanoparticles for Drug Delivery, *Nanomedicine*, 2(1):113-123.

161. Derfus, A.M., Chan, W.C.W. and Bhatia, S.N. 2004. Probing the Cytotoxicity of Semiconductor Quantum Dots, *Nano Lett.*, 4(1):11-18, Feb.

162. Drobohlavova, J., Adam, V. Kizek, R. and Hubalek, J. 2009. Quantum Dots − Characterization, Preparation and Usage in Biological Systems, *Int. J. Mol. Sci.*, 10:656-673, Feb.

163. Hardman, R. 2006. A Toxicologic Review of Quantum Dots: Toxicity Depends on Physicochemical and Environmental Factors, *Environmental Health Perspectives*, 114(2):165-172, Sept.

164. Liu, H.Y. and Vu, T.Q. 2007. Identification of Quantum Dot Bioconjugates and Cellular Protein Co-localization by Hybrid Gel Blotting, *Nano Lett.*, 7(4):1044-1049, Mar.

165. Wu, X., Liu, H., Liu, J., Haley, K.N., Treadway, J.A., Larson, J.P., Ge, N., Peale, F. and Bruchez, M.P. 2002. Immunofluorescent Labeling of Cancer Marker Her2 and other Cellular Targets with Semiconductor Quantum Dots, *Nature Biotech.*, 21:41-46, Jan.

166. Chattopadhyay, P.K., Price, D.A., Harper, T.F., Betts, M.R., Yu, J., Gostick, E., Perfetto, S.P., Goepfert, P., Koup, R.A., De Rosa, S.C., Bruchez, M.P. and Roederer, M. 2005. Quantum Dots Semiconductor Nanocrystals for Immunophenotyping by Polychromatic Flow Cytometry, *Nature Med.*, 12(8):972-977, Aug.

167. Kaji, N., Tokeshi, M. and Baba, Y. 2007. Single-Molecule Measurements with a Single Quantum Dot, *The Chemical Accord*, 7:295-304, Aug.

168. Gao, X., Cui, Y., Levenson, R.M., Chung, L.W.K. and Nie, S. 2004. *In Vivo* Cancer Targeting and Imaging with Semiconductor Quantum Dots, *Nature Biotech.*, 22(8):969-976, Aug.

169. Weng, K.C., Noble, C.O., Paphadjopoulos-Sternberg, B., Chen, F.F., Drummond, D.C., Kirpotin, D.B., Wang, D., Hom, Y.K., Hann, B. and Park, J.W. 2008. Targeted Tumor Cell Internalization and Imaging of Multifunctional Quantum Dots-Conjugated Immunoliposomes *In Vitro* and *In Vivo*, *Nano Lett.*, 8(9):2851-2857, Jul.

170. Walling, M.A., Novak, J.A. and Shepard, J.R.E. 2009. Quantum Dots for Live Cell and *In Vivo* Imaging, *Int. J. Mol. Sci.* 10:441-491, Feb.

171. Guzelian, A.A., Katari, J.E.B., Kadavanich, A.V., Banin, U., Hamad, K., Juban, E. and Alivisatos. 1996. Synthesis of Size-selected, Surface-Passivated InP Nanocrystals, *J. Phys. Chem.*, 100:7212-7219, Feb.

172. Ryu, E., Kim, S., Jang, E., Jun, S., Jang, H., Kim, B. and Kim, S.W. 2009. Step-wise Synthesis of InP/ZnS Core-Shell Quantum Dots and the Role of Zinc Acetate, *Chem. Mater.*, 21(4):573-575, Feb.

173. Gao, X., Yang, L., Petros, J.A., Marshall, F.F., Simons, J.W. and Nie, S. 2005. *In Vivo* Molecular and Cellular Imaging with Quantum Dots, *Anal. Biochem.*, 16:63-72.

174. http://www.cytimmune.com/go.cfm?do=Page.View&pid=26 (Accessed: 12-06-2012)

175. http://www.nanospectra.com/clinicians/aurolasetherapy.html (Accessed: 12-06-2012)

176. Etheridge, M.L., Campbell, S.A., Erdman, A.G., Haynes, C.L., Wolf, S.M., McCullough, J. 2012. The Big Picture on Nanomedicine: The State of Investigational and Approved Nanomedicine Products, *Nanomedicine*, 9(1):1-14, Jun.

177.   Ahn, C.H., Chae, S.Y., Bae, Y.H. and Kim, S.W. 2002. Biodegradable Poly(ethylenemine) for Plasmid DNA Delivery, *Journal of Controlled Release*, 80:273-282, Nov.

178.   Gao, J. and Xu, B. 2009. Applications of Nanomaterials inside Cells, *Nano Today*, 4:37-51, Oct.

179.   Mohan, P. and Rapoport, N. 2010. Doxorubicin as a Molecular Nanotheranostic Agent: Effect of Doxorubicin Encapsulation in Micelles or Nanoemulsions on the Ultrasound-mediated Intracellular Delivery and Nuclear Trafficking, *Molecular Pharmaceutics*, 7(6):1959-1973, Oct.

180.   Kim, G.B. and Kim, Y.P. 2012. Analysis of Protease Activity Using Quantum Dots and Resonance Energy Transfer, *Theranostics*, 2(2):127-138, Feb.

181.   Veiseh, O., Kievit, F.M., Ellenbogen, R.G. and Zhang, M. 2011. Cancer Cell Invasion: Treatment and Monitoring Opportunities in Nanomedicine, *Advanced Drug Delivery Reviews*, 63:582-596, Feb.

182.   Nystrom, A.M. and Wooley, K.L. 2011. The Importance of Chemistry in Creating Well-Defined Nanoscopic Embedded Therapeutics: Devices Capable of the Dual Functions of Imaging and Therapy, *Accounts of Chemical Research*, 44(10):969-978, Mar.

183.   Lovestam, G., Rauscher, H., Roebben, G., Kluttgen, B.S., Gibson, N., Putaud, J.P. and Stamm, H. 2010. Considerations on a Definition of Nanomaterial for Regulatory Purposes, *EU JRC Reference Reports*.

184.   Shenhar, R. and Rotello, V.M. 2003. Nanoparticles: Scaffolds and Building Blocks, *Acc. Chem. Res.*, 36:549-561, Jan.

185.   Thakor, A.S., Jokerst, J., Zavaleta, C., Massoud, T.F. and Gambhir, S.S. 2011. Gold Nanoparticles: A Revival in Precious Metal Administration to Patients, *Nano Lett.*, 11:4029-4036, Aug.

186.   McNeil, S. 2005. Nanotechnology for the Biologist, *Journal of Leukocyte Biology*, 78:585-594, Sept.

187.   Eustis, S. and El-Sayed, M.A. 2005. Why Gold Nanoparticles are more Precious than Pretty Gold: Noble Metal Surface Plasmon Resonance and its Enhancement of the Radiative and Non-radiative Properties of Nanocrystals of Different Shapes, *Chem.Soc. Rev.*, 35:209-217, Nov.

188.   Bunz, U.H.F. and Rotello, V.M.   2010. Gold Nanoparticle-Fluophore Complexes: Sensitive and Discerning "Noses" for Biosystems Sensing, *Angew. Chem. Int. Ed.*, 49:3268-3279, Jun.

189.   Tiwari, P.M., Vig, K., Dennis, V.A. and Singh, S.R.   2011. Functionalized Gold Nanoparticles and Their Biomedical Applications, *Nanomaterials*, 1:31-63, Jun.

190.   Jain, P.K., Lee, K.S., El-Sayed, I.H. and El-Sayed, M.A.   2006. Calculated Absorption and Scattering Properties of Gold Nanoparticles of Different Size, Shape and Composition: Applications in Biological Imaging and Biomedicine, *J. Phys. Chem.*, 110:7328-7248, Feb.

191.   Xu, C., Xu, K., Gu, H., Zhong, X., Guo, Z., Zheng, R., Zhang, X. and Xu, B. 2003. Nitrilotriacetic Acid-Modified Magnetic Nanoparticles as a General Agent to Bind Histadine Tagged Proteins, *J. Am. Chem. Soc.*, 126:3392-3393, Dec.

192.   Singh, N., Manshian, B., Jenkins, G.J.S., Griffiths, S.M., Williams, P.M., Maffeis, T.G.G., Wright, C.J. and Doak, S.H.   2009. Nanogenotoxicology: The DNA Damaging Potential of Engineered Nanomaterials, *Biomaterials*, 30(23):3891-3914, Apr.

193.   Xia, T., Li, N. and Nel, A.E.   2009. Potential Health Impact of Nanoparticles, *Annu. Rev. Public Health*, 30:137-150, Jan.

194.   Pathak, Y. and Thassu, D.   2009. Drug Delivery Nanoparticle Formulation and Characterization, Vol 191, Informa Healthcare, New York.

195.   Skirtach, A.G., Karageorgiev, P., Bedard, M.F., Sukhorukov, G.B. and Mohwald, H.   2008. Reversible Permeable Nanomembranes of Polymeric Microcapsules, *J. Am. Chem. Soc.*, 130:11572-11573, Apr.

196.   Morawska, L., Ristovski, Z., Jayaratne, E.R., Keogh, D.U. and Ling, X. 2008. Ambient Nano and Ultrafine Particles from Motor Vehicle Emissions: Characteristics, Ambient Processing and Implications on Human Exposure, *Atmospheric Environment*, 42:8113-8138, Jul.

197.   Kulmala, M., Vehkamaki, H., Petaja, T., Del Maso, M., Lauri, A., Kerminen, V.M., Birmili, W. and McMurry, P.H.   2004. Formation and Growth Rates of Ultrafine Atmospheric Particles: A Review of Observations, *Aerosol Science*: 35:143-176.

198.   Stern, S. and McNeil, S.E.   2007. Nanotechnology Safety Concerns Revisited, *Tox. Sci. Advance*, 1-59, Jun.

199. Turkevich, J. 1985. Colloidal Gold Part I: Historical and Preparative Aspects, Morphology and Structure, *Gold Bull.*, 18(3):86-91.

200. Kimling, J., Maier, M., Okenve, B., Kotaidis, V., Ballot, H. and Plech, A. 2006. Turkevich Method for Gold Nanoparticle Synthesis Revisited, *J. Phys. Chem. B.*, 110:15700-15707, May.

201. Polte, J., Ahner, T.T., Delissen, F., Sokolov, S., Emmerling, F., Thunermann, A.F. and Kraehnert, R. 2010. Mechanism of Gold Nanoparticles Formation in the Classical Citrate Synthesis Method Derived from Coupled *In Situ* XANES and SAXS Evaluation, *J. An. Chem. Soc.*, 132:1296-1301, Aug.

202. Ji, X., Song, X., Li, S., Bai, Y., Yang, W. and Peng, X. 2007. Size Control of Gold Nanocrystals in Citrate Reduction: The Third Role of Citrate, *J. Am. Chem. Soc.*, 129:13939-13948, Jun.

203. Jana, N.R., Gearheart, L. and Murphy, C.J. 2001. Evidence for Seed-Mediated Nucleation in the Chemical Reduction of Gold Salts to Gold Nanoparticles, *Chem. Mater.*, 13:2313-2322, May.

204. Frens, G. 1973. Controlled Nucleation for the Regulation of the Particle Size in Monodisperse Gold Suspensions, *Nat. Phys. Sci.*, 241:20–22.

205. Jana, N.R.J., Gearheart, L. and Murphy, C.J. 2001. Seeding Growth for Size Control of 5-40nm Diameter Gold Nanoparticles, *Langmuir*, 17:6782-6787, Aug.

206. Jana, N.R. 2005. Gram-Scale Synthesis of Soluble, Near-Monodisperse Gold Nanorods and Other Anisotropic Nanoparticles, *Small*, 1(89):875-882.

207. Narayanan, R. and El-Sayed, M.A. 2005. Catalysis with Transition Metal Nanoparticles in Colloidal Solution: Nanoparticle Shape Dependence and Stability, *J. Phys. Chem.*, 109:12663-12676, Apr.

208. Brown. L.O. and Hutchinson, J.E. 1999. Controlled Growth of Gold Nanoparticles During Ligand Exchange, *J. Am. Chem. Soc.*, 121:882-883, Oct.

209. Basiruddin, S.K., Saha, A., Pradhan, N. and Jana, N.R. 2010. Advances in Coating Chemistry in Deriving Soluble Functional Nanoparticles, *J. Phys. Chem.*, 114:11009-11017, Apr.

210. Sperling, R.A. and Parak, W.J. 2010. Surface Modification, Functionalization and Bioconjugation of Colloidal Inorganic Nanoparticles, *Phil. Trans. R. Soc.*, 268:1333-1383, Feb.

211. Lee, O.S., Prytkova, T.R. and Schatz, G.C. 2010. Using DNA to Link Gold Nanoparticles, Polymers and Molecules: A Theoretical Perspective, *J. Phys. Chem. Lett.*, 1:1781-1788, May.

212. Brust, M., Walker, M., Bethell, D., Schiffrin, D.J. and Whyman, R. 1994. Synthesis of Thiol-derivatised Gold Nanoparticles in a Two-phase Liquid-Liquid System, *Chem. Soc., Chem. Commun.*, 801-802, Dec.

213. Brinas, R.P., Hu, M., Qian, L., Lymar, E.S. and Hainfeld, J.F. 2007. Gold Nanoparticle Size Controlled by Polymeric Au(I) Thiolate Precursor Size, *J. Am. Chem. Soc.*, 130:975-982, Aug.

214. Maye, M.M., Zheng, W., Leibowitz, F.L., Ly, N.K. and Zhong, C.J. 2000. Heating Induced Evolution of Thiolate-Encapsulated Gold Nanoparticles: A Strategy for Size and Shape Manipulations, *Langmuir*, 16:490-497, Sept.

215. Chen, Y., Preece, J.A. and Palmer, R.E. 2008. Processing and Characterization of Gold Nanoparticles for Use in Plasmon Probe Spectroscopy and Microscopy of Biosystems, *Ann. N. Y. Acad. Sci.*, 1130:201-206.

216. Link, S. and El-Sayed, M.A. 1999. Spectral Properties and Relaxation Dynamics of Surface Plasmon Electronic Oscillations in Gold and Silver Nanodots and Nanorods, *J. Phys. Chem. B.*, 103:8410-8426, Aug.

217. He, Y.Q., Liu, S.P., Kong, L. and Liu, Z.F. 2005. A Study on the Sizes and Concentrations of Gold Nanoparticles by Spectra of Absorption, Resonance Rayleigh Scattering and Resonance Non-Linear Scattering, *Spectrochimica Acta Part A*, 61:2861-2866, Oct.

218. Haiss, W., Thanh, N.T.K., Aveyard, J. and Fernig, D.G. 2007. Determination of Size and Concentration of Gold Nanoparticles from UV-Vis Spectra, *Anal. Chem.,* 79:4215-4221, Jun.

219. Link, S. and El-Sayed, M.A. 1999. Size and Temperature Dependence of the Plasmon Absorption of Colloidal Gold Nanoparticles, *J. Phys. Chem. B.*, 103:4212-4217, Apr.

220. Chang, E., Miller, J.S., Sun, J., Yu, W.W., Colvin, V.L., Drezek, R. and West, J.L. 2005. Protease-activated Quantum Dot Probes, *Biochemical and Biophysical Research Communications*, 334:1317-1321, Jul.

221. Medintz, I.L. and Mattousi, H. 2008. Qunatum Dot-Based Resonance Energy Transfer and its Growing Application in Biology, *Phys. Chem. Chem. Phys.*, 11:17-45, Nov.

222. Riegler, J., Ditengou, F., Palme, K. and Nann, T. 2008. Blue Shift of CdSe/ZnS Nanocrystal-Labels Upon DNA-Hybridization, *Journal of Nanobiotechnology*, 6(7).

223. Hezinger, A.F.E., Teβmar, J. and Gopferich, A. 2007. Polymer Coating of Qunatum Dots – A Powerful Tool Toward Diagnostics and Sensorics, *European Journal of Pharmaceutics and Biopharmaceutics*, 68:138-152, Jun.

224. Michalet, X., Pinaud, F.F., Bentolila, L.A., Tsay, J.M., Doose, S., Li, J.J., Sundaresan, G., Wu, A.M., Gambhir, S.S. and Weiss, S. 2005. Quantum Dots for Live Cells, *In Vivo* Imaging and Diagnostics, *Science*, 307(5709):538-544, Jan.

225. Li, L., Daou, J., Texier, I., Chi, T.T.K., Liem, N.Q. and Reiss, P. 2009. Highly Luminescent CuInS$_2$/ZnS Core/Shell Nanocrystals: Cadmium-Free Quantum Dots for *In Vivo* Imaging, *Chem. Mater.*, 21:2422-2429, Apr.

226. Smith, A.M., Duan, H., Mohs, A.M. and Nie, S. 2008. Bioconjugated Quantum Dots for *In Vivo* Molecular and Cellular Imaging, *Advanced Drug Delivery Reviews*, 60:1226-1240, Apr.

227. Reiss, P., Bleuse., J. and Pron, A. 2002. Highly Luminescent CdSe/ZnSe Core/Shell Nanocrystals of Low Size Dispersion, *Nano Lett.*, 2(7):781-784, May.

228. Guyot-Sionnest, P. and Hines, M.A. 1996. Synthesis and Characterization of Strongly Luminescing ZnS-Capped CdSe Nanocrystals, *J. Phys. Chem.*, 100:468-471, Jan.

229. Wang, T., Chen, J.Y., Zhen, S., Wang, P.N., Wang, C.C., Yang, W.L. and Peng, Q. 2009. Thiol-Capped CdTe Quantum Dots with Two-Photon Excitation for Imaging High Autofluorescence Background Living Cells, *J. Fluoresc.*, 19:615-621, Dec.

230. Zheng, J., Zhang, C. and Dickson, R.M. 2004. Highly Fluorescent, Water-Soluble, Size-Tunable Gold Quantum Dots, *Physical Review Letters*, 93(7):077402.

231. Volpe, M.V., Longo, A., Pasquini, L., Casuscelli, V. and Carotenuto, G. 2003. Synthesis and Characterization of Gold-based Quantum Dots, *Journal of Materials Science Letters*, 22:1679-1699.

232. Zheng, J., Nicovich, P.R. and Dickson, R.M. 2007. Highly Fluorescent Noble-Metal Quantum Dots, *Annu. Rev. Phys. Chem.*, 58:409-431, Nov.

233. Dubois, F., Mahler, B., Dubertret, B., Doris, E. and Mioskowski, C. 2006. A Versatile Strategy for Quantum Dot Ligand Exchange, *J. Am. Chem. Soc.*, 129:482-483, Oct.

234. Alivisatos, A.P. 1996. Semiconductor Clusters, Nanocrystals, and Quantum Dots, Science, 271:933-937.

235. Nirmal, M. and Brus, L.E. 1999. Luminescence Photophysics in Semiconductor Nanocrystals, *Acc. Chem. Res.*, 32:407-414.

236. Chan, W.C.W., Maxwell, D.J., Gao, X., Bailey, R.E., Han, M. and Nie, S. 2002. Luminescent Quantum Dots for Multiplexed Biological Detection and Imaging, *Anal. Biotech.*, 13:40-46, Feb.

237. Resch-Genger, U., Grabolle, M., Cavaliere-Jaricot, S., Nitschke, R. and Nann, T. 2008. Quantum Dots Versus Organic Dyes as Fluorescent Labels, *Nature Meth.*, 5(9):763-775, Sept.

238. Adiseshaiah, P.P., Hall, J.B. and McNeil, S.E. 2009. Nanomaterial Standards for Efficacy and Toxicity Assessment, *WIREs Nanome. Nanibiotech.*, 2:99-112.

239. Malik, M.Y., Hashim, M.A., Nabi, F. and Malik, M.A. 2011. Nanotoxicity: Dimensional and Morphological Concerns, *Advances in Phys. Chem.*, 2011:450912, Jan.

240. Dixit, V., Van den Bossche, J., Sherman, D.M., Thompson, D.H. and Andres, R.P. 2006. Synthesis and Grafting of Thiocotic Acid-PEG-Folate Conjugates onto Au Nanoparticles for Selective Targeting of Folate Receptor-Positive Tumour Cells, *Bioconjugate Chem.*, 17:603-609, Feb.

241. Byrne, J.D., Betancourt, T. and Brannon-Peppas, L. 2008. Active Targeting Schemes for Nanoparticle Systems in Cancer Therapeutics, *Advanced Drug Delivery Reviews*, 60:1615-1625, Sept.

242. Zitsmann, S., Kramer, S., Mier, W., Hebling, U., Altmann, A., Rother, A., Berndorff, D., Eisenhut, M. and Haberkom, U. 2007. Identification and Evaluation of a New Tumor Cell-Binding Peptide, FROP-1, *J. Nucl. Med.*, 48(6):965-972.

243. Shadidi, M. and Sioud, M. 2003. Selective Targeting of Cancer Cells Using Synthetic Peptides, *Drug Resistance Updates*, 6:363-371, Nov.

244. Aina. O.H., Liu, R., Sutcliffe, J.L., Marik, J., Pan, C.X. and Lam, K.S. 2007. From Combinatorial Chemistry to Cancer-Targeting Peptides, *Molecular Pharmaceutics*, 4(5):631-651, Jul.

245. Levy, R., Thanh, N.T.K., Doty, R.C., Hussain, I., Nichols, R.J., Schiffrin, D.J., Brust, M. and Fernig, D.G. 2004. Rational and Combinatorial Design of Peptide Capping Ligands for Gold Nanoparticles, *J. Am. Chem. Soc.*, 126:10076-10054, Mar.

246. Wang, Z., Levy, R., Fernig, D.G. and Brust, M. 2005. The Peptide Route to Multifunctional Gold Nanoparticles, *Bioconjugate Chem.*, 16:497-500, Apr.

247. Krpetic, Z., Nativo, P., Porta, F. and Brust, M. 2009. A Multidentate Peptide for Stabilization and Facile Bioconjugation of Gold Nanoparticles, *Bioconjugate Chem.*, 20:619-624, Jan.

248. Zitsman, S., Ehemann, V. and Schwab, M. 2002. Arginine-Glycine-Aspartic Acid (RGD)-Peptide Binds to Both Tumor and Tumor-endothelial Cells *In Vivo*, *Cancer Res.*, 62:5139-5143, Sept.

249. Stern, M. and Herrmann, R. 2005. Overview of Monoclonal Antibodies in Cancer Therapy: Present and Promise, *Critical Reviews in Oncology/Hematology*, 54:11-29, Oct.

250. Gulloti, E. and Yeo, Y. 2009. Extracellularly Activated Nanocarriers: A New Paradigm of Tumor Targeted Drug Delivery, *Molecular Pharmaceutics*, 6(4):1041-1051, Apr.

251. Weiner, L.M. 2006. Fully Human Therapeutic Monoclonal Antibodies, *Journal of Immunotherapy*, 29(1):1-9, Feb.

252. Fitzpatrick, D.P.G., You, J.S., Bemis, K.G., Wery, J.P., Ludwig, J.R. and Wang, M. 2007. Searching for Potential Biomarkers of Cisplatin Resistance in Human Ovarian Cancer using label-free LC/MS-based Protein Quantification Method, *Proteomics Clin. Appl.*, 1:246-263, Nov.

253. Solar, P. and Sytkowski, A.J. 2011. Differentially Expressed Genes Associated with Cisplatin Resistance in Human Ovarian Adenocarcinoma Cell Line A2780, *Cancer Letters*, 309:11-18, May.

254. You, C.C., Verma, A. and Rotello, V.M. 2006. Engineering the Nanoparticle-Biomacromolecule Interface, *Soft Matter*, 2:190-204, Jan.

255. Yezhelyev, M.V., Qi, L., O'Regan, R.M., Nie, S. and Gao, X. 2008, Proton-Sponge Coated Quantum Dots for siRNA Delivery and Intracellular Imaging, *J. Am. Chem. Soc.*, 130:9006-9012, Jan.

256. Wurle-Knirch, J.M, Pulskamp, K. and Krug, H.F. 2006. Oops they did it Again! Carbon Nanotubes Hoax Scientists in Viability Assays, *Nano Lett.*, 6(6):1261-1268, Mar.

257. El-Ansary, E. and Al-Daihan, S. 2009. On the Toxicity of Therapeutically used Nanoparticles: An Overview, *Journal of Toxicology*, 2009:754810.

258.   Liu, Z., Chen, K., Davis, C., Sherlock, S., Cao, Q.Z., Chen, X.Y., Dai, H.J. 2008. Drug Delivery with Carbon Nanotubes for *In Vivo* Cancer Treatment, *Cancer Res.*, 68:6652–6660.

259.   Pisanic, T.R., Blackwell, J.D., Shubayev, V.I., Finones, R.R. and Jin, S. 2007. Nanotoxicity of Iron Oxide Nanoparticle Internalization in Growing Neurons, *Biomaterials*, 28(16):2572–2581.

260.   De Paoll Lacerda, S.H., Park, J.J., Meuse, C., Pristinki, D., Becker, M.L., Karim, A. and Douglas, J.F. 2010. Interaction of Gold Nanoparticles with Common Human Blood Proteins, *ACSNano*, 4(1):365-379, Dec.

261.   Li, J.J., Zou, L., Hartono, D., Ong, C.N., Bay, B.H., Lanry-Yung, L.Y. 2008. Gold Nanoparticles Induce Oxidative Damage in Lung Fibroblasts *In Vitro*, *Adv. Mater.*, 20:138–42.

262.   Sudeep, P.K., Joseph, S.T.S, and Thomas, K.G. 2005. Selective Detection of Cysteine and Glutathione Using Gold Nanorods, *J. Am. Chem. Soc.*, 127:6516-6517, Feb.

263.   Gao, W., Xu, K., Ji, L. and Tang, B. 2011. Effect of Gold Nanoparticles on Glutathione Depletion-Induced Hydrogen Peroxide Generation and Apoptosis in HL7702 Cells, *Toxicology Letters*, 205:86-95, May.

264.   Kong, B., Seog, J.H., Graham, L.M. and Lee, S.B. 2011. Experimental Considerations on the Cytotoxicity of Nanoparticles, *Nanomedicine*, 6(5):929-941.

265.   Love, S.A., Maurer-Jones, M.A., Thompson, J.W., Lin, Y.S and Haynes, C.L. 2012. Assessing Nanoparticle Toxicity, *Annu. Rev. Anal. Chem.*, 5:181-205, Apr.

266.   Kandasamy, K., Choi, C.S. and Kim, S. 2010. An Efficient Analysis of Nanomaterial Cytotoxicity Based on Bioimpedance, *Nanotechnology,* 21:375501.

267.   Chithrani, B.D and Chan, W.C.W. 2007. Elucidating the Mechanism of Cellular Uptake and Removal of Protein Coated Gold Nanoparticles of Different Sizes and Shapes, *Nano Lett.*, 7(6):1542-1550, Mar.

268.   Huang, K., Ma, H., Liu, J., Huo, S., Kumar, A., Wei, T., Zhang, X., Jin, S., Gan, Y., Wang, P.C., He, S., Zhang, X. and Liang, X.J. 2012. Size-Dependent Localization and Penetration of Ultrasmall Gold Nanoparticles in Cancer Cells, Multicellular Spheroids and Tumors *In Vivo*, 6(5):4483-4493, Apr.

269.   Aillon, K.L., Xie, Y., El-Gendy, N., Berkland, C.J. and Forrest, M.L. 2009. Effects of Nanomaterial Physicochemical Properties on *In Vivo* Toxicity, *Advanced Drug Delivery Reviews*, 61:457-466, Apr.

270. Patra, H.K., Banerjee, S., Chaudhuri, U., Lahiri, P. and Dasgupta, A.K. 2007. Cell Selective Response to Gold Nanoparticles, *Nanomedicine: Nanotechnology, Biology and Medicine 3*, 3:111-119, Mar.

271. Soenen, S.J., Manshian, B., Montenegro, J.M., Amin, F., Meermann, B., Thiron, T., Cornelissen, M., Vanhaecke, F., Doak, S., Parak, W.J., De Smedt, S. and Braeckmans, K. 2011. Cytotoxic Effects of Gold Nanoparticles: A Multiparametric Study, *ACSNano*, 6(7):5767-5783, Dec.

272. Arvizo, R.R., Miranda, O.R., Thompson, M.A., Pabelick, C.M., Bhattacharya, R., Robertson, J.D., Rotello, V.M., Prakash, Y.S. and Mukherjee, P. 2010. Effect of Nanoparticle Surface Charge at the Plasma Membrane and Beyond, *Nano Lett.*, 10:2543-2548, Jun.

273. Goodman, C.M., McCusker, C.D., Yilmaz, T. and Rotello, V.M. 2004. Toxicity of Gold Nanoparticles Functionalized with Cationic and Anionic Side Chains, *Bioconjugate Chem.*, 15:897-900, Mar.

274. Murphy, C.J., Gole, A.M., Stone, J.W., Sisco, P.N., Alkilany, A.M., Goldsmith, E.C. and Baxter, S.C. 2008, Gold Nanoparticles in Biology: Beyond Toxicity to Cellular Imaging, *Account of Chemical Research*, 41(12):1721-1730, Feb.

275. Albanese, A., Tang, P.S. and Chan, W.C.W. 2012. The Effect of Nanoparticle Size, Shape, and Surface Chemistry on Biological Systems, *Annu. Rev. Biomed. Eng.*, 14:1-16, Apr.

276. Rzigalinkski, B.A. and Strobl, J.S. 2009. Cadmium-containing Nanoparticles: Perspectives on Pharmacology and Toxicology of Quantum Dots, *Toxicology and Applied Pharmacology*, 238:280-288, Apr.

277. Ballou, B., Ernst, L.A., Andrenko, S., Harper, T., Fitzpatrick, J.A.J., Waggoner, A.S. and Bruchez, M.P. 2007. Sentinel Lymph Node Imaging Using Quantum Dots in Mouse Tumor Models, *Bioconjugate Chem.*, 18:389-396, Nov.

278. Yu, W.W., Chang, E., Drezek, R. and Colvin, V.L. 2006. Water-soluble Quantum Dots for Biomedical Applications, *Biochemical and Biophysical Research Communications*, 348:781-786, Aug.

279. Duan, H. and Nie, S. 2006. Cell-Penetrating Quantum Dots Based on Multivalent and Endosome-Disrupting Surface Coatings, *J. Am. Chem. Soc.*, 129:3333-3338, Nov.

280. Xia, T., Kovochich, M., Liong, M., Meng, H., Kabehle, S., George, S., Zink, J.I. and Nel, A.E. 2009. Polyethyleneimine Coating Enhances the Cellular Uptake of Mesoporous Silica Nanoparticles and Allows for Safe Delivery of siRNA and DNA Constructs, *ACSNano*, 3(10):3273-3286, Aug.

281. Yue, Y., Jin, F., Chen, Y., Kung, H.F., Lin, M.C.M. and Wu, C. 2009. Revisit the Complexation of PEI and DNA – How to Make Low Cytotoxic and Highly Efficient PEI Gene Transfection Non-viral Vectors with a Controllable Chain Length and Structure?, *Journal of Controlled Release*, 140:40-46, Jul.

282. Tian, H.Y., Deng, C., Lin, H., Sun, J., Deng, M., Chen, X. and Jing, X. 2005. Biodegradable Cationic PEG-PEI-PBLG Hyperbranched Block Copolymer: Synthesis and Micelle Characterization, *Biomaterials*, 26:4209-4217, Dec.

283. Liang, B., He, M.L., Xiao, Z.P., Li, Y., Chan, C.Y., Kung, H.F., Shuai, X.T. and Peng, Y. 2008. Synthesis and Characterization of Folate-PEG-Grafted-Hyperbranched-PEI for Tumor-targeted Gene Delivery, *Biochemical and Biophysical Research Communications*, 367:874-880, Jan.

284. Riddles, P.W., Blakeley, R.L. and Zerner, B. 1979. Ellman's Reagent:5,5'-Dithiobis(2-nitrobenzoic acid) – A re-examination, *Anal. Biochem.*, 94:75-81, Jul.

285. Eyer, P., Worek, F., Kiderlen, D., Sinko, G., Stuglin, A., Simeon-Rudolf, V. and Reiner, E. 2003. Molar Absorption Coefficients for the Reduced Ellman Reagent: Reassessment, *Anal. Biochem.*, 312:224-227, Aug.

286. Xu, C., Xu, K., Gu, H., Zhong, X., Guo, Z., Zheng, R., Zhang, X. and Xu, B. 2004. Nitrilotriacetic Acid-Modified Magnetic Nanoparticles as a General Agent to Bind Histidine-Tagged Proteins, *J. Am. Chem. Soc.*, 126:3392-3393, Feb.

287. Zheng, M., Li, Z. and Huang, X. 2004. Ethylene Glycol Monolayer Protected Nanoparticles: Synthesis, Characterization, and Interactions with Biological Molecules, *Langmuir*, 20:4226-4235, Feb.

288. Pierce Biotechnology. 2006. Crosslinking Reagents Technical Handbook.

289. Leo, E., Vandelli, M.A., Cameroni, R. and Forni, F. 1997. Doxorubicin-loaded Gelatin Nanoparticles Stabilized by Glutaraldehyde: Involvement of the Drug in the Cross-linking Process, *International Journal of Pharmaceutics*, 155:75-82, May.

290. Migneault, I., Dartinguenave, C., Bertrand, M.J. and Waldron, K.C. 2004. Glutaraldehyde: Behavior in Aqueous Solution Reaction with Proteins, and Application to Enzyme Crosslinking, *BioTechniques*, 37:790-802, Nov.

291. Etrych, T., Chytil, P., Mrkvan, T., Sirova, M., Rihova, B. and Ulbrich, K. 2008. Conjugates of Doxorubicin with Graft HPMA Copolymers for Passive Tumor Targeting, *Journal of Controlled Release*, 132:184-192, Apr.

292. Pong, B.K., Trout, B.L. and Lee, J.Y. 2008. Modified Ligand-Exchange for Efficient Solubilisation of CdSe/ZnS Quantum Dots in Water: A Procedure Guided by Computational Studies, *Langmuir*, 24:5270-5276, Feb.

293. Dubois, F., Mahler, B., Dubertret, B., Doris, E. and Mioskowski. 2006. A Versatile Strategy for Quantum Dot Ligand Exchange, *J. Am. Chem. Soc.*, 129:482-483, Oct.

294. Susumu, K., Uyeda, H.T., Medintz, I.L., Pons, T., Delehanty, J.B. and Mattoussi, H. 2007. Enhancing the Stability and Biological Functionalities of Quantum Dots via Compact Multifunctional Ligands, *J. Am. Chem. Soc.*, 129:13987-13996, Jul.

295. Fischer, S.J., Benson, L.M., Fauq, A., Naylor, S. and Windebank, A.J. 2008. Cisplatin and Dimethyl Sulfoxide React to Form an Adducted Compound with Reduced Cytotoxicity and Neurotoxicity, *NeuroToxicology*, 29:444-452, Mar.

296. Tamura, Y., Watanabe, F., Nakatani, T., Yasui, K., Fuji, M., Komurasaki, T., Tsuzuki, H., Maekawa, R., Yoshioka, T., Kawada, K., Sugita, K. and Ohtani, M. 1998. Highly Selective and Orally Active Inhibitors of Type IV Collagenase (MMP-9 and MMP-2): *N*-Sulfonylamino Acid Derivatives, *J. Med. Chem.*, 41:640-649, Nov.

297. Stratagene. ArcticExpress™ Competent Cells and ArcticExpress™ (DE3) Competent Cells Instruction Manual, Rev. 050061.

298. Salisbury, C.M., Maly, D.J. and Ellman, J.A. 2002. Peptide Microarrays for the Determination of Protease Substrate Specificity, *J. Am. Chem. Soc.*, 124:14868-14870, Jun.

299. Keller, T.A., Duschi, C., Kroger, D., Sevin-Landais, A.F. and Vogel, H. 1995. Reversible Oriented Immobilization of Histidine-Tagged Proteins on Gold Surfaces Using a Chelator Thioalkane, *Supremolecular Science*, 2:155-160, Apr.

300. Lee, J.K., Kim, Y.G., Chi, Y.S., Yun, W.S. and Choi, I.S. 2004. Grafting Nitrilotriacetic Groups onto Carboxylic Acid-Terminated Self-Assembled Monolayers on Gold Surfaces for Immobilization of Histidine-Tagged Proteins, *J. Phys. Chem.*, 108:7665-7673, Mar.

301. Cao, C. and Sim, S.J. 2007. Signal Enhancement of Surface Plasmon Resonance Immunoassay Using Enzyme Precipitation-Functionalized Gold Nanoparticles: A Femto Molar Level Measurement of Anti-Glutamic Acid Decarboxylase Antibody, *Biosensors and Bioelectronics*, 22:1874-1880, Aug.

302. Ojea-Jimenez, I. and Puntes, V. 2009. Instability of Cationic Gold Nanoparticle Bioconjugates: The Role of Citrate Ions, *J. Am. Chem. Soc.*, 131:13320-13327, Aug.

303. Ueda, E.K.M., Gout, P.W. and Morganti, L. 2003. Current and Prospective Applications of Metal Ion-Protein Binding, *Journal of Chromatography A*, 988:1-23, Dec.

304. Gaberc-Porekar, V. and Menart, V. 2001. Perspectives of Immobilized-Metal Affinity Chromatography, *J. Biochem. Biophy. Methods*, 49:335-360.

305. Chaga, G.S. 2001. Twenty-five Years of Immobilized Metal Ion Affinity Chromatography: Past, Present and Future, *J. Biochem. Biophys. Methods*, 49:313-334.

306. Armstrong, R.N. 1991. Glutathione-S-Transferase: Reaction Mechanism, Structure, and Function, *Chem. Res. Toxicol.*, 4(2):131-140, Apr.

307. Murphy, G., Stanton, H., Cowell, S., Butler, G., Knauper, V., Atkinson, S. and Gavrilovic, J. 1999. Mechanisms for Pro-Matrix Metalloproteinase Activation, *APMIS*, 107:38-44.

308. Olson, M.W., Gervasi, D.C., Mobashery, S. and Fridman, R. 1997. Kinetic Analysis of the Binding of Human Matrix Metalloproteinase-2 and -9 to Tissue Inhibitor of Metalloproteinase (TIMP)-1 and TIMP-2, *The Journal of Biological Chemistry*, 272(47):29975-29983, Sept.

309. Rogers, A. and Gibon, Y. 2009. Chapter 4: Enzyme Kinetics - Theory and Practise, Plant Metabolic Networks (Springer).

310. Eisenthal, R. and Danson, M. 2002. Enzyme Assays: A Practical Approach, 2nd Ed. Oxford: Oxford University Press, 283p.

311. Li, Q., Withoff, S. and Verma, I.M. 2005. Inflammation-Associated Cancer: NF-κB is the Lynchpin, *TRENDS in Immunology*, 26(6):318-325, Jun.

312. Iwakoshi, N.N., Lee, A.H., Vallabhajosyula, P., Otipoby, K.L., Rajewsky, K. and Glimcher, L.H. 2003. Plasma Cell Differentiation and the Unfolded Protein Response Intersect at the Transcription Factor XBP-1, *Nature Immunology*, 4(4):321-329, Mar.

313. Yang, J.M., Xu, Z., Wu, H., Zhu, H., Wu, X. and Hait, W.N. 2003. Overexpression of Extracellular Matrix Metalloproteinase Inducer in Multidrug Resistant Cancer Cells, *Mol. Can. Res.*, 1:420-427, Apr.

314. Davidson, B., Goldberg. I., Gotlieb, W.H., Kopolovic, J., Risberg, B., Ben-Baruch, G. and Reich, R. 2003. Coordinated Expression of Integrin Subunits, Matrix Metalloproteinases (MMP), Angiogenic Genes and ETS Transcription Factors in Advanced Stage Ovarian Carcinoma: A Possible Activation Pathway?, *Cancer and Metastasis Reviews*, 22:102-115.

315. Visse, R. and Nagase, H. 2003. Matrix Metalloproteinases and Tissue Inhibitors of Metalloproteinases: Structure, Function and Biochemistry, *Circ. Res.*, 92:827-839, Mar.

316. Phan, T.B., Nolte, C., Kobayashi, S., Oflal, A.R. and Mayr, H. 2009. Can One Predict Changes from S_N1 to S_N2 Mechanisms?, *J. Am. Chem. Soc.*, 131:11392-11401, Apr.

317. Yemul, O. and Imae, T. 2008. Synthesis and Characterization of Polyethyleneimine Dendrimers, *Colloid. Polym. Sci.*, 286:747-752, Jan.

318. Badia, A.B., Cuccia, L., Demers, L., Morin, F. and Lennox, R.F. 1997. Structure and Dynamics in Alkanethiolate Monolayers Self-Assembled on Gold Nanoparticles: A DSC, FT-IR, and Deuterium NMR Study, *J. Am. Chem. Soc.*, 119:2682-2692, Oct.

319. Shibu, E.S., Muhammed, M.A.H., Tsukuda, T. and Pradeep, T. 2008. Ligand Exchange of $Au_{25}SG_{18}$ Leading to Functionalized Gold Clusters: Spectroscopy, Kinetics and Luminescence, *J. Phys. Chem.*, 112:12168-12176, Apr.

320. Templeton, A.C., Chen, S., Gross, S.M. and Murray, R.W. 1999. Water-soluble, Isolable Gold Clusters Protected by Tiopronin and Coenzyme-A Monolayers, *Langmuir*, 15:66-76, Nov.

321. Du, S., Kendall, K., Toloueinia, P., Mehrabadi, Y., Gupta, G. and Newton, J. 2012. Aggregation and Adhesion of Gold Nanoparticles in Phosphate Buffered Saline, *J. Nanopart. Res.*, 14:758, Jan.

322. Zhao, W., Lin, J. and Hsing, I.M. 2009. Rapid Synthesis of DNA-Functionalized Gold Nanoparticles in Salt Solution Using Mononucleotide-Mediated Conjugation, *Bioconjugate Chem.*, 20(6):1218-1222, Apr.

323. Goon, I.Y., Lai, L.M.H., Lim, M., Munroe, P., Gooding, J.J. and Amal, R. 2009. Fabrication and Dispersion of Gold-Shell-Protected Magnetite Nanoparticles: Systematic Control using Polyethyleneimine, *Chem. Mater.*, 21:673-681, Dec.

324. Lee, J.Y., Choi, Y.S., Suh, J.S., Kwon, Y.M., Yang, V.C., Lee, S.J., Chung, C.P. and Park, Y.J. 2011. Cell-Penetrating Chitoson/Doxorubicin/TAT Conjugates for Efficient Cancer Therapy, *Int. J. Cancer*, 128:2470-2480.

325. King, H.D., Yurgaitis, D., Willner, D., Firestone, R.A., Yang, M.B., Lasch, S.J., Hellstrom, K.E. and Trail, P.A. 1999. Monoclonal Antibody Conjugates of Doxorubicin Prepared with Branched Linkers: A Novel Method for Increasing the Potency of Doxorubicin Immunoconjugates, *Bioconjugate Chem.*, 10:279-288, Dec.

326. Tomlinson, R., Heller, J., Brocchini, S. and Duncan, R. 2003. Polyacetal-Doxorubicin Conjugates Designed for pH-Dependent Degradation, *Bioconjugate Chem.*, 14:1096-1106, Aug.

327. Torchilin, V.P. 2006. Multifunctional Nanocarriers, *Advancecd Drug Delivery Reviews*, 58:1532-1555, Sept.

328. Breunig, M., Bauer, S. and Goepferich, A. 2007. Polymers and Nanoparticles: Intelligent Tools for Intracellular Targeting?, *European Journal of Pharmaceutics and Biopharmaceuticals*, 68:112-128, Jun.

329. Chen Y., Palmer R.E. and Wilcoxon J.P. 2006. Sintering of Passivated Gold Nanoparticles under the Electron Beam, *Langmuir*, 22, 2851 – 2855.

330. Mafuné F., Kohno J., Takeda Y., and Kondow T. 2002. Nanoscale Soldering of Metal Nanoparticles for Construction of Higher-Order Structures, *J. Am. Chem. Soc.*, 125, 1686 - 1687.

331. Brewer, S.H., Glomm, W.R., Johnson, M.C., Knag, M.K. and Franzen, S. 2005. Probing BSA Binding to Citrate-Coated Gold Nanoparticles and Surfaces, *Langmuir*, 21:9303-9307, Jun.

332. Sykora, D., Kasicka, V., Miksik, I., Rezanka, P., Zaruba, K., Matejka, P. and Kral, V. 2010. Application of Gold Nanoparticles in Separation Sciences, *Journal of Separation Science*, 33(3):372-387, Feb.

333. Cai, H.H., Wang, H., Wang, J., Wei, W., Yang, P.H. and Cai, J. 2011. Naked Eye Detection of Glutathione in Living Cells Using Rhodamine B-Functionalized Gold Nanoparticles Coupled with FRET, *Dyes and Pigments*, 92:778-782, Jun.

334. Lim, I.S., Mott, D., Ip, W., Njoki, P.N., Pan, Y., Zhou, S. and Zhing, C.J. 2008. Interparticle Interactions in Glutathione Mediated Assembly of Gold Nanoparticles, *Langmuir*, 24:8857-8863, May.

335. Sendray, J. and Rodkey, F.L. 1961. Apparent Dissociation Constant of Phenol Red as Determined by Spectrophotometry and by Visual Colorimetry, *Clin. Chem.*, 7(6):646-654.

336. Giljohann, D.A., Seferos, D.S., Daniel, W.L., Massich, M.D., Patel, P.C. and Mirkin, C.A. 2010. Gold Nanoparticles for Biology and Medicine, *Angew. Chem. Int. Ed.*, 49:3280-3294, Apr.

337. Smith, A.M., Ruan, G., Rhyner, M.N. and Nie, S. 2006. Engineering Luminescent Quantum Dots for *In Vivo* Molecular and Cellular Imaging, *Annals of Biomedical Engineering*, 34(1):3-14, Feb.

338. Schneiderman, D., Kim, J.M., Senterman, M. and Tsang, B.K. 1999. Sustained Supression of Fas Ligand Expression in Cisplatin-Resistant Human Ovarian Surface Epithelial Cancer Cells, *Apoptosis*, 4(4):271-282.

339. Bertazza, L. and Mocellin, S. 2008. Tumor Necrosis Factor (TNF) Biology and Cell Death, *Frontiers in Bioscience*, 13:2736-2743, Jan.

340. Aggarwal, S., He, T., Fitz-Hugh, W., Rosenthal, K., Field, B., Heidbrink, J., Mesmer, D., Ruben, S.M. and Moore, P.A. 2009. Immune Modulator CD70 as a Potential Cisplatin Resistance Predictive Marker in Ovarian Cancer, *Gynecologic Oncology*, 115:430-437, Oct.

341. Abu-Hadid, M., Wilkes, J.D., Elakawi, Z., Pendyala, L. and Perez, R.P. 1997. Relationship between Heat Shock Protein 60 (HSP60) mRNA Expression and Resistance to Platinum Analogues in Human Ovarian and Bladder Carcinoma Cell Lines, *Cancer Letters*, 119:63-70, Apr.

342. Shen, D.W., Akiyama, S.I., Schoenlein, P., Pastan, I. and Gottesman, M.M. 1995. Characterization of High-Level Cisplatin-Resistant Cell Lines Established from a Human Hepatoma Cell Line and Human Adenocarcinoma Cells: Cross-Resistance and Protein Changes, *British Journal of Cancer*, 71:676-683.

343. Ciocca, D.R. and Calderwood, S.K. 2005. Heat Shock Proteins in Cancer: Diagnostic, Prognostic, Predictive, and Treatment Implications, *Cell Stress & Chaperones*, 10(2):86-103.

344. Plumb, J.A., Strathdee, G., Sludden, J., Kaye, S.B. and Brown, R. 2000. Reversal of Drug Resistance in Human Tumor Xenografts by 2'-Deoxy-5-

azacytidine-Induced Demethylation of the *hMLH1* Gene Promotor, <u>*Cancer Res.*</u>, 60:6039-6044, Nov.

345. Blasi, M.F., Ventura, I., Aquilina, G., Degan, P., Bertario, L., Bassi, C., Radice, P. and Bignami, M. 2006. A Human Cell-Based Assay to Evaluate the Effects of Alterations in the *MLH1* Mismatch Repair Gene, <u>*Cancer Res.*</u>, 66(18):9036-9044, Sept.

346. Ghosh, J.C., Dohi, T., Kang, B.H. and Altieri, D.C. 2008. Hsp60 Regulation of Tumor Cell Apoptosis, <u>*The Journal of Biological Chemistry*</u>, 283(8):5188-5194, Feb.

347. Cicchillitti, L., Michele, M.D., Urbani, A., Ferlini, C., Donati, M.B., Scambia, G. and Rotillo, D. 2008. Comparative Proteomic Analysis of Paclitaxel Sensitive A2780 Epithelial Ovarian Cancer Cell Line and its Resistant Counterpart A2780TC1 by 2D-DIGE: The Role of ERp57, <u>*Journal of Proteome Research*</u>, 8:1902-1912, Oct.

348. Ding, X., Mohd, A.B., Huang, Z., Baba, T., Bernardini, M.Q., Lyerly, H.K., Berchuck, A., Murphy, S.K., Buermeyer, A.B. and Devi, G.R. 2009. MLH1 Expression Sensitises Ovarian Cancer Cells to Cell Death Mediated by XIAP Inhibition, <u>*British Journal of Cancer*</u>, 101:269-277, Jun.

349. Matei, D.E. and Nephew, K.P. 2010. Epigenetic Therapies for Chemoresensitization of Epithelial Ovarian Cancer, <u>*Gynecologic Oncology*</u>, 116:195-201, Oct.

350. Caamano, J. and Hunter, C.A. 2002. NF-κB Family of Transcription Factors: Central Regulators of Innate and Adaptive Immune Functions, <u>*Clin. Microbiol. Rev.*</u>, 15(3):414-429, Jul.

351. Asadollahi, R., Hyde, C.A.C. and Zhong, X.Y. 2010. Epigenetics of Ovarian Cancer: From the Lab to the Clinic, <u>*Gynecologic Oncology*</u>, 118:81-87, Apr.

352. Kroll, A., Pillukat, M.H., Hahn, D. and Schnekenburger, J. 2009. Current *In Vitro* Methods in Nanoparticle Risk Assessment: Limitations and Challenges, <u>*European Journal of Pharmaceutics and Biopharmaceutics*</u>, 72:370-377, Aug.

353. Berridge, M.V. and Tan, A.S. 1998. Trans-Plasma Membrane Electron Transport: A Cellular Assay for NADH- and NADPH-oxidase Based on Extracellular, Superoxide-Mediated Reduction of the Sulfonated Tetrazolium Salt WST-1, <u>*Protoplasma*</u>, 205:74-82, Aug.

354.   Lewinski, N., Colvin, V. and Drezek, R. 2007. Cytotoxicity of Nanoparticles, *Small*, 4(1):26-49, May.

355.   Sethuraman, V.A., Na, K. and Bae, Y.H. 2006. pH-Responsive Sulfonamide/PEI System for Tumor Specific Gene Delivery: An *In Vitro* Study, *Biomacromolecules*, 7:64-70, Oct.

356.   Kabaniv, A.V. 2006. Polymer Genomics: An Insight into Pharmacology and Toxicology of Nanomedicines, *Advanced Drug Delivery Reviews*, 58:1597-1621, Oct.

357.   Nimesh, S., Goyal, A., Pawar, V., Jayaraman, S., Kumar, P., Chandra, R., Singh, Y. and Gupta, K.C. 2006. Polyethyleneimine Nanoparticles as Efficient Transfecting Agents for Mammalian Cells, *Journal of Controlled Release*, 110:457-468, Oct.

358.   Thomas, M. and Klibanov, A.M. 2002. Conjugation to Gold Nanoparticles Enhances Polyethyleneimine's Transfer of Plasmid DNA into Mammalian Cells, *Proc. Natl. Acad. Sci.*, 100(16):9138-9143, Aug.

359.   Alkilany, A.M. and Murphy, C.J. 2010. Toxicity and Cellular Uptake of Gold Nanoparticles: What we have learned so far?, *J. Nanopart. Res.*, 12:2313-2333, Nov.

360.   Sonavane, G., Tomoda, K. and Makino, K. 2008. Biodistribution of Colloidal Gold Nanoparticles after Intravenous Administration: Effect of Particle Size, *Colloids and Surfaces B: Biointerfaces*, 66:274-280, Jul.

361.   Mailander, V. and Landfester, K. 2009. Interaction of Nanoparticles with Cells, *Biomacromolecules*, 10:2379-2400, May.

362.   Rieznichenko, L.S., Dybkova, S.M., Gruzina, T.G., Ulberg, Z.R., Todor, I.N., Lukyanova, N.Y., Shpyleva, S.I. and Chekhun, V.F. 2012. Gold Nanoparticles Synthesis and Biological Activity Estimation *In Vitro* and *In Vivo*, *Exp. Oncol.*, 34(1):25-28, Jan.

363.   Wani, M.Y., Hashim, M.A., Nabi, F., Malik, M.A. 2011. Nanotoxicity: Dimensional and Morphological Concerns, *Advances in Physical Chemistry*, 2011(450912):15p.

364.   Jain, P.K., El-Sayed, I. and El-Sayed, M.A. 2007. Gold Nanoparticles Target Cancer, *NanoToday*, 2(1):18-29, Feb.

365.   Jia, C.J. and Schuth, F. 2011. Colloidal Metal Nanoparticles as a Component of Designed Catalyst, *Phys. Chem. Chem. Phys.*, 13:2457-2487, Jan.

366. Narayanan, R. and El-Sayed, M.A. 2005. Catalysis with transition Metal Nanoparticles in Colloidal Solution: Nanoparticle Shape Dependence and Stability, *J. Phys. Chem. B.*, 109:12663-12676, Apr.

367. Astruc, D. 2008. Chapter 1: Transition-Metal Nanoparticles in Catalysis: From Historical Background to the State-of-the-Art, Nanoparticles and Catalysis (Wiley), 1-48.

368. Grabar, K.C., Brown, K.R., Keating, C.D., Stranick, S.J., Tang, S.L. and Natan, M.J. 1997. Nanoscale Characterization of Gold Colloid Monolayers: A Comparison of Four Techniques, *Anal. Chem.*, 69:471-477, Feb.

369. Weisbecker, C.S., Merrit, M.V. and Whitesides, G.M. 1996. Molecular Self-Assembly of Aliphatic Thiols on Gold Colloids, *Langmuir*, 12:3763-3772, Sept.

370. Mirza, A.Z. and Shamshad, H. 2011. Preparation and Characterization of Doxorubicin Functionalized Gold Nanoparticles, *European Journal of Medicinal Chemistry*, 46:1857-1860, Feb.

371. Shon, Y.S., Gross, S.M., Dawson, B., Porter, M. and Murray, R.W. 2000. Alkanethiolate-Protected Gold Clusters Generated from Sodium S-Dodecylthiosulfate (Bunte Salts), *Langmuir*, 16:6555-6561, May.

372. Gu, Y.J., Cheng, J., Man, C.W.Y., Wong, W.T. and Cheng, S.H. 2011. Gold-Doxorubicin Nanoconjugates for Overcoming Multidrug Resistance, *Nanomedicine*, 8:204-211, Jun.

373. Wang, F., Wang, Y.C., Dou, S., Xiong, M.H., Sun, T.M. and Wang, J. 2011. Doxorubicin-Tethered Responsive Gold Nanoparticles Facilitate Intracellular Drug Delivery for Overcoming Multidrug Resistance in Cancer Cells, *ACSNano*, 5(5):3679-3692, Apr.

374. Beijnen, J.H., Van der Houwen, O.A.G.J., Voskuilen, M.C.H. and Underberg, W.J.M. 1986. Aspects of the Degradation Kinetics of Doxorubicin in Aqueous Solution, *International Journal of Pharmaceutics*, 86:90215-2.

375. Kim, D., Lee, E.S., Park, K., Kwon, I.C. and Bae, Y.H. 2008. Doxorubicin Loaded pH-sensitive Micelle: Antitumoral Efficacy against A2780/DOX Tumor, *Pharm. Res.*, 25(9):2074-2082, Dec.

376. Brenner, D.E., Wiernik, P.H., Wesley, M. and Bachur, N.R. 1984. Acute Doxorubicin Toxicity: Relationship to Pretreatment Liver Function, Response, and Pharmacokinetics in Patients with Acute Nonlymphocytic Leukemia, *Cancer*, 53:1042-1048.

377. Biocolor Life Science Assays Internet Manual. Downloaded 11-01-2012 (www.biocolor.co.uk).

378. Meyer, M., Essack, M., Kanyanda, S. and Rees, J.G. 2008. A Low-cost Flow Cytometric Assay for the Detection and Quantification of Apoptosis using an Anionic Halogenated Fluorescein Dye, *BioTechniques*, 45:317-320, Sept.

379. Sjostrom, J. and Makela, T. 2006. Chapter 1: Apoptosis and the Cell Cycle in Human Disease, Encyclopaedia of Life Sciences, Wiley, 1-6.

380. D'Amelio, M., Tino, E. and Cecconi, F. 2008. The Apoptosome: Emerging Insights and New Potential Targets for Drug Design, *Pharmaceutical Research*, 25(4):740-751, Aug.

381. Liu, J.R., Opipari, A.W., Tan, L., Jiang, Y., Zhang, Y., Tang, H. and Nunez, G. 2002. Dysfunctional Apoptosome Activation in Ovarian Cancer: Implications for Chemoresistance, *Cancer Res.*, 62:924-931, Feb.

382. Lowe, S.W. and Lin, A.W. 2000. Apoptosis in Cancer, *Carcinogenesis*, 21(3):485-495.

383. Ullrich, E., Bonmort, M., Mignot, G., Kroemer, G. and Zitvogel, L. 2008. Tumor Stress, Cell Death and the Ensuing Immune Response, *Cell Death and Differentiation*, 15:21-28, Nov.

384. Zhou, J., Zhang, S., Ong, C.N. and Shen, H.M. 2006. Critical Role of Pro-apoptotic Bcl-2 Family Members in Andrographolide-induced Apoptosis in Human Cancer Cells, *Biochemical Pharmacology*, 72:132-144, Apr.

385. Kalyanaraman, B., Joseph, J., Kalivendi, S., Wang, S., Konorev, E. and Kotamraju, S. 2002. Doxorubicin-induced Apoptosis: Implications in Cardiotoxicity, *Mol. Cell. Biochem.*, 234:119-124.

386. Hancock, J.T., Desikan, R. and Neill, S.J. 2001. Role of Reactive Oxygen Species in Cell Signalling Pathways, *Biochemical Society Transactions*, 29(2):345-350, Sept.

387. Kim, B.Y.S., Rutka, J.T., and Chan, W.C.W. 2010. Nanomedicine, *N. Engl. J. Med.*, 363:2434-2443, Dec.

388. Mushonga, P., Onani, M.O., Madiehe, A.M. and Meyer, M. 2013. One-pot Synthesis and Characterization of InP/ZnSe Semiconductor Nanocrystals, *Matt. Lett.*, 95:37-39, Jan.

APPENDIX

Table A1: p-Values calculated for the Lineweaver-Burke obtained enzyme kinetic parameters (Section 3.3.2, Table 3.8)

ANOVA Subjects	p-Values		
	Vmax	Km	kcat
No inhibitors vs I1	8.14E-01	1.76E-05	4.60E-01
No inhibitors vs I2	9.57E-01	2.14E-01	4.53E-01
No inhibitors vs CTX1	1.16E-02	8.43E-04	7.61E-03
No inhibitors vs CTX2	3.27E-02	1.47E-02	2.24E-02
I1 vs I2	8.03E-01	2.45E-02	5.75E-01
I1 vs CTX1	2.60E-01	1.63E-03	3.16E-01
I1 vs CTX2	3.34E-01	2.17E-03	3.54E-01
I2 vs CTX1	3.49E-01	6.97E-01	2.46E-01
I2 vs CTX2	3.15E-01	6.88E-01	1.61E-01
CTX1 vs CTX2	2.21E-01	3.22E-01	2.23E-01

*p-Values calculated with student's two-tailed T-test T-test.
$p < 0.05$ indicates statistical signifigance.

Table A2: p-Values calculated for the UV-Vis Spectra of AuNPs synthesized with different additon tempos (Section 4.3.2, Figure 4.7)

	p-Values					
	Slow-A	Slow-B	Slow-C	Fast-A	Fast-B	Fast-C
Slow-A	-	1.81E-06	2.12E-01	1.26E-35	4.56E-49	9.09E-37
Slow-B	-	-	9.06E-04	1.89E-20	1.83E-36	4.25E-23
Slow-C	-	-	-	4.16E-30	8.19E-30	1.61E-29
Fast-A	-	-	-	-	4.97E-08	1.47E-01
Fast-B	-	-	-	-	-	7.05E-05
Fast-C	-	-	-	-	-	-

*p-Values calculated with student's two-tailed T-test T-test.
$p < 0.05$ indicated statistical signifigance

Table A3: p-Values calculated for the EDX analysis of AuNPs synthesized with different additon tempos (Section 4.3.2, Table 4.1) as well as different amounts of NaBH$_4$ (Section 4.3.3, Table 4.4)

ANOVA Subjects	p-Values							
	Dry Weight	C	N	O	Na	P	Au	Cl
Fast vs. Slow	1.36E-01	5.59E-02	1.87E-01	8.32E-02	1.04E-01	2.44E-01	2.20E-01	2.77E-01
AuNP-GSH A vs. AuNP-GSH B	3.76E-01	4.70E-01	5.97E-01	1.04E-01	1.41E-01	2.06E-02	1.91E-01	3.95E-01
AuNP-GSH A vs. AuNP-GSH C	9.85E-01	4.49E-01	9.82E-01	6.23E-01	3.05E-01	1.45E-01	3.24E-01	4.33E-01
AuNP-GSH A vs. AuNP-GSH D	5.47E-01	4.36E-01	5.78E-01	2.47E-01	4.29E-01	2.97E-01	7.20E-01	5.42E-01
AuNP-GSH A vs. AuNP-PEI A	3.11E-04	6.71E-02	1.67E-01	6.18E-01	4.92E-02	1.93E-01	1.94E-01	2.56E-02
AuNP-GSH A vs. AuNP-PEI B	5.30E-03	9.14E-03	1.60E-02	2.92E-02	1.49E-02	2.14E-02	9.84E-01	3.41E-01
AuNP-GSH A vs. AuNP-PEI C	2.86E-03	1.67E-02	1.54E-03	9.45E-01	1.50E-01	1.59E-01	7.61E-01	5.64E-01
AuNP-GSH A vs. AuNP-PEI D	4.59E-03	2.47E-02	1.90E-03	2.36E-01	2.97E-02	1.64E-03	6.89E-01	5.73E-01
AuNP-GSH B vs. AuNP-GSH C	1.07E-01	2.84E-01	1.45E-01	7.86E-02	4.08E-01	4.36E-01	3.98E-01	9.29E-02
AuNP-GSH B vs. AuNP-GSH D	5.23E-02	1.46E-01	8.25E-01	1.84E-03	7.54E-01	4.60E-01	2.80E-01	5.08E-01
AuNP-GSH B vs. AuNP-PEI A	3.16E-03	1.14E-01	2.51E-01	2.85E-01	4.75E-02	2.96E-01	3.63E-01	3.10E-02
AuNP-GSH B vs. AuNP-PEI B	3.10E-03	6.05E-03	1.13E-02	5.58E-01	9.42E-01	6.10E-02	4.48E-04	4.71E-04
AuNP-GSH B vs. AuNP-PEI C	1.09E-02	2.41E-03	5.48E-03	2.58E-01	4.39E-01	5.83E-01	1.66E-02	7.98E-02
AuNP-GSH B vs. AuNP-PEI D	2.50E-04	1.25E-03	7.27E-04	1.97E-01	6.47E-02	1.06E-02	2.26E-02	8.42E-03
AuNP-GSH C vs. AuNP-GSH D	5.86E-01	6.80E-01	6.51E-01	6.69E-02	5.53E-01	5.13E-01	4.37E-01	7.74E-01
AuNP-GSH C vs. AuNP-PEI A	5.26E-03	1.14E-01	1.92E-01	5.71E-01	5.19E-02	4.22E-01	5.95E-01	2.94E-02
AuNP-GSH C vs. AuNP-PEI B	1.62E-03	6.06E-03	7.54E-03	1.83E-01	1.13E-02	2.35E-01	4.61E-03	1.31E-04
AuNP-GSH C vs. AuNP-PEI C	1.11E-02	1.98E-03	7.10E-03	8.33E-01	1.31E-01	9.81E-01	1.15E-02	8.03E-02
AuNP-GSH C vs. AuNP-PEI D	1.45E-03	6.87E-04	1.57E-03	4.15E-01	1.77E-02	1.74E-01	9.89E-02	1.03E-02
AuNP-GSH D vs. AuNP-PEI A	1.15E-03	1.14E-01	3.72E-02	9.90E-01	7.63E-02	6.90E-01	3.38E-01	3.44E-02
AuNP-GSH D vs. AuNP-PEI B	4.40E-03	6.31E-03	2.13E-02	2.94E-02	1.62E-01	8.05E-01	5.77E-01	2.54E-02
AuNP-GSH D vs. AuNP-PEI C	8.20E-03	2.28E-03	3.25E-02	3.64E-01	8.61E-01	6.75E-01	2.52E-01	8.23E-02
AuNP-GSH D vs. AuNP-PEI D	3.85E-04	8.12E-04	2.88E-02	1.72E-02	1.82E-01	9.14E-01	8.40E-01	7.82E-03
AuNP-PEI A vs. AuNP-PEI B	6.46E-01	5.98E-02	3.31E-02	3.14E-01	6.99E-02	6.64E-01	4.46E-02	1.05E-01
AuNP-PEI A vs. AuNP-PEI C	9.55E-02	1.35E-01	9.63E-02	3.54E-01	6.52E-02	3.05E-01	4.03E-02	1.73E-02
AuNP-PEI A vs. AuNP-PEI D	6.85E-02	2.31E-01	7.57E-02	3.07E-01	7.77E-02	6.02E-01	7.14E-02	7.88E-02
AuNP-PEI B vs. AuNP-PEI C	1.65E-01	3.23E-01	4.21E-01	2.82E-01	4.72E-02	3.47E-02	2.49E-01	3.05E-01
AuNP-PEI B vs. AuNP-PEI D	1.48E-01	2.87E-01	4.98E-01	5.21E-01	1.94E-01	4.20E-01	3.47E-01	1.36E-01
AuNP-PEI C vs. AuNP-PEI D	9.76E-01	2.80E-01	2.84E-01	3.05E-01	9.69E-04	1.07E-01	2.81E-01	7.32E-01

*p-Values calculated with student's two-tailed T-test T-test. p < 0.05 indicated statistical signifigance.
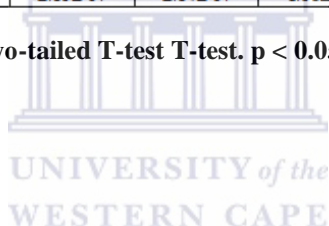
Table A4: p-Values calculated determined for different % aurate salt used during AuNP synthesis (Sections 4.3.2 and 4.3.3, Table 4.2 and Table 4.5)

ANOVA Subjects	p-Value	
	%Au Used	% Au Lost
Fast vs. Slow	2.20E-01	2.20E-01
AuNP-GSH A vs. AuNP-GSH B	1.91E-01	1.91E-01
AuNP-GSH A vs. AuNP-GSH C	3.24E-01	3.24E-01
AuNP-GSH A vs. AuNP-GSH D	7.20E-01	7.20E-01
AuNP-GSH A vs. AuNP-PEI A	1.94E-01	1.94E-01
AuNP-GSH A vs. AuNP-PEI B	9.84E-01	9.84E-01
AuNP-GSH A vs. AuNP-PEI C	7.61E-01	7.61E-01
AuNP-GSH A vs. AuNP-PEI D	6.89E-01	6.89E-01
AuNP-GSH B vs. AuNP-GSH C	3.98E-02	3.98E-02
AuNP-GSH B vs. AuNP-GSH D	2.80E-01	2.80E-01
AuNP-GSH B vs. AuNP-PEI A	3.63E-01	3.63E-01
AuNP-GSH B vs. AuNP-PEI B	4.48E-04	4.48E-04
AuNP-GSH B vs. AuNP-PEI C	1.66E-02	1.66E-02
AuNP-GSH B vs. AuNP-PEI D	2.26E-02	2.26E-02
AuNP-GSH C vs. AuNP-GSH D	4.37E-01	4.37E-01
AuNP-GSH C vs. AuNP-PEI A	5.95E-01	5.95E-01
AuNP-GSH C vs. AuNP-PEI B	4.61E-03	4.61E-03
AuNP-GSH C vs. AuNP-PEI C	1.15E-02	1.15E-02
AuNP-GSH C vs. AuNP-PEI D	9.89E-02	9.89E-02
AuNP-GSH D vs. AuNP-PEI A	3.38E-01	3.38E-01
AuNP-GSH D vs. AuNP-PEI B	5.77E-01	5.77E-01
AuNP-GSH D vs. AuNP-PEI C	2.52E-01	2.52E-01
AuNP-GSH D vs. AuNP-PEI D	8.40E-01	8.40E-01
AuNP-PEI A vs. AuNP-PEI B	4.46E-02	4.46E-02
AuNP-PEI A vs. AuNP-PEI C	4.03E-02	4.03E-02
AuNP-PEI A vs. AuNP-PEI D	7.14E-02	7.14E-02
AuNP-PEI B vs. AuNP-PEI C	2.49E-01	2.49E-01
AuNP-PEI B vs. AuNP-PEI D	3.47E-01	3.47E-01
AuNP-PEI C vs. AuNP-PEI D	2.81E-01	2.81E-01

*p-Values calculated with student's two-tailed T-test T-test.
 $p < 0.05$ indicated statistical signifigance.

Table A5: p-Values calculated for the time-based DOX release from AuNP-PEI A surface (Section 4.4.4, Figure 4.30)

Time (min)	p-Values
30:60	3.29E-04
60:180	3.57E-04
180:720	6.89E-01
720:1440	1.70E-01

*p-Values calculated with student's two-tailed T-test T-test.
 $p < 0.05$ indicated statistical signifigance.

Table A6: p-Values calculated for A2780/A2780cis response to PEI and DOX dose-response assays (Figure 5.4, Section 5.2.2.1)

	A2780		A2780cis	
uM	DOX	PEI	DOX	PEI
250 vs. 125	3.00E-01	1.14E-01	3.71E-02	3.89E-01
250 vs. 63	2.01E-01	3.42E-01	1.35E-01	3.26E-01
250 vs. 32	7.44E-03	1.32E-02	1.20E-01	6.40E-01
250 vs. 16	1.43E-02	3.01E-02	8.05E-02	7.83E-01
250 vs. 8	2.01E-02	7.26E-03	1.35E-01	2.20E-02
250 vs. 4	5.45E-03	1.17E-03	1.27E-01	1.37E-01
125 vs. 63	6.94E-01	2.56E-01	2.69E-01	9.64E-01
125 vs. 32	4.57E-02	1.07E-02	1.17E-01	5.04E-01
125 vs. 16	3.39E-02	3.47E-02	1.69E-01	1.89E-01
125 vs. 8	2.69E-02	1.29E-02	5.91E-02	5.64E-02
125 vs. 4	1.65E-02	1.71E-03	1.33E-01	5.15E-02
63 vs. 32	1.51E-02	7.65E-01	2.79E-01	6.40E-01
63 vs. 16	1.14E-02	1.20E-01	6.67E-01	3.07E-01
63 vs. 8	8.71E-03	8.91E-02	1.35E-01	3.10E-02
63 vs. 4	4.11E-03	2.78E-02	2.86E-01	2.32E-02
32 vs. 16	4.32E-02	6.19E-02	8.14E-01	7.83E-01
32 vs. 8	5.70E-02	2.42E-02	1.37E-01	1.67E-01
32 vs. 4	3.56E-02	7.67E-03	4.59E-01	2.96E-02
16 vs. 8	1.46E-01	4.45E-01	4.56E-01	2.20E-02
16 vs. 4	7.33E-01	3.03E-01	4.89E-01	5.76E-02
8 vs. 4	7.20E-01	6.15E-02	5.82E-01	1.37E-01

*p-Values calculated with student's two-tailed T-test. $p < 0.05$ indicated statistical signifigance.

Table A7: p-Values calculated for A2780/A2780cis dose-response to differentially synthesized AuNPs (Figure 5.5, Section 5.2.2.2)

		p-Values		
		A2780		
pM	AuNP-PEI A	AuNP-PEI B	AuNP-PEI C	AuNP-PEI D
1000:500	2.56E-03	5.61E-02	1.26E-02	8.98E-03
500:250	1.92E-02	5.89E-03	1.63E-02	6.72E-03
250:125	5.33E-01	3.09E-01	7.06E-02	8.64E-02
125:62	9.59E-01	9.45E-02	2.91E-01	5.30E-01
62:32	3.15E-01	3.24E-01	9.17E-01	6.47E-01

		A2780cis		
pM	AuNP-PEI A	AuNP-PEI B	AuNP-PEI C	AuNP-PEI D
1000:500	9.77E-03	4.33E-01	1.13E-02	4.15E-03
500:250	1.25E-01	5.02E-02	4.31E-04	4.84E-03
250:125	1.65E-01	2.23E-02	7.47E-04	2.97E-03
125:62	9.31E-01	8.63E-01	1.58E-01	5.15E-02
62:32	7.64E-01	5.68E-01	2.46E-01	4.93E-01

*p-Values calculated with ANOVA (single factor). $p < 0.05$ indicated statistical signifigance.

Table A8: p-Values calculated for A2780/A2780cis dose-response DOX loaded AuNPs (Figure 5.6, Section 5.2.3.2)

p-Values				
A2780				
pM	AuNP-PEI	10% PEG	20% PEG	30% PEG
1000 (42):500(21)	1.21E-03	7.27E-04	9.04E-04	6.92E-01
500(21):250(10.5)	3.69E-04	5.31E-03	1.42E-01	3.60E-03
250(10.5):125(5.3)	5.96E-01	8.64E-03	2.09E-01	2.43E-01
A2780cis				
pM	AuNP-PEI	10% PEG	20% PEG	30% PEG
1000 (42):500(21)	2.66E-03	1.28E-03	8.18E-01	1.51E-01
500(21):250(10.5)	9.66E-03	4.61E-03	5.62E-03	2.35E-01
250(10.5):125(5.3)	6.07E-01	1.19E-02	3.45E-02	1.03E-02

*p-Values calculated with ANOVA (single factor). $p < 0.05$ indicated statistical signifigance.

Table A9: p-Values calculated for A2780cis apoptosis in response to various stimulants (Figure 5.8, Section 5.2.3.3)

p-Values	
AuNP-PEI:Control	4.17E-02
30% PEG:Control	5.57E-03
H2O2:Control	4.80E-05
DOX:Control	9.42E-04
AuNP-PEI:30% PEG	1.44E-02
AuNP-PEI:H2O2	8.87E-05
AuNP-PEI:DOX	2.96E-02
30% PEG:H2O2	3.73E-01
30% PEG:Dox	1.03E-01
H2O2:Dox	4.46E-03

*p-Values calculated with ANOVA (single factor). $p < 0.05$ indicated statistical signifigance.

Table A10: p-Values calculated for A2780cis GSH/GSSG deplation in response to various stimulants (Figure 5.12, Section 5.2.3.5)

p-Values		
	GSH Depletion	GSSG Depletion
AuNP-PEI:Control	1.35E-02	2.67E-02
30% PEG:Control	2.02E-03	2.94E-04
H2O2:Control	1.93E-03	4.25E-05
DOX:Control	1.70E-03	6.19E-05
AuNP-PEI:30% PEG	3.86E-03	3.47E-03
AuNP-PEI:H2O2	6.73E-03	3.72E-03
AuNP-PEI:DOX	5.01E-03	3.78E-03
H2O2:DOX	3.05E-01	5.28E-01

*p-Values calculated with ANOVA (single factor). $p < 0.05$ indicated statistical signifigance.

Table A11: Sequence alignment of wild type MMP2 (Genbank Accession: NM_004530.4) with the utilized cDNA seq (*BamHI* is highlighted)

```
                   Score     Expect    Identities      Gaps    Strand
                 1595 bits(1768) 0.0    1432/1797(80%)  0/1797(0%) Plus/Plus

Query*  1    ATGGAGgcgctgatggcgcgcggcgcgctgaccggcccgctgcgcgcgctgtgcctgctg   60
             ||||||||||| |||||  ||  ||||||| || || ||  ||| |  ||||| || || |||
Sbjct† 312   ATGGAGGCGCTAATGGCCCGGGGCGCGCTCACGGGTCCCCTGAGGGCGCTCTGTCTCCTG   371

Query  61    ggctgcctgctgAGCCATGCGGCGGCGGCGCCGAGCCCGATTATTAAATTTCCGGGCGAT   120
             |||||||||||||||  || || |||||||       || || || || || |||||||
Sbjct 372    GGCTGCCTGCTGAGCCACGCCGCCGCCGCGCCGTCGCCCATCATCAAGTTCCCCGGCGAT   431

Query  121   GTGGCGCCGAAAACCGATAAAGAACTGGCGGTGCAGTATCTGAACACCTTTTATGGCTGC   180
             || || || ||||| || ||||| |||| |||| ||||| ||||||||| ||||||||||
Sbjct 432    GTCGCCCCCAAAACGGACAAAGAGTTGGCAGTGCAATACCTGAACACCTTCTATGGCTGC   491

Query  181   CCGAAAGAAAGCTGCAACCTGTTTGTGCTGAAAGATACCCTGaaaaaaaTGCAGAAACTG   240
             || || || |||||||||||||||||||||||||||||| || || || || |||||||| |
Sbjct 492    CCCAAGGAGAGCTGCAACCTGTTTGTGCTGAAGGACACACTAAAGAAGATGCAGAAGTTC   551

Query  241   TTTGGCCTGCCGCAGACCGGCGATCTGGATCAGAACACCATTGAAACCATGCGCAAACCG   300
             ||||| ||||| ||||| || ||||| || ||||| ||||| || || |||||| || ||
Sbjct 552    TTTGGACTGCCCCAGACAGGTGATCTTGACCAGAATACCATCGAGACCATGCGGAAGCCA   611

Query  301   CGCTGCGGCAACCCGGATGTGGCGAACTATAACTTTTTTCCGCGCAAACCGAAATGGGAT   360
             |||||||||||||||| |||||||| |||| |||| || ||| || |||| ||| |||||
Sbjct 612    CGCTGCGGCAACCCAGATGTGGCCAACTACAACTTCTTCCCTCGCAAGCCCAAGTGGGAC   671

Query  361   AAAAACCAGATTACCTATCGCATTATTGGCTATACCCCGGATCTGGATCCGGAAACCGTG   420
             || |||||||| ||  || |    | |||||||  || || |||||| ||  || || |||
Sbjct 672    AAGAACCAGATCACATACAGGATCATTGGCTACACACCTGATCTGGACCCAGAGACAGTG   731

Query  421   GATGATGCGTTTGCGCGCGCGTTTCAGGTGTGGAGCGATGTGACCCCGCTGCGCTTTAGC   480
             ||||||||| ||||| || || || ||||||||||||||||||||| |||||| ||| |
Sbjct 732    GATGATGCCTTTGCTCGTGCCTTCCAAGTCTGGAGCGATGTGACCCCACTGCGGTTTTCT   791

Query  481   CGCATTCATGATGGCGAAGCGGATATTATGATTAACTTTGGCCGCTGGGAACATGGCGAT   540
             || || |||||||| ||||| || ||  || || |||||||||||||||| |||||||||
Sbjct 792    CGAATCCATGATGAGAGGGCAGACATCATGATCAACTTTGGCCGCTGGGAGCATGGCGAT   851

Query  541   GGCTATCCGTTTGATGGCAAAGATGGCCTGCTGGCGCATGCGTTTGCGCCGGGCACCGGC   600
             || || || ||||| ||||| ||||| ||  |||| ||||| ||||| ||  || |||||
Sbjct 852    GGATACCCCTTTGACGGTAAGGACGGACTCCTGGCTCATGCCTTCGCCCCCAGGCACTGGT   911

Query  601   GTGGGCGGCGATAGCCATTTTGATGATGATGAACTGTGGACCCTGGGCGAAGGCCAGGTG   660
             || || || ||   ||||||||||||| |||| ||||| || |||| |||||||| |||
Sbjct 912    GTTGGGGGAGACTCCCATTTTGATGACGATGAGCTATGGACCTTGGGAGAAGGCCAAGTG   971

Query  661   GTGCGCGTGAAATATGGCAACGCGGATGGCGAATATTGCAAATTTCCGTTTCTGTTTAAC   720
             || || || ||||| ||||| ||||| |||| ||  || || |||||  ||   |||||
Sbjct 972    GTCCGTGTGAAGTATGGGAACGCCGATGGGGAGTACTGCAAGTTCCCCCTTCTTGTTCAAT   1031

Query  721   GGCAAAGAATATAACAGCTGCACCGATACCGGCCGCAGCGATGGCTTTCTGTGGTGCAGC   780
             ||||| || || |||||||||||||| ||||||||||||||||||||||  ||||||  |
Sbjct 1032   GGCAAGGAGTACAACAGCTGCACTGATACCGGCCGCAGCGATGGCTTCCTCTGGTGCTCC   1091

Query  781   ACCACCTATAACTTTGAAAAAGATGGCAAATATGGCTTTTGCCCGCATGAAGCGCTGTTT   840
             |||||||| ||||||||  || |||||||| |||||| ||||||| ||||||  || |||
Sbjct 1092   ACCACCTACAACTTTGAGAAGGATGGCAAGTACGGCTTCTGTCCCCATGAAGCCCTGTTC   1151

Query  841   ACCATGGGCGGCAACGCGGAAGGCCAGCCGTGCAAATTTCCGTTTCGCTTTCAGGGCACC   900
             |||||||||||||||||| |||||||||| ||||| ||||| ||||| || |||||||||
Sbjct 1152   ACCATGGGCGGCAACGCTGAAGGACAGCCCTGCAAGTTTCCATTCCGCTTCCAGGGCACA   1211

Query  901   AGCTATGATAGCTGCACCACCGAAGGCCGCACCGATGGCTATCGCTGGTGCGGCACCACC   960
             || |||||  ||||||||||| ||  |||||||||||||| ||||||||||||||||||
Sbjct 1212   TCCTATGACAGCTGCACCACTGAGGGCCGCACGGATGGCTACCGCTGGTGCGGCACCACT   1271

Query  961   GAAGATTATGATCGCGATAAAAAATATGGCTTTTGCCCGGAAACCGCGATGAGCACCGTG   1020
             || || || || || || ||  || |||||| || ||  || |||| || |||  |||||
Sbjct 1272   GAGGACTACGACCGCGACAAGAAGTATGGCTTCTGCCCTGAGACCGCCATGTCCACTGTT   1331

Query  1021  GGCGGCAACAGCGAAGGCGCGCCGTGCGTGTTTCCGTTTACCTTTCTGGGCAACAAATAT   1080
             || || ||  || ||||  |||| ||| || || |||| || || || |||||||||||
Sbjct 1332   GGTGGGAACTCAGAAGGTGCCCCCTGTGTCTTCCCCTTCACTTTCCTGGGCAACAAATAT   1391
```

```
Query  1081  GAAAGCTGCACCAGCGCGGGCCGCAGCGATGGCAAAATGTGGTGCGCGACCACCGCGAAC  1140
             || |||||||||||||| ||||||||| || || || |||||||| |||||||| || |||
Sbjct  1392  GAGAGCTGCACCAGCGCCGGCCGCAGTGACGGAAAGATGTGGTGTGCGACCACAGCCAAC  1451

Query  1141  TATGATGATGATCGCAAATGGGGCTTTTGCCCGGATCAGGGCTATAGCCTGTTTCTGGTG  1200
             || |||||||| ||||| |||||||| ||||| || || || || |||||||| || |||
Sbjct  1452  TACGATGATGACCGCAAGTGGGGCTTCTGCCCTGACCAAGGGTACAGCCTGTTCCTCGTG  1511

Query  1201  GCGGCGCATGAATTTGGCCATGCGATGGGCCTGGAACATAGCCAGGATCCGGGCGCGCTG  1260
             || || || || |||||||| || ||||| ||||| ||    ||| || || || || |||
Sbjct  1512  GCAGCCCACGAGTTTGGCCACGCCATGGGGCTGGAGCACTCCCAAGACCCTGGGGCCCTG  1571

Query  1261  ATGGCGCCGATTTATACCTATACCAAAAACTTTCGCCTGAGCCAGGATGATATTAAAGGC  1320
             ||||| || ||||| ||||| ||||| ||||| || |||  |||||||||| || || |||
Sbjct  1572  ATGGCACCCATTTACACCTACACCAAGAACTTCCGTCTGTCCCAGGATGACATCAAGGGC  1631

Query  1321  ATTCAGGAACTGTATGGCGCGAGCCCGGATATTGATCTGGGCACCGGCCCGACCCCGACC  1380
             ||||||||| || ||||| ||    || || ||||| || |||||||||||| ||||| ||
Sbjct  1632  ATTCAGGAGCTCTATGGGGCCTCTCCTGACATTGACCTTGGCACCGGCCCCACCCCCACG  1691

Query  1381  CTGGGCCCGGTGACCCCGGAAATTTGCAAACAGGATATTGTGTTTGATGGCATTGCGCAG  1440
             ||||||||| || || || || || |||||||||||| ||||| |||||||||||| ||||
Sbjct  1692  CTGGGCCCTGTCACTCCTGAGATCTGCAAACAGGACATTGTATTTGATGGCATCGCTCAG  1751

Query  1441  ATTCGCGGCGAAAttttttttttttAAAGATCGCTTTATTTGGCGCACCGTGACCCCGCGC  1500
             || || || || || || || || || || || |||||||| || ||||| || |||| ||
Sbjct  1752  ATCCGTGGTGAGATCTTCTTCTTCAAGGACCGGTTCATTTGGCGGACTGTGACGCCACGT  1811

Query  1501  GATAAACCGATGGGCCCGCTGCTGGTGGCGACCTTTTGGCCGGAACTGCCGGAAAAAATT  1560
             || || || |||||| ||||||||||| ||||| ||||| || |||||||| |||||| ||
Sbjct  1812  GACAAGCCCATGGGGCCCCTGCTGGTGGCCACATTCTGGCCTGAGCTCCCGGAAAAGATT  1871

Query  1561  GATGCGGTGTATGAAGCGCCGCAGGAAGAAAAAGCGGTGTTTTTTGCGGGCAACGAATAT  1620
             |||||||| || || || || ||||| || || || |||||| ||||| || || |||||
Sbjct  1872  GATGCGGTATACGAGGCCCCACAGGAGGAGAAGGCTGTGTTCTTTGCAGGGAATGAATAC  1931

Query  1621  TGGATTTATAGCGCGAGCACCCTGGAACGCGGCTATCCGAAACCGCTGACCAGCCTGGGC  1680
             ||||| ||    || |||||||||||||| || ||| || || || |||||||||||||||
Sbjct  1932  TGGATCTACTCAGCCAGCACCCTGGAGCGAGGGTACCCCAAGCCACTGACCAGCCTGGGA  1991

Query  1681  CTGCCGCCGGATGTGCAGCGCGTGGATGCGGCGTTTAACTGGAGCaaaaacaaaaaaaaCC  1740
             ||||| || ||||| ||||| ||||| ||||| ||||||||||||| |||||||||| || ||
Sbjct  1992  CTGCCCCCTGATGTCCAGCGAGTGGATGCCGCCTTTAACTGGAGCAAAAACAAGAAGACA  2051

Query  1741  TATACCTTTGCGGGCGATAAATTTTGGCGCTATAACGAAGTGaaaaaaaaaaTGGAT  1797
             || | |||||| || |||||||| ||| ||| || || || ||||| || ||||||||
Sbjct  2052  TACATCTTTGCTGGAGACAAATTCTGGAGATACAATGAGGTGAAGAAGAAAATGGAT  2108
```

* cDNA MMP2

† Wild type MMP2